Design Optimization of Flexible Aircraft Wings Using Tow-steered Composites
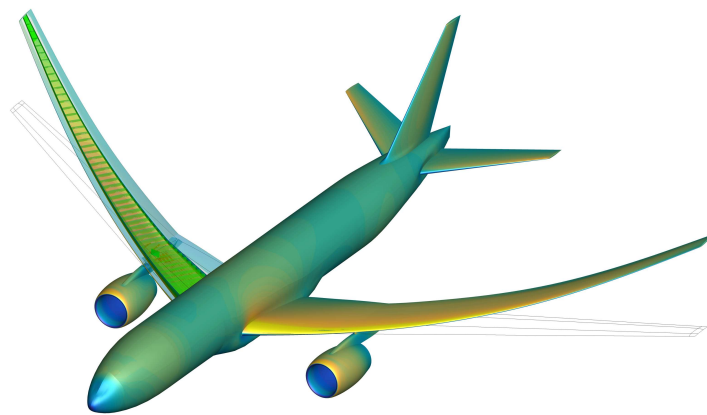
by

Timothy R. Brooks

A dissertation submitted in partial fulfillment
of the requirements for the degree of
Doctor of Philosophy
(Aerospace Engineering)
in the University of Michigan
2018

Doctoral Committee:

Professor Joaquim R. R. A. Martins, Chair
Professor Carlos E. S. Cesnik
Professor Kazuhiro Saitou
Professor Veera Sundararaghavan

Timothy R. Brooks

timryanb@umich.edu

ORCID iD: 0000-0002-0884-9688

To my parents, without their support and sacrifice I could
not have accomplished this work.

ACKNOWLEDGEMENTS

There are many people that I must acknowledge for helping to make the achievement of this work possible. First, it is imperative that I recognize my advisor, Professor Joaquim R. R. A. Martins. His passion for optimization in engineering (and life) has inspired me and my work since I first took his aircraft design course in my undergraduate studies. It is under his guidance that I have become the researcher that I am today and for this I am sincerely grateful.

I would also like to thank the remaining members of my doctoral committee—Professor Carlos Cesnik, Professor Veera Sundararaghavan, and Professor Kazuhiro Saitou—for their time and consideration. Their patience, insight, and encouragement have greatly increased the quality of the work presented here.

This accomplishment would not have been possible without the efforts of the previous MDOLab alumni, whose contributions form the foundation for this work. Specifically, I would like to acknowledge Dr. Gaetan K. W. Kenway for his help in defining the uCRM aeroelastic benchmark models developed and used throughout the remainder of this thesis. I also must acknowledge Professor Graeme J. Kennedy, whose guidance and well-written finite-element solver made many of the developments in this work possible. Furthermore, I would also like to thank the members of my research group: Ney Secco, Eirikur Jonsson, Sicheng He, Sandy Mader, Justin Gray, Nicolas Bons, Shamsheer Chauhan, and John Jasa. It is thanks to them that my time in the Ph.D. program at Michigan has been such a unique pleasure.

Lastly, but most certainly not least, I must acknowledge my parents. Looking back, it

has been a long eight years since I first started my college career. Despite the many twists and turns I have encountered on this journey, your support has remained relentless. I could never repay you for all that you have done, but know that I will forever be grateful.

TABLE OF CONTENTS

LIST OF FIGURES

LIST OF TABLES

LIST OF APPENDICES

LIST OF ABBREVIATIONS

AD automatic differentiation

ADODG aerodynamic design optimization discussion group

AFP automatic fiber placement

AIAA American Institute of Aeronautics and Astronautics

AR aspect ratio

BDF bulk data file

BVP boundary value problem

CFD computational fluid dynamics

CLT classical laminate theory

CNC computer numerically controlled

CRM common research model

CSM computational structural mechanics

DMO discrete material optimization

DOC direct operating cost

DOF degrees of freedom

DPW drag prediction workshop

FAA Federal Aviation Administration

FEA finite element analysis

FEM finite element method

FFD free form deformation

FSDT first-order shear deformation theory

GA genetic algorithm

GeoMACH Geometry-centric MDAO of aircraft configurations with high fidelity

ICAO International Civil Aviation Organization

KKT Karush-Kuhn-Tucker

KS Kreisselmeier–Steinhauser

MAC mean aerodynamic chord

MACH MDO of aircraft configurations with high fidelity

MDO multidisciplinary design optimization

MITC mixed interpolation of tensorial components

MTOW maximum take off weight

NASA National Aeronautics and Space Administration

OML outer mold line

RANS Reynolds-averaged Navier–Stokes

SA Spalart–Allmaras

SNOPT Sparse Nonlinear Optimizer

TACS Toolkit for Analysis of Composite Structures

uCRM undeflected common research model

VAT variable angle tow

ABSTRACT

In the last 30 years since their introduction into aerospace applications, composites have become increasingly used, making up as much as 50% of modern aircraft by weight. Considering this fact, it is surprising that most aircraft today are only scratching the surface of the true potential of composite technology with traditional uniaxial fibers. With the introduction of automatic fiber placing machines, the fiber direction in laminae is now allowed to be steered spatially throughout each layer. This process is known as composite tow steering and has been shown to have improved performance over its uniaxial fiber counterpart with no additional weight penalty.

With modern aircraft moving toward larger and more flexible wing designs, it is reasonable to expect that a tow-steered composite wing structure can be tailored to outperform its unsteered counterpart. However, given the highly coupled nature of the aerodynamics and structural response of the problem it is not obvious nor intuitive to find the composite fiber pattern that would yield an optimal result. High-fidelity aerostructural solvers have been proven effective for accurately capturing the trade-offs between relevant design disciplines for such aircraft. Such solvers allow for the performance of tow-steered wing structures to be analyzed in great detail. By complementing these solvers with gradient-based numerical optimization, high dimensional design spaces can be explored relatively efficiently. Such methods make it possible to quantify the maximum benefits offered by tow-steered wing structures.

In this thesis, a number of aerostructural optimizations are performed to compare the performance of aluminum, conventional composite and tow-steered composite wing de-

signs. For these studies, a set of benchmark aeroelastic aircraft models are developed based on the NASA Common Research Model. A design parameterization scheme, constitutive model, and relevant manufacturing constraints are then developed for tow-steered structures. A fuel burn minimization is then performed for a tow-steered and conventional composite wing design. When applied to a Boeing-777-type aircraft wing, tow steering is found to offer improvements of up to 2.4% in fuel savings and 24% in wing weight under the limited set of design constraints, relative to the optimized conventional composite design. This improvement was found to be due to a combination of improved passive aeroelastic tailoring and local strength tailoring in high-stressed regions in the tow-steered structure. For a higher aspect ratio wing design improvements of up to 1.5% and 14% in fuel savings and wing weight are found. Finally, the trade-off between structural weight and fuel burn performance is explored through a Pareto front study. This study compares the performance of an aluminum, conventional and tow-steered composite wing. In this study, it is found that when wing planform is free to vary, tow-steering offers improvements of up to 1.5% in fuel savings for a fuel-burn-optimized design and 1.6% in total aircraft weight savings for the structural-weight-optimized.

CHAPTER 1

Introduction

1.1 Motivation

The commercial airline industry is one of the largest transportation sectors in the world. Commercial aircraft carry 4 billion passengers worldwide per year and this number is forecasted to increase at a rate of 3.6% per year [1]. By 2036 this number is projected to nearly double, growing to 7.8 billion passengers per year. While this rate of growth is impressive, it is outpacing the annual increase in aircraft efficiency. Figure 1.1 shows that as a result of this growth, CO_2 emissions from the aviation industry is still on the rise. This trend is in spite of an improvement of 45% in fuel efficiency of new aircraft from 1968 to 2014, or an annual reduction of 1.3% per year [2].

This trend has caused an increase in concerns over the environmental impact of aviation. These concerns led to the International Civil Aviation Organization (ICAO), the international regulator for commercial aviation industry, to set a goal in 2009 of increasing the annual improvement in fuel efficiency of new aircraft to 2.0% until 2020 and achieving carbon neutral growth from 2020 on [4]. Studies by authors like Kharina and Rutherford [2] have shown that, without a significant improvement, the current trend in efficiency is not on track to meet the ICAO's goals by 2020.

This has lead aircraft manufacturers to consider new ways of improving efficiency in next-generation aircraft designs. Some of these studies have focused on pursuing these performance improvements through unconventional design concepts such as blended wing bodies, electric propulsion aircraft, and truss braced wings. While others have focused on new manufacturing techniques that would improve the performance of already flying conventional tube-and-wing type aircraft. The focus of this work will be on the latter.

One manufacturing technique of particular interest is composite tow steering. Composite materials have recently seen large growth in use in aircraft structures with the introduction of the automatic fiber placement (AFP) machine. Tow steering is a manufacturing
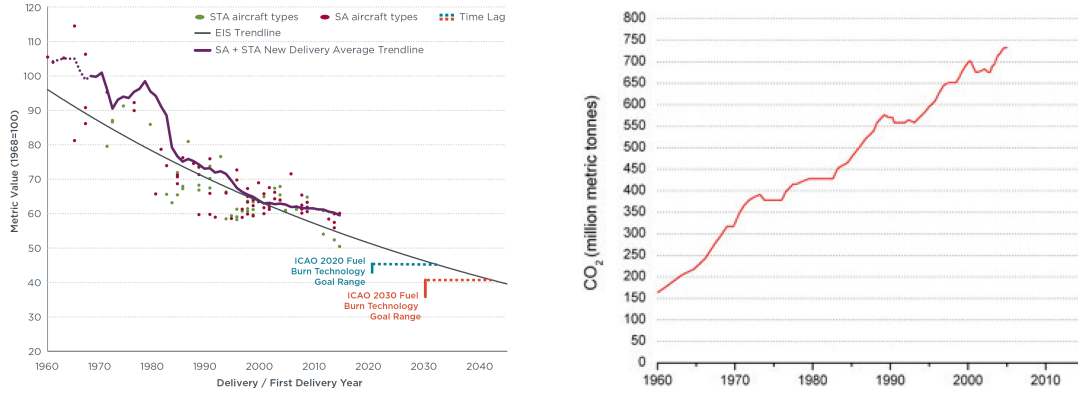
Figure 1.1: Comparison of trend in new commercial aircraft fuel burn (left) [2] and CO_2 emissions (right) [3] show emissions still increasing despite annual improvement in aircraft efficiency.

technique that improves upon these designs by taking full advantage of the anisotropic behavior of the composite materials. When applied to flexible-wing design tow-steered composites provide a number of theoretical advantages to their conventional composite counterpart. The technique has yet to be applied and tested on full scale aircraft structures, leaving the extents of the benefits still largely unknown.

The goal of this work is to use multidisciplinary design optimization (MDO) to quantify the benefit of composite tow steering for flexible wing design relative to the conventional structural design techniques used today. To motivate this, a review of the relevant topics and concepts will be given. First, we will start with a general overview of the AFP manufacturing process for composite structures and the state-of-the-art tow-steering composite design technique. Next, a general definition of aeroelastic tailoring will be provided along with past historical examples of its application in aeronautical design. Next, a summary of the general MDO approach will be given, followed by a review of previous works considering design optimization of tow-steered structures. This will be followed by a list of novel contributions to field of study that this thesis will provide. Finally, an outline of the remaining chapters of this thesis will be provided.

1.1.1 Automatic fiber placing/tow steering

Starting in 1966 carbon fiber-reinforced composites became readily available for commercial use [5]. These composite materials quickly gained popularity in the field of structural design, due to their high stiffness/strength-to-weight ratios. Despite this fact, composite materials have only relatively recently, in the past two decades, found their way onto primary structural components (wings, fuselages, stabilizers, etc.) in the aerospace design
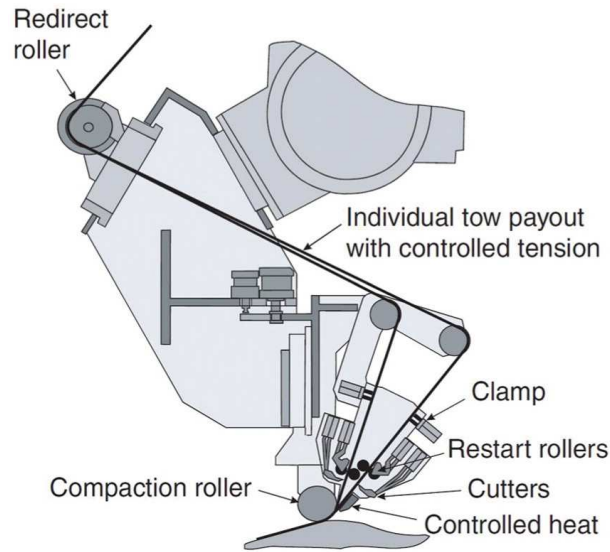
Figure 1.2: Schematic of Automated Fiber Placing machine tool [6]

industry. The reason for this delay is that prior to this period, the prepreg used to layup the composite laminate had to be cut and laid down by hand by highly-skilled technicians. This lead to an incredibly slow and expensive manufacturing process for large primary composite aerospace structures. This limitation initially relegated the use of composites to only smaller secondary components. What changed was the introduction of the AFP machine, which could efficiently lay up large composite structures automatically. This breakthrough lead to the current trend in wide-scale adoption of composite materials in primary aerospace structures seen today.

The earliest prototypes for composite laying AFP equipment were developed based on the tools of computer numerically controlled (CNC) machines for metallic structures [7]. One of the primary differences between the AFP and CNC design processes is that AFP can be considered a form of additive manufacturing, whereas CNC is subtractive. A schematic of an AFP machine is shown in Figure 1.2. The AFP layup process works as follows: first a continuous strip of resin-impregnated unidirectional fiber-reinforced tape is fed into the machine head, where it is heated up and rolled down to bond it to the surface of the mold used to define the structural shape. The structural surface can feature multiple directions of curvature. Subsequent layers of tape are then stacked in order to build up the composite laminate. The machine has the ability to cut and rotate the tape during the layup process.

The tow layup paths are defined automatically by a pre-set computer program. By specifying the tape paths to be parallel and straight within each layer and rotating the orientation of the tow paths layer to layer, a conventional quasi-isotropic composite laminate can be laid up relatively quickly and efficiently.

AFP has several advantages to hand-laid composite designs [8]:

- Less man-hours per produced part.

- Reduction in wasted material during layup.

- Elimination of human-based error sources.

- Composites can be laid up on geometrically complex structures.

- Reduced requirement for in-process inspection.

These factors lead to large-scale composite structures being able to be produced with relatively lower manufacturing cost and time. This innovation lead to the boom in the adoption of the AFP process, and consequently composite materials in primary aircraft structures, we see today. A list of aircraft designs utilizing AFP and their relevant components prior to the year 2000 is given in Table 1.1. To date, one of the largest applications of AFP in aerospace structures has been on the Boeing 787, whose fuselage and nose sections were designed through AFP, Figure 1.3.

Table 1.1: Aircraft designs utilizing AFP since 2000 [9].

Aircraft	Relevant Components
F-18 E/F	Inlet Duct, Aft Center Side Skins, Stabilator Skins
C-17 Globemaster	Fan Cowl Doors, Landing Gear Pods
Bell Agusta 609	Fuselage Panels
V-22 Osprey	Aft fuselage, Side Skins, Drag Angle, Sponsons, Grips
Premier I	Fuselage Sections
Hawker Horizon	Fuselage Sections
F22 Raptor	Stabilator Pivot Shaft
Sea Launch	Payload Fairing

It is important to note that there is no requirement that tow paths of the AFP must be straight and parallel. Indeed, AFP machines are capable of specifying general curvilinear tow paths in each layer of the laminate. This process is known as tow steering and provides the ability to locally specify the fiber direction for each layer of the laminate. Figure 1.4 shows an example exploded view of a typical conventional and tow-steered composite laminate. Tow steering provides two key theoretical advantages over conventional composites

(a) AFP layup of fuselage section [10]

(b) Completed fuselage section. Image copyright of Boeing.

Figure 1.3: AFP used extensively in design of Boeing 787 fuselage.

Conventional
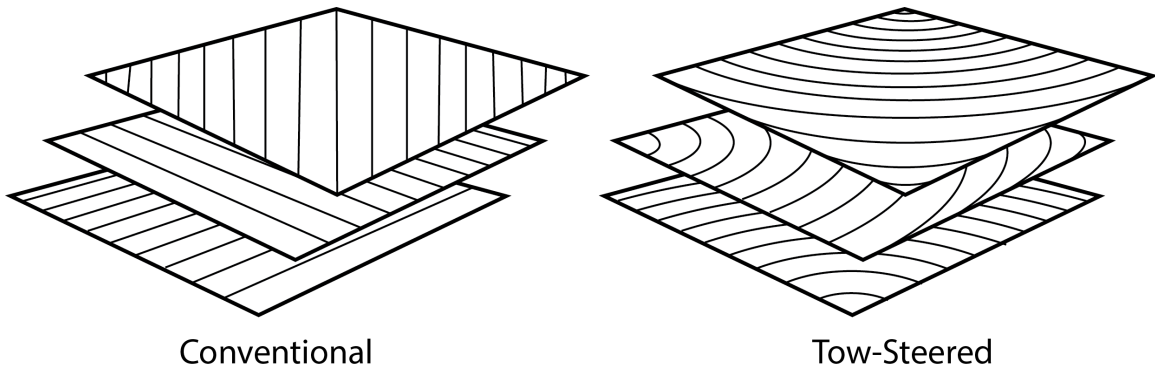
Tow-Steered

Figure 1.4: Example comparison of conventional (left) and tow-steered (right) layups

in wing design. The first being that tow steering allows the designer the freedom to take advantage of global tailoring, load alleviation through bend-twist coupling, in some areas, as will be discussed in detail in the following section. While other areas can be locally tailored by designing the tow paths to manipulate and align more closely with the expected critical structural load paths, increasing structural strength.

Tow steering still remains an area of active research, with much work still left to be done [11, 12]. Given that the structural composition of recent transport aircraft, such as the Boeing 787 and Airbus A350XWB, are made up of as much as 50% in advanced composite materials by structural weight [13, 14], it is surprising that aircraft manufactures still have yet to take full advantage of the benefits offered by their anisotropic nature. Part of the reason for this is that there is only limited work quantifying the benefits of adding tow steering into the composite design of complex structural components, such as the wing structure. Another challenge in the design of tow-steered structures is that it is not obvious nor intuitive what the tow paths should look like for a wing structure that takes maximal advantage

of directional stiffness properties. As mentioned previously, it is for these reasons that the benefits of tow-steered wing design will be studied through the use of MDO in this thesis.

1.1.2   Aeroelastic tailoring

In an effort to continually reduce fuel burn and improve aircraft efficiency modern commercial transport aircraft have been trending toward higher aspect ratio wing designs, in order to reduce aerodynamic induced drag. Increasing the aspect ratio of the wing has the often undesired effect of increasing the flexibility of the wing structure. As the flexibility of the structure increases, the deformation of the structure due to aerodynamic loading can become large enough to effect the aerodynamic performance of the aircraft. This leads to a complex coupling between the aerodynamic and structural performance of the aircraft, a multi-disciplinary field of interest known as aeroelasticity.

For many decades after the introduction of the first airplanes in the early 1900's the effects of aeroelasticity were largely seen as a nuisance. The nature of aeroelasticity was poorly understood at the time, often leading to deviations in aircraft performance and unforeseen static and dynamic failure modes that could not be explained by single discipline analysis. As the theory of aeroelasticity began to be developed in the following decades a greater insight into physical nature of the coupled aerodynamic and structural disciplines emerged. Further improvements in the field came as numerical methods became readily available, improving the accuracy and predictive capabilities of the field. In recent decades, the understanding of aeroelastic design has become great enough that researchers have begun looking at ways of taking advantage of its effects in the design of flexible aircraft structures. This approach in aircraft design is a concept known as aeroelastic tailoring.

Shirk et al. [15] define aeroelastic tailoring as "the embodiment of directional stiffness into an aircraft structural design to control aeroelastic deformation, static or dynamic, in such a fashion as to affect the aerodynamic and structural performance of that aircraft in a beneficial way." In wing design, this is often accomplished by designing the wing structure to feature a coupling between its bending and torsional response. One way of introducing this coupling in the structure is through the use of unbalanced plies in composite layups. Depending on the orientation of the unbalance, different coupling behaviors can be achieved. If the laminate fibers in the wing skins are biased forward a bend-up/twist-up (divergent) response is obtained, swept back fibers feature a bend-up/twist-down (convergent) behavior, and unbiased/balanced laminates feature no (neutral) coupling. Figure 1.5 shows an example of the coupling behavior for different composite bias directions.
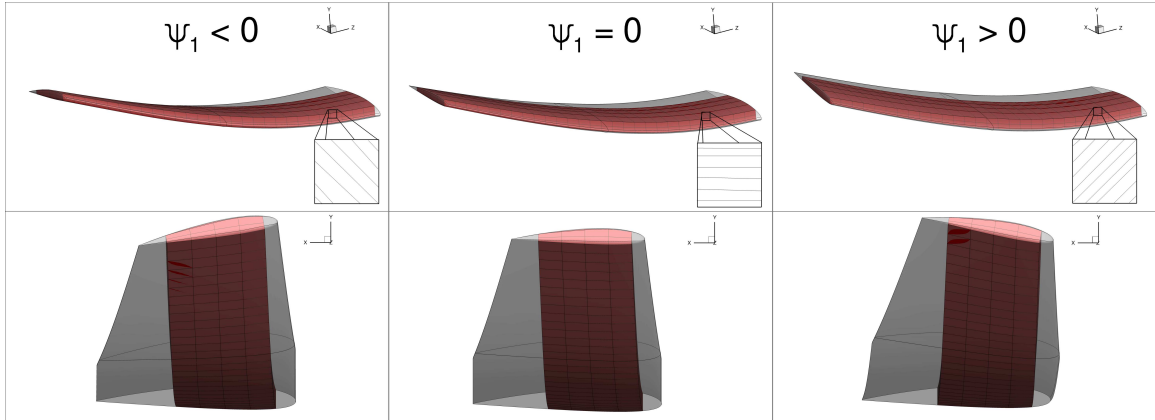
Figure 1.5: Example of divergent, neutral, and convergent bend-twist coupling for composite wingbox
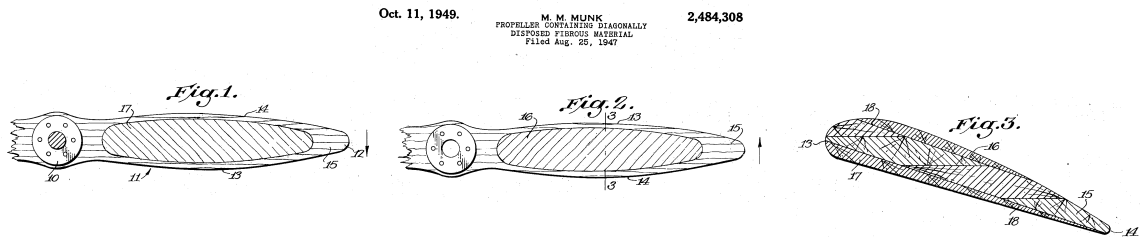
Figure 1.6: Early example of aeroelastic tailoring in wooden propeller design. Adapted from U.S. Patent 2484308 [16]

1.1.2.1 Historical examples of aeroelastic tailoring

While aeroelastic tailoring has been a topic of growing interest in the past few decades, it is not a new concept. Examples of its application can be seen much earlier in the field of aeronautical design. One of the earliest examples of aeroelastic tailoring can be seen as early as 1949 in a U.S. patent filed by Munk [16] for an aeroelastically tailored propeller, seen in Figure 1.6. In this patent, Munk notes that typical fixed-pitch propeller blades have a tendency to elastically increase in pitch as the thrust is increased, an undesirable behavior for propeller performance. Munk proposed orienting the fibers of the wood in the blades diagonally in order to induce the opposite effect through additional material bend-twist coupling. In this way, the invention Munk proposed was a fixed-pitch propeller that could achieve the performance of a variable-pitch propeller through aeroelastic deformation alone.

One of the most recent examples of aeroelastic tailoring is in the design of the Grumman X-29, Figure 1.7. The X-29 was an experimental aircraft developed in the 80's that featured a very unique forward-swept wing. The reason aircraft designers typically sweep the wings

on transonic aircraft is for the reduction in wave drag that it provides. The same reduction in drag can be achieved be sweeping the wing forward or back. Sweeping the wing forward has the benefit of improving the aircraft maneuverability.

Despite the aerodynamic benefits of forward-swept wings, nearly all transonic aircraft feature swept-back wings. The reason for this is that sweep has a similar effect on the bend-twist coupling of the structure as unbalanced composite laminates. Swept-forward wings feature a divergent bend-twist coupling, while swept-back wings feature convergent coupling. This means that, for a forward-swept wing, as the aerodynamic loads cause the wing to bend up, the torsional coupling will cause the wing to twist up. This upward elastic twist increases the local incidence of the wing relative to the freestream, further increasing the aerodynamic loads on the wing. This can lead to an aeroelastic instability, known as divergence, if the coupling exceeds the elastic restoring forces of the structure, leading to structural failure. For conventional forward-swept wing designs the only way of preventing this phenomena is by designing a sufficiently stiff wing structure, leading to large weight penalties.

The X-29 was designed to address this problem by taking advantage of the anisotropic behavior of unbalanced composite laminates in the wingbox structure. By biasing the direction of the plies in the skin to elicit a convergent material bend-twist coupling, the designers were able to reverse the divergent behavior of the wing due to forward sweep. This increased the aeroelastic stability of the wing without significant weight penalty. Despite the success of aeroelastic tailoring on the X-29 program, the method was deemed to be infeasible for large-scale aircraft production at the time, due to the fact that the composite wing structures had to be laid up by hand. As mentioned in the previous section, with the introduction of the AFP process in the past several decades, this is no longer necessarily a problem for future aircraft designs. Due to the coupled nature of the involved physics, more recent investigations in the applications of aeroelastic tailoring have focused on utilizing MDO approaches to quantify the full benefits with respect to flexible aircraft design, as will be discussed in the following section.

1.1.2.2 Passive load alleviation

Another application of aeroelastic tailoring is the concept of *passive load alleviation*. Passive load alleviation is achieved by designing the wing structure to feature a convergent bend-twist behavior. This allows the aircraft wing to be designed to achieve an elliptical lift distribution under nominal cruise flight conditions, reducing aircraft induced drag. As the lift on the wing is increased, to perform a maneuver, the wing will deflect up further, but also twist down. This has the effect of shifting the lift distribution inboard, reducing
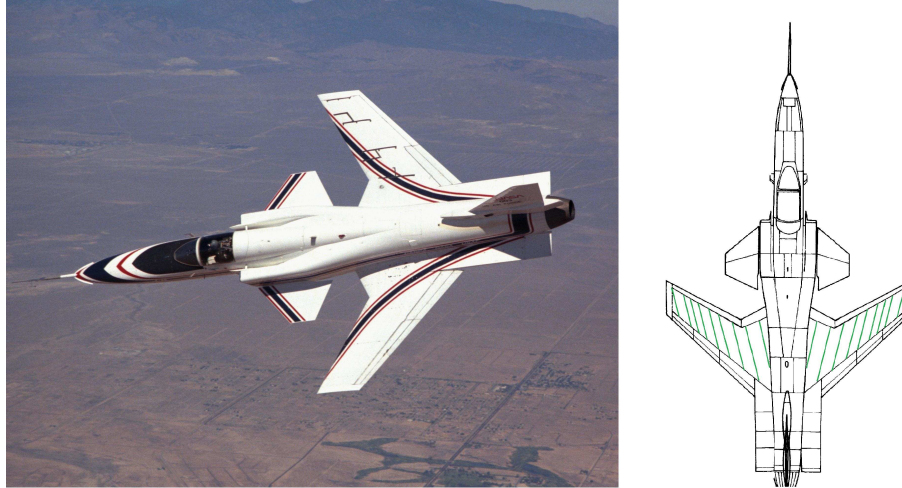
Figure 1.7: The Grumman X-29 utilized unbalanced composite laminates to counteract the forward-swept wings divergent behavior.

the structural bending moment at the root of the wing and allowing a lighter structure to be used. An example of this can be seen in Figure 1.8. This allows the aircraft performance at cruise, which is typically aerodynamically critical, to be decoupled from the performance of the maneuver conditions, which are typically structurally critical.

The term "passive" refers to the fact that the load alleviation is achieved solely through the aeroelastic deformations and can be elicited by tailoring the direction stiffness of the wingbox structure. This is opposed to active load alleviation, where load alleviation is achieved through the use of control systems used to directly alter the aerodynamic shape of the wing and hence control the lift distribution. An example of an active approach, which has also seen great interest in the past decade, are morphing trailing-edge wings [17, 18, 19, 20]. The focus of this work will be on passive load alleviation of flexible-winged aircraft.

As mentioned previously, since most transonic aircraft designs feature swept-back wings, which have a naturally convergent bend-twist coupling, most of these designs already feature this property to a certain degree. It has been shown that passive load alleviation is achievable for both isotropic metallic and balanced quasi-isotropic composite designs through the use of gradient-based high-fidelity aerostructural optimization [21, 22, 23]. The potential benefit that we may expect to find of a tow-steered optimized design is the ability to complement the already present load alleviation due to sweep by steering the fiber paths forward in certain locations of the structure, increasing the bend-twist coupling and thus the passive load alleviation capabilities of the design. This leads to a potential reduction in structural weight for little to no additional penalty in cruise performance.

9
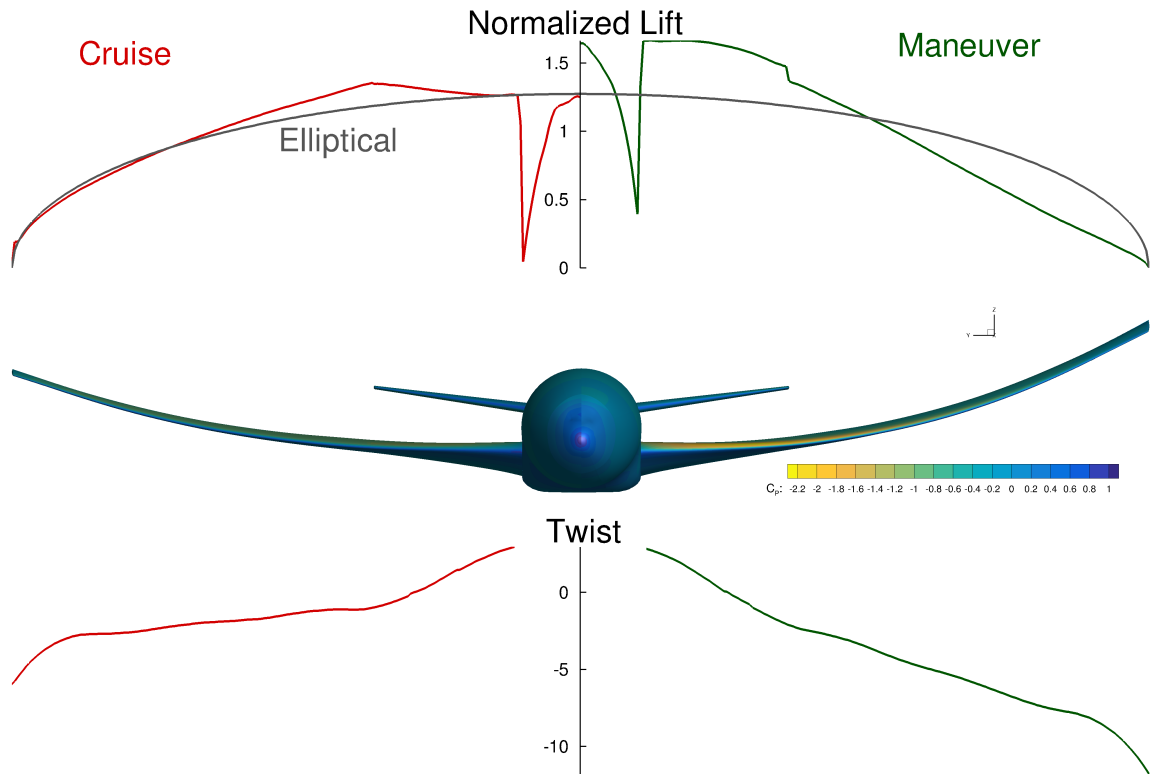
Figure 1.8: Example of passive load alleviation through aeroelastic tailoring

1.1.3 Multidisciplinary design optimization

The availability of high-fidelity numerical-based simulation tools, such as computational fluid dynamics (CFD) for aerodynamic analysis and finite element analysis (FEA) for structural analysis, have revolutionized the field of aerospace design. These tools have the advantage of being much more accurate than a lower-fidelity simplified model and are able to be used in both the conceptual and detailed design phases of the design procedure. These tools have also significantly reduced the amount of experimental testing required in the design process, saving a great amount of time and money and allowing for quicker testing of different iterations of design concepts to find a good design.

In aircraft design, what qualifies as a "good" design is not always entirely clear. Historically, it has been left up to the intuition of the designers in each discipline group as to what constitutes a good design. It is then up to each discipline group to design their respective components of the aircraft to meet that metric, while conforming to the constraints of the other design groups. This approach works for relatively simple designs, but as aircraft systems become more complex and disciplines more coupled, the aspects that define a good design can become quite subtle and sometimes unintuitive. Furthermore, miscommunica-

tion between design groups can lead to months of redesigning and significant amounts of money being lost on the program further down the line. This motivates a more rigorous approach to the design process for complex and coupled design systems and was the impetus for the development of the tools of MDO.

The origins of MDO are rooted in the pioneering of design optimization in the structural design community in the 60's [24, 25]. After the marked success of structural optimization in 70's, applications to multidisciplinary design problems soon followed in various engineering industries during the 80's [26, 27]. Because of the interdisciplinary nature of the aircraft design process, the aircraft industry proved a particularly fertile environment for the maturation of the MDO process.

1.1.3.1 Background

The general design optimization problem can be formulated as follows:

$$
\begin{aligned}
\text{minimize} \quad & f(\boldsymbol{x}) \\
\text{with respect to} \quad & \boldsymbol{x} \\
\text{subject to} \quad & \boldsymbol{c}(\boldsymbol{x}) = 0 \\
& \widehat{\boldsymbol{c}}(\boldsymbol{x}) \leq 0
\end{aligned}
$$

Where the scalar f is the design objective function, $\boldsymbol{x}$, $\boldsymbol{c}$, and $\widehat{\boldsymbol{c}}$ are vectors containing the problem design variables, equality and inequality constraints, respectively. Examples of objectives for typical design problems can be design weight, aerodynamic drag, manufacturing cost, etc. Typical design variables might be structural sizing, design shape, or operation parameters. Typical constraints include: design volume, structural failure, and flight stability. When the design problem considered is governed by multiple coupled design disciplines, such as aerodynamics and structures for a flexible wing, the problem is referred to as an MDO problem.

If the optimization problem can be solved analytically, a common approach is the method of Lagrange multipliers. In this approach, a new composite function, known as the Lagrangian, is formed as a linear combination of the objective and constraint functions. Differentiation of this function with respect to its parameters lead to a set of nonlinear equations, known as the Karush-Kuhn-Tucker (KKT) conditions, that when solved guarantee a constrained minimum has been found.

If the problem must be solved numerically, there are two classes of approaches: gradient-based and gradient-free. Gradient-based approaches attempt to iteratively approximate the problem Lagrangian and solve the KKT conditions. For this reason, gradient information is required of the objective and constraint functions with respect to the design variables.

Gradient-based methods include Quasi-Newton, requires first-order sensitivities, as well as Newton, requires at least second-order sensitivities, methods [28, 29]. On the other hand, gradient-free algorithms attempt to solve the problem with no sensitivity information. This is typically done iteratively through heuristic approaches such as genetic algorithm (GA) or evolutionary algorithms [30, 31, 32, 33].

Both gradient-based and gradient-free approaches have benefits as well as drawbacks. Gradient-based methods require the problem objective and constraints be continuous and differentiable. Gradient-based approaches guarantee rapid (quadratic) convergence to a constrained minimum, but no guarantee of global optimality. This can be particularly problematic if the design problem features multiple local minimum. Gradient-free approaches, by definition, do not require the associated design functions to be differentiated, an often pain-staking process for sophisticated numerical simulations. Gradient-free methods have a much slower convergence rate, but many can guarantee a sense of global optimality if run for a sufficiently long time.

Figure 1.9 shows an example comparison between the scaling of gradient-free and gradient-based approaches with respect to optimization problem size (# of design variables). This plot makes it clear that for practical design problems gradient-free approaches scale up to only roughly $\mathcal{O}(10)$ design variables before the problem becomes prohibitively expensive. Gradient-based approaches can scale up to well over $\mathcal{O}(10^3)$ design variables without significant additional expense. $\mathcal{O}(10)$ design variables may be suitable for the parametrization of smaller design studies, such as the structural optimization of a composite plate. However, for more complex coupled aerospace system designs, such as the flexible wing aircraft design considered in this work, the number of design variables required to sufficiently parametrize the design will likely be $\mathcal{O}(10^3)$. For this reason, all problems solved in the remainder of this work will be conducted using gradient-based optimization. It will therefore be part of the onus for this work to show that the presence of local minima is not a prevalent issue in the wing design optimizations considered in the remainder of this work.

1.1.3.2 Prior work

Optimization of composites with spatially varying stiffness is a topic that has been explored by various researchers. Most of the previous work has focused on structural optimization of simple plate structures. These studies have shown the structural benefits of variable stiffness structures ability to redistribute internal loads. A number of authors have performed optimization of composite plates with spatially varying stiffness, by breaking the laminate up into a number of square patches each of which take on one of a number of discrete ply
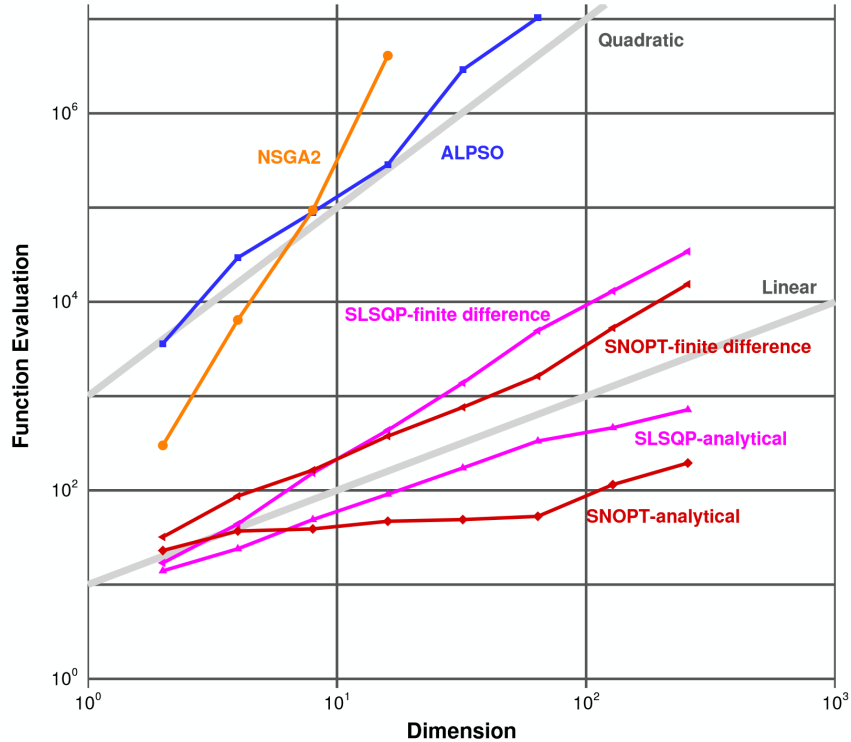
Figure 1.9: Gradient-based optimizers (SNOPT and SLSQP) scale much more favorably for large design problems than gradient-free approaches (NSGA2 and ALPSO) [34]

orientations ($0°$, $\pm45°$, $90°$, etc.) [35, 36, 37, 38, 39]. This discrete approach to structural optimization is know as discrete material optimization (DMO). The disadvantage of this approach to spatially varying stiffness laminates is that as the number of patches increases, the resulting design becomes infeasible to manufacture. The benefit that a tow-steered laminate would have over such a laminate is that the ply angles in theory can take any value and vary continuously throughout the laminate. This allows the layup procedure to be efficiently automated.

The ability of variable angle tow (VAT) or tow-steered laminates to redistribute load paths in plate structures has been explored by a number of authors. This is often done by optimizing the continuous tow-paths of each layer for plate-like structures. This includes studies that tailored the tow-steered panels for maximum strength [40, 41, 42]. For example, Hyer and Charette [42], used an iterative procedure to align the tow paths with the direction of maximum principal stress for a plate under tension. The authors found up to a 89% improvement in first-ply failure strength relative to a conventional quasi-isotropic plate. They also note that this improvement in strength came at the expense of a lower critical buckling load, demonstrating the need for buckling considerations in the optimization. In addition to these studies, other authors have considered the effect of tow steer-

13

ing on buckling performance [43, 44, 45, 46, 47, 48, 49]. For example, Ijsselmuiden et al. [43] showed an improvement of up to 189% in buckling load for a VAT laminate panel when compared to a quasi-isotropic design. Work conducted by Wu et al. [47, 50] also showed additional benefits in the post-buckling regime, by maximizing the post-buckled axial stiffness of compressed tow-steered plates. The ability of tow-steered structures to mitigate stress concentrations around structural discontinuities, such as holes, has been another topic interest. These studies have shown that tow steering is capable of reducing the stress in these regions, improving the strength and buckling performance of the panel [45, 42, 51, 49, 52]. All of these accomplishments are made possible by the ability of tow-steered laminates to more effectively redistribute loads.

While these improvements are impressive, authors such as Lozano et al. [12] have pointed out the need for consideration of manufacturing constraints such as tow-path turning radius and the presence of gaps and overlaps in the design of VAT composites. Many of these studies have included considerations for manufacturing constraints. The most common constraint considered is that of the tow-path turning radius [53, 46, 48]. Authors such as Blom et al. [54] have considered the presence of gaps and overlaps in the AFP laid up design. In the case of Blom et al. [54] the tow paths were defined using a streamline analogy, with the optimization objective being to minimize the thickness build up due to prepreg tape overlap.

There has only been a few studies looking into the aeroelastic benefits offered by tow-steered composites for simple plate or beam-like structures. Using a simplified low-fidelity aerodynamic strip theory coupled to a thin-walled structural beam model, Haddadpour and Zamani [55] were able to perform an investigation of the aeroelastic benefits of a tow-steered composite wing for flutter performance through gradient-based optimization. In this work, they found up to a 15% improvement in the critical velocity at which flutter occurred for the tow-steered wing relative to a straight fiber design. In work by Stodieck et al. [56] a simplified two-dimensional tow-steered composite wing was optimized with the goal of improving flutter/divergence airspeed and dynamic gust response. In this work, the wing was idealized as a flat plate, with the aerodynamics modeled, again, using a strip theory and the structures a Rayliegh-Ritz plate model. From this work, it was concluded that improvements of up to 24% in gust load alleviation and 7% in aeroelastic instability airspeed could be achieved relative to conventional laminates. Studies by Stanford and Jutte [57, 58] extended this work to a more realistic wingbox geometry based on the National Aeronautics and Space Administration (NASA) common research model (CRM). The model featured a shell-based finite element method (FEM) structural model coupled to a medium-fidelity aerodynamic panel method. In this work, the authors demonstrated a

15% decrease in structural weight and 47% decrease in aggregate stress relative to a conventional composite structure. In the case of Jutte et al. [57, 58] and Stodieck et al. [59], a gradient-free GA approach was taken to perform the optimizations in the study. This limited the number of design variables in the study to $\mathcal{O}(10)$, severely limiting the exploration of the design space. Though these works were useful in quantifying the benefits of tow steering to wing design, their insights were limited by the simplicity of the designs.

Only recently have authors begun to consider tow-steered aeroelastic wing design in greater detail. A more recent investigation conducted by Stodieck et al. [60] considered the benefits of tow steering to a more realistic wing design. In this work, the designs performance of the CRM aircraft was optimized for several structural sizing maneuver flight conditions. While in this work the choice was made to utilize a more efficient gradient-based optimization approach, the design sensitives were computed through finite-difference, again limiting the number of design variables to roughly 176 due to computational expense. Despite this, the authors found that by adding tow steering to the design, weight savings of up to 12% could be achieved relative to a conventional composite design. This study also included consideration for dynamic flight conditions, including gust analysis as well as flutter onset, but these constraints were found to be largely inactive in sizing the design when compared to the static maneuver constraints. A similar study by Stanford and Jutte [61] extended the investigation to high aspect ratio wing design and found up to a 8.8% reduction in structural mass. Both improvements in structural weight were made possible, at least in part, through the additional aeroelastic tailoring of the wing structure provided by the design freedom of tow-steered composites.

The work presented here will differ from these previous aeroelastic studies in several regards. First, in the previous work the only design variables considered were largely structural, while the geometry (i.e. shape) was not free to be directly parametrized by the optimizer. In this work, the optimizer is allowed to control the geometry of the wing as well, giving it more freedom to tailor the performance of the wing. Secondly, none of these works, with the exception of Haddadpour and Zamani [55], considered the effect AFP-specific manufacturing constraints during the design optimization. For this study, we formulate several tow steering design metrics to identify regions of manufacturing difficulty, such as tape paths featuring high curvature as well as regions featuring large gaps and overlaps. We then provide these metrics as constraints for the optimization problem to ensure than resulting designs are manufacturable. Finally, both works utilized a lower fidelity strip or panel-based method to model the aerodynamics. The results presented here utilize a detailed three-dimensional outer mold line (OML) aircraft geometry analyzed using a high-fidelity RANS-based CFD solver to model the aerodynamic loads of the aircraft.

Studies conducted by Lyu et al. [62] have shown that while low-fidelity approaches to design optimization have their usefulness, they come with the risk of taking advantage of any missing physics of the model. An example of this is how an inviscid aerodynamic model, either potential flow or Euler-based, will miss the effects of flow separation, leading to a design that may be sub-optimal when run with a higher fidelity RANS CFD analysis. Kenway and Martins [21], Liem et al. [63], and Burdette et al. [18] found that high-fidelity aerostructural optimization has the potential to improve on-design performance. These previous studies focused on design optimization of conventional aluminum CRM-type geometries. The goal of the present work is to quantify the benefit of an unconventional tow-steered design relative to its conventional composite counterpart for flexible-wing design.

1.2 Thesis objectives

The primary goal of this work is to quantify the benefits of applying tow-steered composites to aeroelastic wing design of long range commercial aircraft. With this goal in mind, the objectives of this thesis are as follows:

1. Develop a set of benchmark aeroelastic models for the future study of next-generation aircraft designs.

2. Develop a general framework for the parametrization and optimization of tow-steered composite structures.

3. Derive relevant AFP/Tow-steering manufacturing constraints and their corresponding sensitivities.

4. Compare aerostructurally optimized composite wing designs with and without tow steering for fuel burn performance to quantify benefits of tow steering

5. Extend trends by performing a Pareto front study varying the design optimization objective between fuel burn and structural weight on a conventional aluminum, composite, and tow-steered wing

6. Provide a 27% scaled tow-steered wingbox structural model through aerostructural design optimization for construction by Aurora Flight Sciences and structural testing by NASA.

1.3 Thesis outline

As mentioned previously, to achieve the objective of this thesis a high-fidelity aerostructural optimization framework, MDO of aircraft configurations with high fidelity (MACH), will be utilized and developed upon. In Chapter 2, a brief overview will be given of the MACH framework and theory that makes the gradient-based high-fidelity optimization considered in this work possible. The remainder of this thesis is structured as follows. In Chapter 3 the first objective will be addressed with the introduction of the undeflected common research model (uCRM) benchmark aerostructural models. These models will then provide the necessary baseline designs with which I will conduct the following aerostructural design studies. Following this, in Chapter 4, objective 2 of this thesis will be addressed with the introduction a general framework for the parametrization and optimization of tow-steered structures, pySteer. Objective 3 is a necessary step to achieving the final objective of this work, objective 6. To this end, in Chapter 5 relevant manufacturing constraints for AFP and tow-steered structures will be discussed, followed by the translation of these constraints into mathematical identities suitable for gradient-based optimization. The mathematical relationships between these constraints will also be explored in this chapter, leading to further insight into their nature. In Chapter 6, a series of structural optimizations will be used to verify the implementation of the pySteer framework as well as explore in greater detail the effects of manufacturing constraints and address the presence of local minima.

The next two chapters will serve to address the main thrust of this thesis: quantifying the benefits of tow-steered structures for aeroelastic wing design. To this end, in Chapter 7 an aerostructural fuel burn optimization will be conducted on the uCRM models with a conventional and tow-steered composite wing design. These results will provide quantification of the benefits of tow steering for increasing aircraft fuel efficiency as well as insight into the nature of those benefits, addressing objective 4. These results will then be expanded upon in Chapter 8 by allowing the wing planform (sweep, span, and wing area) to vary during the optimization of a conventional metallic, composite, and tow-steered composite wing design. A number optimization for each design will be performed, varying the weightings of the objective between aircraft fuel burn and structural weight, creating three Pareto front, one for each design. This study will allow for the comparison of the relative benefits between conventional metallic, composite, and tow-steered composite wing designs, in addition to giving further insight into the trend between wing span/aspect ratio and design objective for each design. This will serve to address objective 5.

Finally, a summary of the previous findings as well as concluding remarks will be given in Chapter 9. In this chapter the current progress of the final objective, objective 6, will be

given. After this suggestions for additional considerations in future work to further build upon these results will be made.

CHAPTER 2

Computational framework

To accurately assess the aeroelastic performance of flexible wing designs, such as the CRM geometry, a framework featuring a tightly coupled high-fidelity aerodynamic and structural mechanics solver is required. To this end, the work in this thesis was conducted using the MACH framework [22]. The key development in the MACH framework that allows for efficient computation of aerostructural design sensitivities with respect to large numbers of variables is the adjoint method. Through the remainder of this section, we briefly describe the components in this framework. Kennedy and Martins [64] and Kenway et al. [22] provide more detailed descriptions.

2.1 Adjoint background

Once the decision has been made to use gradient-based approaches for numerical design optimization, the question still remains of how to acquire the necessary sensitivities from the coupled high-fidelity physics simulations. The most straight forward approach is a finite-differencing scheme, where each design variable is perturbed by a small amount about the current solution. The gradient can then be approximated by taking the ratio of the change of each output to the change in each input. The main advantage to this approach is that it requires no additional changes be made to the internal code of the simulation tools. The disadvantage is that due to the finite precision nature of digital computing, the accuracy of the computed sensitivities are subject to subtractive cancellation error, limiting the minimum allowable step size and hence the accuracy for nonlinear problems. The second disadvantage to this approach is that the computational cost scales with the number of design variables. For instance, if $\mathcal{O}(10^3)$ design variables are used this means $\mathcal{O}(10^3)$ additional CFD/FEA solves per optimization iteration, for which there may be $\mathcal{O}(10^2)$ of in a typical optimization. This fact renders this approach prohibitively expensive for large design problems with high-fidelity models.

An alternative approach is to perturb each design variable by a small imaginary step, a technique known as the complex step. This method has the benefit of eliminating any error associated with subtractive cancellation, allowing an arbitrarily small step size to be taken, guaranteeing down to machine precision accurate sensitivities for sufficiently small step sizes [65]. This has the benefit of addressing the accuracy issue of the finite-difference approach, however requires that the internal code of the physics solvers to be able to accept complex arguments. In addition, the computational cost of this approach still scales with the number of design variables, making it unusable for large design problems.

One approach that addresses both the issue of scalability and accuracy is the adjoint method. The adjoint approach can be derived by realizing that the solution to any nonlinear problem–be it CFD, FEA, or a coupled CFD/FEA–can be written as follows:

$$\boldsymbol{R}(\boldsymbol{x}, \boldsymbol{y}) = 0 \tag{2.1}$$

Where $\boldsymbol{x}$ is again the design variable vector set by the user as an input and $\boldsymbol{y}$ are the state variables of physics solver. In a FEA the state variables would be the structural displacements at the nodes, while for a finite-volume CFD solver these are the flux quantities in each cell. $\boldsymbol{R}$ is what is called the residual, when this vector is zero a solution satisfying the governing equations of the physics problem has been found. It is the job of every physics solver to find the state variables, $\boldsymbol{y}$, for the corresponding input, $\boldsymbol{x}$, that satisfies this equation. The variable $\boldsymbol{\psi}$, known as the adjoint, can be found by solving the linear equation below:

$$\frac{\partial \boldsymbol{R}}{\partial \boldsymbol{y}}^{T} \boldsymbol{\psi} = \frac{\partial I}{\partial \boldsymbol{y}}^{T}, \tag{2.2}$$

for each objective/constraint function, I, of interest. The total sensitivities with respect to the design variables can then be obtained through:

$$\frac{dI}{d\boldsymbol{x}} = \frac{\partial I}{\partial \boldsymbol{x}} - \boldsymbol{\psi}^{T} \frac{\partial \boldsymbol{R}}{\partial \boldsymbol{x}}, \tag{2.3}$$

It should be pointed out that each partial derivative term–$\frac{\partial \boldsymbol{R}}{\partial \boldsymbol{y}}$, $\frac{\partial f}{\partial \boldsymbol{y}}, \frac{\partial f}{\partial \boldsymbol{x}}$, and $\frac{\partial \boldsymbol{R}}{\partial \boldsymbol{x}}$–can be computed cheaply through finite-difference, complex step, or automatic differentiation (AD), since they do not require that the residuals of the governing equations be solved, only re-evaluated. In fact, the most computationally expensive part of the procedure is the linear solve for the adjoint of each design function in Equation (2.2). This means that the adjoint approach scales with the number functions of interests rather than the number of design variables. This makes the adjoint method preferable for optimization problems where: $n_{dv} >> n_f$. This includes the design problems considered in the remainder of this work,

20

where the number of design variables are $\mathcal{O}(10^3)$ and the number of design functions are $\mathcal{O}(1)$. The main disadvantage to this method is that access to the source code of each solver is required in order to access the state variable and residual information.

Martins et al. [66] showed that this method can be generalized to multidisciplinary analysis by partitioning each of the vectors by each disciplinary variable. For instance, for an aerostructural solver the variables become:

$$
\mathbf{y} = \begin{bmatrix} \mathbf{y}_A \\ \mathbf{y}_S \end{bmatrix}, \qquad \mathbf{R} = \begin{bmatrix} \mathbf{R}_A \\ \mathbf{R}_S \end{bmatrix}, \qquad \boldsymbol{\psi} = \begin{bmatrix} \boldsymbol{\psi}_A \\ \boldsymbol{\psi}_S \end{bmatrix}
$$

Where the subscript A and S denote variables corresponding to the aerodynamic and structural solver, respectively. It is the adoption of this approach in the MACH framework that makes the consideration of the detailed design optimization problems in this work possible.

2.2 The MACH framework

For the purposes of high-fidelity aeroelastic analysis, this framework is comprised of both a RANS-based CFD and structural FEA solver. The two solvers are coupled by a CFD mesh warping algorithm, which is used to propagate the structural deflections of the wing to the CFD volume mesh. The framework also allows for the variations in the wing geometry by utilizing a shape parametrization algorithm that allows for changes in both aerodynamic and structural shape of the wing during the optimization. Lastly, a gradient-based optimizer utilizes the aerostructural derivatives computed using a coupled adjoint approach to solve the optimization problem. The MACH framework has proven effective in a number of aerostructural design optimization studies [21, 67, 18, 68, 69].

2.2.1 Aerodynamic solver

A high-fidelity CFD solver is necessary for capturing the full physics of the aerodynamics. In the MACH framework ADflow [62], a second order finite-volume CFD solver, is used. ADflow is capable of solving both the steady Euler and Reynolds-averaged Navier–Stokes (RANS) equations on structured multiblock and overset meshes, with some capability of unsteady and time spectral analysis. ADflow is used to compute the aerodynamic forces, such as lift, drag, and pitching moment. Through the use of a discrete adjoint implementation, developed by Mader et al. [70] and Lyu et al. [62] using AD, derivatives of aerodynamic functions of interest with respect to large numbers of design variables are computed efficiently. The aerodynamic analyses considered in this work will be exclusively

steady RANS, utilizing both overset and multiblock meshes. In order to model turbulence a single equation Spalart–Allmaras (SA) model is used.

2.2.2 Structural solver

To accurately compute the aeroelastic deflection of the wing, a high-fidelity structural solver is also required. The structural solver used in the MACH framework is the Toolkit for Analysis of Composite Structures (TACS) [71]. TACS is a computational structural mechanics (CSM) solver that is specifically designed for solving structures consisting of thin shell components, which are typical in aerospace structures. The solver employs a parallel direct factorization method, which allows it to efficiently and accurately solve the poorly conditioned structural problems that are inherent in thin shell structures. In addition to computing the structural displacements, TACS computes other structural functions of interest, such as material failure and buckling loads. Like its aerodynamic counterpart, TACS features an efficient adjoint method for computing structural sensitivities.

2.2.3 Mesh movement

A mesh movement algorithm is required to perform aerostructural analysis and to apply changes in geometric shape during optimization. The purpose of the mesh movement is to regenerate a new CFD mesh given changes in the surface geometry. It takes the changes to the wing surface geometry and corresponding surface mesh, and propagates them through the volume of the CFD mesh. The main mesh movement algorithm used in MACH is an inverse distance weighting method, like that described by Uyttersprot [72]. This method has the benefit of preserving the mesh quality near surfaces, which is necessary for capturing boundary layer effects.

2.2.4 Aerostructural solver

To solve aerostructural problems, there must be a coupling scheme between the structural and aerodynamic solvers. In MACH, this coupling is accomplished through a block Gauss–Seidel scheme. First, the tractions due to the aerodynamic loads are solved using ADflow. These loads are then applied to the TACS finite-element model from which the displacements of the wing can be calculated along with structural functions of interest, such as buckling and material failure. The structural displacements are then transferred to the nodes on the surface of the wing in the CFD mesh using a system of rigid links, as proposed by Brown [73]. The displacements at the surface nodes are then extrapolated to the rest of the
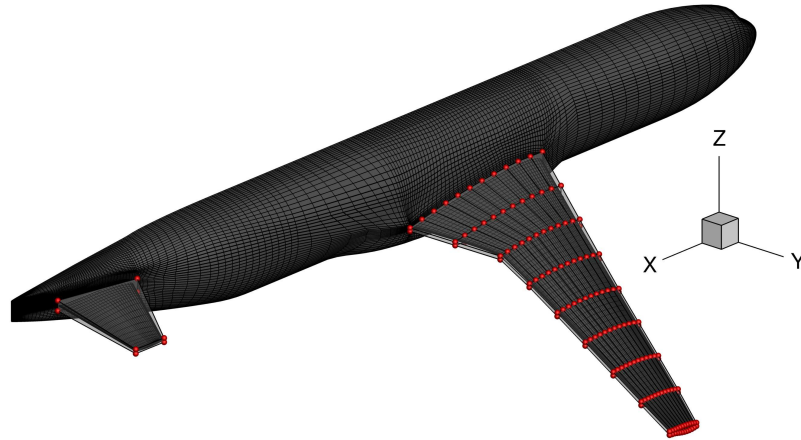
Figure 2.1: FFD volume and control points (red spheres) used for this work.

nodes throughout the CFD volume mesh using the mesh movement algorithm mentioned above. The aerodynamics is solved again for the new mesh, and the process is repeated until convergence. As with the previous solvers, the aerostructural solver is capable of assembling the coupled adjoint from the adjoint of each discipline, structures and aerodynamics, to evaluate the coupled aerostructural derivatives required to solve the design optimization problem [22]. This approach computes the cross-disciplinary sensitivities inherent to flexible wing design in an accurate and efficient manner, enabling gradient-based optimization with $\mathcal{O}(10^3)$ design variables.

2.2.5   Geometric parametrization

For the optimization, the wing shape and planform are parametrized through a free form deformation (FFD) volume. The implementation is that of Kenway and Martins [21]. The surface of the wing is embedded in a volume with control points distributed over its surface. As the control points move, the shape inside the volume deforms in a continuous manner, giving the optimizer control over the cross-sectional shape, twist, and planform (sweep and span) of the wing. There is an additional smaller sub-FFD that encloses the horizontal stabilizer, which allows for control over its incidence to trim the aircraft. An example of the FFD model used for this work is shown in Figure 2.1. In total, there are 240 control points distributed on the surface of this FFD volume to parameterize the wing geometry.

2.2.6 Optimizer

As mentioned previously, due to the large number of design variables considered in the design optimizations in this work and the relative computational expense of the high-fidelity solvers used, a gradient-based approach was required. Aerostructural design problems typically feature a large sparse constraint Jacobian. Therefore, it is desirable to use an optimizer that takes advantage of the sparse nature of the problem. For this reason, all optimization problems in this work are solved using the Sparse Nonlinear Optimizer (SNOPT) [28], a quasi-Newton gradient-based optimizer that works well for optimization problems featuring large numbers of sparse nonlinear constraints. The optimization tool is wrapped using the Python interface pyOPT [74]. SNOPT sits on top of the aerostructural solver in the MACH framework, providing the current design variables to the solvers as inputs and requesting the objective, constraints, and corresponding sensitivities as outputs at each major iteration of the optimization.

CHAPTER 3

uCRM: A common aerostructural model

In this chapter, the aerostructural models used throughout the remainder of this work, the uCRM, will be introduced. The goal of developing the uCRM models was to provide a robust aerostructural baseline design, not just for this study of tow-steering, but also for future aeroelastic design and optimization studies utilizing next generation design techniques. The uCRM family consists of two models: an aspect ratio 9 model based on the CRM (uCRM-9) and a higher aspect ratio, 13.5, variant (uCRM-13.5). The models consist of an aerodynamic OML geometry as well as an internal wingbox structure. Both benchmark models are developed using a conventional metallic aluminum structural design. This chapter will also serve as a convenient introduction to the standard MACH framework for conventional structural designs. In the following chapters, this framework will be expanded upon to consider unconventional tow-steered wing designs as well.

The structure of the remainder of this chapter is as follows: first a brief motivation will be given on the need for a universal benchmark model for aeroelastic design and optimization. Next, the procedure used to define the uCRM-9 geometry and structural wingbox model will be described. Following this, the steps used to transform the planform of the uCRM-9 model to its higher aspect ratio (AR) variant, the uCRM-13.5, will be outlined. Finally, the buffet-constrained multipoint aerostructural optimization used to finalize the definition of the uCRM-13.5 wing geometry and structure will be described and the results assessed, followed by concluding remarks on the models.

3.1 Motivation

Modern RANS-based CFD solvers feature a variety of turbulence models and parameters that differ from solver to solver. These modeling differences may result in small solution differences for the same geometry and flight condition depending on which solver is used. To validate and compare different CFD solvers, a number of benchmark geometries have

been developed. These benchmarks include geometries such as the ONERA M6 wing [75], the German Aerospace Research Center DLR-F4 [76], and the NASA Common Research Model (CRM) [77]. The CRM was developed to be representative of a long-range twin-aisle transport aircraft configuration and has been used in the American Institute of Aeronautics and Astronautics (AIAA) drag prediction workshop (DPW) since 2008 [77]. The CRM geometry features a fuselage, wing, horizontal tail, engine nacelle and pylon.

Since the CRM was originally intended for the validation of various CFD tools, the geometry of the wing was designed to match the deflected state of the configuration under a nominal 1 g cruise condition. This is ideal from the aerodynamic analysis point of view, since it eliminates the need to find the aeroelastically deformed shape experienced during the flight condition. For single-point aerodynamic shape optimization a single flying shape is also acceptable, but such optimizations do not yield practical results because the resulting performance is not robust with respect to changes in flight conditions. However, when performing aerodynamic shape optimization while considering multiple flight conditions, using a single rigid shape is no longer appropriate, since different flight conditions yield different wing shapes. Thus, even for a purely aerodynamic analysis, aeroelastic effects may need to be taken into consideration. As an example, Keye et al. [78] showed significant aeroelastic deformations were experienced in the wind tunnel test of the CRM model. Furthermore, they show that to accurately predict the drag polar, these aeroelastic deformations must be accounted for in the CFD analysis.

Despite the challenges mentioned above, a series of aerodynamic shape optimization cases based on the 1 g deflected shape of the CRM wing have been considered for the aerodynamic design optimization discussion group (ADODG) benchmarks [79, 80, 81, 82, 83, 84, 85]. Many of these works found that single-design-point aerodynamic optimization lead to results with poor off-design performance and that multiple flight conditions must be considered to lead to a practical and robust design [82, 79]. More recently, several optimization cases featuring multiple design conditions were also defined and solved [81, 86]. These benchmark cases have been successful in getting practitioners from academia and industry to solve the same problem. Herein, the aim is to leverage the efforts invested into the validation, verification, and design optimization of the CRM wing by developing the uCRM aerostructural benchmarks.

While the application of numerical optimization offers promising results for aerodynamic wing design, it is not without drawbacks. To capture the inherent coupling between the structural response and the aerodynamics of the wing at these various flight conditions, an aeroelastic model is required. There has been some recent interest in using the CRM configuration as a model for aerostructural (static aeroelastic), aeroelastic, and aeroser-

voelastic analysis and design. The transonic conditions for which the CRM was designed for makes it an ideal model for an aeroelastic benchmark. A number of aeroelastic studies featuring optimization have been conducted based on the CRM geometry using panel methods [57, 87]. This includes the work of Klimmek [88], in which an aeroelastic model for the CRM was developed using an inverse design optimization to recover the jig geometry. This model was later used in a RANS-based aerostructural design optimization study conducted by Keye et al. [89]. Although low-fidelity models incur a lower computational cost and are widely used in industry for preliminary design, the optimization tends to exploit the physics missing from such models, so a conservative approach is required. One example of missing physics was observed by Lyu et al. [62], where for an Euler-based aerodynamic optimization, the design converged to an excessively thick airfoil near the root of the wing. When this model was analyzed using a RANS-based solver, the performance was worse than the initial design due to shock induced separation effects that the Euler model missed.

There have already been a number of efforts utilizing higher fidelity static aerostructural optimization that feature a RANS-based CFD solver coupled with a CSM solver using the AR 9 model developed in this work, the uCRM-9 [90, 91]. Due to a continual push for increased aircraft efficiency and reduction in fuel burn, there has also been growing interest in enabling high AR wings without a disproportionate weight penalty through the use of future technologies such as tow-steered composites [92, 68], morphing trailing edge wings [18], and additive manufactured wingbox topologies [93]. Each of these studies was conducted using the 13.5 AR model developed in this work, the uCRM-13.5.

While these studies showed a marked improvement in performance robustness over the single-point design, they neglected buffet, which is a critical consideration in transonic wing design. In the transonic flight regime, shocks may occur over the upper surface of the wing during cruise flight. These shocks increase in strength with both lift coefficient and Mach number. Shocks can lead to strong interactions between oscillations in the shock position and shock-induced flow separation, causing an unsteady aerodynamic instability known as *transonic buffet*. This phenomenon is undesirable because it results in intense structural vibration and may lead to loss of aircraft control. To ensure a safe aircraft, regulations require a sufficient margin between buffet onset and the nominal operating cruise envelope. This requirement ensures the ability to maneuver during cruise, by increasing lift, without experiencing buffet.

Since buffet is inherently an unsteady phenomenon, in general, to accurately model it requires expensive unsteady aerodynamic simulations. Recently, Kenway and Martins [94] developed a formulation to constrain buffet onset in design optimization using a separation-based prediction metric based on steady CFD analysis. They found that buffet onset could

be correlated with the amount of separated flow seen on the upper surface of the wing, and that for the CRM, buffet onset occurs when this separated flow area reaches 4% of the wing reference area. Once the prediction metric was validated for the CRM, they compared the design optimizations performed with and without the constraint enforced. They concluded that when the constraint was not enforced, the aircraft did not have the required margin at the peak performance flight conditions, and thus the aircraft would have to fly at a suboptimal Mach and lift coefficient to satisfy the buffet onset margin. The designs obtained while enforcing the buffet onset constraint, however, exhibited peak performance right at the buffet onset boundary. Thus, a buffet onset constraint must be enforced to achieve a practical wing designs through optimization. For this reason, in this work the same approach will be used to predict and constrain buffet onset when defining the proposed aerostructural models.

Because of the growing interest in aerostructural analysis and optimization on the CRM model and future high AR wing designs, the goal of the present work is to develop two aerostructural benchmark geometries: an AR 9 wing based on the CRM, the *uCRM-9*, and a higher AR (13.5) variant, the *uCRM-13.5*. Since aerostructural analyses will be performed using these models, the 1 g "built-in" deflections become problematic and the jig (undeflected) shape must instead be defined. The goal is that these models provide a useful benchmark for aeroelastic studies. To this end, all files associated with these designs—both geometry and mesh files—are publicly available [1]. The details of the files provided are included in Appendix A.

3.2   uCRM-9 definition

For both the uCRM-9 and the uCRM-13.5, only the structure of the wingbox is modeled. Although structural models for the wingbox of the CRM are available from the CRM website,[2] these models are based on the flight shape of the wing. For this reason, the undeflected wing jig shape and structural model for the wing must be designed. The uCRM-9 model is designed with a constraint that its jig shape and structure deforms into the shape of the original OML of the CRM model at its nominal cruise condition ($M = 0.85$, $C_L = 0.5$ at 37 000 ft) [95].

The procedure used to accomplish this can be summarized as follows. First, a wingbox layout is defined based on a similar aircraft. The structure is then sized using representative aerodynamic loads. Then, an inverse design procedure is applied, iteratively removing the

---

[1]http://mdolab.engin.umich.edu/content/ucrm
[2]https://commonresearchmodel.larc.nasa.gov/fem-file/

deflection from the OML and wingbox geometry, while updating the structural sizing to ensure that the aeroelastically deflected shape matched the nominal deflection profile of the CRM. This is similar to the design procedure used by Kenway et al. [90] with a few key differences. In the original work, the stiffeners were not modeled in the wingbox structural model, while in this work they are modeled using a smeared stiffness approach. In addition, when the wingbox is sized, buckling constraints are enforced for all the maneuver loads, whereas in the previous work only material failure was considered. Finally, the aerodynamic model used for this work utilize a finer mesh and includes the horizontal stabilizer in the geometry. In the remainder of this section, this procedure will be described in more detail.

3.2.1 Wingbox structural definition

In the first step of the uCRM-9 design process, a realistic wingbox layout is defined. Due to the proprietary nature of internal wing structures, there is no publicly available data on wingboxes for modern transport aircraft. For this reason, the layout is based on publicly available cutaway drawings of the Boeing 777-200ER aircraft, since it is the most similar aircraft to the CRM in terms of size and performance. Figure 3.1 shows the planform view of the 777-200ER extracted from the aircraft planning document [96] superimposed with a best-guess of the wingbox outline (left), and the CRM planform with the proposed wingbox layout (right). Using digital versions of the Boeing 777 drawing, the extent of the wingbox is estimated at the wing root and tip. These measurements are then rounded off to obtain the percentage locations with respect to the local chord listed in Table 3.1. This information was sufficient to define the wingbox structure planform for the CRM geometry. The wingbox for the CRM was then generated using the same proportions (front and rear spar location, rib spacing, etc.) and structural layout of the Boeing 777 wingbox. Due to differences in sweep and span, the Boeing 777 wingbox layout could not be used directly in the CRM planform.

The CRM wingbox is composed of an upper and lower skin, two spars, 49 ribs, and an engine mount panel. The leading edge spar is straight, except for a kink at the wing-body junction, while the trailing edge spar features an additional kink at the Yehudi break. The center wingbox section includes 4 ribs oriented parallel to the fuselage, while the remaining 45 ribs are distributed along the span of the wing perpendicular to the leading edge, with the exception of the close out rib at the tip. An additional panel is included between two ribs at the Yehudi break. This panel is used to mount the engine to the wing, along with the leading edge spar at this location. The structural model also includes external non-
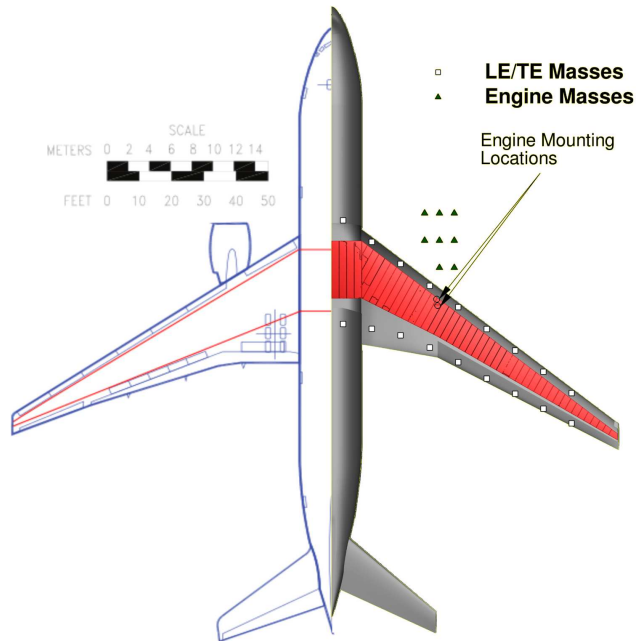
Figure 3.1: Boeing 777 (left) and uCRM-9 (right). The CRM has a slightly lower wing area and span, and more sweep than the Boeing 777.

Table 3.1: Spar locations (as percentage of the local chord) estimated for the Boeing 777 wingbox and values used for the uCRM-9 wingbox.

	777 estimated (%)	uCRM-9 (%)
Leading edge spar root	10.4	10
Leading edge spar tip	36.1	35
Trailing edge spar root	59.6	60
Trailing edge spar tip	60.7	60
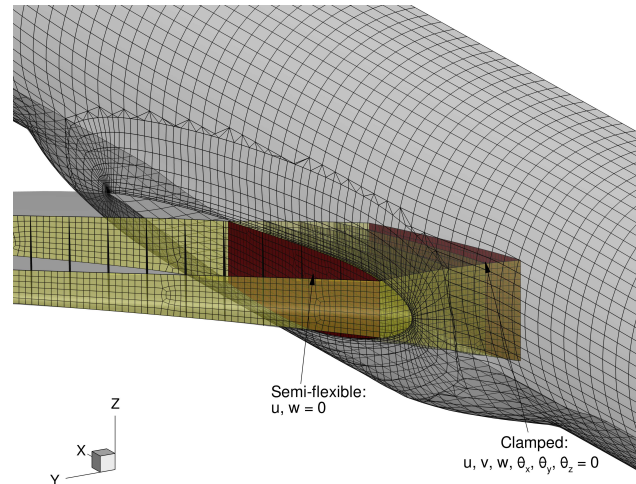
Figure 3.2: The wingbox structure is clamped at the symmetry plane, and partially constrained at the wing-fuselage junction.

structural masses. The masses include discrete leading and trailing edge lumped masses (Figure 3.1), used to model the effect of the mounted actuators and control surfaces. These masses are attached at spanwise locations along either spar. Finally, the inertial effects of the engine as well as the fuel weight present in the fuel bays of the wingbox are included by adding the appropriate masses.

Figure 3.2 illustrates the boundary conditions used to link the wingbox structural FEM to the fuselage geometry. The inner most wingbox rib is clamped at the symmetry plane, so all the displacements and rotations for the elements in that rib are fixed to zero. In addition, the rib at the wing-fuselage junction is constrained such that the vertical and longitudinal displacements are fixed. Thus, small displacements in the spanwise direction and rotation are permitted, allowing for some bending deformation in this region. However, these displacements are very small in practice.

Once the planform of the wingbox has been defined, an in-house tool is used to generate the geometry of the wingbox and its components conforming with the wing OML. Figure 3.3 shows the final wingbox for the CRM. A commercial grid generation tool, ICEM-CFD, was used to generate surface meshes for the wingbox geometry. The FEM mesh used for this model consist of 10 285 second-order mixed interpolation of tensorial components (MITC) shell elements [97, 71] with a total of 156 826 degrees of freedom (DOF). This initial wingbox provides an initial guess for the structure of the wing jig shape. However, because this first guess is based on the CRM OML it also features the "built-in" 1 g deflection in its geometry. This deflection will be removed in the subsequent inverse design
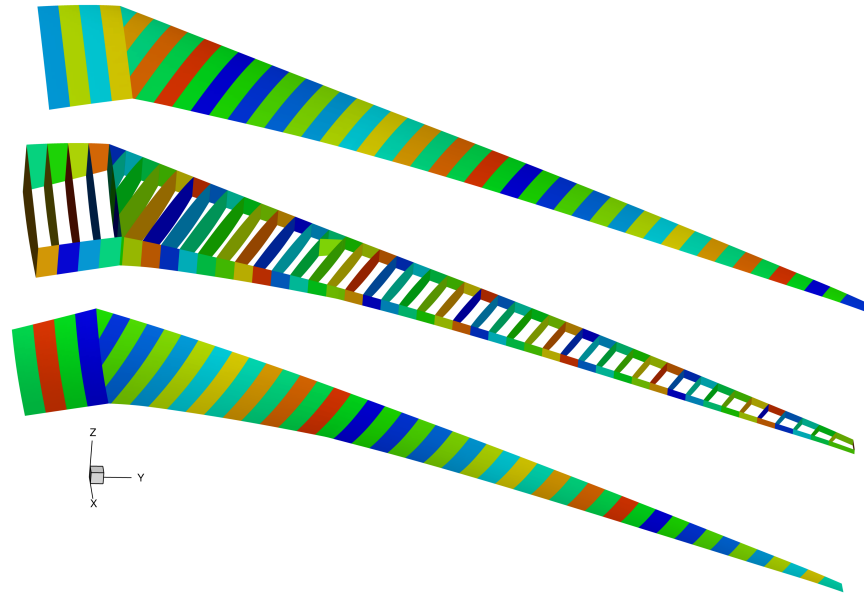
Figure 3.3: uCRM-9 wingbox layout, each colored panel represents a component independently structural sized by the optimizer.

procedure, so that the CRM wing geometry can be recovered from the jig through structural deflection of the wingbox.

3.2.2 Aerodynamic loads

A fixed aerodynamic load distribution is used to recover the undeflected shape of the wing. This aerodynamic load distribution was computed using RANS CFD for CRM wing-body-tail configuration at its nominal cruise condition. The CFD meshes used for this analysis are based on those provided for the 4th Drag Prediction Workshop, but with a flight Reynolds number matching the full scale aircraft, as opposed to wind tunnel conditions. The CFD grid used for this model was an overset mesh consisting of 9.82 million volume cells. Figure 3.4 shows the CRM mesh and C_p distribution for the nominal flight condition. The converged aerodynamic pressure and skin friction forces are then stored as tractions (force per unit area). For the inverse design procedures, these tractions are only applied to the wingbox, since the other components of the design are assumed to be rigid.

3.2.3 Structural model sizing

Once the aerodynamic loads are fixed, the wingbox components are then sized through numerical optimization. All components in the wingbox structure are modeled using aluminum 7000 series alloy, whose properties are listed in Table 3.2.
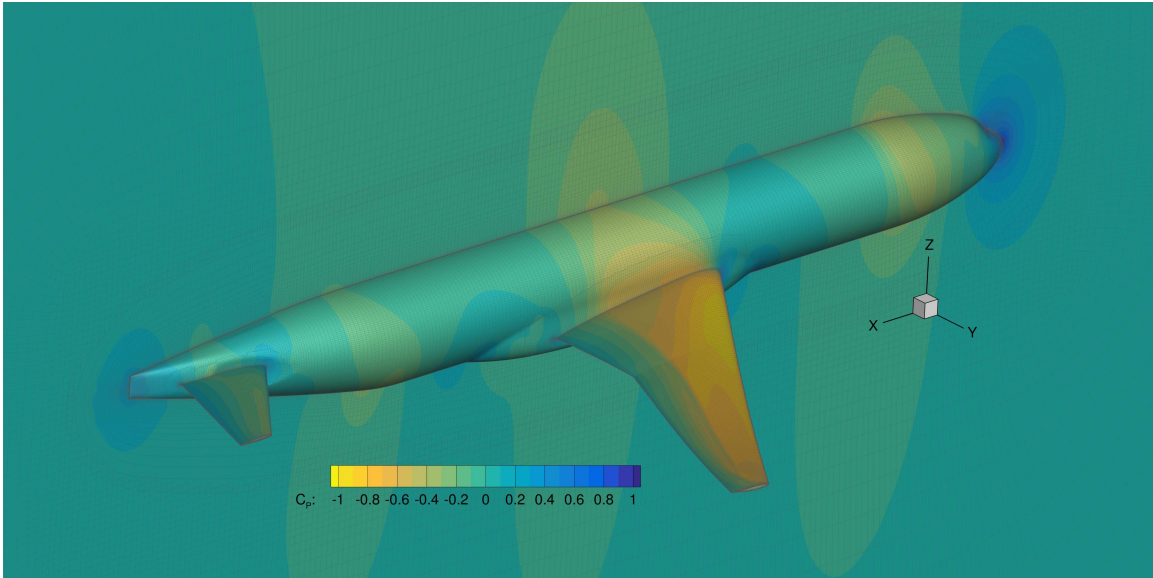
Figure 3.4: CRM wing-body-tail CFD solution and mesh used to generate loads.

Table 3.2: Wingbox material properties.

Parameter	Value
Density	2780 kg/m^3
Modulus	73.1$\times10^9$ Pa
Poisson Ratio	0.3
Yield Strength	420$\times10^6$ Pa

Like all modern transport aircraft, this proposed wingbox uses blade-stiffened panels for the skins, ribs, and spars. The stiffeners are not included explicitly in the FEM model of the wingbox. Instead, the effect of their stiffness are modeled by homogenizing (smearing) them into the wingbox panels stiffness. This model assumes that the density of the stiffeners is high relative to the panel bay dimensions, and that the wingbox panels have a cross-section as shown in Figure 3.5. For simplicity, it is assumed that the blade and flange thicknesses are equal, $t_w = t_b$, and $w_b = h_s$. Kennedy et al. [98] describes the smeared stiffness approach in more detail.
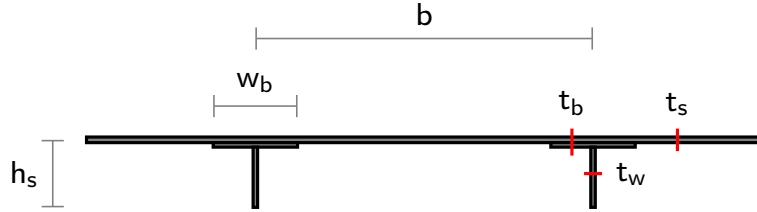
Figure 3.5: Panel-stiffener parametrization used in the smeared stiffness approach [98].

Using this approach, a panel-level buckling analysis can be performed while considering multiple buckling modes. These buckling modes include: intra-stiffener skin buckling, stiffener buckling, and coupled stiffener-skin buckling modes. All three buckling modes are aggregated into a single scalar value using a Kreisselmeier–Steinhauser (KS) function [99, 100], which can be written as,

$$KS = c_{\max} + \frac{1}{\rho_{\text{KS}}} \ln[\sum_{i=1}^{N} \exp(\rho_{\text{KS}}(c_i - c_{\max}))] \tag{3.1}$$

Where c_i is each buckling margin constraint evaluated at the centroid of each element in the aggregation domain, $c_i \geq 1$ implies that the component has buckled. In addition, $c_{\max}$ is the maximum value of all of the c_i's evaluated in the domain. Lastly, ρ_{KS} is a penalty parameter; the larger this value, the closer the aggregation becomes to the discrete maximum function it is meant to model. The KS also has the added benefit of being a conservative approximation to the maximum function, guaranteeing that all designs satisfying the constraint will not violate the true maximum function it approximates.

The structural sizing of the wingbox is obtained through a structural optimization. The optimization consists of minimizing the mass while enforcing failure and buckling constraints for a 2.5 g and a −1 g maneuver load condition. The loads are computed through an intermediate high-fidelity aerostructural analysis and are frozen during the structural op-

timization procedure. The skin, ribs, and spar panels are constrained not to fail or buckle with a safety factor of 1.5 being applied to the loads. In this structural sizing procedure, other load cases that are important in practical aircraft design, such as taxi bumps, roll maneuvers, and dynamic gust conditions are not included. However, the load cases considered here suffice for a representative structural model for academic research.

The structural analysis includes inertial load relief from the structure, engine, and fuel. The engine mass corresponds roughly to the mass of a GE90 engine (7500 kg) and the fuel inertial loads can reach up to 55 000 kg of fuel stored in the fuel bays of each half wingbox. The design variables are stiffener pitch (spacing), stiffener height, stiffener thickness, and panel thickness. The stiffener pitch for the upper and lower skins are equal everywhere. The remaining structural variables are free to change (within their bounds) from one panel to the next. Figure 3.6 shows the panel variable distribution across the primary wing structure.

3.2.4   Jig OML and wingbox inverse design procedure

Given the 1 g OML of the original CRM, the wingbox structural layout and sizing, and the aerodynamic loads, the jig shapes for the OML and wingbox are next determined. This is accomplished by solving a least squares optimization problem where the difference between the CRM OML points X_T and points on the displaced jig shape under the nominal 1 g loads, X_{disp}, is minimized. The displaced points are found by taking the jig points and adding the structural displacements u from the applied aerodynamic loads ($X_{\text{disp}} = X_{\text{jig}} + u$). The optimizer changes only the geometry of the wing jig through the FFD x, y, and z coordinates to match the two sets of points. The goal is to match the two sets of points X_T and X_{disp} such that the flying shape of the CRM wing is achieved through the structural displacement at the nominal flight condition. Once the FFD shape variables are found, we apply them to the initial CRM geometry and wingbox to remove the deflection and achieve a new approximate jig geometry. The new wingbox geometry is then structurally resized by using another structural optimization. The procedure is then repeated until the subsequent geometry changes are deemed to be negligible. This procedure is described in detail in Algorithm 1, where $\mathbf{K}$ and F are, respectively, the FEM stiffness matrix and external (including aerodynamic and inertial) nodal force vector of the wingbox structure.

At the end of each iteration of the inverse design procedure, the location of the tractions must be updated to reflect their new locations relative to the updated jig geometry. Several outer loop iterations are required, since the generation of the new structural geometry re-orients the ribs to be vertical. This is a small correction, but there is a noticeable change
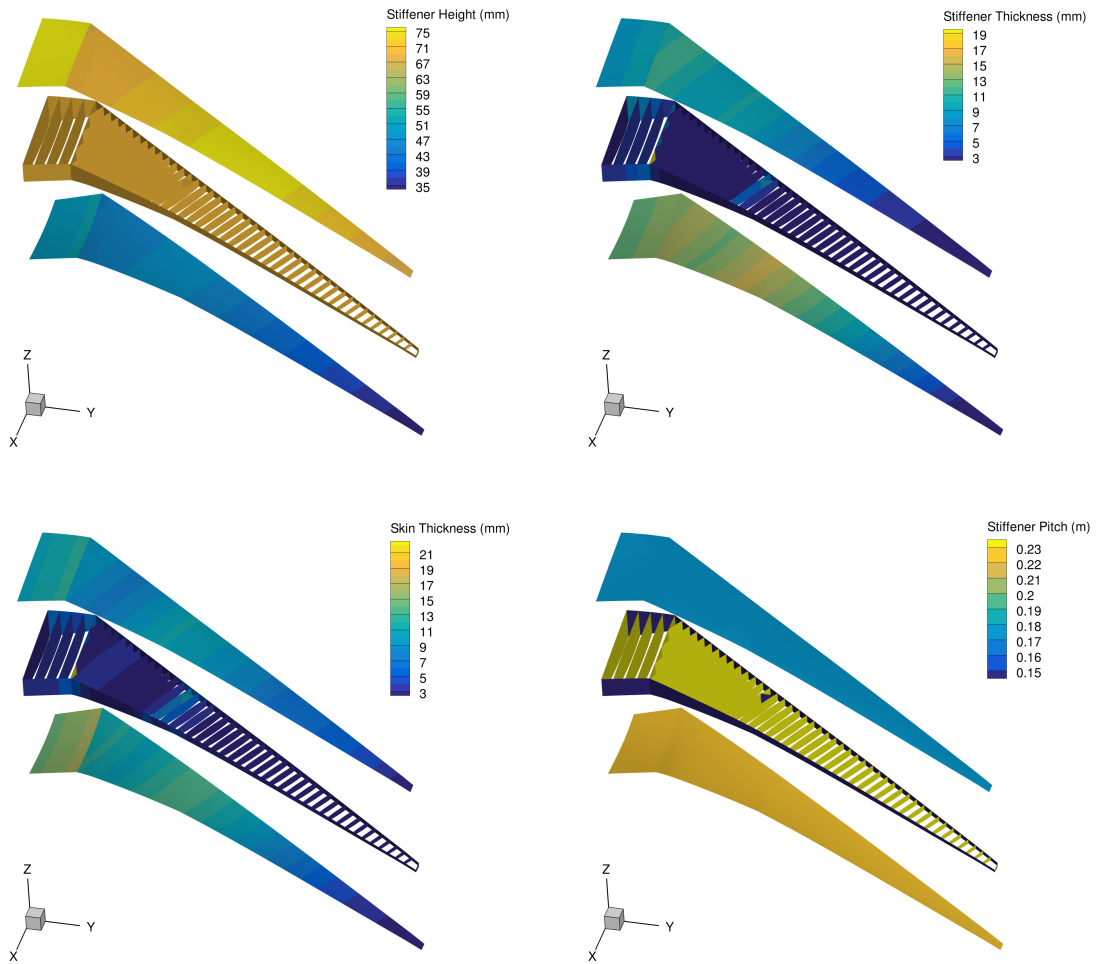
Figure 3.6: Distribution of stiffener height, stiffener thickness, skin thickness, and stiffener pitch for the uCRM-9 structural design.

Algorithm 1 Inverse design procedure for uCRM-9

1: Set $X_T \leftarrow$ surface $< 0 >$ .igs   ▷ Set CRM wing target coordinates

2: Set $n = 0$ ▷ Set iteration counter

3: Set continue=True   ▷ Set inverse design procedure convergence flag

4: **while** continue **do**   ▷ Begin inverse design procedure

5:     $F = F < n >$ ▷ Read the forces on the current surface mesh

6:     FFD $\leftarrow$ FFD $< n >$ .fmt   ▷ Read the current FFD file

7:     $X_{\text{jig}} \leftarrow$ surface $< n >$ .igs   ▷ Read the current surface file

8:     Set $K \leftarrow$ wingbox $< n >$ .bdf   ▷ Assemble FEM stiffness matrix using current structural mesh, wingbox$< n >$.bdf

9:     Set converged=False   ▷ Set optimization convergence flag

10:     **while not** converged **do**   ▷ Start optimization loop; Minimize I wrt FFD variables

11:        FFD $\leftarrow x_{\text{dv}}$ ▷ Update FFD with new optimization design variables

12:        $X_{\text{jig}} \leftarrow$ FFD   ▷ Update jig shape with current FFD design variables

13:        F $\leftarrow$ FFD   ▷ Update force locations with current FFD design variables

14:        $K \leftarrow X_{\text{jig}}$ ▷ Update FEM stiffness matrix

15:        Solve $Ku = $ F   ▷ Evaluate structural displacements

16:        $X_{\text{disp}} \leftarrow u$ ▷ Extrapolate displacement to wing surface to find displaced shape

17:        $I = \frac{1}{2}|||X_{\text{disp}} - X_T|||$ ▷ Evaluate objective

18:        **if** I is minimized **then**   ▷ Check optimization convergence; KKT conditions

19:           converged=True

20:     $F < n + 1 >= F$ ▷ Update the positions of the tractions on approximate jig shape

21:     FFD $< n + 1 >$ .fmt $\leftarrow$ FFD   ▷ Generate new FFD file using the current design variables.

22:     surface $< n + 1 >$ .igs $\leftarrow X_{\text{jig}}$ ▷ Generate new surface file, surface$< n + 1 >$.igs

23:     wingbox $< n + 1 >$ .bdf $\leftarrow X_{\text{surface}} < n + 1 >$ ▷ Generate new structural wingbox based on surface$< n + 1 >$

24:     **if** $|||X_{\text{surface}} < n + 1 > -X_{\text{surface}} < n > ||| < \epsilon$ **then**   ▷ Check if continuous surface has changed

25:        continue=False   ▷ If not end design procedure

26:     **else**

27:        $n = n + 1$ ▷ If so increment iteration counter

---

between iterations one and two.

Figure 3.7 shows the sequence of inverse design results leading to the finalized wing jig. The $n = 0$ shape represents the original CRM wing geometry. After three outer iterations of the above procedure, the changes in successive jig shapes are small. By the final iteration the objective of the least square inverse design optimization only changes by roughly 0.11% in subsequent iterations. The surface for $n = 3$ is nearly indistinguishable from the $n = 2$ surface, only differing near the tips. The mass of the final structure of the wingbox, including both wings, is 23 916 kg, which is comparable to the mass of 22 988 kg that Klimmek [88] found for the CRM by using a similar procedure, with a panel code for the aerodynamic model. The jig shapes for this OML and corresponding wingbox geometry
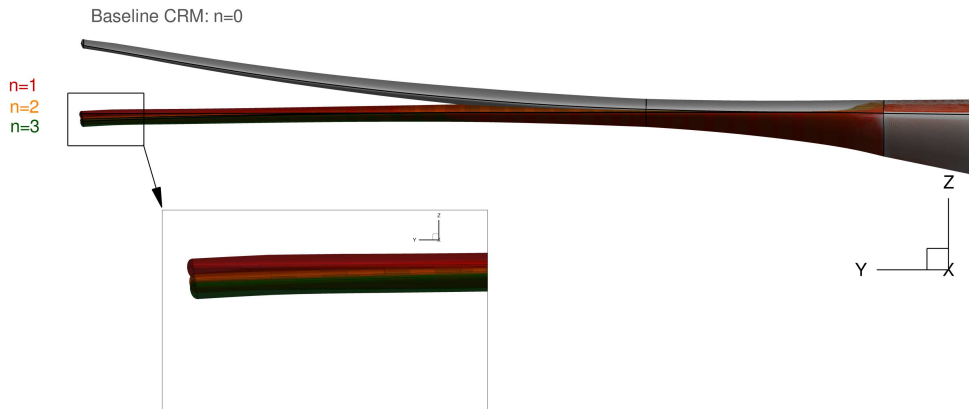
Figure 3.7: Inverse design iteration history for uCRM-9 wing jig.

define the uCRM-9. A three-view of the finalized uCRM-9 model can be seen in Figure 3.8.

3.2.5 Aerostructural verification

To verify the resulting jig shapes and wingbox sizing, an aerostructural analysis of the uCRM-9 was performed and compared with an aerodynamic analysis of the CRM at cruise. Figure 3.9 shows a comparison of the upper surface C_p contours and aerodynamic coefficients of interest. From these results, the C_p distributions were found to be in good agreement, although there are slight differences that can be attributed to the 0.04 deg angle of attack difference in the aerostructural solution. This difference in angle of attack was necessary to match the lift coefficient of the original CRM case. Despite the difference in angle of attack the drag coefficient values differ by roughly 0.001%, which is approaching the solution tolerance of the aerostructural solver. By looking at the pitching moment, C_{M_y}, of both models, a slightly larger difference of around 4% can be seen; this difference is likely a result of the difference in angle of attack between the two models. Although the two models are in good agreement at the nominal cruise condition, the aerostructural analysis depends on the load transfer scheme used to couple the aerodynamic and structural solvers, as well as the aerodynamic and structural solvers themselves. This can lead to inevitable discrepancies in aerostructural solutions from solver to solver.

As can be seen in Figure 3.7, the uCRM-9 has almost zero dihedral over the outer sections of the wing. This indicates that almost all of the spanwise wing curvature in the CRM geometry is due to aerostructural coupling. The wing-twist distribution of the uCRM

38
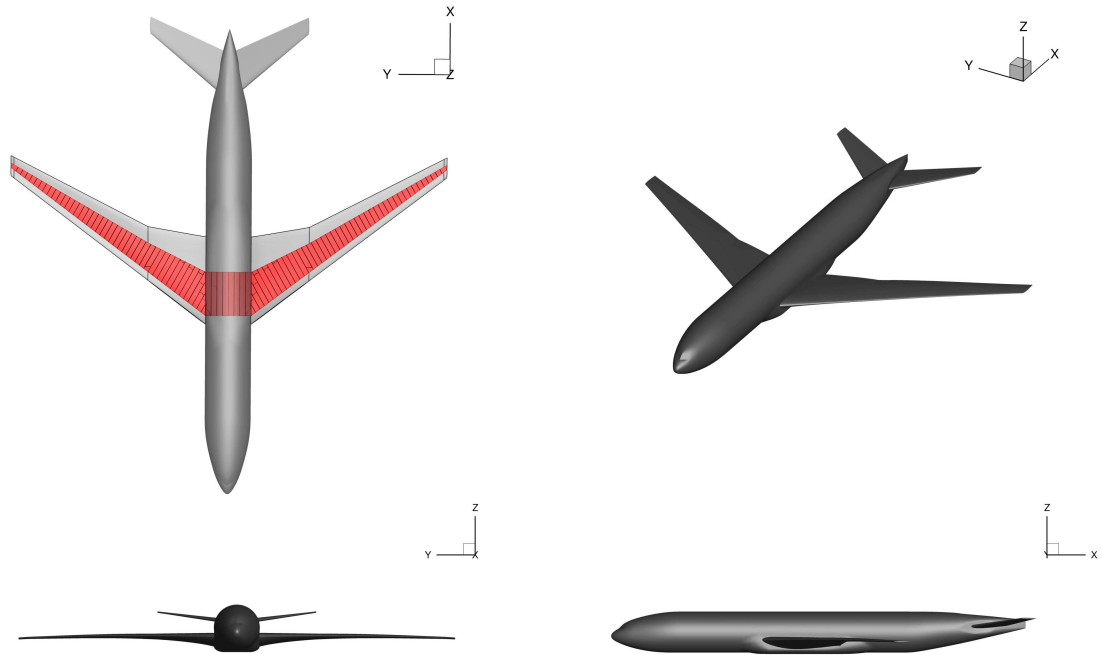
Figure 3.8: Three view of the finalized uCRM-9 wing planform and structural geometry.

C_p: -1 -0.84 -0.68 -0.52 -0.36 -0.2 -0.04 0.12 0.28 0.44 0.6 0.76 0.92

CFD CRM Wing-Body-Tail
C_L: 0.5000
C_D: 225.998 counts
C_{My}: -0.0436
α: 2.045

Aerostructural uCRM-9
C_L: 0.5000
C_D: 225.994 counts
C_{My}: -0.0454
α: 2.014

A = 18%

B = 37%

C = 59%

D = 89%
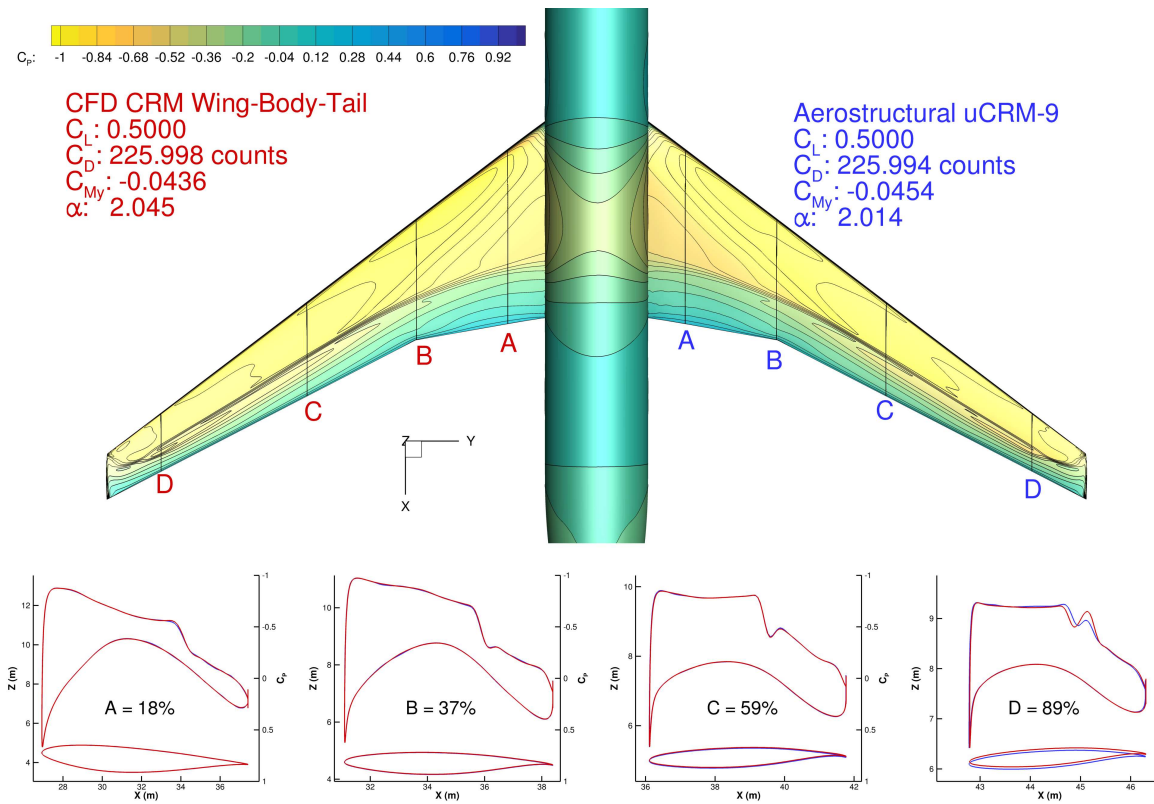
Figure 3.9: C_p contour comparison of original CRM geometry CFD solution and uCRM aerostructural solution.

39
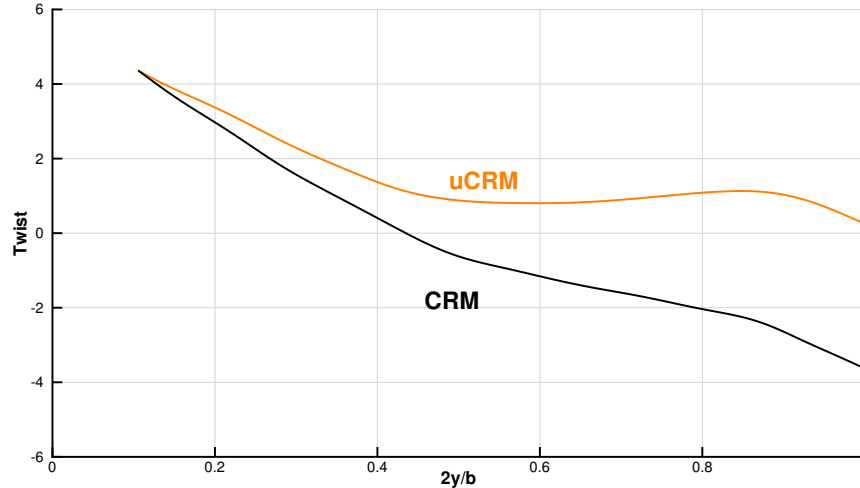
Figure 3.10: Comparison of spanwise twist distributions between the CRM and the uCRM (jig shape).

configuration has been extracted and compared it to the original geometry (Figure 3.10). The difference in twist near the wingtip is about 4°and this gap reduces to zero near the root. The uCRM-9 has a nearly constant twist over the outer half of the semi-span. This twist difference highlights how important aerostructural coupling on swept transonic wings are, even at cruise conditions. This jig-twist distribution is comparable to the twist distribution found using a similar procedure carried out by Klimmek [88] who used a panel code for the aerodynamic model.

While the proposed inverse design procedure produces an excellent jig approximation for the CRM, a simpler alternative approach consists in removing the deflections from the cruise condition to get the jig shape without then recomputing the displacements. Using this approach, the aerodynamic tractions are applied to the wingbox of the original CRM wing ($n = 0$). The wingbox structural displacements are then computed and extrapolated to the aerodynamic surface. Since the resulting wing has roughly twice the desired amount of deflection, the FFD control points can then be used to remove the computed structural displacements from the initial geometry in a single iteration. While this method is more straightforward than the proposed inverse design procedure, it assumes that the wingbox deflection profile has no effect on the structural displacements under the nominal 1 g CRM loads. For completeness, this simplified procedure is performed, and the resulting jig geometry compared to that produced by the previous inverse design procedure. In Figure 3.11 the displacements under the 1 g loads are shown before and after the geometric deflection from the wingbox was removed. Removing the deflection from the geometry has a noticeable effect on the in-plane structural displacements (u and v), while the transverse displacement
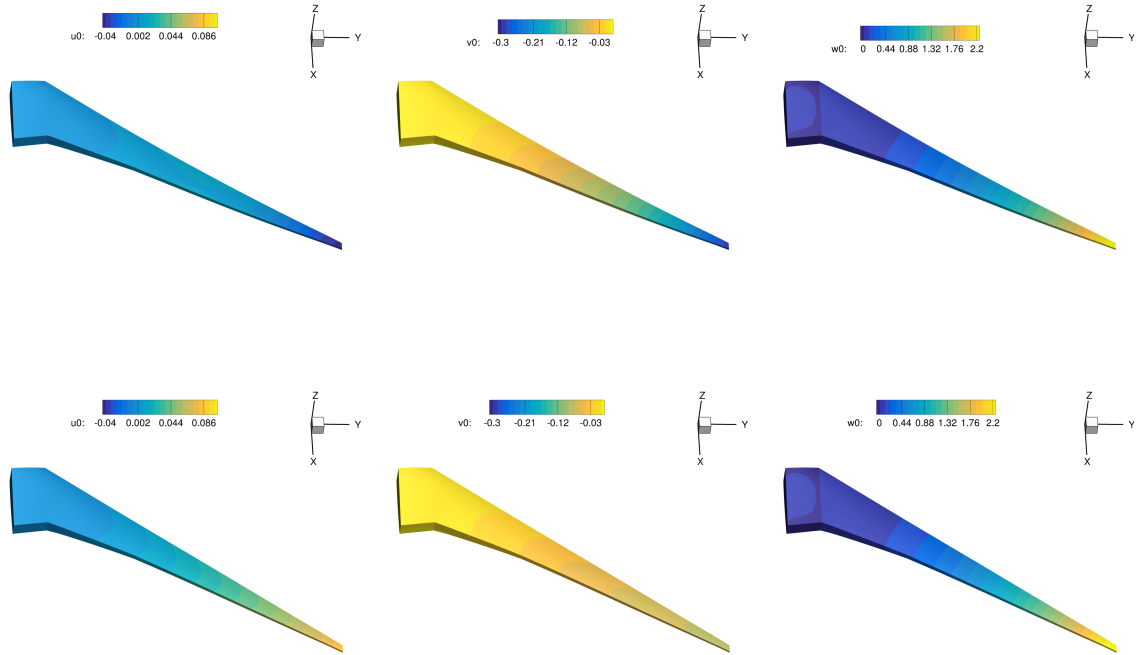
Figure 3.11: Comparison of structural displacements before (top) and after (bottom) the deflection is removed from the CRM wingbox under the same 1 g cruise loads. Left to right: displacements in the x, y, and z directions.

(w) remains largely unchanged. This is because this alternative approach is not an iterative procedure and misses the effect that rotation of the structural components of the wingbox has on its stiffness. This means that the alternate jig differs slightly from the CRM geometry under its nominal 1 g loads. While these differences are small, they do lead to an error of 0.5% in drag when comparing the aerostructural solution to the aerodynamic solution of the CRM, as compared to a 0.001% difference on the inverse design model. For this reason, it was decided to keep the previous inverse designed geometry as the final uCRM-9 jig model.

3.2.6 Grid convergence study

Now that the uCRM-9 aerostructural model has been finalized, a grid convergence study will be performed to assess both the convergence properties of the model, as well as the aerostructural solver. This study consists in performing a coupled aerostructural analysis of the model about its nominal cruise condition with three levels of CFD-CSM mesh refinement: coarse, medium, and fine. The fine grids are the same CFD-CSM meshes used in the

aerostructural verification described in Section 3.2.4. To obtain the coarse grid, the CFD mesh of the fine discretization is coarsened by a factor of 8 and the CSM mesh by a factor of 4. The medium size grids are obtained by creating an intermediate mesh size family in between the fine and coarse grids. The sizes of CFD-CSM the grids used in this study are listed in Table 3.3.

Table 3.3: uCRM-9 CFD-CSM grid sizes

Quantity	Coarse	Medium	Fine
CFD cells	1 232 948	3 629 280	9 822 874
CSM DOFs	142 428	356 328	571 716

Next, an aerostructural analysis on the uCRM-9 model is performed, matching the C_L for all three grid levels. A comparison of the aerodynamic and structural solutions, as well as the mesh size for all three grid levels is shown in Figure 3.12. From the aerodynamic results, the pressure distributions on the wing look similar overall, differing only slightly near the shock as the mesh is refined. Similarly, on the structural model, the von Mises stress distribution is relatively insensitive to mesh size, confirming that the structural model has an adequate number of DOFs. Table 3.4 lists additional aerodynamic and structural metrics of interest for this refinement study. While all three mesh levels produce similar results, several trends can be noticed. First, as the mesh is refined, C_D decreases. This should come as no surprise, since as the CFD mesh is refined, the spurious drag caused by the numerical viscosity of the model decreases. In addition to this, the displacement of the wing tip increases slightly as the mesh is refined. This is a general trend seen in CSM theory where the stiffness of a structure decreases as the number of DOFs increase. The drag value plotted against the grid factor for each grid is shown in Figure 3.13. From this plot, it can see that all three grid solutions lie along the Richardson extrapolation line, showing that grids are in the linear convergence region expected for a second-order CFD scheme.

Table 3.4: uCRM-9 aerostructural grid convergence results

Quantity	Coarse	Medium	Fine
Angle of attack (°)	2.044	2.026	2.019
C_D (counts)	238.9	229.9	226.0
C_{M_y}	−0.0441	−0.0445	−0.0454
Tip displacement (m)	2.591	2.592	2.594
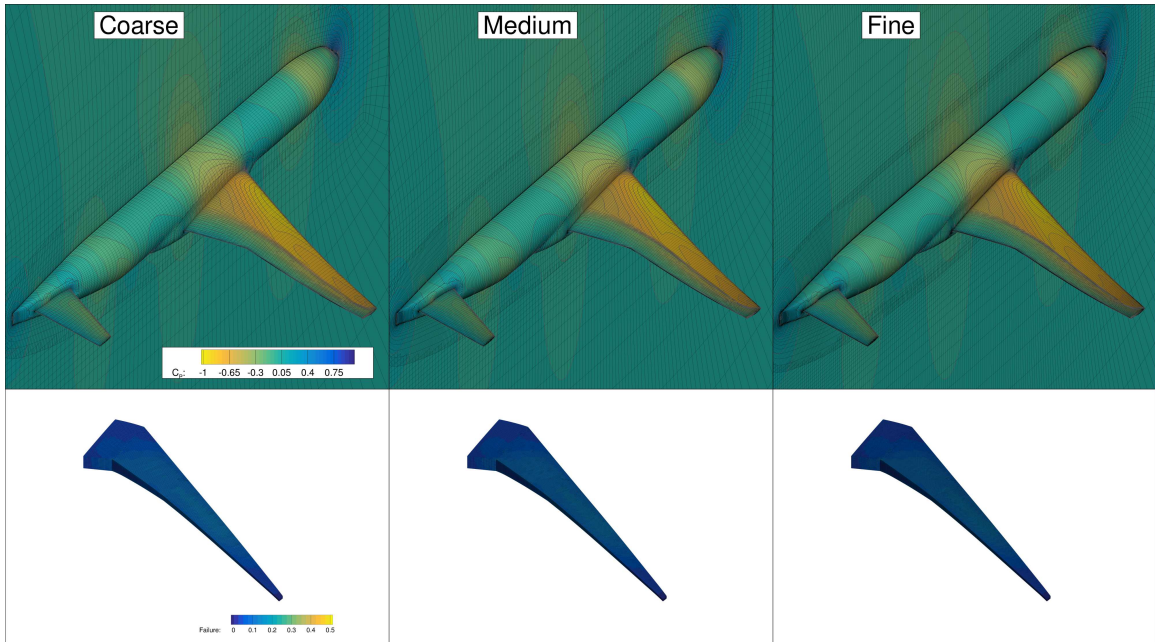
Figure 3.12: Aerostructural solution and mesh for uCRM-9 grid convergence study. Aerodynamic pressure coefficient contours (top) and von Mises structural stress values as a fraction of yield stress. Left to right: coarse, medium, and fine meshes.
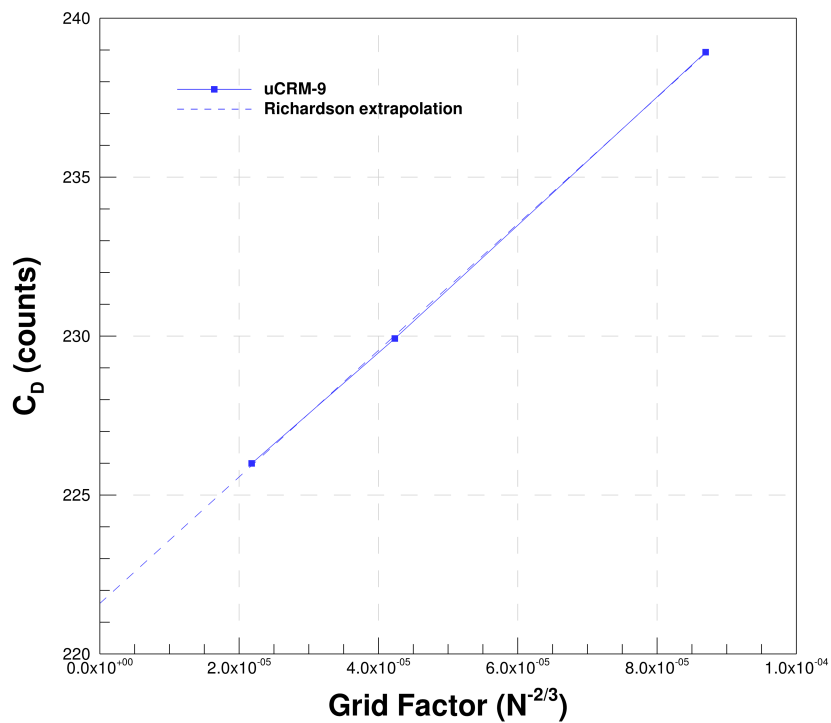
Figure 3.13: Aerostructural drag convergence for the uCRM-9 model.

3.3 uCRM-13.5 definition

The uCRM-13.5 model is the result of a full aerostructural design optimization where the wing OML and the structural sizing are optimized simultaneously. This is in contrast to the uCRM-9 model, where the CRM OML is preserved, and only a structural sizing optimization is performed. The uCRM-13.5 wing maintains overall compatibility with the remainder of the CRM aircraft but is meant to represent higher AR wings that are expected in future aircraft designs. In this way, the resulting aircraft is a higher span derivative of the CRM. The goal of this model is to develop a straightforward modification of the well-tested CRM configuration with a clear connection to that configuration. The extension of the uCRM-9 to obtain the required 13.5 aspect ratio is complicated by the fact that the same wing loading and landing gear location must be preserved to avoid a cascade of design changes that would affect the preliminary sizing. Keeping in mind the constraints imposed by a common fuselage, empennage, and propulsion system, it is decided to keep the reference area fixed.

3.3.1 Planform and general characteristics

The uCRM-13.5 wing planform was designed by first taking the uCRM-9 planform and extending the wing span until an aspect ratio of 13.5 was achieved, as specified by NASA [61]. Similar to the uCRM-9, the uCRM-13.5 reference area is based on the Wimpress area. The wing Wimpress area is kept constant, to ensure that the wing loading remained unchanged. While the Wimpress area remains unchanged, the gross wing area (full projected area, including the area covered by the fuselage) increases by 12.9%.

The uCRM-13.5 has a smaller taper ratio of 0.25 compared to the 0.275 value of the uCRM-9. In addition to this, the Yehudi break spanwise location is moved from 37% to 40% span. These changes are made to keep the Wimpress area unchanged while ensuring adequate space for the landing gear. Figure 3.15 shows the uCRM-13.5 planform in comparison with uCRM-9.

To minimize the change in aircraft longitudinal stability characteristics, the entire uCRM-13.5 planform is shifted forward to align the 1/4 chord mean aerodynamic chord (MAC) location with the uCRM-9 reference point location (also at the 1/4 chord MAC location). This leaves the nominal moment arm of the horizontal and vertical stabilizers unchanged. This leaves the nominal moment arm of the horizontal and vertical stabilizers unchanged, and also offers the additional benefit of distributing the movement in the side of body chord to the leading and trailing edges, thereby minimizing any changes required to the wing-body fairing. A three-view rendering of the uCRM-13.5 planform is shown in Figure 3.16.

$$S_{\text{Wimp}} = S_{\text{trap}} + 2\left(S_{\text{CDE}} + S_{\text{ABDC}} \times \frac{\overline{CD}}{\overline{CF}}\right)$$
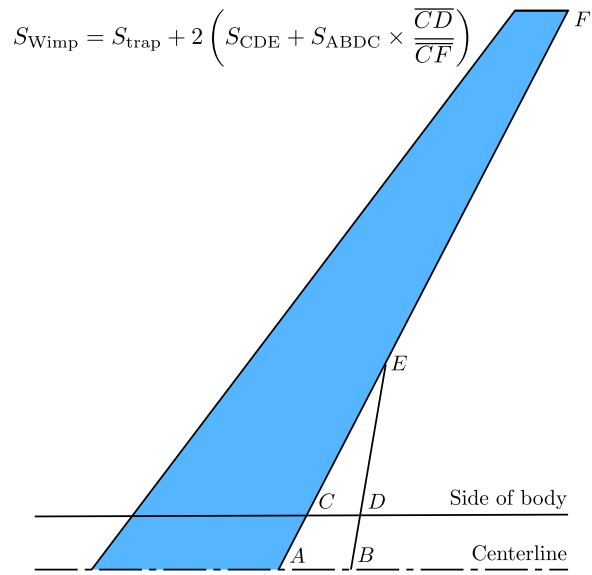
Figure 3.14: Wimpress wing reference area definition.
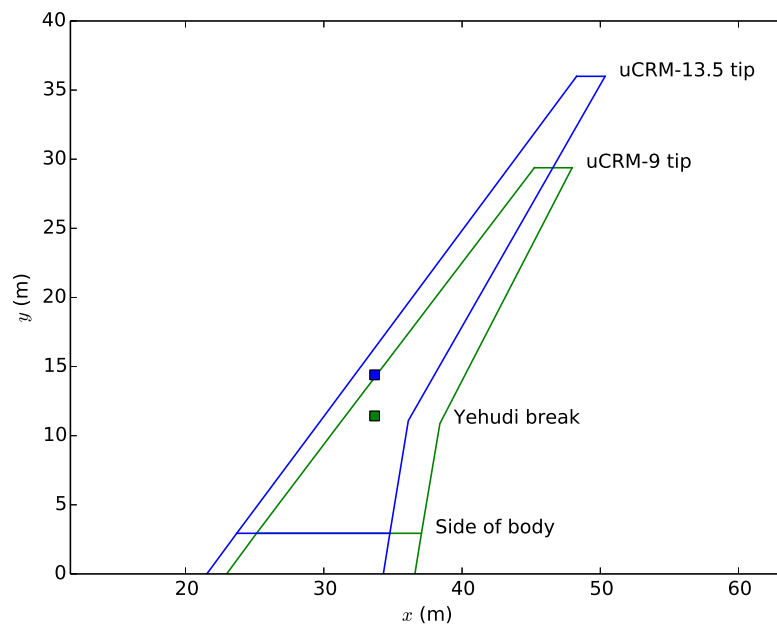
Figure 3.15: Comparison of the uCRM-13.5 (blue) and uCRM-9 (green) wing planforms with locations of 1/4 chord MAC (squares).

Note that like the uCRM-9, the uCRM-13.5 has no built-in dihedral. The key geometric parameters of the uCRM-9 and uCRM-13.5 planforms are listed in Table 3.5.

Table 3.5: uCRM specifications

Parameter	uCRM-9	uCRM-13.5	Units
Aspect ratio	9.0	13.5	–
Span	58.76	72.00	m
Root chord	13.62	16.02	m
Side of body chord	11.92	13.85	m
Yehudi chord	7.26	5.36	m
MAC	7.01	5.36	m
Tip chord	2.736	1.915	m
Wimpress reference area	383.74	384.05	m^2
Gross area	412.10	465.22	m^2
Exposed area	337.05	377.45	m^2
1/4 chord sweep	35	35	deg
Taper ratio	0.275	0.250	–
Gear post depth	0.736	0.648	m

The structural wingbox planform is shown in Figure 3.16. The uCRM-13.5 wingbox is designed to have the same topology as the uCRM-9, except for the number of ribs. To preserve the buckling resistance of the skin panels, the absolute rib spacing is kept the same, and hence the uCRM-13.5 has 9 additional ribs for a total of 58. The trailing edge spar also features a more distinctive kink at the Yehudi break. This is done to move the spar forward in this region and to ensure that the spar depth did not become so small as to become a manufacturing concern. The engine is also assumed to be mounted in the same absolute spanwise position.

3.3.2 uCRM-13.5 aerostructural design optimization

Like the uCRM-9, the uCRM-13.5 is based on a traditional aluminum wingbox structure. A 13.5 AR wing is pushing the limits of what is currently possible with conventional aluminum wing design. As a result, an aerostructural analysis of this model while keeping a similar cross-sectional, twist, and structural sizing distribution as the uCRM-9, reveals that this design performs poorly due to the additional structural deformation caused by the increased wing flexibility. For this reason, unlike for uCRM-9, a full aerostructural design optimization that takes these effects into account was performed to achieve an optimal wing for the uCRM-13.5 configuration. Buffet onset constraints are also enforced in the design optimization to obtain a wing that can be used for a transonic transport aircraft that meets Federal Aviation Administration (FAA) regulations.
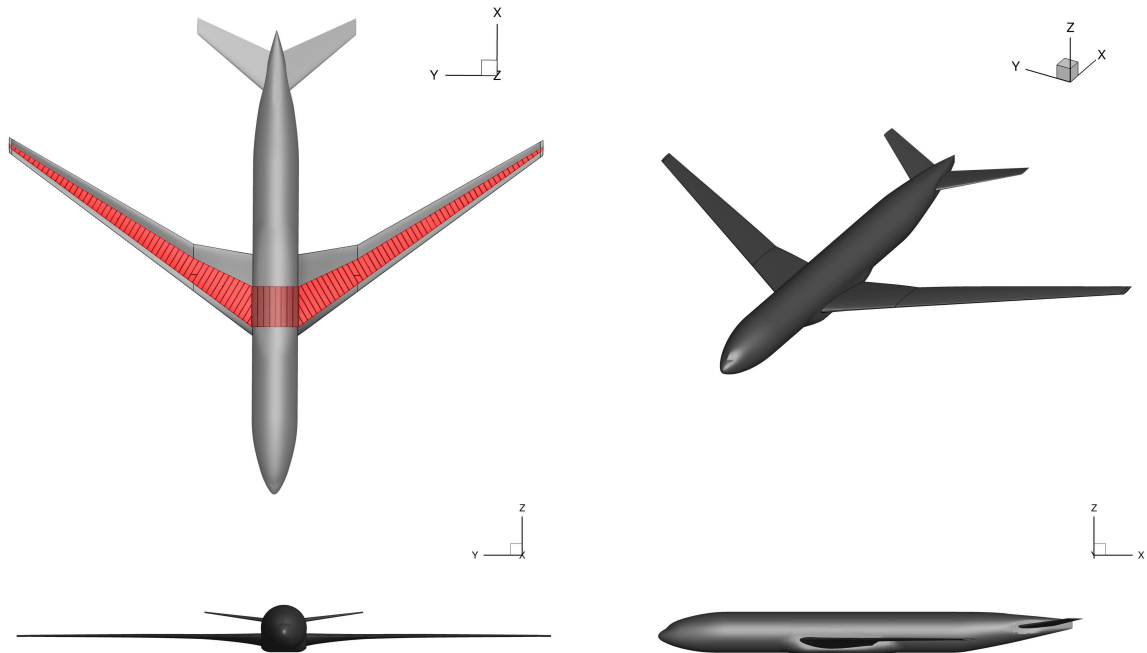
Figure 3.16: Three view of the uCRM-13.5 wing planform and structural geometry.

In the remainder of this section, a complete description of the design optimization problem that was used to obtain the uCRM-13.5 benchmark model will be given. The initial wing weight is estimated from a structural optimization preformed prior to the aerostructural optimization. The structural model used in this optimization features second-order MITC shell elements and a total of $190\,710$ DOFs. A wing-body-tail overset CFD mesh consisting of a total of 1.23 million volume cells, similar to the coarse mesh used in Section 3.2, is used to compute the aerodynamics.

The flight conditions considered consist of a five point cruise stencil, two buffet constraint conditions, and three maneuver conditions. The initial optimization flight conditions are listed in Table 3.6, where MTOW is the maximum takeoff weight of the aircraft. The five cruise design conditions form a cross in Mach–C_L space. This is done to ensure that the fuel burn of the design is robust with respect to varying aircraft weights and flight speeds. The center of the cruise stencil, condition 1, corresponds to the nominal CRM cruise condition ($M = 0.85$, $C_L = 0.5$). Conditions 2 and 3, are offsets of ± 0.025 in C_L relative to the nominal cruise condition. Conditions 4 and 5 are offsets of ± 0.01 in Mach number relative to the nominal condition, with the constraint that they maintain the same physical lift.

The two buffet conditions are chosen to constrain buffet onset at two points: a high lift

condition, and a high Mach condition. The first buffet point applies a 1.3 g margin on the highest lift at cruise (condition 3). The second buffet condition is at $M = 0.89$, with the constraint that the lift match that of the nominal cruise (condition 1). All buffet and cruise conditions are evaluated at an altitude of 37,000 ft. Similar to the uCRM-9, the uCRM-13.5 is structurally sized not to exceed the yield stress or buckling load at the -1 g and 2.5 g maneuver conditions. In addition, a 1 g cruise gust condition is added to the structural sizing analysis. The purpose of the cruise with gust flight condition is to provide a case that structurally sizes the wing for conditions when the aircraft experiences a sudden gust load around cruise but is not given a sufficient amount of time to shift the loads inboard through passive load alleviation. The loads for the gust condition are modeled by analyzing static cruise loads of the design at the Mach crossover point and applying a 1.3 load factor to the aerodynamic loads.

Table 3.6: Initial flight condition stencil

Number	Condition	FB weight (T_i)	Mach (M)	C_L/Lift	Altitude (ft)
1	Cruise	1/5	0.85	0.5	37,000
2	Cruise	1/5	0.85	0.475	37,000
3	Cruise	1/5	0.85	0.525	37,000
4	Cruise	1/5	0.84	0.512	37,000
5	Cruise	1/5	0.86	0.488	37,000
6	Buffet	0	0.85	0.683	37,000
7	Buffet	0	0.89	0.456	37,000
8	2.5 g maneuver	0	0.64	$2.5 \cdot$ MTOW	0
9	-1 g maneuver	0	0.64	$-$MTOW	0
10	Cruise with gust	0	0.85	MTOW	27,300

3.3.2.1 Objective

The objective of the optimization is to minimize the average fuel burn at the cruise conditions. For this optimization, the fuel burned during the taxiing, takeoff, climb, and descent phases of the flight are neglected. The fuel burn for each cruise condition is computed using the Breguet range equation,

$$\text{FB}_i = \text{ZFW} \left(\exp \left(\frac{R \, \text{TSFC}}{V_{\infty_i} \, (L/D)_i} \right) - 1 \right), \tag{3.2}$$

where ZFW is the aircraft zero-fuel weight, R is the range, TSFC is the thrust-specific fuel consumption of the engine, and V_{∞_i} and $(L/D)_i$ are the flight speed and lift-to-drag ratio at the i-th cruise condition, respectively. To compute the objective, the weighted average

of the fuel burns from all five cruise conditions is taken,

$$\text{Obj} = \sum_{i=1}^{N} T_i \cdot \text{FB}_i, \tag{3.3}$$

in this case the weighting for each condition is set to be equal, $T_i = \frac{1}{5}$.

Since the model does not include the vertical tail or engine nacelles and corresponding pylons, 35 counts of drag are added to the CFD computed drag coefficient to account for these missing components. The zero-fuel weight of the aircraft is computed from the wing-box finite-element model along with a set of fixed weight components—fuselage, payload, non-structural masses, engines, etc.—using the following formula:

$$\text{ZFW} = 1.25 \times W_{\text{Wing}} + \text{Fixed Weight} + \text{Reserve Fuel Weight} + \text{Secondary Wing Weight}, \tag{3.4}$$

where W_{wing} is the weight computed by the wingbox structural model. The factor of 1.25 accounts for additional weight associated with fasteners, overlaps, and other components not modeled in the idealized wingbox. Table 3.7 list other design parameters used to compute the objective function.

Table 3.7: Design optimization specifications

Parameter	Value	Units
Initial cruise altitude	$37,000$	ft
Initial Maximum take-off weight (MTOW)	$297,500$	kg
Maximum landing weight (MLW)	$213,180$	kg
Maximum zero fuel weight (MZFW)	$195,040$	kg
Operational empty weight	$138,100$	kg
Design range	$7,725$	nm
Design payload	$34,000$	kg
Reserve fuel	$15,000$	kg
Initial wing weight	$30,286$	kg
Fixed weight	$107,814$	kg
Thrust specific fuel consumption (TSFC)	0.53	lb/(lbf $\cdot$ h)

3.3.2.2 Design variables

To take full advantage of the possible gains in high-fidelity aerostructural wing design optimization, a large number of design variables is required. In RANS-based aerodynamic shape optimization, Lyu et al. [79] showed that at least 200 wing shape variables are required to achieve a good trade-off between the optimal result and the number of variables.

Table 3.8: uCRM-13.5 optimization design variables.

Variable/function	Description	Quantity
x_{α_i}	Angle of attack for each case	10
x_{tail}	Tail trim angle for each case	10
x_{twist}	Wing twist	8
x_{shape}	FFD control points	240
$x_{\text{panel thick}}$	Panel thickness skin/spars/ribs	287
$x_{\text{stiff thick}}$	Panel stiffener thickness skin/spars/ribs	184
$x_{\text{stiff height}}$	Panel stiffener height skin/spars/ribs	184
$x_{\text{panel length}}$	Panel length skin/spars/ribs	184
$x_{\text{stiff pitch}}$	Panel stiffener pitch skin/spars/ribs	4
$C_{L_0}^*$	Nominal cruise target lift coefficient	1
	Total design variables	**1,112**

For structural sizing based on detailed wingbox FEMs, the more sizing variables that are included, the more the optimizer can reduce the weight and leave material only where it is needed. The design variables can be broken down into three groups: geometric variables, aerodynamic variables, and structural variables. A total of 1,112 design variables are used for this design optimization and they are listed in Table 3.8.

The geometric design variables include the airfoil cross-sectional shape distribution over the span of the wing. The optimizer controls these shapes by perturbing the z-coordinate of each control point on the FFD surface containing the wing, shown as red spheres in Figure 2.1. The optimizer also controls the spanwise twist distribution of the wing by rigidly rotating each chordwise set of FFD control points. The optimizer cannot change the planform (sweep, span, and reference area), because it is desired to keep it fixed for the design.

The aerodynamic design variables include the angle of attack for each of the 10 flight conditions. The angle-of-attack variables are necessary to satisfy the lift constraint for each condition. In addition to the angle-of-attack variables, a horizontal stabilizer incidence angle variable is also included for each flight condition. This variable ensures that the aircraft can trim out the pitching moment about its center of gravity for each flight condition.

A target nominal lift coefficient design variable is used to allow the nominal cruise condition to change and ensure an optimal cruise C_L as the design changes. The other four flight conditions follow this changing nominal condition using the specified C_L. Only the cruise and buffet points are affected by the moving stencil, since the maneuver conditions are constrained to match the aircraft MTOW. The purpose of allowing the optimizer to

move the position of the cruise stencil in C_L is to give control over the designs cruise altitude. This means that as the nominal cruise C_L increases, the aircraft must fly at a higher cruise altitude to carry the same weight.

The remaining design variables consist of the structural design variables used to parameterize the wingbox. These variables include the stiffener pitch of the upper skin, lower skin, leading edge spar, and trailing edge spar, since the pitch is assumed to be constant across each of these components. As a result of the panel-based smeared stiffness approach, described in Section 3.2, three additional design variables are used for each wingbox rib bay section: panel thickness, stiffener thickness, and stiffener height. The only exception to this are the ribs, all of which share stiffener design variables. Additionally, the panel length is included as a design variable for each panel to simplify the panel buckling computations. Since the panel dimensions change with the geometry during the optimization, a nonlinear consistency constraint is added for each panel length variable to ensure that they match the respective geometric panel lengths of each component.

3.3.2.3 Constraints

To achieve a meaningful and physically realizable design, many constraints must be considered in the optimization problem. In total, the design optimization enforces 1,328 linear and nonlinear constraints, as listed in Table 3.9.

The first set of these constraints is to ensure steady trimmed flight for each design condition. For the cruise and buffet conditions this means that the lift coefficient, C_{L_i}, for that condition must match the value defined by the moving cruise flight conditions stencil. For the maneuver conditions, the constraint is specified for the physical lift, such that the lift equals the MTOW multiplied by the respective load factor, n, where the MTOW is based on the fuel burn computed from the first cruise condition as shown below:

$$\text{MTOW} = \text{ZFW} + \text{FB}_0. \tag{3.5}$$

The separation-based buffet constraint is used for the two buffet design points. Constraining buffet at these two points, ensures that all cruise points remain in the envelope defined by the 1.3 g margin to buffet onset, as required by flight regulations [101].

The next set of constraints related to the geometry of the design are imposed to prevent physically unrealizable designs. There is a constraint on the wing leading edge radius preventing it from decreasing relative to the baseline. This is done to prevent the optimizer from compromising the high-lift performance for takeoff and landing, a condition that is not included explicitly in the optimization problem formulation. Lyu et al. [79] showed

Table 3.9: uCRM-13.5 optimization design constraints.

Variable/function	Description	Quantity
$C_{L_i} = C_{L_i}^*$	Cruise and buffet lift conditions	7
$L = n_i\text{MTOW}$	Maneuver lift conditions	3
$C_{M_y}^i = 0$	Trimmed flight	10
$\text{Sep}_i \leq 0.04$	Buffet separation constraints	2
$t_{\text{LE}}/t_{\text{LE}_{\text{init}}} \geq 1.0$	Leading edge radius	20
$t_{\text{TE}}/t_{\text{TE}_{\text{init}}} \geq 1.0$	Trailing edge thickness	20
$(t/c)_{\text{TE,spar}} \geq 0.80(t/c)_{\text{TE spar}_{\text{init}}}$	Minimum trailing edge spar height	20
$V - V_{\text{fuel}} \geq 0.0$	Minimum fuel volume	1
$L_{\text{panel}} - x_{\text{panel length}} = 0$	Target panel length	266
$\text{KS}_{\text{fail}} < 1.0$	2.5 g and cruise w/ gust material failure	8
$\text{KS}_{\text{buckling}} < 1.0$	2.5 g, -1 g and cruise w/ gust buckling	9
$\left\| x_{\text{panel thick}_i} - x_{\text{panel thick}_{i+1}} \right\| \leq 0.0025$	Skin thickness adjacency	258
$\left\| x_{\text{stiff thick}_i} - x_{\text{stiff thick}_{i+1}} \right\| \leq 0.0025$	Stiffener thickness adjacency	258
$\left\| x_{\text{stiff height}_i} - x_{\text{stiff height}_{i+1}} \right\|$	Stiffener height adjacency	258
$x_{\text{stiff thick}} - x_{\text{panel thick}} < 0.005$	Maximum stiffener-skin difference	172
$\Delta z_{\text{TE,upper}} = -\Delta z_{\text{TE,lower}}$	Fixed trailing edge	8
$\Delta z_{\text{LE,upper}} = -\Delta z_{\text{LE,lower}}$	Fixed leading edge	8
	Total constraints	**1,328**

that transonic wing optimizations without this constraint yield designs with unrealistically sharp leading edges.

Additionally, a constraint is applied to the wing trailing edge to prevent the thickness from decreasing. This is done to prevent the optimizer from producing designs with excessively thin trailing edges, which leads to manufacturing and handling issues. Like the trailing edge, a constraint is placed on the depth of the wing at the location of the trailing edge spar. This is done, again, to prevent manufacturing difficulties, as well as to ensure that there is adequate room for the actuators and control surfaces to be mounted on the spar.

There is a volume constraint on the fuel bay of the wing that ensures that there is enough volume for the fuel required to complete the mission, including reserve fuel. The last of the sets of geometric constraints consist of 16 linear constraints on the FFD shape variables that prevent the leading edge from moving vertically relative to the trailing edge. This ensures that no inadvertent twist is added to the wing through the shape variables, and guarantees that the twist and shape variables are independent.

The remaining constraints are applied to the structure of the wing. The 2.5 g maneuver and 1 g cruise with gust conditions each use four KS material failure constraint aggregation functions: one each for the upper skin, lower skin, ribs, and spars. For these conditions,

aggregated buckling constraints are enforced only for the upper skin, ribs, and spars. For the $-1\,\mathrm{g}$ condition, only the buckling constraints are enforced for the lower skin, ribs, and spars. This is because the $-1\,\mathrm{g}$ case is not critical in sizing for stress like the $2.5\,\mathrm{g}$ and the $1\,\mathrm{g}$ cruise condition. As mentioned previously, there are also consistency constraints for each panel to ensure that the panel length used for the buckling calculations are consistent with the physical dimensions of the panel. Finally, hundreds of linear adjacency constraints are applied to ensure that the panel thickness, and stiffener thickness and heights do not change too abruptly from panel to panel.

3.3.3   Results

In addition to the uCRM-13.5 design produced by the optimization procedure described in the previous section, three additional designs are provided as references. The first reference design is the baseline unoptimized uCRM-13.5 design. This design features the initial uCRM-13.5 planform extended from the uCRM-9, with the cross-sectional shape and twist distributions remaining unchanged. After the planform is updated, the baseline structure is then resized through a structural optimization, to ensure the wingbox does not fail or buckle under the new aeroelastic loads. As mentioned previously, since the aeroelastic properties differ greatly between the uCRM-9 and uCRM-13.5 due to the increase in wing flexibility it can be expected that this design performs poorly, hence the need for re-optimization. The two other reference designs are based on the uCRM-9. The first of these two is the uCRM-9 baseline design, defined in the previous section. The other AR 9 reference is developed by starting with the uCRM-9 baseline and optimizing using same buffet-constrained multipoint aerostructural optimization design procedure used to obtain the uCRM-13.5 optimized design. The goal of this design is to use it in a comparison with the uCRM-13.5 and assess the effect that the higher AR wing has on the performance. The aerostructural performance of the uCRM-9 and uCRM-13.5 baseline designs are analyzed at the nominal cruise conditions for the CRM, described in Section 3.2.

For the uCRM-9 based optimization, the coarse mesh described in Section 3.2 is used, to be comparable with the size of the meshes used for the uCRM-13.5 optimization. The buffet-constrained multipoint optimizations are run on 1,000 processors (roughly 100 processors per flight condition) for up to 48 hours. The iteration histories for both optimizations are plotted in Figure 3.17. The objective function is the fuel burn in percent of the design MTOW. The feasibility and optimality are a measurement of the constraint violation and satisfaction of the first-order KKT conditions, respectively [28]. In both cases the optimizer gradually reduces the objective while improving the feasibility of the design.
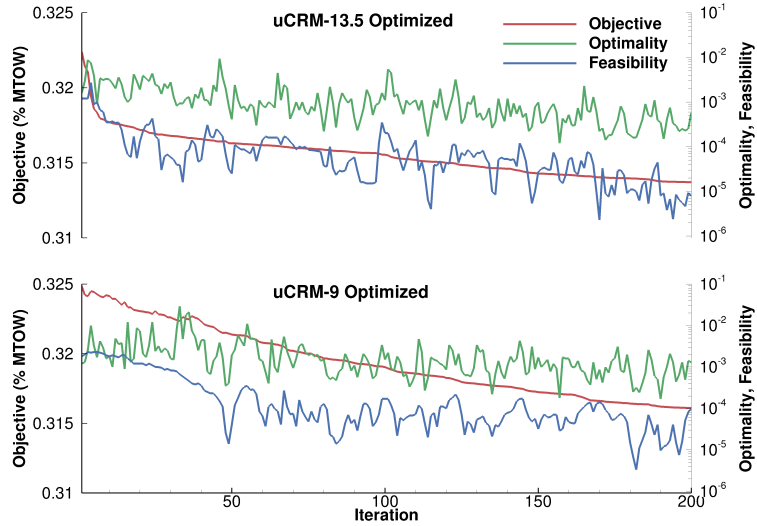
Figure 3.17: Optimization convergence histories for the each cases

Figures 3.18 and 3.19 compare the two uCRM-13.5 based designs and the two uCRM-9 based designs, respectively. In the top left corner of these figures the cruise C_p distribution of each design is shown, as well as a front view with the deflection of the wing at various flight conditions. Shown below this, are the spanwise aerodynamic quantities of interest: normalized lift distribution, wing twist, and wing thickness-to-chord ratio (t/c). Shown in the upper right-hand corner are the structural values of interest: mass equivalent structural thickness distribution of the wingbox panels, as well as the buckling and material failure constraints for the 2.5 g maneuver condition (the most restrictive of the maneuver conditions) over each wingbox component. Finally, shown below this are four airfoil slices and the corresponding C_p distributions at various spanwise locations along the wing. Additionally, both optimized designs are free to translate their cruise and buffet design conditions with respect to C_L during the optimization. The final flight conditions from the uCRM-13.5 and uCRM-9 optimizations are listed in Table 3.10 and 3.11, respectively.

uCRM-13.5 Baseline
MTOW: 306214 kg
Fuel burn: 105120 kg
L/D: 19.07
Wing mass: 30475 kg

uCRM-13.5 Optimized
MTOW: 284256 kg
Avg Fuel burn: 84072 kg
Avg L/D: 22.91
Wing mass: 30032 kg

Equivalent Thickness (mm): 4 9.6 15.2 20.8 26.4 32

C_P: -1 -0.8 -0.6 -0.4 -0.2 0 0.2 0.4 0.6 0.8 1

Buckling: 0 0.15 0.3 0.45 0.6 0.75 0.9

Failure: 0 0.15 0.3 0.45 0.6 0.75 0.9

Buckling

Failure

2.5 g
Cruise
Jig
-1.0 g

Normalized Lift

Cruise
2.5 g
Elliptical

Elliptical

Twist

t/c

A = 16%

B = 35%

C = 58%

D = 89%

C_P

Figure 3.18: Comparison of uCRM-13.5 baseline (left) with optimized uCRM-13.5 (right) aerostructural designs.
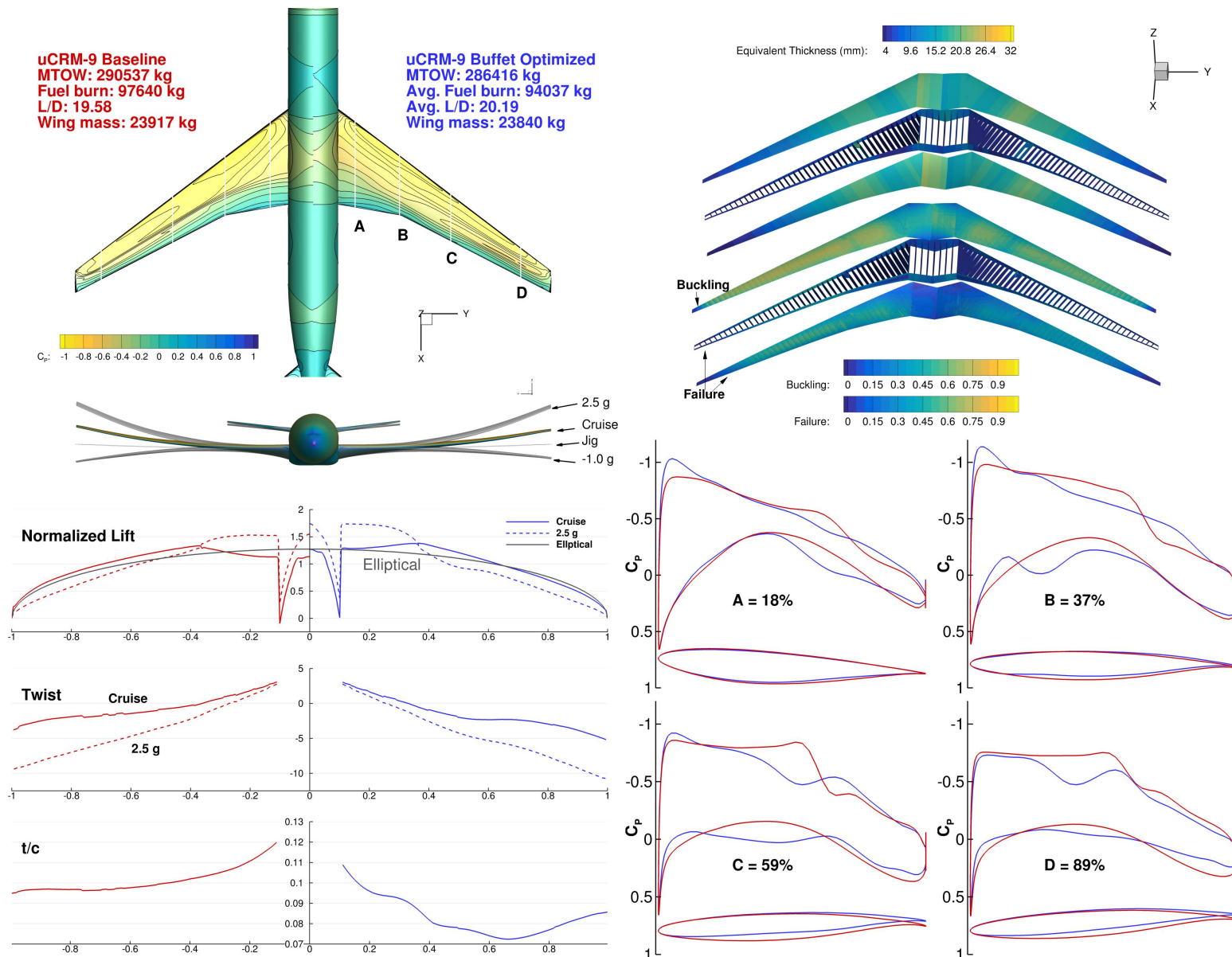
Figure 3.19: Comparison of the finalized uCRM-9 baseline (left) with optimized uCRM-9 (right) aerostructural designs.

Table 3.10: Optimized uCRM-13.5 final flight condition stencil.

Point	Condition	Mach	C_L
1	Cruise	0.85	0.549
2	Cruise	0.85	0.524
3	Cruise	0.85	0.574
4	Cruise	0.84	0.562
5	Cruise	0.86	0.536
6	Buffet	0.85	0.746
7	Buffet	0.89	0.501

Table 3.11: Optimized uCRM-9 final flight condition stencil.

Point	Condition	Mach	C_L
1	Cruise	0.85	0.515
2	Cruise	0.85	0.490
3	Cruise	0.85	0.540
4	Cruise	0.84	0.527
5	Cruise	0.86	0.503
6	Buffet	0.85	0.702
7	Buffet	0.89	0.470

By looking at Figure 3.18, several key differences can be observed between the baseline and optimized uCRM-13.5 designs. First, a large difference in fuel burn performance can be seen, with a 20.0% (21 048 kg) improvement in the optimized aircraft's favor. By looking at the L/D values for both designs, it is seen that the reason for the difference in fuel burn is primarily due to the baseline design's poorer aerodynamic performance. Comparing the normalized lift and twist distributions yields further insight into how the optimizer improves the aerodynamic performance: The optimization was able to obtain a more elliptically loaded spanwise lift distribution at cruise, which reduces the induced drag on the wing. The reason for the baseline design's non-elliptical lift distribution is that the wing features too much washout at the tips. This excessive washout means that very little lift is generated in the outboard region of the wing and that the lift inboard has to increase to compensate. In addition to causing the lift distribution to deviate from elliptical, increasing the induced drag, this also causes a strong shock to occur in the inboard region of the wing, increasing the wave drag. The optimizer removes the additional washout by twisting the wing tips up, leading to a more aerodynamically efficient design. The t/c distribution shows that the optimizer reduces the airfoil thickness of the wing to decreased the drag. A lower t/c also mitigates buffet onset. This allows the optimized design to fly at a slightly higher C_L, which improves the L/D.

Comparing the uCRM-9 baseline and optimized designs in Figure 3.19, shows that the optimized design is able to reduce the fuel burn by 3.7% (3 603 kg). The reason for this more modest improvement in fuel burn is that the CRM, which the uCRM-9 baseline design is based on, is already a well designed aircraft. This means that little improvement can be made to the design. Analyzing the structural weight of both designs reveals that the structural weight of the wing remains largely unchanged. This is despite a significant reduction in the wing thickness distribution over the span for the optimized design. Looking at the normalized lift distribution for these designs reveals that the optimizer accomplishes this by shifting the maneuver load inboard, which reduces the structural load at the root of the wing, while maintaining elliptical lift distribution during cruise to reduce drag. This passive load alleviation is enabled by the structural bend-twist coupling inherent in swept-back wings. Looking at the t/c distribution of the wing again shows a trend of reduction in wing thickness relative to the baseline in order to meet the buffet constraint.

By comparing the uCRM-13.5 in Figure 3.18 with the uCRM-9 designs in Figure 3.19, it can be seen that the baseline uCRM-13.5 performs worse than the lower AR designs in terms of fuel burn and L/D. This is despite the inherent induced drag benefit offered from a larger wing span, confirming the need for a full aerostructural optimization to produce a more realistically performing model. By comparing the uCRM-9 designs to the optimized uCRM-13.5, it can be concluded that the increase in AR results in a 10.6% reduction in fuel burn. This is despite a 20.6% increase in structural weight associated with the higher AR wing design. By looking at the structural thickness distribution along the panels of the wingbox, it can be seen that the difference in weight is due to the thicker wingbox near the Yehudi break of the wing. Again, this makes sense because the longer span of the AR 13.5 designs also means a larger moment arm for the aerodynamic loads, which increases the internal forces in the wing, requiring more structural material. By comparing the normalized lift distribution between each design, it is found that the lower AR wings achieve an even more elliptical lift distribution during cruise flight, while the higher AR wings shift the load more inboard. This is because the structural weight penalty associated with an even more elliptical spanwise wing loading outweighs the aerodynamic benefit due to the lower drag for the larger span wings.

Figure 3.20 shows a fuel burn contour plot as a function of Mach and C_L for both designs. This plot corresponds to different flight performance for the design at varying flight speeds and aircraft weights. By using this plot, both the robustness of each design and the margin between buffet onset and the cruise flight envelope can be assessed. The line denoted as 1.3 g buffet boundary shows the boundary for all of the operational conditions that have at least a 1.3 g margin to buffet onset. Ideally, all points in the cruise stencil
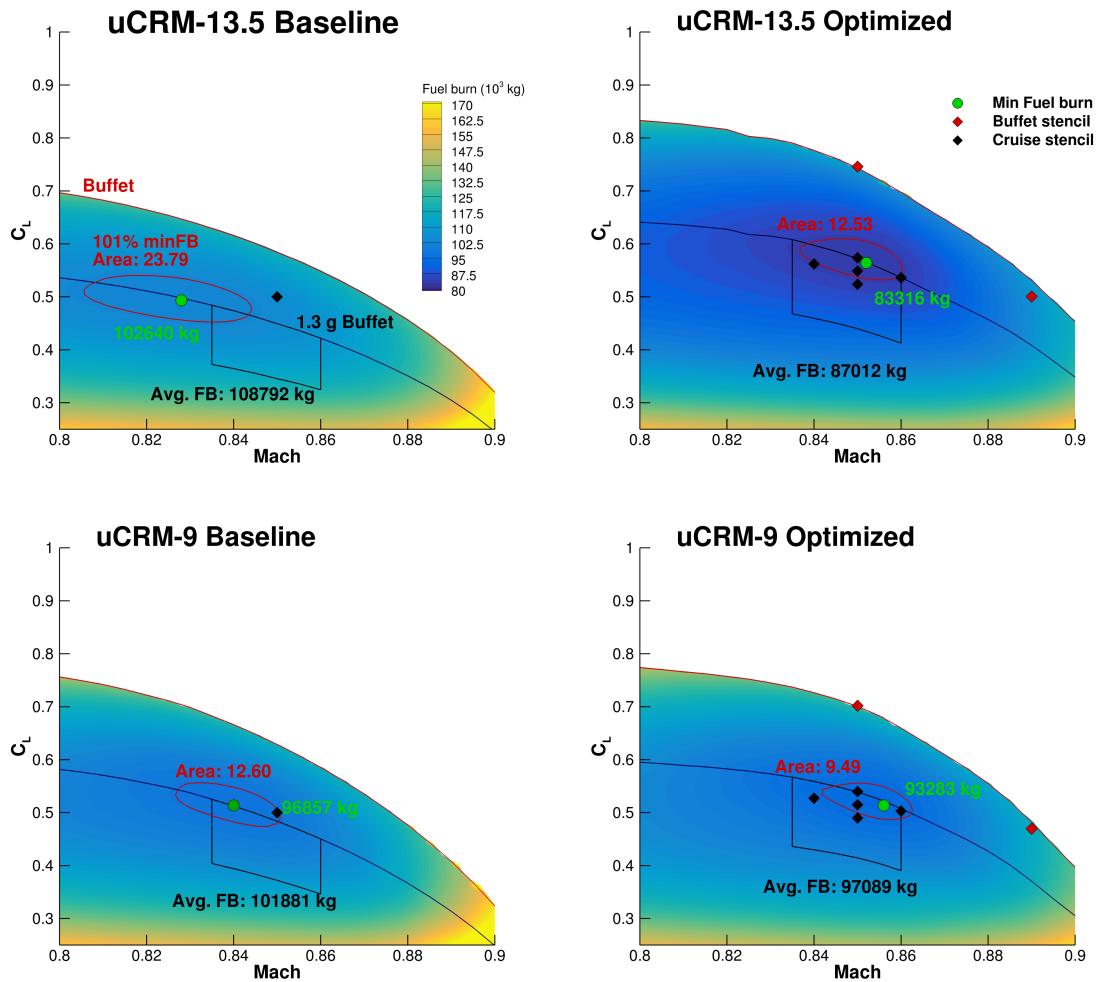
Figure 3.20: Fuel burn performance contours of each design as well as buffet and 1.3 g margin to buffet envelopes. The 101% minimum fuel burn contours and average integrated fuel burn performance give a measurement of each designs robustness.

would lie below this line to comply with FAA regulations. It can be seen that the nominal cruise condition of the baseline uCRM-13.5 design is not within this feasible region. This emphasizes the importance of considering buffet onset in the design optimization for the uCRM-13.5. The uCRM-9 baseline design cruise point is also slightly outside of the 1.3 g buffet region, but noticeably less so than the uCRM-13.5 baseline case, reinforcing the fact that this is already a well-designed aircraft. It is found that on the optimized uCRM-9 design, the optimizer increases the feasible region, allowing the optimizer to move the cruise points to a higher C_L to achieve a better performance. As mentioned previously, this is made possible by an overall decrease in the spanwise t/c distribution on the buffet optimized uCRM-9 design.

The box under the 1.3 g buffet boundary line in Figure 3.20 is what is called *fuel burn performance integration region*. The fuel burn in this region is averaged to assess the real-world performance of the design. Ideally, this region should overlap with the cruise stencil, and both should lie close to the global minimum fuel burn on the plot. However, because the buffet boundary is so restrictive in the case of the baseline uCRM-13.5 design, the integration region, nominal cruise point, and minimum fuel burn condition do not align in Mach-C_L design space, causing a reduction in average fuel burn performance. It can be seen that the optimizer is able to raise the performance integration region by moving the stencil up in C_L on the optimized uCRM-13.5, which ultimately leads to a decrease of 20.0% in average fuel burn.

To better quantify the measurement of robustness, the contour corresponding to 101% of the minimum fuel burn is plotted, in red, along with the corresponding area enclosed by this contour for each design. This gives us an idea of how quickly the design performance decays away from the optimal design point, which translates to robustness with respect to flight conditions. The baseline uCRM-13.5 design has the largest 101% contour region, meaning that it is the most robust of the four designs. However, despite its robustness, it is consistently outperformed by all three designs at any given point in this region of the flight envelope. From the 101% contour lines of the optimized uCRM-9 and uCRM-13.5 designs, it can be seen that the optimizer was able to improve the overall fuel burn over the entire flight envelope while keeping the designs fairly robust when compared to the baseline uCRM-9 design. This is due to the fact that both optimized designs consider performance at multiple flight conditions in the optimization.

Given that the uCRM-9 optimization did not improve the baseline by that much, it was decided to keep the baseline uCRM-9 configuration as the reference, to keep the connection to the original CRM shape. For the uCRM-13.5, since the baseline performs so poorly, it is logical to choose the aerostructurally optimized version to be the reference.

3.4 Summary

This work was motivated by a lack of benchmark aeroelastic models for transonic aircraft analysis and design. The NASA CRM, which is an excellent aerodynamic model that has been widely used, was leveraged to develop two static aeroelastic models: one with a conventional AR, and another with a higher AR to be representative of next-generation wings. To accurately capture the appropriate "physics" associated with transonic flexible wing design a coupled high-fidelity MDO approach is utilized to define both models. Both of these models' geometries feature the jig or undeflected wing shape, making them appropriate for the use in aerostructural and aeroelastic analysis, as well as wing aerostructural design optimization studies.

The first model, the uCRM-9, is a design with an aspect ratio 9 wing that deforms into the CRM geometry under its nominal cruise flight condition of $M = 0.85$, $C_L = 0.5$. Since this model is defined to be the jig or undeflected shape of the CRM wing it is appropriate for use in aeroelastic studies. This design was obtained by first defining a realistic wingbox topology for the CRM and sizing it through a structural optimization subject to aerodynamic loads. An inverse design procedure was then performed where the deflection of the CRM wing was iteratively removed from the geometry using FFD shape variables. The procedure was repeated for several iterations until a reasonably converged results was obtained. In order to verify that the design procedure produced a reasonable approximation to the jig shape of the CRM wing, a static aerostructural analysis was performed. From this, the model was found to be within 0.001% agreement with the drag produced by a CFD analysis of the CRM about its nominal cruise condition. Finally, an aerostructural grid convergence study was performed on the model. From this study it was also possible to conclude that the meshes used to create this model were reasonably well converged.

The second aeroelastic model, the uCRM-13.5, is a higher aspect ratio winged variant of the CRM. The motivation for the development of this model is for studies of new technology concepts with the goal of enabling higher aspect ratio wing designs. Due to the higher degree of flexibility present in the wing design an aerostructural optimization study was performed to obtain a reasonable geometry and structural sizing for this model. Through this study the importance of considering multiple flight conditions in the optimization to achieve a robust design was shown, with the multi-point optimized design achieving a 20.0% reduction in average fuel burn over its integrated flight envelope relative to the baseline design. In addition, since buffet onset performance was included and constrained the optimized design was also able to increase the size of the flight envelope, again demonstrating the necessity for buffet onset considerations with respect to transonic wing design

optimization. Furthermore, by including the uCRM-9 in the optimization study it was confirmed that the design, and by extension the CRM, was already relatively well designed, the optimizer only being able to improve it by a modest 3.7%. As one might expect by extending the aspect ratio of the CRM wing from 9 to 13.5 a reduction of roughly 10.6% in fuel burn can be seen, due mostly to a reduction in induced drag on the wing.

As mentioned previously, all models developed in this chapter are publicly available and include files for the geometry, structures, and external mass distributions. These models provide not only a benchmark for the design studies throughout the rest of this thesis, but also for future high-fidelity aerodynamic, structural, and aeroelastic studies—both static and dynamic. Further developments, such as the inclusion of structural dynamic modal analysis, are expected to result in variable-fidelity models and models that better capture dynamic aeroelastic phenomena.

CHAPTER 4

PySteer: A framework for parametric structural optimization

In the previous chapter, the uCRM models with conventional metallic structural designs were introduced, in this chapter, the parametrization of the structural model will be extended to unconventional tow-steered composite designs. One of the key differences of a AFP manufactured structure is the continuous spatial nature of the AFP layup process. Due to this fact, a panel-level structural parametrization, as described in Chapter 3, would no longer be appropriate and an alternative approach must be devised. For this reason, pySteer, a python-based tool for the parametrization of tow-steered and variable stiffness structures was developed. pySteer represents a major development in this work and has made parametric tow-steered optimization possible in the MACH framework. In pySteer, the variable stiffness properties—pattern orientation and panel thickness—are parametrized using interpolations from B-spline control points distributed over each parametric surface of the structure. The B-spline interpolation engine used in this work is borrowed from the Geometry-centric MDAO of aircraft configurations with high fidelity (GeoMACH) framework, developed by Hwang and Martins [102]. Throughout the remainder of this chapter a walk through of the computational work flow relating pySteer to the MACH framework will be given. The approach used to model the constitutive properties of the tow-steered elements in the FEM model will also be explained.

4.1   Initialization

pySteer is first initialized by the user by providing the structural FEM mesh as an input in the form of a Nastran bulk data file (BDF). pySteer then assigns each component of the model—ribs, spars, skins, etc.—a python object. The user then has the ability to specify to pySteer which of the components should have parametrically varying properties. All of

the elements in the components flagged as non-parametric will share the same constitutive properties, thickness and ply orientations, and the design variables for these components will be set at a panel-level, as in the previous chapter. For the wingboxes considered in this work, the skins and spars are specified as parametric components while the ribs are non-parametric.

The components flagged as parametric are then assigned a number of B-spline control point distributed along their surface. The GeoMACH B-spline engine used in this work requires that each of the 3D surfaces specified by the user have a 2D parametric mapping as well, as shown below,

$$\vec{r} = \vec{r}(\xi, \eta), \tag{4.1}$$

where ξ and η are parametric variables and $(\xi, \eta) \in [0, 1]$. This is problematic because often times these structural models will be generated by a commercial mesh generation tool, such as ICEMCFD, and these parameters will not be available to the user as an output. For this reason, pySteer has the capability to generate a ξ-η mapping based on the surface mesh of each component in the BDF. The user need only specify the four locations (nodes) along the surface boundary where the corners of the parametric map—$(\xi, \eta) = (0,0), (0,1), (1,0), (1,1)$— are desired to occur. It is important to note that the corners of the parametric map need not correspond to actual corners in the geometry. Indeed, the surface being parametrized may have more or less than four distinct corners on its boundary. The user needs only specify four locations on the surface boundary where these parametric extremes should be located. These corners need to be specified for each component the user wants to designate as parametric.

Once this is done, the nodes on the boundary of each component surface mesh are traversed, starting at the first corner node and proceeding through the remaining three until the first node is cycled back to. The arc-distance of each node on each of the four segments defined by the four corner nodes are computed, starting with the first corner node at 0. The ξ and η coordinates of each of the nodes on each segment are then assigned linearly based on their arc-distance from the two corner nodes that define that segment. At the end of this step, a parametric map has now been defined only for the boundary nodes of the surface mesh.

The remaining nodes inside the surface boundary are then solved for as a Laplacian boundary value problem (BVP):

$$\nabla^2 \xi = 0, \qquad \nabla^2 \eta = 0 \tag{4.2}$$

This Laplacian mapping has two advantages. The first being that it guarantees that the

resulting parametric map for each surface will be smooth. Secondly, since each component surface mesh is the subset of a larger FEM mesh, these problems can be solved efficiently through finite element analysis. To save time, pySteer also has the option to append the parametric coordinates for each parametric component, once solved, to the loaded BDF and read them off on future runs.

Once the parametric map is computed for each surface, the user can specify the number of requested control points in each parametric direction. The control points are then distributed uniformly in the parametric space, (ξ, η). Examples of resulting ξ, η parametric maps and B-spline control point distributions for various input meshes can be seen in Figure 4.1. After this step, the initialization of pySteer is complete and the structural variables can be set at the control points for each parametric component. pySteer will then create an internal instance of the structural solver, TACS, and the structural analysis or optimization can proceed.

4.2 Computational work flow

In the scheme of the MACH framework, pySteer can be thought of as a "middle-man" between the optimizer, pyOptSparse, and structural solver, TACS. Figure 4.2 shows a diagram of the computational work flow for a tow-steered aerostructural optimization involving pySteer. In this setup, the optimizer provides two inputs to the aerostructural problem: the aerodynamic, $\boldsymbol{x}^A$, and structural, $\boldsymbol{x}^S_{\text{cp}}$, design variable vectors. The aerodynamic design variables, $\boldsymbol{x}^A$,—which may contain variables that control the aircraft angle-of-attack, wing shape, twist, etc.—are passed directly to the CFD solver, ADFlow. This part of MACH remains completely unchanged from what was described in Chapter 2. On the structural side, the structural design variables, $\boldsymbol{x}^S_{\text{cp}}$, are set at the B-spline control points for each parametric component. pySteer then interpolates the design variable values to the nodes to create a nodal design variable vector, $\boldsymbol{x}^S_n$. By the nature of the B-spline interpolation, this takes the form of a linear transformation:

$$\boldsymbol{x}^S_n = \boldsymbol{C}(\boldsymbol{\xi}_n, \boldsymbol{\eta}_n)\,\boldsymbol{x}^S_{\text{cp}} \tag{4.3}$$

Where $\boldsymbol{C}$ is the B-spline transformation matrix which interpolates the values from the control points to each node. $\boldsymbol{C}$ is a function only of the parametric coordinates of each nodes, $\boldsymbol{\xi}_n$ and $\boldsymbol{\eta}_n$, and remains constant during the optimization. These nodal design variables are then passed to TACS and are then used to set and assemble the element stiffness matrices. Once this is done, the structural problem, or aerostructural problem in conjunction with

65
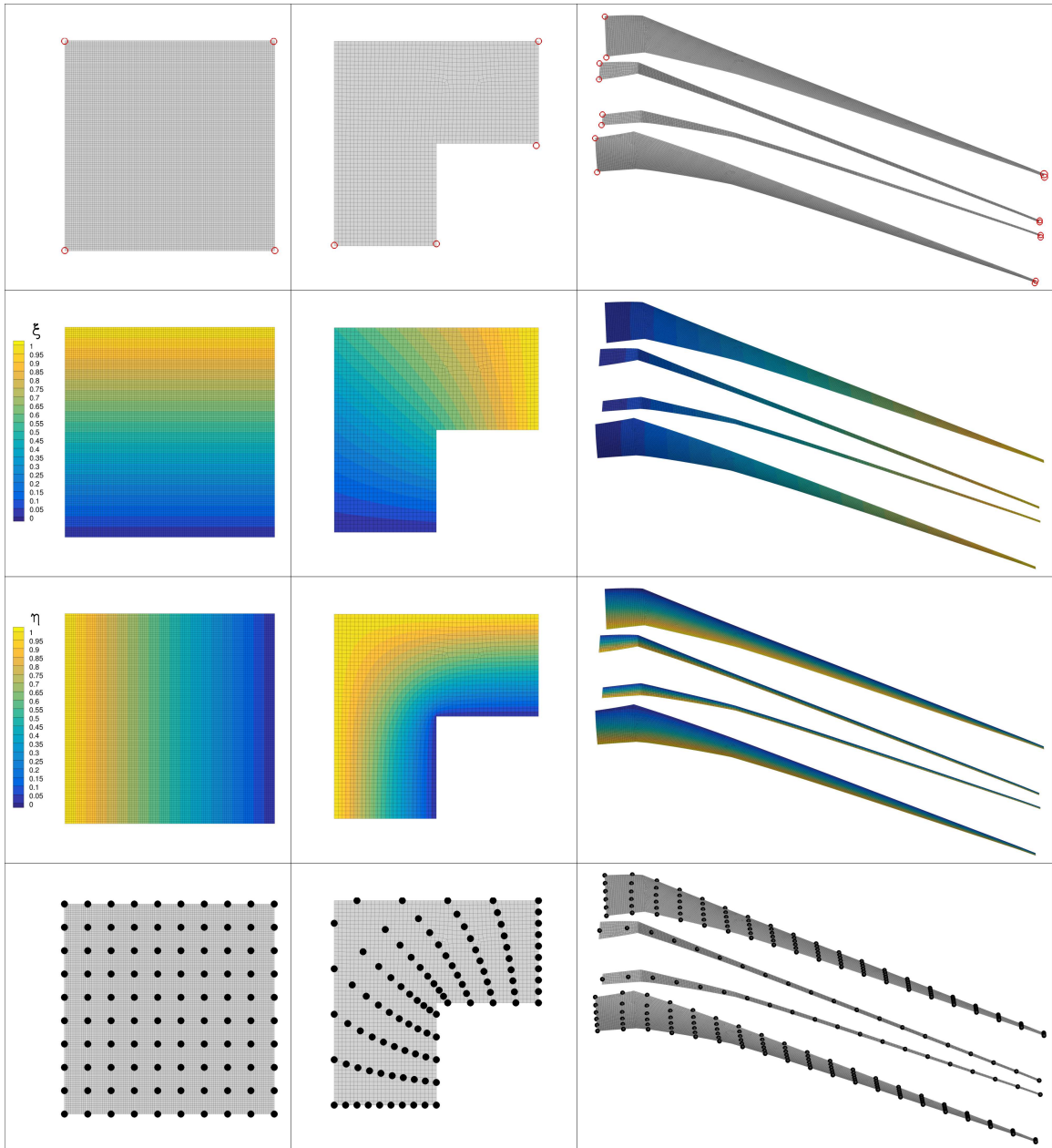
Figure 4.1: Examples of the parametric map generation procedure: (top) Input meshes and user-defined parametric corners (red circles), (middle) resulting ξ and η parametric distributions, (bottom) resulting B-spline distribution
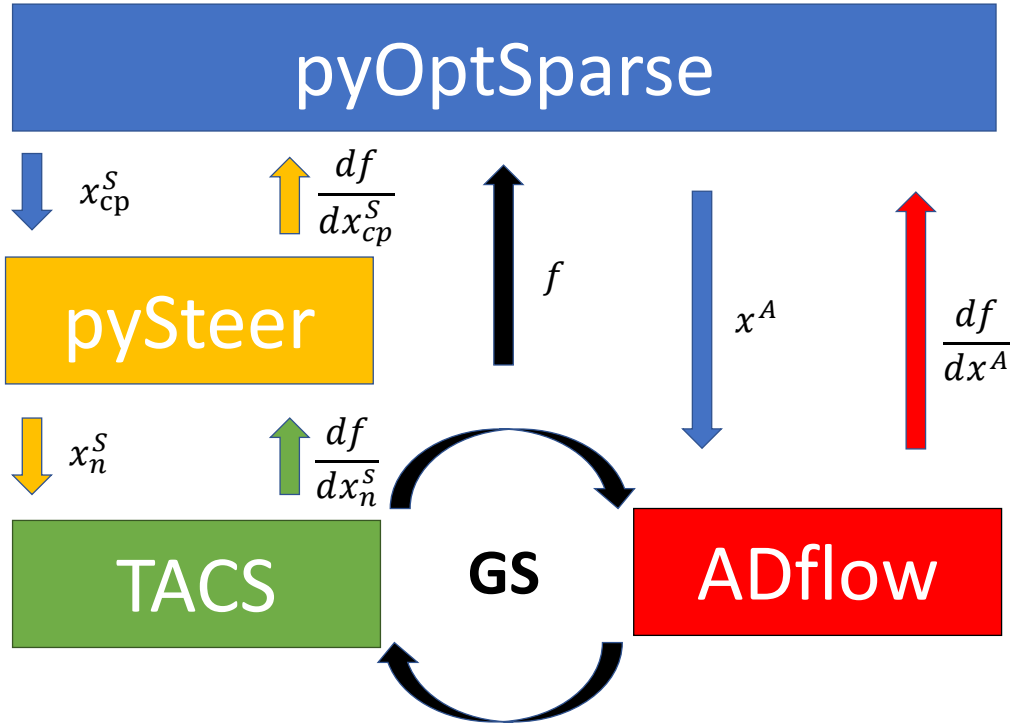
Figure 4.2: pySteer hierarchy

ADFlow, can then be solved. The relevant design functions of interest, f, are then passed back to the optimizer. In the case of a structural optimization these functions may include values such as weight, stress, and buckling and in the case of aerostructural optimization can also include lift, drag, and moment. In addition to translating structural design variables between the optimizer and TACS, pySteer is also responsible for computing relevant tow-steering manufacturing constraints, as will be discussed in Chapter 5.

After the optimizer completes a major iteration the function sensitivities must then be provided by the aerostructural solver. This is done through solving the coupled adjoint between TACS and ADFlow in the aerostructural solver, as described in Chapter 2. Once the coupled adjoint is solved, TACS and ADFlow provide the sensitivity of the functions of interest with respect to the nodal structural design variables, $\frac{df}{dx_n^S}$, and aerodynamic design variables, $\frac{df}{dx^A}$, respectively. Since TACS sees the design variables as being defined at each node of the structure, the number of components in the sensitivity vector, $\frac{\mathrm{d}f}{\mathrm{d}\boldsymbol{x}_n^S}$, is on the order of the number of FEM nodes, or $\mathcal{O}(10^4)$ for a typical wingbox structure considered in this work. While computation of a sensitivity vector of this size would be prohibitively expensive for a finite-difference-based method, as mention in Section 2.1, little to no additional computational time is required for an adjoint-based approach. This is because the adjoint approach's computational effort scales with the number of functions of interest, f,

and not the number of design variables.

Once this step is completed, the aerodynamic sensitivities, $\frac{\mathrm{d}f}{\mathrm{d}\boldsymbol{x}^A}$, are passed directly back to the optimizer. The nodal structural sensitivity is passed back to pySteer to compute the control point sensitivity, as given below:

$$\frac{\mathrm{d}f}{\mathrm{d}\boldsymbol{x}^S_{\mathrm{cp}}} = \frac{\mathrm{d}f}{\mathrm{d}\boldsymbol{x}^S_n}\,\boldsymbol{C}(\boldsymbol{\xi}_n, \boldsymbol{\eta}_n) \tag{4.4}$$

This is given by the chain rule, since by Equation (4.3):

$$\frac{\mathrm{d}\boldsymbol{x}^S_n}{\mathrm{d}\boldsymbol{x}^S_{\mathrm{cp}}} = \boldsymbol{C}(\boldsymbol{\xi}_n, \boldsymbol{\eta}_n)$$

This step reduces the structural design variable vector size from the order of the number of structural nodes, typically $\mathcal{O}(10^4)$, to the number of B-spline control points, typically $\mathcal{O}(10^2)$. The newly computed control point structural sensitivities are then passed back from pySteer to the optimizer along with the sensitivities for the tow-steering manufacturing constraints. Once both the aerodynamic and structural sensitives are received by the optimizer the step for the next major iteration of the optimization can be computed.

4.3 Wingbox constitutive model

Now that the parameterization scheme for pySteer has been discussed, the choice of structural design variables must still be decided. A common approach in the investigation of tow-steering design optimization is a two-step optimization procedure [49, 43, 61, 50]. In the first step, an initial gradient-based optimization over the design is performed using the layups stiffness components, or lamination parameters, directly as design variables. This provides the advantage of allowing the stacking sequence of plies, a discrete variable, to be considered during the design procedure. In the second step, a GA is generally used to attempt to translate the optimal lamination parameters into physically realizable tow paths and stacking sequences.

In this work, it was decided to avoid this approach for two reasons. The first is that in the second step of the procedure it is difficult to both match the optimal lamination parameters, while still respecting relevant manufacturing constraints. Secondly, the design problems considered in this work feature $\mathcal{O}(10^3)$ design variables, for which a gradient-free, GA, approach would not reasonably scale up to. Instead, the design problem will be formulated in a continuous fashion by parameterizing the tow paths directly and neglecting the effects of stacking sequence.

For the wing design optimization, only the panels of the upper and lower skins of the wingbox are tow-steered. Rather than optimizing each layer individually, leading to an unwieldy number of design variables, the panel laminates of each skin is defined by four ply orientations, and a panel thickness distribution, t_p. During the layup process each pattern is assumed to be repeated through the thickness of the laminate at a frequency corresponding to that orientation's ply fraction. The laminate is assumed to be relatively thick and therefore composed of many repeated layers. This assumption has two benefits. The first is that since the laminate thickness is much larger than the ply thickness, the optimization problem can be treated as continuous with respect to the laminate thickness. Thus, the discrete nature of the plies is neglected. The second benefit is that because the laminate consists of a few unique layers repeated many times through the thickness of the laminate, a homogenized material stiffness can be defined based on the relative frequency of occurrence through the thickness—the ply fraction—of each unique layer, so long as the stacking pattern does not vary through the thickness. This allows the effect of the stacking sequence to be safely neglected during the optimization for sufficiently thick laminates. This procedure is explained further in the following section.

In the case of the conventional unsteered composite structures considered in this thesis, there are four allowable ply orientations ($0°, 45°, -45°, 90°$). The distribution for the tow-steered laminate is similar; however, the angles are now offset by an angle that varies parametrically through the skin of the wingbox ($\theta_0(\xi, \eta), \theta_0(\xi, \eta) + 45°, \theta_0(\xi, \eta) - 45°, \theta_0(\xi, \eta) + 90°$), where ξ, and η are the parametric coordinates describing the wingbox surfaces. This results in four unique steered patterns on each skin that are repeated throughout the layup procedure of each skin at a frequency corresponding to their ply fraction. The reason for doing this is to ensure one dominant steered pattern, with three other offset patterns to ensure some off-axis strength. In this work, the ply fractions for both composite skin designs (conventional and tow-steered) are fixed for the optimization to (62.5%, 12.5%, 12.5%, 12.5%) for each respective ply orientation.

For the conventional and tow-steered composite designs the panel thickness is allowed to vary continuously and parametrically across the skins, in order to represent the continuous nature of the AFP layup process. For this reason, the local panel thickness, $t_p(\xi, \eta)$, of the skins and spars are set using B-spline control points distributed along each component. In the case of the tow-steered design, the tow-orientation offset of the skins, $\theta_0(\xi, \eta)$, are also set parametrically through the same B-splines, while for the conventional design these variables are turned off. Figure 4.3 shows an example tow-steered layup for one of the wingbox skins. The remaining design variables on the tow-steered model, stiffener thickness and height, are set using the wingbox structural patches, as described in Chapter 3
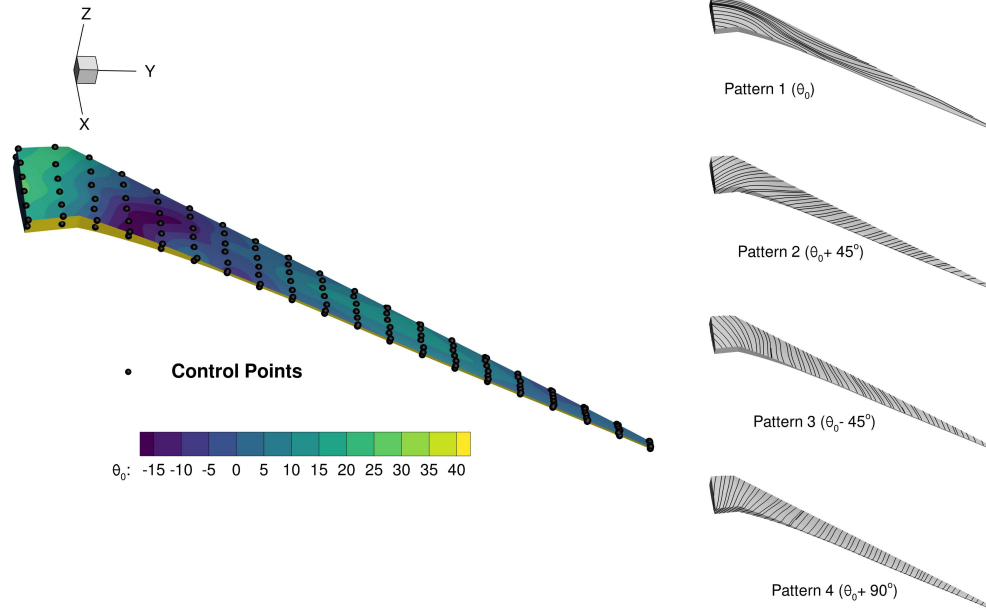
Figure 4.3: Example of the procedure used to define the main tow path and subsequent patterns

and shown in Figure 3.3, since only the panels are assumed to be laid up through the AFP process.

4.3.1 Smeared stiffness approach

The stiffness of the wingbox panels is modeled again using the smeared stiffness approach described by Kennedy et al. [98]. In this approach, to avoid the issues in dealing with the discrete nature of the composite stacking sequence in the panels and stiffeners, the stiffness of the laminate is homogenized through the thickness based on the fractions of plies in the panel and stiffeners, f_i^p and f_i^s respectively, at each angle through the thickness of the laminate, as follows:

$$\bar{\boldsymbol{Q}}^p(\xi, \eta) = \sum_{i=1}^{4} \boldsymbol{Q}(\theta_i^p(\xi, \eta)) \cdot f_i^p, \qquad \bar{\boldsymbol{Q}}^s = \sum_{i=1}^{4} \boldsymbol{Q}(\theta_i^s) \cdot f_i^s, \tag{4.5}$$

where $\boldsymbol{Q}$ is the stiffness matrix of the ply in the global frame, and $\bar{\boldsymbol{Q}}^p$ and $\bar{\boldsymbol{Q}}^s$ are the homogenized in-plane ply stiffness matrix of the panel and stiffener laminates, respectively. For the conventional unsteered wingbox components both the panel and stiffener allowable plies are the same, $\theta_i^p = \theta_i^s = \{0°, 45°, -45°, 90°\}$. While for the tow-steered skins, $\theta_i^p = \{\theta_0(\xi, \eta), \theta_0(\xi, \eta) + 45°, \theta_0(\xi, \eta) - 45°, \theta_0(\xi, \eta) + 90°\}$ and $\theta_i^s = \{0°, 45°, -45°, 90°\}$.

For this work the stiffener and panel ply fractions are set to be equal for each component, $f_i^p = f_i^s$, and are given in Table 4.1.

Table 4.1: Ply fraction breakdown by wingbox component

Component	$f_i^{(p/s)}$
Skins	$\{0.625, 0.125, 0.125, 0.125\}$
Spars/Engine mount	$\{0.125, 0.375, 0.375, 0.125\}$
Ribs	$\{0.375, 0.375, 0.125, 0.125\}$

The overall laminate stiffness is then computed as combination of the stiffness of the panels and the stiffeners:

$$
\begin{aligned}
\boldsymbol{A}(\xi, \eta) &= t_p(\xi, \eta) \cdot \bar{\boldsymbol{Q}}^p(\xi, \eta) + \boldsymbol{A}^s, & \boldsymbol{B}(\xi, \eta) &= \boldsymbol{B}^s, \\
\boldsymbol{D}(\xi, \eta) &= \frac{t_p^3(\xi, \eta)}{12} \cdot \bar{\boldsymbol{Q}}^p(\xi, \eta) + \boldsymbol{D}^s, & \boldsymbol{A}_s(\xi, \eta) &= t_p(\xi, \eta) \cdot \bar{\boldsymbol{Q}}_s^p(\xi, \eta) + \boldsymbol{A}_s^s
\end{aligned}
\tag{4.6}
$$

Where $\boldsymbol{A}$, $\boldsymbol{B}$, $\boldsymbol{D}$, and $\boldsymbol{A}_s$ are the laminate membrane, membrane-bending coupling, bending, and out-of-plane shear stiffness matrices from first-order shear deformation theory (FSDT). The non-zero stiffener contributions to the components of the stiffness matrices are given by:

$$
\begin{aligned}
A_{11}^s &= \frac{E_s A_s}{p_s}, & B_{11}^s &= -\frac{h_s}{2p_s} E_s A_s, \\
D_{11}^s &= \frac{E_s(h_s^2 A_s + 4I_s)}{4p_s}, & {A_s}^s_{11} &= \frac{5 G_s A_s}{6p_s}
\end{aligned}
\tag{4.7}
$$

where h_s, p_s, A_s, and I_s are the stiffener height, pitch, cross-sectional area, and second moment of area, respectively. E_s is is the stiffener extensional modulus and is given by $E_s = \bar{Q}_{11}^s - \frac{\bar{Q}_{21}^s \bar{Q}_{12}^s}{\bar{Q}_{66}^s}$.

As mentioned previously, this method neglects the effect of stacking sequence on the bending stiffness of the laminate, but works well for thick laminates with many repeated plies. The finite-element code then computes the stiffness and mass properties of the models from the nodes using isoparameteric elements based on Gaussian quadrature.

4.3.2   Laminate failure analysis

One of the structural constraints enforced during the optimization is that nowhere in the structure is the laminate, neither panel nor stiffener, allowed to exceed a failure criterion

within a safety factor of 1.5. The failure criteria is evaluated at the centroid of each element in the CSM structural model. The failure criterion used for this study was a maximum strain failure criterion, which can be written as follows:

$$\max \left\{ \frac{\epsilon_1}{\epsilon_{1_t}}, \frac{\epsilon_1}{\epsilon_{1_c}}, \frac{\epsilon_2}{\epsilon_{1_2}}, \frac{\epsilon_2}{\epsilon_{2_c}}, \frac{\gamma_{12}}{\gamma_{12_s}}, -\frac{\gamma_{12}}{\gamma_{12_s}} \right\}, \tag{4.8}$$

where ϵ_1, ϵ_2, and γ_{12} are the in-plane strains parallel, transverse, and shearing relative to the layer's local fiber direction, respectively. In addition, ϵ_{1_t} and ϵ_{2_t} are the maximum allowable strain in tension, both parallel and transverse to the fiber direction. Likewise, ϵ_{1_c} and ϵ_{2_c} are the maximum allowable strains in compression. Finally, γ_{12_s} is the maximum allowable shear strain along the fiber. Due to its discontinuous nature, the maximum function is again approximated using the KS method.

This constraint is applied as a first-ply failure in which no ply in laminate is allowed to fail. Since the stacking sequence is never explicitly defined in the analysis, the ply failure must be conservatively evaluated in the outermost layer for each local fiber orientation given by each unique pattern. After the failure constraint has been evaluated for each element, the constraint is then aggregated one more time over all of the elements in each component of the wingbox, (ribs, spars, and wing skin) using the KS aggregation.

4.3.3 Panel buckling analysis

Each panel of the wingbox is also constrained not to buckle for specified load conditions. This is approximated through a simplified panel-level buckling analysis of the stiffened panels applied on every component in the wingbox. This buckling analysis considers both longitudinal and shear buckling modes through several different buckling mechanisms, including: inter-stiffener panel buckling, stiffener buckling, and global panel buckling. The first step of the procedure is to compute the panels' critical buckling loads for each mechanism, both in compression ($N_{1,cr}$) and shear ($N_{12,cr}$). These values are dependent on the panels' local stiffness as well as geometric properties. Once these critical values have been obtained the constraint is then applied to every element in the panel as a conservative envelope of the form:

$$B(N_1, N_{12}) = \frac{N_{12}^2}{N_{12,cr}^2} + \frac{N_1}{N_{1,cr}} \leq 1, \tag{4.9}$$

for all three buckling mechanisms. This method has the benefit of being cheap to compute relative to performing a full buckling eigenvalue analysis for each panel. Like the failure constraints, the buckling constraints are evaluated at the centroid of every element and then aggregated over each component group using a KS function. More details of this approach

are provided by Kennedy et al. [98].

CHAPTER 5

Manufacturing considerations

In this chapter, the consideration of AFP-specific manufacturing constraints for tow-steered layups are introduced and formulated. Since part of the goal of this research is to provide a scaled tow-steered wingbox structure for manufacturing through gradient-based optimizations, these constraints are critical to ensuring that subsequent designs could be realistically produced with modern-day AFP machines.

In particular, three constraints are considered to ensure that the tow in the laminate varies smoothly and is thus realizable with an AFP machine. The first of these constraints is on the minimum turning radius of the tow path, $R_{\min}$. This constraint is defined by the manufacturer to prevent the prepreg tow from twisting over on itself or puckering out of plane as the tow is laid down by the head of the AFP machine. An example of tow puckering can be seen in Figure 5.1a. More aggressive values of minimum turning radii can be achieved by laying down paths with narrower prepreg tow, but for the same layup area this leads to an increase in manufacturing time and cost. The next constraint considered is related to the presence of gaps and overlaps of the prepreg tow. As the prepreg tow is laid down there will be regions in the layup that will either be void or where two portions of adjacent tow overlap due to fixed width of tow. Depending on the structural application, gaps and overlaps may not be desirable, as these regions can potentially lead to unwanted thickness variations if they are allowed to build up during the layup process, see Figure 5.1b. AFP machines typically have preprogrammed rules for cutting and adding tow to prevent gaps and overlaps from becoming excessively large. However, if these regions happen frequently in the layup, they can lead to an unacceptable increase in manufacturing time and effort. For this reason, we also wish to develop a constraint to bound how frequently tows need to be cut and added by the AFP machine. The final constraint on the tow-steered design is on the ply drop rate of the design. If plies are dropped too quickly spatially through the layup of the laminate, undesired inter-laminar stress concentrations can occur, leading to a reduction in strength. This restricts how quickly the panel thickness is allowed to vary across the surface.
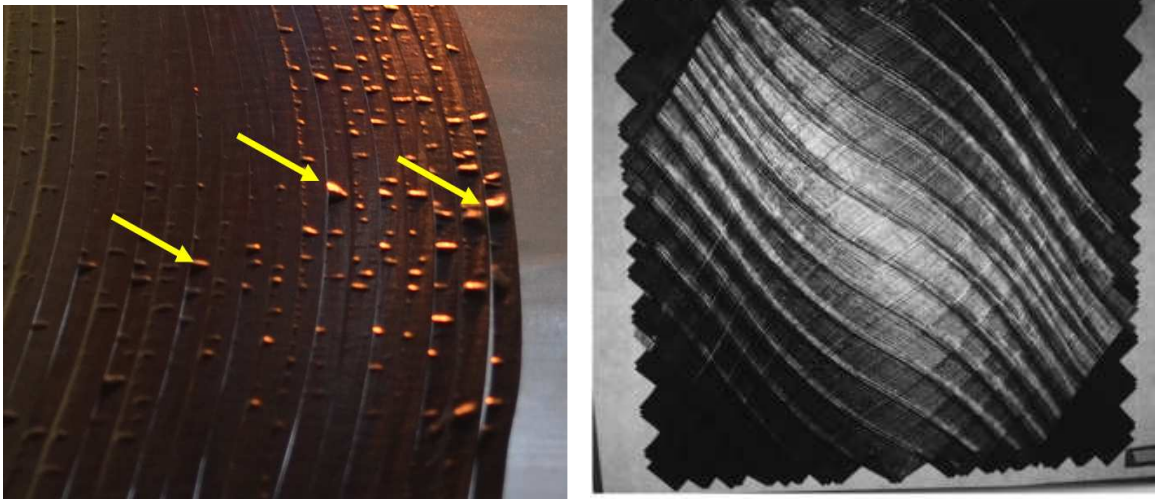
(a) Tow puckering for curved tow path[1]   (b) Thickness build up due to overlaps [103]

Figure 5.1: Example of tow-steering defects due to AFP layup process

The manufacturing constraints derived throughout the remainder of this chapter will be for a general 2D tow pattern. All of these results can be easily extended to curved 2D surfaces by replacing the coordinates x and y with arc-length parametric coordinates u and v. These new parametric coordinates differ slightly from the non-dimensional parametric coordinates, ξ and η, introduced in Chapter 4, in that u and v will now have units of length. We will now continue the derivation with the 2D Cartesian coordinates, x and y.

The ply drop rate is the most straightforward of the three manufacturing constraints. This can be enforced by constraining the magnitude of the thickness gradient distribution, $||\nabla t_p(x, y)||$. The remaining two constraints, tow-path curvature and tow cut/add rates, require further work to derive. In the remainder of this chapter, it will be shown that an arbitrary tow-steered pattern can be defined as a 2D unit vector field. This definition allows for the manufacturing constraints on tow-path curvature and gaps/overlaps to be related to the curl and divergence of the vector field, respectively. Figure 5.2 provides a preview of how these two quantities can be used to identify regions of manufacturing difficulty in a layup.

---

[1]Courtesy of Benjamin Smith from the Aurora Flight Sciences company

(a) Curl contour

(b) Divergence contour
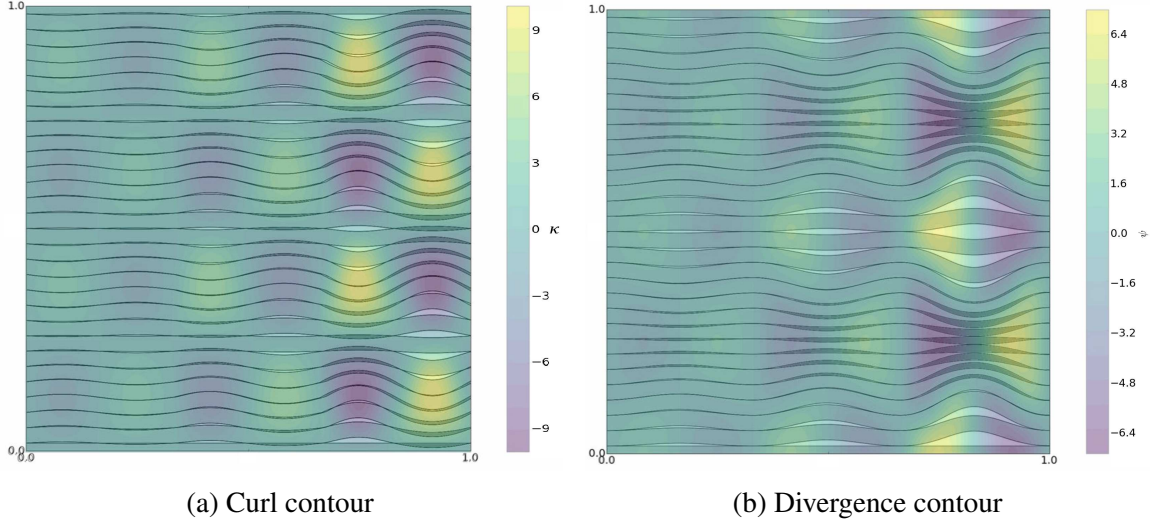
Figure 5.2: The curl, κ, and divergence, ψ, contours can be used to identify regions of manufacturing difficulty.

5.1 Curl-curvature and divergence-gap/overlap relationship

Consider a 2D unit vector field, $\vec{v}$, defined by a tow-angle distribution, $\theta(x, y)$, as shown in Figure 5.3, such that:

$$\vec{v}(\theta) = \cos(\theta)\hat{\mathbf{i}} + \sin(\theta)\hat{\mathbf{j}} \tag{5.1}$$

For the sake of conciseness, θ's explicit dependence on x and y is omitted. The streamlines of the vector field $\vec{v}$ represent the ideal tow paths of the tow-steered laminate ply. The circulation of the tow paths per unit area can be measured by taking the curl of the vector field. Performing the curl operation on the vector field and taking the only non-zero vector component gives:

$$\kappa(x, y) = (\nabla \times \vec{v}(\theta)) \cdot \hat{\mathbf{k}} = \left(\nabla \times \left(\cos(\theta)\hat{\mathbf{i}} + \sin(\theta)\hat{\mathbf{j}} \right) \right) \cdot \hat{\mathbf{k}} = \frac{\partial\theta}{\partial x}\cos(\theta) + \frac{\partial\theta}{\partial y}\sin(\theta) = \nabla\theta \cdot \vec{v}(\theta) \tag{5.2}$$

This states that the curl of the vector field is the directional derivative of the angle, θ, in the tangential direction, $\vec{v}$, which is the definition of the curvature for a parametric curve. This relationship provides a simple method to compute the tow-path curvature, and, by using the inverse relationship between curvature and turning radius, the turning radius.

While the relationship between curl and curvature is clear from the derivation above, the same is not the case for the relationship between divergence and gaps/overlaps. This relationship can be motivated by drawing an arbitrarily small control volume, Ω, and taking

76
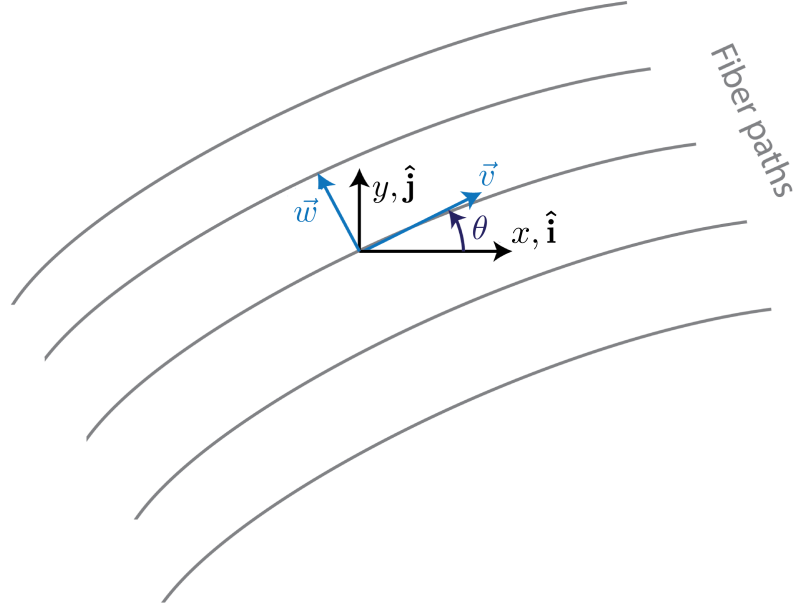
Figure 5.3: Tow path vector definitions.

the flux per unit area, ψ, of the tow paths passing through its boundary, C, as shown in Figure 5.4. The flux of tow paths per unit area is then given by the limit:

$$\psi = \lim_{|\Omega| \to 0} \frac{1}{|\Omega|} \oint_C \vec{v} \cdot \hat{\mathbf{n}} \, \mathrm{d}s,$$

where $|\Omega|$ is the area of Ω. From the above definition the units for ψ are clearly $[\text{Length}]^{-1}$. Through the use of Gauss's theorem, this quantity can be directly related to the vector field divergence:

$$\psi = \nabla \cdot \vec{v} \tag{5.3}$$

Substituting Equation (5.1) into the above, we get:

$$\psi(x,y) = \nabla \cdot \vec{v}(\theta) = \nabla \cdot (\cos(\theta)\hat{\mathbf{i}} + \sin(\theta)\hat{\mathbf{j}}) = \frac{\partial \theta}{\partial x}(-\sin(\theta)) + \frac{\partial \theta}{\partial y}(\cos(\theta)) = \nabla \theta \cdot \vec{w}(\theta),$$
$$\tag{5.4}$$

where $\vec{w}$ is the in-plane unit normal vector to the tow path tangent vector $\vec{v}$. Thus, analogously to the curvature, the divergence is the directional derivative of the angle in the transverse direction.

At this point, we still have yet to make a connection between ψ and the gap/overlap formation of the pattern. This relationship can be intuitively shown through the following qualitative argument. If $\psi > 0$ in a region of the pattern, then the density of tow paths
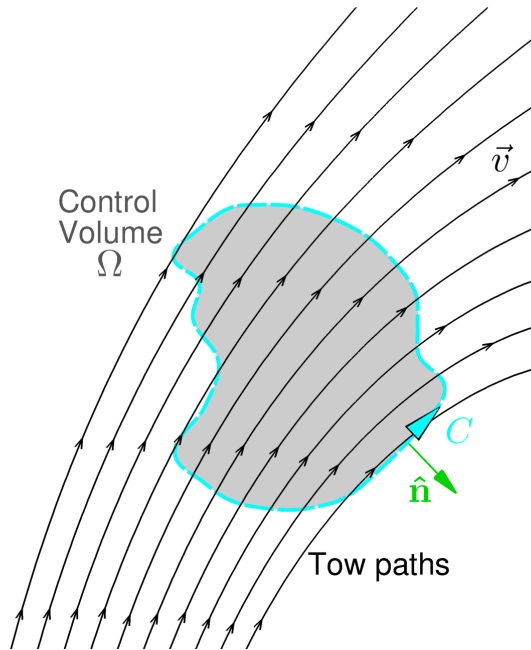
Figure 5.4: The divergence quantifies the flux of tow paths through an arbitrary control volume.

entering the control volume is larger than that of the exiting tow paths, indicating that a gap is likely to form. Likewise, if $\psi < 0$, the tow paths exiting the volume have greater density than those entering, indicating that an overlap is likely to form. Finally, if $\psi = 0$, the density of tow paths entering and exiting the volume are equal and no gap/overlap growth is expected. This means that, according to Equation (5.4), the local tow paths should be as close to parallel as possible to reduce the likelihood of gaps and overlaps in the pattern.

Now that we have developed a qualitative relationship, we can proceed to derive a more quantitative relationship. First, consider two adjacent tow paths, p_1 and p_2, whose streamlines define the centerlines for two prepreg tow strips of width w, as shown in Figure 5.5. We assume that the centerlines of these tow paths are initially separated by a distance δw, where δ is the shift distance of the adjacent tow strip in percent tow width. If $\delta < 1$, the initial offset between the adjacent tow paths is smaller than the tow width, leading to an initial overlap. Likewise, if $\delta > 1$, there is a gap at the initial seeding points for the tows. Finally, if $\delta = 1$, the edges of the tow are coincident and there is no gap or overlap initially.

To find how the gap or overlap between these two tow paths propagate, we first need to find the separation between the two paths as a function of arc-distance traveled, $h(s)$. This separation distance is measure perpendicularly to path 1, p_1. By drawing an infinitesimal

78
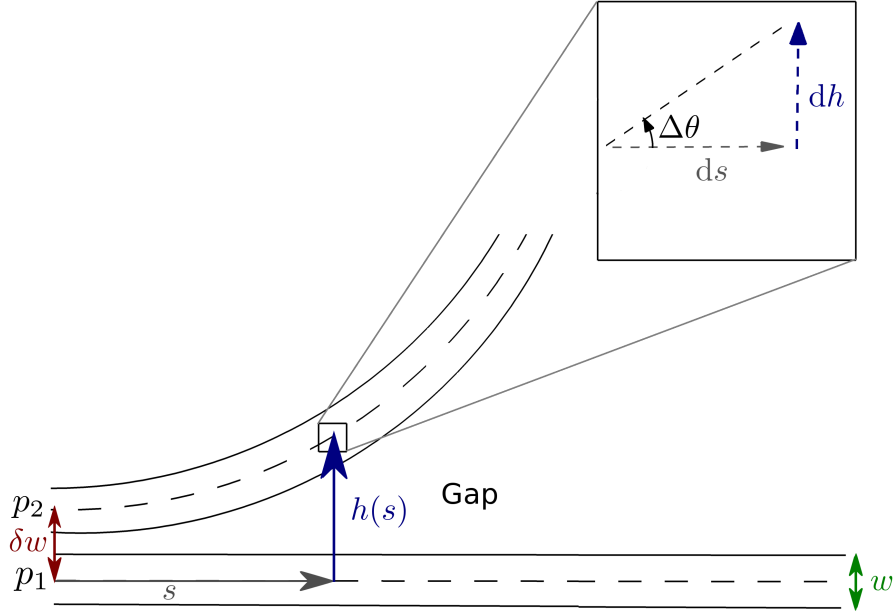
Figure 5.5: Gap propagation between two adjacent tow paths.

triangle along p_2, we derive:

$$\mathrm{d}h = \tan(\Delta\theta(s))\,\mathrm{d}s \tag{5.5}$$

As long as the angle between the two tow path directions is small, we can use the approximation:

$$\tan(\Delta\theta(s)) \approx \Delta\theta(s) \tag{5.6}$$

Substituting this into Equation (5.5) yields:

$$\mathrm{d}h = \Delta\theta(s)\,\mathrm{d}s \tag{5.7}$$

Next, by realizing that the angle between the two tow paths can be approximated by the directional derivative of θ in the transverse direction of p_1, and recognizing the definition of divergence from Equation (5.4) gives:

$$\Delta\theta(s) \approx \nabla\theta \cdot h\,\vec{w}(s) = h\,\psi(s) \tag{5.8}$$

Substituting this into Equation (5.7) and moving both h terms to the same side yields:

$$\frac{\mathrm{d}h}{h} = \psi(s)\,\mathrm{d}s$$

79

Next, integrating both sides and remembering that by definition $h(0) = \delta w$, we get:

$$\int_{\delta w}^{h(s)} \frac{\mathrm{d}h}{h} = \int_0^s \psi(s') \, \mathrm{d}s'$$

Evaluating the left integral gives:

$$\ln\left(\frac{h(s)}{\delta w}\right) = \int_0^s \psi(s') \, \mathrm{d}s'$$

Next, moving everything but $h(s)$ to the right hand side reveals the desired relationship:

$$h(s) = \delta w \exp\left(\int_0^s \psi(s') \, \mathrm{d}s'\right)$$

Subtracting the tow width gives the distance between the edges of either tow or the height of the gap/overlap between them:

$$h_{g/o}(s) = w\left(\delta \exp\left(\int_0^s \psi(s') \, \mathrm{d}s'\right) - 1\right) \tag{5.9}$$

A positive value of $h_{g/o}$ indicates a gap, while a negative values indicates an overlap. Finally, dividing by the tow width yields:

$$\frac{h_{g/o}}{w}(s) = \delta \exp\left(\int_0^s \psi(s') \, \mathrm{d}s'\right) - 1 \tag{5.10}$$

which is the gap/overlap size nondimensionalized with respect to tow width.

Comparing this quantitative relationship between the gap/overlap size and divergence to the qualitative argument made earlier reveals that the two are in good agreement. If $\psi(s) < 0$, then $h_{g/o}/w$ asymptotically decays to a value of -1, indicating 100% overlap. This result should makes sense, since overlaps greater than this should not be possible. Conversely, if $\psi(s) > 0$, then $h_{g/o}/w$ grows positively, indicating a growing gap. Though this quantity is unbounded from above in theory, this relationship breaks down for large gap sizes. If $\psi(s) = 0$, then $h_{g/o}/w$ remains constant, indicating no gap/overlap growth.

Equation (5.10) leads to the conclusion that the percentage gap/overlap in a region of the pattern is independent of the tow width used to lay up the pattern. This means that as the width of tow is decreased, the total area of gaps and overlaps in the layup remains constant. This is because according to Equation (5.9), the size of the gaps and overlaps in the layup scale linearly with tow size (i.e., $\mathcal{O}(w)$), while the number of gaps and overlaps scales with the inverse of tow width (i.e., $\mathcal{O}(1/w)$), since more tow paths mean more adjacent regions

Decreasing tape size
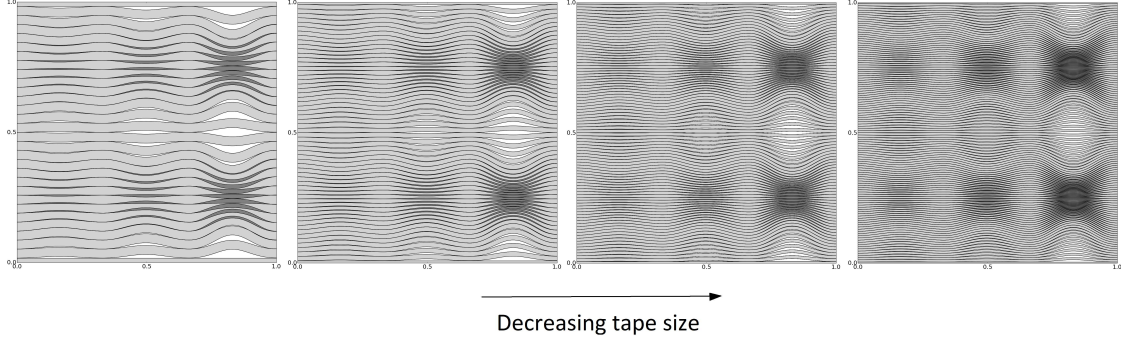
Figure 5.6: Gaps and overlaps do not improve as tow width is decreased.

for gaps and overlaps to occur. This means the total area of gap or overlap in the pattern must scale with $\mathcal{O}\left(w/w\right) = \mathcal{O}(1)$, or in other words remain constant. This effect can be seen clearly in Figure 5.6.

To verify the accuracy of Equation (5.10), one of the patterns from Figure 5.6 is seeded at two tow locations. The exact percentage of gap or overlap adjacent to the strip is then compared to the approximate value predicted by Equation (5.10). The results for both tow paths are shown in Figure 5.7. From these plots, we can see that the approximate values predicted by Equation (5.10) are in good agreement with the actual size of gaps measured in the layup. The gap/overlap size measured by Equation (5.10) is only on one side of the tow. In the case of an overlap, this value should be doubled to get the total overlap area for both sides of the strip, by symmetry. Examples of analytical tow patterns with closed-form solutions for their curvature, divergence, and gap/overlap propagation values are available in Appendix B.

Next, we wish to use Equation (5.10) to derive an alternate, and perhaps more physically meaningful, interpretation of the divergence, ψ. This can be revealed by first differentiating Equation (5.10) with respect to s, as shown below:

$$\frac{\mathrm{d}\left(h_{g/o}/w\right)}{\mathrm{d}s}(s) = \psi(s)\delta \exp\left(\int_0^s \psi(s')\,\mathrm{d}s'\right) \tag{5.11}$$

Finally, recognizing that in regions where the gaps or overlap is small:

$$\delta \exp\left(\int_0^s \psi(s')\,\mathrm{d}s'\right) \approx 1 \tag{5.12}$$

Substituting this into Equation (5.11) yields:

$$\frac{d\left(h_{g/o}/w\right)}{\mathrm{d}s}(s) \approx \psi(s), \tag{5.13}$$

81
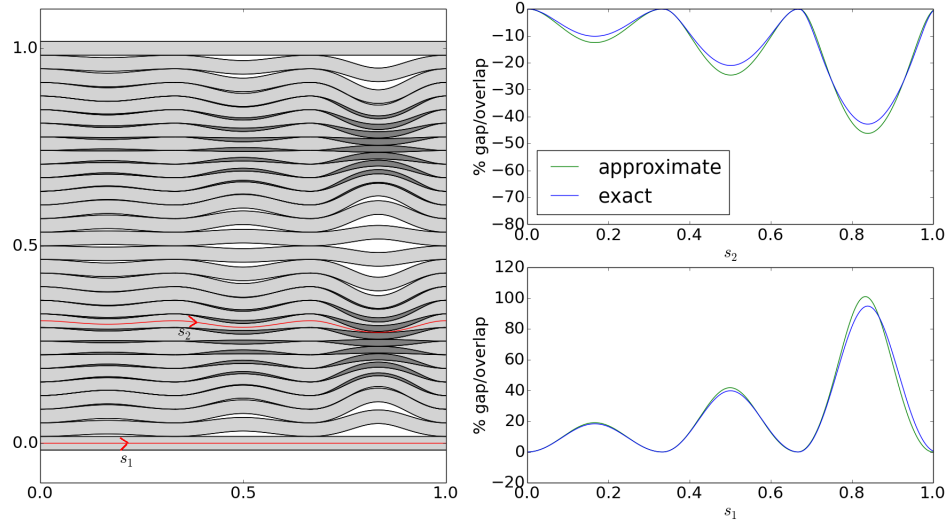
Figure 5.7: The predicted gap/overlap propagation agrees well with actual measured amount for example layup.

which leads to an alternate, but equivalent, interpretation of the divergence. The divergence, ψ, in a region of a pattern can be approximately defined as the rate of growth of small gaps/overlaps as a fraction of tow width per unit length of tow laid. This means that, for example, laying down tow in a region featuring a divergence value of $0.2\,\mathrm{m}^{-1}$ corresponds to a gap growth rate of 20% per meter. This definition provides a more intuitive way of specifying the divergence as a manufacturing constraint, since it relates to gap/overlap growth.

5.2   Bound for minimum tow cut and addition length

As mentioned in Section 1.1.3.2, a number of studies have already considered the application of numerical design optimization to tow-steered laminates. In many of these works, the main manufacturing constraint considered is on the minimum turning radius. This is usually enforced through a constraint on the curvature magnitude, as given below:

$$-\frac{1}{R_{\mathrm{min}}} \leq \kappa \leq \frac{1}{R_{\mathrm{min}}}$$

However, there are a number of other manufacturing constraints relating to tow gaps and overlaps that have yet to be considered as constraints in the context of design optimization.

The first of these constraints is that of the tow minimum cut length, L_{cut}. Tow paths are

Tows which cannot be placed
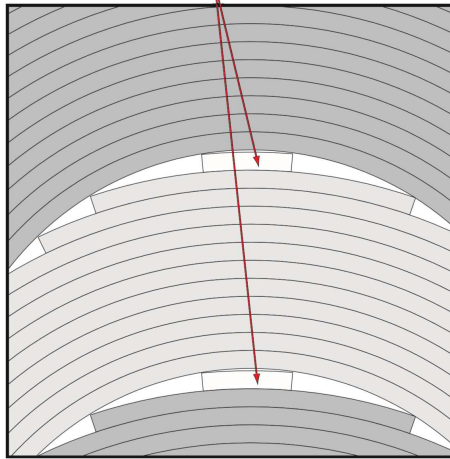
Figure 5.8: Example of minimum cut length restriction (Reproduced from Blom [104]).

typically cut by the AFP machine in the layup process to avoid regions of excessive overlap. This value, L_{cut}, refers to the smallest length of tow that can be laid by the AFP machine before the tow can be cut. This length is typically dictated by the distance between the spool storing the prepreg tow and the cutting mechanism on the AFP machine. Figure 5.8 is an example of a tow pattern that fails to meet the minimum cut length constraint. The second constraint is on the minimum tow addition length, L_{add}. This defines the minimum amount of tow laid for two adjacent tow paths before the machine may consider adding an additional tow in between a gap of the current two. While the previous constraint was a limitation of the AFP machine, this constraint is at the discretion of the designer. Smaller values of L_{add} mean that additional tows need to be placed more frequently in between gaps of adjacent tow paths, leading to higher manufacturing cost and time.

Typically, AFP machines are programmed to add and drop tows based on a gap and overlap percentage rule. For instance, if a gap between two tow paths in a region exceeds a predefined gap percentage rule, $h_{g/o}/w \geq a_g$, the AFP machine starts a new tow centered between the gap of the previous two. Likewise, if the overlap between two tows exceeds the overlap percentage rule, $h_{g/o}/w \leq -a_o$, the machine is programmed to cut one of the tows. It is therefore reasonable to expect that both of the constraints defined above should depend on these values. A typical gap/overlap rule used by designers is a 50% gap/ 50% overlap rule, where $a_g = a_o = 0.5$.

Both L_{cut} and L_{add} can be evaluated explicitly for a given pattern using Equation (5.10). This requires a numerical integration and knowledge of the starting locations of AFP tow paths. In the context of a design optimization, however, this may be difficult to evaluate. Therefore, it would be beneficial to derive a conservative lower bound for these values
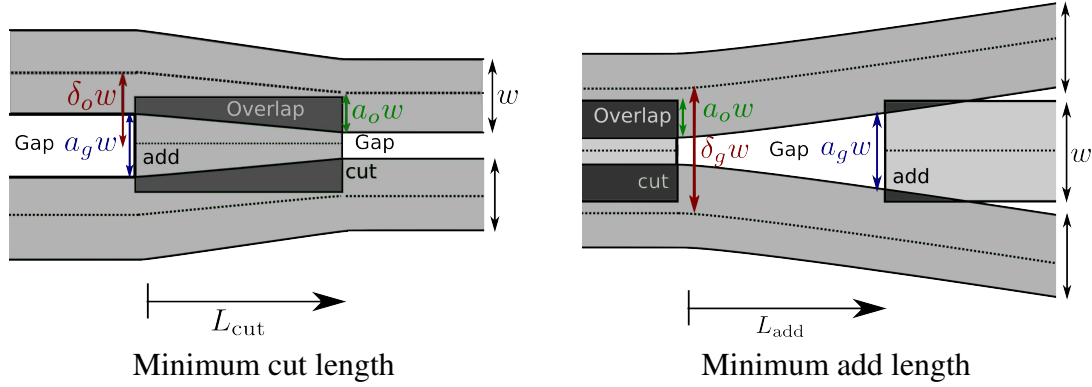
Figure 5.9: Example of worst-case scenario cut/add sizes.

independent of AFP seeding location.

This can be accomplished by considering the worst-case scenario for either case. As mentioned previously, a tow cut is only made by the machine when the overlap rule is about to be violated. This means that the worst-case to analyze for cut length would be a case where the tow starts with some initial overlap value at its initial seeding location. This occurs at locations where a tow is added in a gap to prevent the gap rule from being violated. Likewise, worst-case for the add length occurs in regions where there is some initial amount of gap height at the beginning of this length. This typically occurs right after a tow is cut to satisfy the overlap rule. Figure 5.9 illustrates both of these cases.

Substituting the symbols from Figure 5.9 into Equation (5.10) yields:

$$- a_o = \delta_o \exp \left(\int_0^{L_{\text{cut}}} \psi(s') \, ds' \right) - 1, \qquad a_g = \delta_g \exp \left(\int_0^{L_{\text{add}}} \psi(s') \, ds' \right) - 1 \quad (5.14)$$

By further analyzing Figure 5.9, we can derive the following relationships between the minimum cut/add length offsets (δ_o and δ_g), and the gap/overlap rules (a_g and a_o):

$$2\delta_o w = w + a_g w, \qquad \delta_g w = w + (w - 2a_o w)$$

Solving for each offset parameter yields:

$$\delta_o = \frac{1 + a_g}{2}, \qquad \delta_g = 2(1 - a_o) \qquad (5.15)$$

Note that not all combinations of gap and overlap rules (a_g and a_o) are permitted. We can see from Figure 5.9 when a tow is cut, a gap of size $\delta_g - 1$ is present immediately after the cut. If the resulting gap size already violates the gap rule, then it is impossible to satisfy

both the gap and overlap rule. Thus, we require that:

$$\delta_g - 1 \leq a_g$$

Substituting in for δ_o and rearranging terms leads to the following inequality:

$$a_g \geq 1 - 2a_o \tag{5.16}$$

Next, substituting Equation (5.15) into Equation (5.14) yields:

$$-a_o = \frac{1 + a_g}{2} \exp \left(\int_0^{L_{\text{cut}}} \psi(s') \, ds' \right) - 1, \qquad a_g = 2(1 - a_o) \exp \left(\int_0^{L_{\text{add}}} \psi(s') \, ds' \right) - 1 \tag{5.17}$$

At this point, Equation (5.17) still depends on the AFP starting location of the tow paths, implicitly, through the inclusion of the integration of the divergence term, $\int_0^{L_{\text{cut}}} \psi(s') ds'$. From Figure 5.9, it is clear that $\psi(s) < 0$ and $\psi(s) > 0$ for the worst-case scenario of the minimum cut and add length, respectively. Thus, we can conservatively bound each integral in Equation (5.17) by using the minimum and maximum divergence values in the pattern:

$$\psi_{\text{max}} = \arg\max_{x,y} \psi(x, y), \qquad \psi_{\text{min}} = \arg\min_{x,y} \psi(x, y) \tag{5.18}$$

Equation (5.17) can then be further simplified by assuming the divergence remains constant in these regions. This leads to the relationship:

$$-a_o = \frac{1 + a_g}{2} \exp(\psi_{\text{min}} L_{\text{cut}}) - 1, \qquad a_g = 2(1 - a_o) \exp(\psi_{\text{max}} L_{\text{add}}) - 1$$

Finally, solving for the minimum and maximum divergence and rearranging terms yields:

$$\psi_{\text{min}} = -\frac{\ln\left(\frac{1 + a_g}{2(1 - a_o)}\right)}{L_{\text{cut}}}, \qquad \psi_{\text{max}} = \frac{\ln\left(\frac{1 + a_g}{2(1 - a_o)}\right)}{L_{\text{add}}}$$

Using these values, a conservative bound can now be placed on the divergence everywhere in the tow pattern, as follows:

$$-\frac{\ln\left(\frac{1 + a_g}{2(1 - a_o)}\right)}{L_{\text{cut}}} \leq \psi \leq \frac{\ln\left(\frac{1 + a_g}{2(1 - a_o)}\right)}{L_{\text{add}}} \tag{5.19}$$

This constraint ensures that the minimum cut and add lengths are respected regardless of choice of AFP seeding location. By further analyzing Equation (5.19), it becomes clear that

Equation (5.16) prevents either side of the bounds in Equation (5.19) from swapping signs. According to Equation (5.19), as $L_{\text{cut}}, L_{\text{add}} \to \infty$, the minimum cut/add length requirement becomes more strict and the divergence everywhere must drop to zero. Conversely, if $L_{\text{cut}}, L_{\text{add}} \to 0$, the minimum cut/add length requirement is relaxed, and the divergence becomes unbounded. If no overlaps are allowed (i.e. $a_o = 0$) and the gap rule is set to the smallest value allowed by Equation (5.16) (i.e. $a_g = 1$), the divergence is again forced everywhere to zero. If the overlap rule is relaxed and $a_o \to 1$, implying that tows never need to be cut, the divergence again becomes unbounded.

Equation (5.19) is a sufficient condition to guarantee that the minimum cut and add length restrictions are met, but it is not a necessary condition. This means that if the divergence of a tow pattern exceeds these bounds, this does not necessarily guarantee that the layup violates the minimum cut/add length requirements. However, the only way to verify this for these patterns is to check the cut/add lengths at each of the AFP seeding locations through Equation (5.10).

5.3 Divergence-curvature relationship for rotated patterns

In the previous section, a derivation of the relationship between the manufacturing constraints of a general tow-steered pattern and its divergence and curvature was given. Next, we wish to develop a relationship between these values for patterns offset by a constant angle, as described in Chapter 4. We start by defining two tow path vector fields, $\vec{v_0}$ and $\vec{v_1}$, parametrized by angle distributions θ_0 and θ_1, respectively. The two vector fields are related by the fact that $\vec{v_1}$ is offset from $\vec{v_0}$ by a constant angular offset, $\Delta\theta$, such that:

$$\theta_1 = \theta_0 + \Delta\theta$$

If we now take the curvature of the second vector field, we get:

$$\kappa_1(x,y) = \nabla\theta_1 \cdot \vec{v_1}(\theta_1) = \nabla\theta_1 \cdot (\cos(\theta_1)\hat{\mathbf{i}} + \sin(\theta_1)\hat{\mathbf{j}}) = \frac{\partial\theta_1}{\partial x}\cos(\theta_1) + \frac{\partial\theta_1}{\partial y}\sin(\theta_1) \quad (5.20)$$

Substituting in $\theta_1 = \theta_0 + \Delta\theta$ and using the fact that $\partial\theta_1/\partial x = \partial\theta_0/\partial x$ and $\partial\theta_1/\partial y = \partial\theta_0/\partial y$, and $\Delta\theta$ is a constant we obtain:

$$\kappa_1(x,y) = \frac{\partial\theta_0}{\partial x}\cos(\theta_0 + \Delta\theta) + \frac{\partial\theta_0}{\partial y}\sin(\theta_0 + \Delta\theta) \quad (5.21)$$
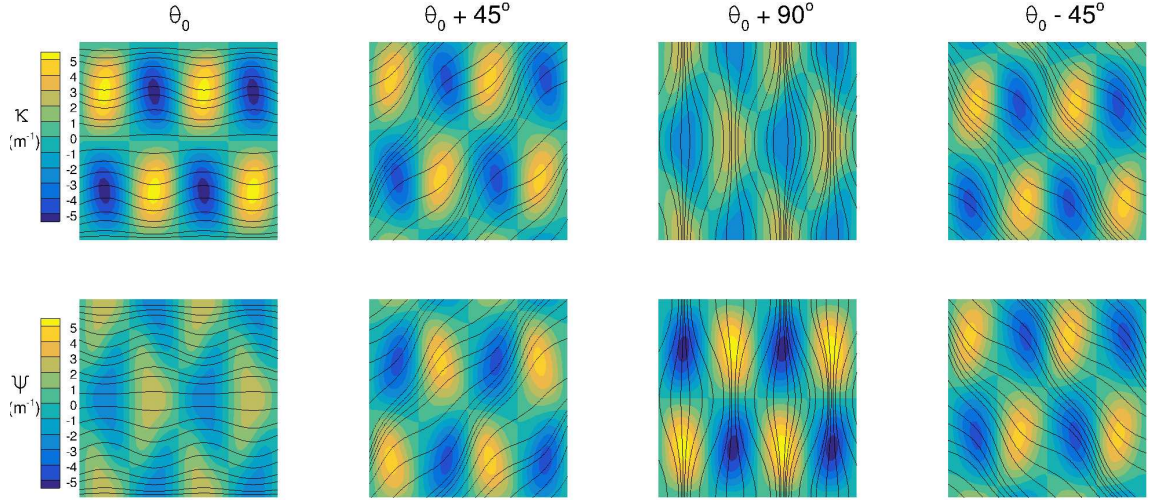
Figure 5.10: Example of the divergence-curvature relationship for offset patterns.

Finally, using the trigonometric identities $\cos(\theta_0 + \Delta\theta) = \cos(\theta_0)\cos(\Delta\theta) - \sin(\theta_0)\sin(\Delta\theta)$ and $\sin(\theta_0 + \Delta\theta) = \sin(\theta_0)\cos(\Delta\theta) + \cos(\theta_0)\sin(\Delta\theta)$, collecting terms, and recognizing the divergence and curvature terms derived previously, yields:

$$\begin{aligned}
\kappa_1(x,y) &= \frac{\partial\theta_0}{\partial x}(\cos(\theta_0)\cos(\Delta\theta) - \sin(\theta_0)\sin(\Delta\theta)) + \frac{\partial\theta_0}{\partial y}(\sin(\theta_0)\cos(\Delta\theta) + \cos(\theta_0)\sin(\Delta\theta)) \\
&= (\frac{\partial\theta_0}{\partial x}\cos(\theta_0) + \frac{\partial\theta_0}{\partial y}\sin(\theta_0))\cos(\Delta\theta) + (\frac{\partial\theta_0}{\partial x}(-\sin(\theta_0)) + \frac{\partial\theta_0}{\partial y}\cos(\theta_0))\sin(\Delta\theta) \\
&= \kappa_0\cos(\Delta\theta) + \psi_0\sin(\Delta\theta)
\end{aligned} \tag{5.22}$$

In a similar fashion, we can derive the following equation for the divergence:

$$\psi_1(x,y) = -\kappa_0\sin(\Delta\theta) + \psi_0\cos(\Delta\theta) \tag{5.23}$$

These relationships show that the divergence and curvature of two tow-steered patterns offset by a constant angle are inherently related. Note that if the offset is exactly $90°$, the divergence and curvature switch magnitudes between the two patterns. We can see this effect in Figure 5.10. This means that when considering multiple patterns offset by a constant angle, the more stringent of the two constraints (tow-path divergence or tow-path curvature) ends up being the active constraint for each ply.

5.4 Zero-divergence and zero-curl patterns

In Section 5.1 a relationship between the curl, divergence, tow-path curvature, and gaps/overlaps for a general tow-steered pattern was derived. From this relationship, it is natural to wonder if there are tow-steered patterns with zero divergence, zero curl, or both everywhere in the layup. To answer this question, we can start by looking at a general pattern, $\vec{v}_\psi$, for which the divergence is zero.

$$\nabla \cdot \vec{v}_\psi = 0 \tag{5.24}$$

From the principles of vector calculus, it is known that Equation (5.24) defines what is called an "incompressible" vector field. This means that vector field pattern can be defined as the curl of another vector field, as shown below:

$$\vec{v}_\psi = \nabla \times \vec{\phi}(x, y) \tag{5.25}$$

Because $\vec{v}_\psi$ is a 2D vector field, $\vec{\phi}$ must be orthogonal to the tow pattern field, $\vec{v}_\psi$, and therefore can be defined by a stream function, $\phi(x, y)$:

$$\vec{\phi}(x, y) = \phi(x, y)\,\hat{\mathbf{k}} \tag{5.26}$$

Substituting Equation (5.26) into Equation (5.25) gives:

$$\vec{v}_\psi = \frac{\partial \phi}{\partial y}\hat{\mathbf{i}} - \frac{\partial \phi}{\partial x}\hat{\mathbf{j}} \tag{5.27}$$

Finally, remembering that by definition $\vec{v}_\psi$ should be a unit vector:

$$\vec{v}_\psi \cdot \vec{v}_\psi = 1 \tag{5.28}$$

Substituting Equation (5.27) into Equation (5.28) yields:

$$\frac{\partial \phi}{\partial x}^2 + \frac{\partial \phi}{\partial y}^2 = 1 \tag{5.29}$$

This is a very well-known nonlinear Partial Differential Equation (PDE), often encountered in the fields of electro-magnetics and optics, known as the Eikonal equation. The solution, ϕ, to this equation is called a signed distance function. The function value at each point, $\phi(x, y)$, is defined as the distance from that point to a boundary curve, Ω, where the sign denotes which side of the boundary the point lies on. A common approach to obtaining

these solutions is the fast marching method [105]. Since $\phi(x, y)$ is a stream function of a 2D vector field, by definition, the streamlines of the tow patterns can be reproduced by plotting the iso-contours of ϕ. In this case, the curvature for these patterns can be computed by applying the curl, as defined in Equation (5.2), to Equation(5.27):

$$\kappa_\psi = \left(\nabla \times \left(\frac{\partial \phi}{\partial y} \hat{\mathbf{i}} - \frac{\partial \phi}{\partial x} \hat{\mathbf{j}} \right) \right) \cdot \hat{\mathbf{k}} = -\left(\frac{\partial^2 \phi}{\partial x^2} + \frac{\partial^2 \phi}{\partial y^2} \right) = -\nabla^2 \phi \qquad (5.30)$$

This equation provides an effective way of evaluating and constraining the curvature of any zero-divergence Eikonal solution.

This motivates an alternative approach to using B-spline interpolation to define the orientation field, $\theta(x, y)$, and subsequently the corresponding tow pattern, as described in Chapter 4. Instead, we can define the tow pattern as a level set function that is parametrized by the boundary, Ω. This is an approach that has seen growing interest in tow-steering design optimization [106, 107, 108].

By using Equation (5.22), a complementary family of zero-curl tow patterns, $\vec{v}_\kappa$, can be obtained by defining a corresponding orthogonal pattern to each zero-divergence solution. An alternative but equivalent definition for the zero-curl tow patterns is to define a number of seed locations on the boundary curve, Ω, and march out perpendicularly to the curve in all directions. A similar approach in the derivation of the zero-curl solution can be taken as the zero-divergence solution, leading back to the Eikonal equation (5.29), where ϕ now represents a scalar potential field, in this case $\vec{v}_\kappa = \nabla \phi$ and $\psi_\kappa = \nabla^2 \phi$.

Examples of zero-divergence and corresponding zero-curl patterns are shown in Figure 5.11. As one would expect from Equations (5.2) and (5.4), all of the paths for the divergence-free solutions are locally parallel, while the tow orientation remains constant along tow-paths for the curl-free solutions.

If Ω has no local curvature, that is if Ω is piece-wise linear, the resulting pattern will feature no curvature nor divergence. Figure 5.12 shows examples of patterns featuring both zero curl and divergence; the pattern on the left is an unsteered unidirectional pattern, which intuitively should have zero divergence and curvature. While some of these patterns contain what can be considered curvature singularities at the sharp corners of the pattern, the zero curvature condition is still satisfied everywhere except at these points. While these regions may seem problematic for the turning radius manufacturing constraint described in the previous sections, this problem can be alleviated by having the AFP machine cut the tow at these corners, rotate the machine head, and continue laying in the new direction. If these regions occur frequently throughout the pattern, then the manufacturing of the pattern may become difficult.
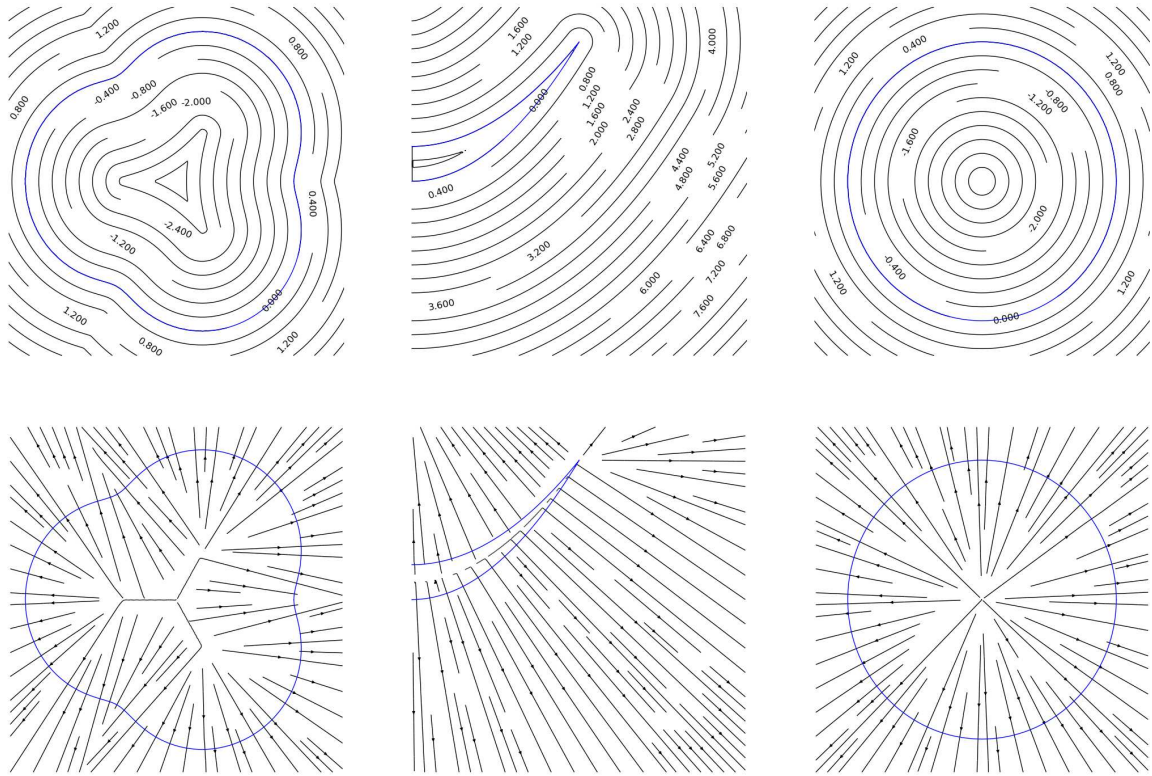
Figure 5.11: Zero-divergence (top) and corresponding zero-curl (bottom) Eikonal solutions, boundary curve, Ω (blue).
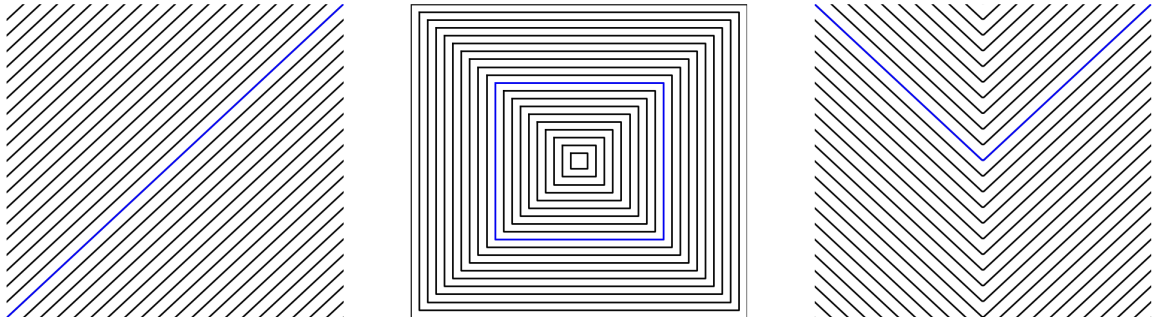
Figure 5.12: Example of Eikonal solutions with no divergence/curvature.

The zero-divergence and zero-curl patterns have the desirable manufacturing properties of being free of gaps/overlaps and curvature, respectively. These families of solutions represent the extreme limits on either the gaps/overlaps or tow-path curvature. In general, tow patterns with superior structural performance can be achieved by allowing for some amount of both divergence and curvature throughout the pattern. It is for these reasons that it was decided to retain the more general tow-pattern parametrization laid out in Chapter 4.

5.5   Sensitivities

Now that general derivations for these three constraints have been established, their computation and corresponding sensitivities can be related to the B-spline control point design variables used by pySteer. Due to the fact that none of these constraints require a physics solver (CSM or CFD) to evaluate, their sensitivities can be computed analytically without the assistance of the adjoint method. To allow for the computation of these constraints on a general 3D surface, we will now return to the more general parameteric coordinate definition. In this definition the 2D coordinates x and y used in the previous section can be replaced with 2D parameteric coordinates u and v. Based on Equation (5.2) and (5.4), the curvature and divergence at each node of the FEM surface mesh computation is:

$$\boldsymbol{\kappa}_n = \boldsymbol{\theta}_{n,u} \cos(\boldsymbol{\theta}_n) + \boldsymbol{\theta}_{n,v} \sin(\boldsymbol{\theta}_n), \qquad \boldsymbol{\psi}_n = -\boldsymbol{\theta}_{n,u} \sin(\boldsymbol{\theta}_n) + \boldsymbol{\theta}_{n,v} \cos(\boldsymbol{\theta}_n) \qquad (5.31)$$

Where the subscript n denotes the values at the nodes of FEM surface mesh and the subscript parameter preceded by a comma denotes a partial derivative (i.e. $(\cdot)_{,u} = \frac{\partial(\cdot)}{\partial u}$). Similarly for the thickness gradient:

$$||\nabla \boldsymbol{t}_n||^2 = \boldsymbol{t}_{n,u}^2 + \boldsymbol{t}_{n,v}^2 \qquad (5.32)$$

The relation of these values to the B-spline control point values is fairly straightforward:

$$\boldsymbol{x}_n = \boldsymbol{C}(\boldsymbol{\xi}_n, \boldsymbol{\eta}_n)\, \boldsymbol{x}_{cp}, \qquad \boldsymbol{x}_{n,u} = \boldsymbol{T}^{-1}(\boldsymbol{\xi}_n, \boldsymbol{\eta}_n)\, \boldsymbol{x}_{n,\boldsymbol{\xi}}, \qquad \boldsymbol{x}_{n,\boldsymbol{\xi}} = \boldsymbol{C}_{,\boldsymbol{\xi}}(\boldsymbol{\xi}_n, \boldsymbol{\eta}_n)\boldsymbol{x}_{cp} \quad (5.33)$$

Where $\boldsymbol{x}$ represents either the tow angle variables, $\boldsymbol{\theta}$, or thickness variables, $\boldsymbol{t}$. The bold subscripts variables have been adopted as shorthand notation for the concatenation of partial derivative with respect to each coordinate, as shown below:

$$(\cdot)_{,\boldsymbol{u}} = \begin{bmatrix} \frac{\partial(\cdot)}{\partial u} \\ \frac{\partial(\cdot)}{\partial v} \end{bmatrix}, \qquad (\cdot)_{,\boldsymbol{\xi}} = \begin{bmatrix} \frac{\partial(\cdot)}{\partial \xi} \\ \frac{\partial(\cdot)}{\partial \eta} \end{bmatrix}$$

C is the B-spline matrix that interpolates the values from the control points to the nodes of the surface, $C_{,\xi}$ is a matrix that gives the partial derivative of the B-spline interpolation surface with respect to the non-dimensional parametric coordinates ξ and η. T is the Jacobian which relates non-dimensional parameteric coordinates (ξ and η) to their dimensional counterparts (u and v), and is defined in Equation (5.34).

$$
T = \begin{bmatrix} \frac{\partial \boldsymbol{u}_n}{\partial \boldsymbol{\xi}_n} & \frac{\partial \boldsymbol{u}_n}{\partial \boldsymbol{\eta}_n} \\ \frac{\partial \boldsymbol{v}_n}{\partial \boldsymbol{\xi}_n} & \frac{\partial \boldsymbol{v}_n}{\partial \boldsymbol{\eta}_n} \end{bmatrix} = \begin{bmatrix} \frac{\partial u_1}{\partial \xi_1} & & & \frac{\partial u_1}{\partial \eta_1} & & \\ & \ddots & & & \ddots & \\ & & \frac{\partial u_n}{\partial \xi_n} & & & \frac{\partial u_n}{\partial \eta_n} \\ \frac{\partial v_1}{\partial \xi_1} & & & \frac{\partial v_1}{\partial \eta_1} & & \\ & \ddots & & & \ddots & \\ & & \frac{\partial v_n}{\partial \xi_n} & & & \frac{\partial v_n}{\partial \eta_n} \end{bmatrix}
\tag{5.34}
$$

Both C and $C_{,\xi}$ are provided as outputs by GeoMACH's B-spline engine, while $T(\xi_n, \eta_n)$ is computed by pySteer. For the sake of conciseness the explicit dependence of C, $C_{,\xi}$, and T on $\boldsymbol{\eta}_n$ and $\boldsymbol{\xi}_n$ will be dropped.

Using the above definitions, the sensitivities of each constraint can be computed in a straight forward manner using the chain rule:

$$
\frac{\mathrm{d}\boldsymbol{\kappa}_n}{\mathrm{d}\boldsymbol{\theta}_{cp}} = \frac{\partial \boldsymbol{\kappa}_n}{\partial \boldsymbol{\theta}_n} \frac{\mathrm{d}\boldsymbol{\theta}_n}{\mathrm{d}\boldsymbol{\theta}_{cp}} + \frac{\partial \boldsymbol{\kappa}_n}{\partial \boldsymbol{\theta}_{n,u}} \frac{\mathrm{d}\boldsymbol{\theta}_{n,u}}{\mathrm{d}\boldsymbol{\theta}_{n,\xi}} \frac{\mathrm{d}\boldsymbol{\theta}_{n,\xi}}{\mathrm{d}\boldsymbol{\theta}_{cp}}, \qquad \frac{\mathrm{d}\boldsymbol{\psi}_n}{\mathrm{d}\boldsymbol{\theta}_{cp}} = \frac{\partial \boldsymbol{\psi}_n}{\partial \boldsymbol{\theta}_n} \frac{\mathrm{d}\boldsymbol{\theta}_n}{\mathrm{d}\boldsymbol{\theta}_{cp}} + \frac{\partial \boldsymbol{\psi}_n}{\partial \boldsymbol{\theta}_{n,u}} \frac{\mathrm{d}\boldsymbol{\theta}_{n,u}}{\mathrm{d}\boldsymbol{\theta}_{n,\xi}} \frac{\mathrm{d}\boldsymbol{\theta}_{n,\xi}}{\mathrm{d}\boldsymbol{\theta}_{cp}},
\tag{5.35}
$$

Similarly, for the thickness gradient:

$$
\frac{\mathrm{d}(||\nabla \boldsymbol{t}_n||^2)}{\mathrm{d}\boldsymbol{t}_{cp}} = \frac{\partial (||\nabla \boldsymbol{t}_n||^2)}{\partial \boldsymbol{t}_{n,u}} \frac{\mathrm{d}\boldsymbol{t}_{n,u}}{\mathrm{d}\boldsymbol{t}_{n,\xi}} \frac{\mathrm{d}\boldsymbol{t}_{n,\xi}}{\mathrm{d}\boldsymbol{t}_{cp}},
\tag{5.36}
$$

Where $\frac{\partial \boldsymbol{\kappa}_n}{\partial \boldsymbol{\theta}_n}$ and $\frac{\partial \boldsymbol{\kappa}_n}{\partial \boldsymbol{\theta}_{n,u}}$ are diagonal matrices as shown below:

$$
\begin{aligned}
\frac{\partial \boldsymbol{\kappa}_n}{\partial \boldsymbol{\theta}_n} &= \begin{bmatrix} \frac{\partial \kappa_1}{\partial \theta_1} & & \\ & \ddots & \\ & & \frac{\partial \kappa_n}{\partial \theta_n} \end{bmatrix} \\
&= \begin{bmatrix} -\theta_{1,u}\sin(\theta_1) + \theta_{1,v}\cos(\theta_1) & & \\ & \ddots & \\ & & -\theta_{n,u}\sin(\theta_n) + \theta_{n,v}\cos(\theta_n) \end{bmatrix}
\end{aligned}
\tag{5.37}
$$

$$
\frac{\partial \boldsymbol{\kappa}_n}{\partial \boldsymbol{\theta}_{n,\boldsymbol{u}}} =
\begin{bmatrix}
\frac{\partial \kappa_1}{\partial \theta_{1,u}} & & & \frac{\partial \kappa_1}{\partial \theta_{1,v}} & \\
& \ddots & & & \ddots & \\
& & \frac{\partial \kappa_n}{\partial \theta_{n,u}} & & & \frac{\partial \kappa_n}{\partial \theta_{n,v}}
\end{bmatrix}
$$

$$
=
\begin{bmatrix}
\cos(\theta_1) & & & \sin(\theta_1) & \\
& \ddots & & & \ddots & \\
& & \cos(\theta_n) & & & \sin(\theta_n)
\end{bmatrix}
\tag{5.38}
$$

Similar definitions can be given for $\frac{\partial \boldsymbol{\psi}_n}{\partial \boldsymbol{\theta}_n}$, $\frac{\partial \boldsymbol{\psi}_n}{\partial \boldsymbol{\theta}_{n,\boldsymbol{u}}}$, and $\frac{\partial(||\nabla \boldsymbol{t}_n||^2)}{\partial \boldsymbol{t}_{n,\boldsymbol{u}}}$. Using the relationships above, Equation (5.35) can be rewritten as:

$$
\frac{\mathrm{d}\boldsymbol{\kappa}_n}{\mathrm{d}\boldsymbol{\theta}_{cp}} = \frac{\partial \boldsymbol{\kappa}_n}{\partial \boldsymbol{\theta}_n}\boldsymbol{C} + \frac{\partial \boldsymbol{\kappa}_n}{\partial \boldsymbol{\theta}_{n,\boldsymbol{u}}}\boldsymbol{T}^{-1}\boldsymbol{C}_{,\boldsymbol{\xi}}, \qquad
\frac{\mathrm{d}\boldsymbol{\psi}_n}{\mathrm{d}\boldsymbol{\theta}_{cp}} = \frac{\partial \boldsymbol{\psi}_n}{\partial \boldsymbol{\theta}_n}\boldsymbol{C} + \frac{\partial \boldsymbol{\psi}_n}{\partial \boldsymbol{\theta}_{n,\boldsymbol{u}}}\boldsymbol{T}^{-1}\boldsymbol{C}_{,\boldsymbol{\xi}},
\tag{5.39}
$$

Similarly, for the thickness gradient:

$$
\frac{\mathrm{d}(||\nabla \boldsymbol{t}_n||^2)}{\mathrm{d}\boldsymbol{t}_{cp}} = \frac{\partial(||\nabla \boldsymbol{t}_n||^2)}{\partial \boldsymbol{t}_{n,\boldsymbol{u}}}\boldsymbol{T}^{-1}\boldsymbol{C}_{,\boldsymbol{\xi}}
\tag{5.40}
$$

CHAPTER 6

Structural optimization

In Chapter 4, the tow-steering parametrization tool, pySteer, was introduced. In Chapter 5, the relevant manufacturing constraints for a tow-steered composite structure were reviewed and translated into mathematical relationships suitable for gradient-based optimization. Before proceeding to a fully coupled aerostructural optimization for a tow-steered wing structure, it is worth developing an intuitive understanding of tow-steering optimization through a series of simpler structural optimization problems. Performing a structural optimization first allows the purely structural benefits of tow-steering, such as manipulation of local structural load paths, to be isolated from its aeroelastic benefits (aeroelastic tailoring). This also allows for the exploration of the effects of manufacturing constraints on the design problem. This will provide insight for the later aerostructurally optimized designs that might otherwise be difficult to interpret.

In the remainder of this chapter, four structural optimization problems will be considered. The first three problems are based on structural plate optimizations. These problems are meant to build up an understanding of parametric structural optimization by studying the effect of increasing number of control points and manufacturing constraints on the optimization problem. For the first two problems, a verification for the pySteer parametrization scheme is included to show that solutions found by previous authors can be reproduced given a sufficiently refined B-spline distribution. The final problem will then apply the full tow-steering parametrization and manufacturing constraints to the uCRM-9 structural wingbox model to address: the potential benefits that tow-steering has to offer for wingbox structural design optimization and possible presence of local minima in the optimization problem.
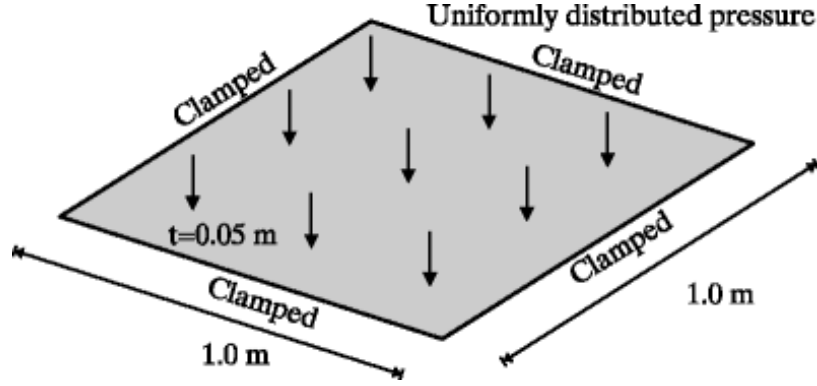
Figure 6.1: Compliance minimization problem proposed by Hvejsel et al. [36]

6.1 Compliance minimization

To assess the robustness of the B-spline parameterization, a composite plate compliance minimization problem, originally proposed by Lund and Stegmann [37], is solved. In this problem, a 1 m x 1 m x 0.05 m single-ply plate is clamped on all edges and subjected to a uniform pressure of 100 kPa loading on the top. The objective of this optimization is to minimize the compliance of the plate with respect to the ply angles. A diagram of the problem is given in Figure 6.1.

The optimization problem can be summarized as below:

$$\text{minimize} \quad \tfrac{1}{2}\boldsymbol{u}^T\boldsymbol{K}\boldsymbol{u}$$
$$\text{with respect to} \quad \theta_{cp}$$

Where $\boldsymbol{u}$ is a vector containing the nodal displacements and $\boldsymbol{K}$ is the global stiffness matrix of the FEM model. The compliance is minimized subject to each of the control point tow angles parameterizing the design. For this case, only a single-ply optimization is considered, however multi-ply optimization is possible as well. The composite properties used for the problem are listed below in Table 6.1.

Table 6.1: Compliance minimization material properties

Property	E_1 [GPa]	E_2 [GPa]	G_{12} [GPa]	G_{13} [GPa]	G_{23} [GPa]	ν_{12}	X_t [MPa]	X_c [MPa]	Y_t [MPa]	Y_c [MPa]	S_{12} [MPa]	ρ [kg/m^3]
Value	54.0	18.0	9.0	9.0	9.0	0.25	2410.0	1040.0	73.0	173.0	71.0	1550

This problem was previously solved using DMO by Hvejsel et al. [36], where the angles were forced to take discrete values (0°, ±45°, etc.) in each element of the mesh. In our case, we relax that requirement and allow a continuous fiber distribution parametrized by pySteer's B-spline control points. The discrete solution of Hvejsel et al. [36] was used as a

benchmark and their result can be seen in Figure 6.2. The plate model used for this study contained 10,000 shell elements. The continuous optimization case was run with 25, 100, and 400 control points uniformly distributed throughout the plate, and in each case, we started with all the fibers in the x-direction (i.e. $0°$).

All three optimization cases converge relatively quickly, with the largest optimization case taking roughly a minute to complete on a standard four-core desktop machine. The optimization results for each case are shown in Figure 6.3. It can be seen that the optimal designs for the discrete and continuous cases are similar in pattern: the fibers point radially towards the edges and form a diamond toward the center. Due to their smooth nature, the B-splines have a more difficult time modeling the sharp angle changes seen in the boundary between the inner and outer square regions. The final compliance for the 25, 100, and 400 control point designs was 10.19 J, 9.14 J and 8.89 J, respectively. For reference, the discrete case yields a compliance of 8.83 J, while the initial zero degree case yields 12.26 J. It is not surprising to see that as the number of control point is increased, the minimum compliance decreases. This is because the smooth nature of B-spline interpolation puts a limit on how quickly the ply orientations can vary and thus match the discrete case. The fact that as the number of control points are increased the solution of the continuous optimization problem approaches that of the discrete optimization verifies that the B-spline parametrization utilized by pySteer is capable of reproducing previous variable stiffness optimization results given a sufficiently refined B-spline distribution.
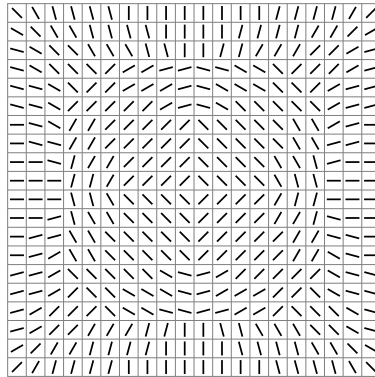
Figure 6.2: Solution to the discrete compliance minimization case (8.83 J) [36]

6.1.1 The effect of the tow-path curvature constraint

Now, we will investigate the effect that the tow-path curvature constraint, as defined in Chapter 5, has on the design problem. To do this the 400 control point case is rerun with increasingly restrictive maximum curvature values ($\kappa_{\max} = [20\,\mathrm{m}^{-1}, 10\,\mathrm{m}^{-1}, 5\,\mathrm{m}^{-1}]$). Max-
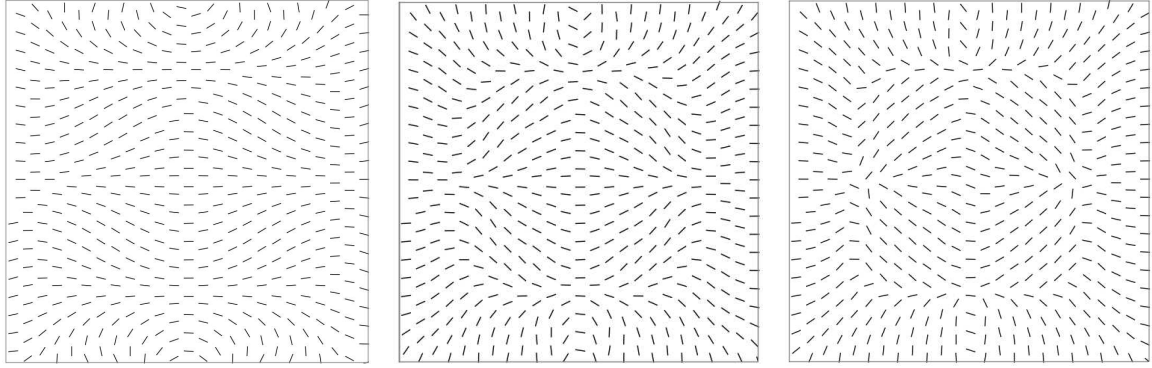
(a) 25 Control points (10.19 J)   (b) 100 Control points (9.18 J)   (c) 400 Control points (8.89 J)

Figure 6.3: Clamped plate solutions for variable tow angles

imum curvature is approximated by computing the curvature at each FEM node and aggregating the values into a single constraint with a KS function. The tow-path curvature for the unconstrained case is computed in Figure 6.4 (a) as reference baseline. From this we find the highest curvature regions occur at the center of the top and bottom edges of the plate. The curvature-constrained optimized results are shown in Figure 6.4 (b)-(d). It should be pointed out that as the curvature constraint is made more restrictive, the computational time of the optimization increases as well, due to the fact that a larger number of major iterations are required to converge. The computational time ranged from roughly 2.5 minutes in the least constrained case ($\kappa_{\mathrm{max}} = 20\,\mathrm{m}^{-1}$) to roughly 23 minutes in the most constrained case ($\kappa_{\mathrm{max}} = 5\,\mathrm{m}^{-1}$). As one would expect, as the maximum allowable curvature is decreased, the tow paths in the center top and bottom edges of the plate are forced to curve wider arcs, increasing the turning radius. Interestingly, the plate solution loses its four-way symmetry as the curvature constraint is decreased to $5\,\mathrm{m}^{-1}$. It is important to note that while even as the curvature constraint is increased, there still remain regions where the tow paths converge and diverge from one another. These are regions where gaps and overlaps are likely to occur and demonstrate that simply constraining the tow-path curvature is not sufficient to eliminate these regions. Finally, it is not a surprise that as the curvature constraint becomes more restrictive, the optimal compliance increases. This leads to a reduction of about 2.3% in compliance performance for the least constrained case to a reduction of 17% for the most severe case. This loss in compliance performance is due to the fact that as we increasingly constrain curvature, we are limiting how quickly the optimizer can spatially vary the tow paths.

(a) $\kappa_{max} = \infty$, (8.89 J)   (b) $\kappa_{max} = 20$ m^{-1}, (9.10 J)   (c) $\kappa_{max} = 10$ m^{-1}, (9.46 J)   (d) $\kappa_{max} = 5$ m^{-1}, (10.42 J)
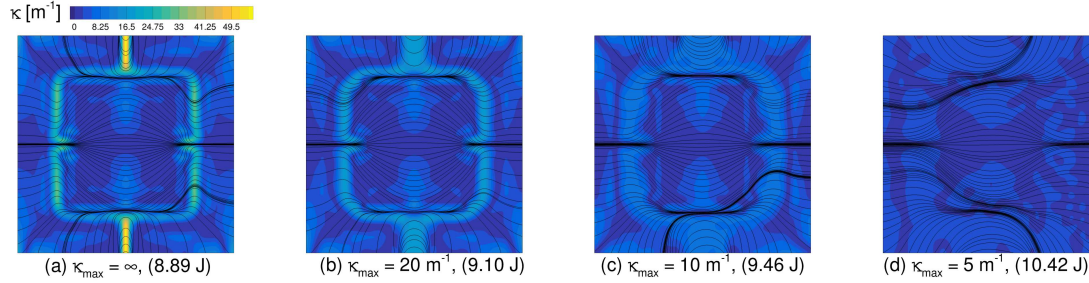
Figure 6.4: Effect of increasing curvature constraint on optimization

6.2 Mass minimization

Next, we will test the B-spline control points' capability of reproducing variable thickness solutions. The optimization problem performed here is a mass minimization of a clamped isotropic plate (0.32 m x 0.32 m) under a 400 kPa pressure load, originally proposed by Arreckx et al. [109]. The material properties are given in Table 6.2.

Table 6.2: Mass minimization material properties

Property	Value
E	70 GPa
ν	0.3
σ_{YS}	300 MPa
ρ	2780.0 kg/m^3

The design variables of the optimization problem are the thickness distribution of the plate, controlled through the B-spline control points. The upper and lower bounds for the plate thickness are 3 mm and 7 mm, respectively. The plate is subject to a von Mises yield stress constraint aggregated over the elements of the model using a KS function. The plate model features 1600 shell elements and to simplify the problem a quarter of the plate is modeled with symmetry boundary conditions applied to the unclamped edges. A diagram of the structural problem can be seen in Figure 6.5. The optimization problem is summarized below:

$$\begin{array}{rl} \text{minimize} & \text{Mass} \\ \text{with respect to} & 3\,\text{mm} \leq t_{cp} \leq 7\text{mm} \\ \text{subject to} & \text{KS}_{\text{yield}} \end{array}$$

This case makes for an interesting structural optimization problem, as the problem is statically indeterminate, meaning that the plate stress as a function of thickness cannot be analytically found without solving the structural problem. Because of this the only remaining approach is a numerical optimization scheme. Similar to the previous verification

98
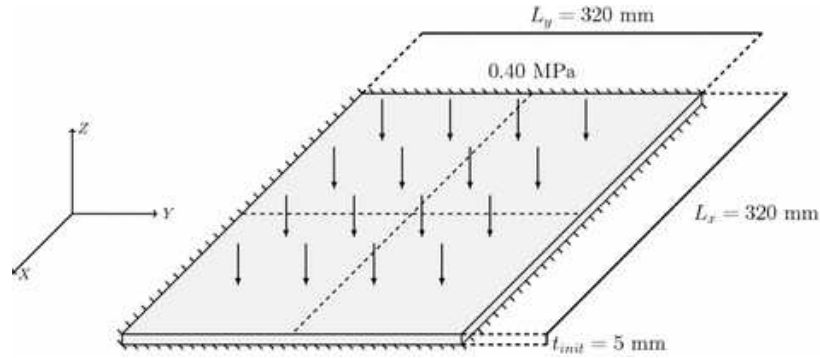
Figure 6.5: Mass minimization problem proposed by Arreckx et al. [109]

problem, the original authors solved this problem by assigning each element a thickness variable, for a total of 1600 design variables. Their thickness variables in this case, however, were not restricted to discrete values. Their optimized solution yielded a minimum mass of 0.281 kg and can be seen in Figure 6.6.

Several optimization are again performed with varying number of control points: 25, 100, and 400 points. Similar to the previous case the optimization converged relatively quickly, requiring roughly a minute for the largest case on four core desktop machine. The results for each optimization case can be seen in Figure 6.7. As one might expect, the optimizer reinforces the regions of the plate near the clamped edges where the bending loads are expected to be the largest. A large portion of the plate remains under-stressed with respect to the von Mises yield constraint and as such the optimizer reduces these regions to gage thickness. Here we see a similar trend to the previous optimization problem, in that as the number B-spline control points are refined the original solution is approached.

6.2.1 The effect of the thickness gradient constraint

Next, we investigate the effect of the thickness gradient constraint on the optimization. To do this the previous optimization is rerun with a constraint on the maximum thickness gradient magnitude of $20 \, \text{cm/m}$ and $10 \, \text{cm/m}$. Similar to the curvature, the maximum thickness gradient is approximated by aggregating the values from all nodes with a KS function. Again the 400 control point unconstrained case will be used as a reference, Figure 6.8 (a). From Figure 6.8 (a), it can be seen that the region featuring the sharpest change in thickness are near the reinforced regions on the clamped edges of the plate. As mentioned in Chapter 5 these regions of sharp variation are undesirable as they may lead to stress concentrations and potentially structural failure. The constrained optimized solutions can be found in Figure 6.8 (b) and (c). From these results, it is clear that as the gradient constraint becomes more severe, the sharp thickness variation region seen previously in the
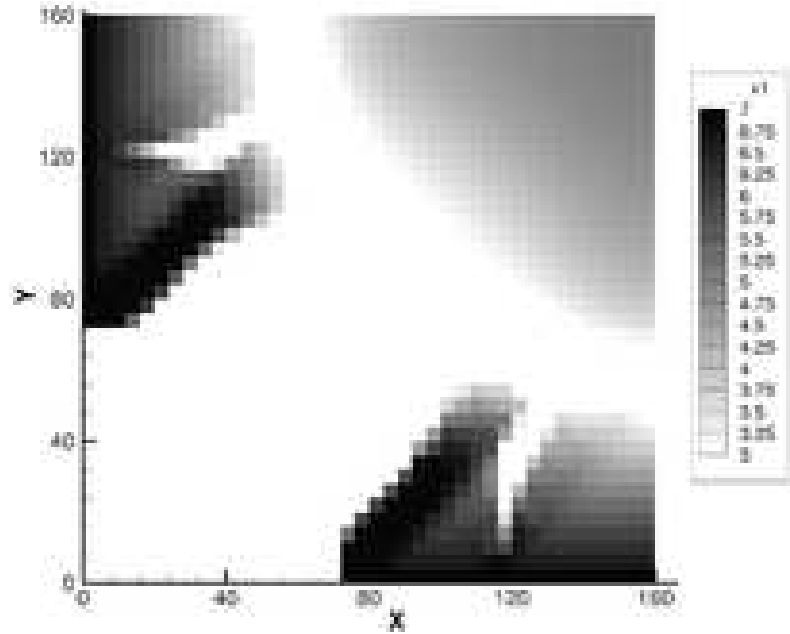
Figure 6.6: Arreckx et al. [109] mass minimized quarter plate solution (0.281 kg)

unconstrained case becomes smoothed out. Somewhat surprisingly for this case, despite the noticeable difference in the design, only a slight penalty is paid in terms of additional weight (roughly 3% for the worst case). This is due to the fact that a large portion of the plate is already at minimum thickness, meaning that the thickness gradient constraint has no effect in these regions.

6.3 Stress minimization

Next, the ability of tow steering to locally tailor structural performance through the manipulation of load paths will be investigated. To this end, we perform a structural design optimization of a single-ply "L"-shaped plate. The inner corner of the plate is filleted to ensure that the stress remains bounded in this region. The plate is 5 mm thick, clamped on one edge, and has a distributed shear force of 4 kN/m applied to one of its free edges. The plate's dimensions, loading, and boundary conditions are shown in Figure 6.9. The material properties for the laminate are listed in Table 6.1. The FEM mesh used to model this problem consists of approximately 7500 plate elements. Without having to solve the finite-element problem, it is well known that a stress concentration occurs at the corner of the plate. This stress concentration might be representative of certain regions in a wingbox design where local stress concentrations are expected to occur, such as the wing-fuselage intersection, Yehudi break of the wing, or engine mounting location.

(a) 25 Control points (0.303 kg) (b) 100 Control points (0.288 kg) (c) 400 Control points (0.285 kg)
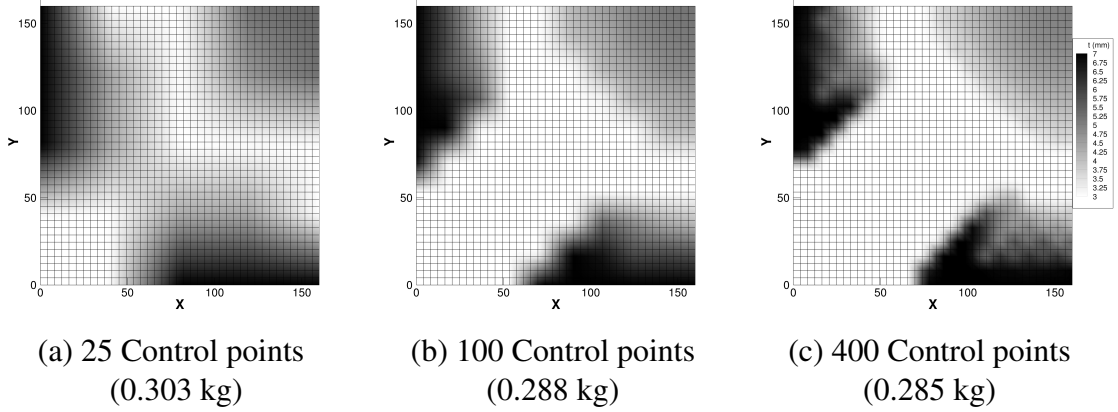
Figure 6.7: pySteer mass minimized quarter plate solutions

The objective of the optimization problem is to minimize the maximum Tsai–Wu stress in the plate, which is given by:

$$\sigma_{\text{TW}} = \sqrt{\frac{\sigma_{11}^2 + (X_c - X_t)\sigma_{11}}{X_t X_c} + \frac{\sigma_{22}^2 + (Y_c - Y_t)\sigma_{22}}{Y_t Y_c} + \left(\frac{\sigma_{66}}{S_{12}}\right)^2}, \tag{6.1}$$

where σ_{11}, σ_{22}, and σ_{66} are the tangential, transverse, and shear stresses relative to the local fiber orientation; X_t/X_c and Y_t/Y_c are the tension and compression ply strengths parallel and transverse to fiber direction, respectively. Similarly, S_{12} is the ply shear strength in the fiber reference frame. The maximum stress is approximated by first evaluating the stress at each structural node, and then using a KS aggregation over the domain of the plate. The design variables for the optimization problem are the fiber orientations, set through 100 B-spline control points. The design problem includes a minimum turning radius constraint. For this problem, the minimum turning radius, R_{min}, is set to 0.1 m.

The optimization problem can be stated as:

$$\begin{aligned} \text{minimize} \quad & \text{KS}(\sigma_{\text{TW}}) \\ \text{with respect to} \quad & \theta_{\text{cp}} \\ \text{such that} \quad & -\frac{1}{R_{\text{min}}} \leq \kappa \leq \frac{1}{R_{\text{min}}} \end{aligned}$$

For this study, an unsteered unidirectional design is used as a baseline. The results for both the unsteered baseline and optimized tow-steered plates can be seen in Figure 6.10. From the results, it can be seen that, as expected, a sharp stress concentration occurs at the interior corner of the plate. On the tow-steered design, the optimizer is able effectively able to redistribute the stress more uniformly over the domain of the plate, reducing the maximum stress by roughly 68%. This significant reduction in stress concentration means

101

t (mm)

||∇t|| (cm/m)

(a)$||\nabla t||_{max} = \infty$, (0.285 kg) (b) $||\nabla t||_{max} = 20$ cm/m, (0.288 kg) (c) $||\nabla t||_{max} = 10$ cm/m, (0.293 kg)
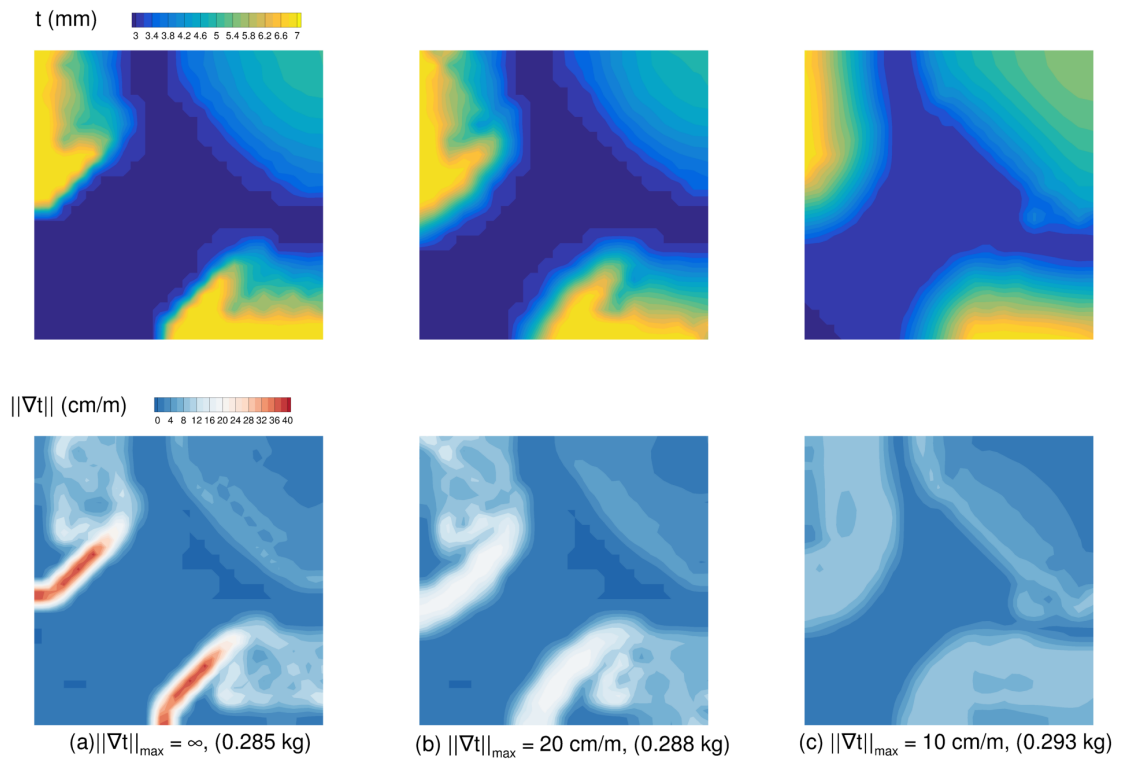
Figure 6.8: Effect of increasing thickness gradient constraint on optimization, thickness contours (top) and thickness gradient magnitude (bottom)
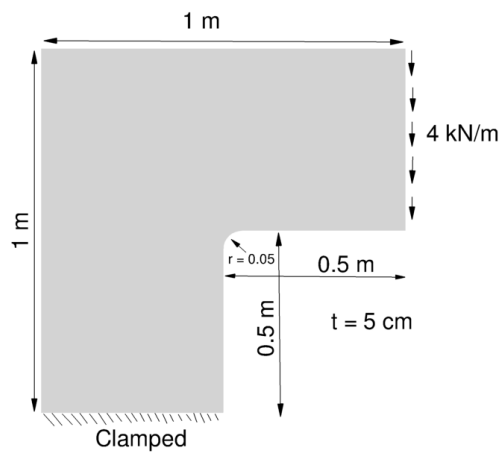
Figure 6.9: Problem definition for stress minimization optimization

σ_{TW} 0.1 0.3 0.5 0.7 0.9 1.1 1.3 1.5 1.7 1.9 2.1 2.3 2.5 2.7 2.9

Unsteered (σ_{max} = 2.313)   Steered (σ_{max} = 0.739)
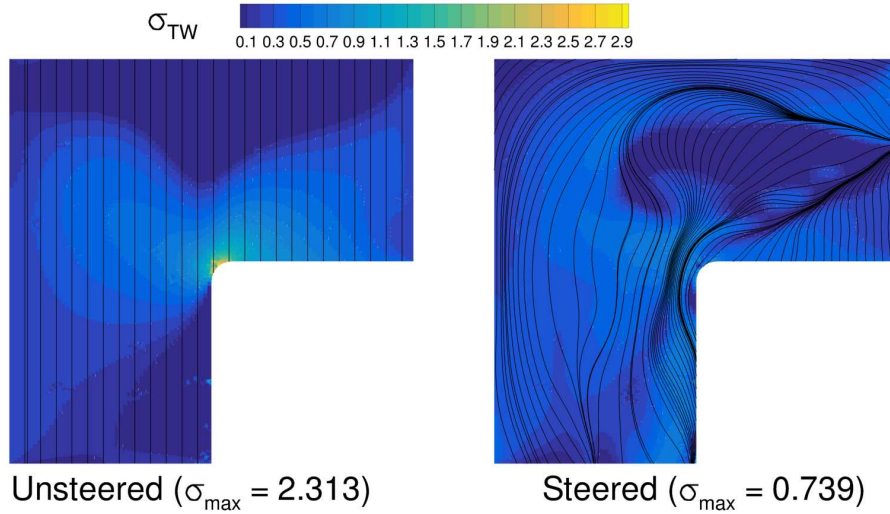
Figure 6.10: Unsteered baseline (left) and stress-minimized steered solution (right)

that through more effectively utilizing the directional stiffness properties of the composite a less reinforced layup can be used in this region.

6.3.1 The effect of the tow cut/add length constraint

Next, we will examine the effect of the final tow-steering constraint, the minimum tow cut and add length. Before continuing further it is worth examining the optimized tow pattern in Figure 6.10 in greater detail. While the design is very effective in redistributing the structural loads, most of the tow paths emanate from the point on the right-most edge of the plate. In addition to this region, there also several other locations in the pattern where tow paths converge on each other. Plotting the tow-path divergence, ψ, in Figure 6.11 (a) helps to highlight these regions. As mentioned previously, these regions are particularly problematic as they will likely lead to severe gaps and overlaps in the AFP layup process, requiring frequent tow cuts to manufacture. To address this, we will now re-optimize the design, adding in a minimum tow cut/add length constraint. To gain an understanding of the effect this constraint has on the design problem we again perform several optimizations with varying degrees of constraint severity, $L_{cut} = L_{add} = [0.025\,\text{m}, 0.1\,\text{m}, 0.4\,\text{m}]$. Again, the maximum divergence constraint used to bound the tow cut/add lengths is approximated with a KS function.

The results of the divergence constrained optimizations are shown in Figure 6.11 (b) - (d). As should be expected, the tow paths become more uniformly spaced as the constraint becomes more restrictive. The increasingly restrictive constraint comes at a cost in objective performance. Nevertheless, the most restrictive case (Figure 6.11 (d)) is still able to

(a) $L_{cut} = L_{add} = 0$ m, $\sigma_{max} = 0.739$ (b) $L_{cut} = L_{add} = 0.025$ m, $\sigma_{max} = 0.746$ (c) $L_{cut} = L_{add} = 0.1$ m, $\sigma_{max} = 0.793$ (d) $L_{cut} = L_{add} = 0.4$ m, $\sigma_{max} = 0.974$

Decreasing $|\psi_{max}|$, $|\psi_{min}|$
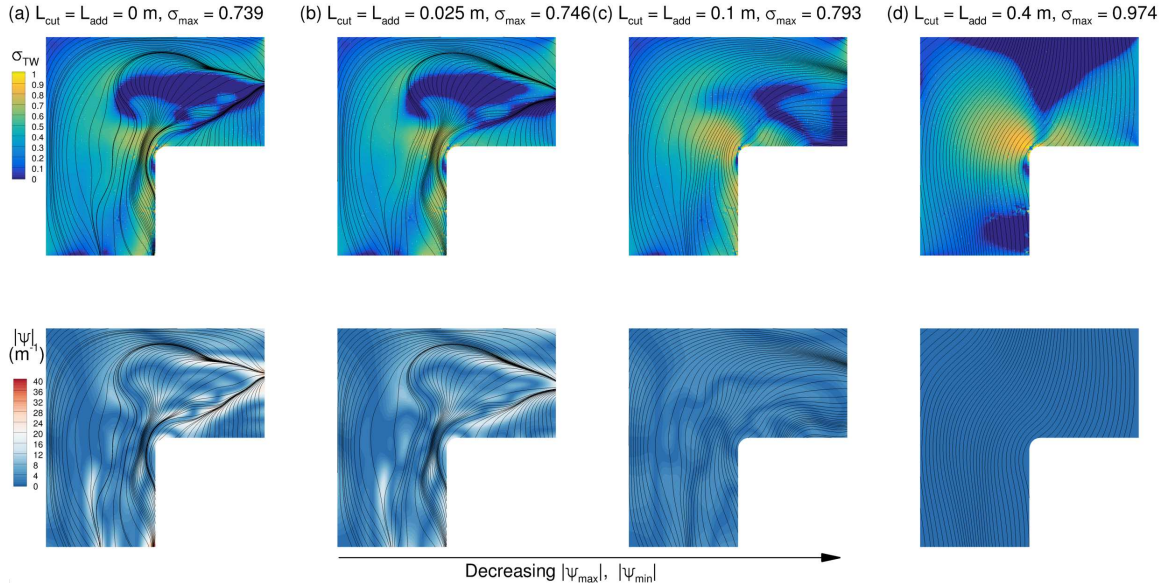
Figure 6.11: Optimization results showing Tsai–Wu stress (top) and tow-path divergence (bottom).

decrease the maximum stress by 58% relative to the baseline design. This trend can be followed until the desired minimum tow cut/add length in the design has been met, as given by Equation (5.19).

6.4 Wingbox mass minimization

Now that the structural benefits and manufacturing constraints have been explored in detail for simple plate structures, it is time to extend the study to a more complex problem. In this final structural design optimization study, we apply the tow-steered optimization scheme to the uCRM-9 wingbox. The objective of the optimization problem is to minimize the structural mass of the wingbox. The design variables for the problem include the main tow path orientation and panel thickness variables set at each B-spline control point on the skins, θ_0^{cp} and t_p^{cp}, respectively. In addition to this, variables are included to structurally size the ribs, spars, and stiffeners of the model as well. The stiffeners and skin tow patterns are modeled using the smeared stiffness approach detailed in Section 4.3.

For this problem, two load cases with fixed aerodynamic loads from a 2.5 g pull up and -1.0 g dive maneuver, respectively, are considered. The design constraints include the tow-path curvature, divergence and panel thickness variation constraints introduced in Chapter 5. Additionally, we then apply an aggregated material failure and panel buckling constraint for the ribs, spars, and skins with a safety factor of 1.5. A value of 70 in. was

used for $R_{\min}$, while a value of 1.3 mm/m was used for $||\nabla t_0||$. For simplicity, the maximum divergence magnitude is set equal to the maximum curvature, this corresponds to a minimum cut/add length value of 0.72 m for 50% gap/overlap rule. These three manufacturing constraints are evaluated at the centroid of each element and the aggregated over each panel of the wingbox using a KS aggregation. The material properties used for the plies in the ribs, spars, and skins of the wingbox are given in Table 6.3. A summary of the optimization problem is given in Table 6.4. As a baseline reference, an additional unsteered structural optimization is performed as well by removing the tow-path design variables, θ_0^{cp}.

Table 6.3: Mechanical properties for the composites used on skin, ribs, and spars

Material	E_1 [GPa]	E_2 [GPa]	G_{12} [GPa]	G_{13} [GPa]	G_{23} [GPa]	ν_{12}	X_t [MPa]	X_c [MPa]	Y_t [MPa]	Y_c [MPa]	S [MPa]	ρ [kg/m^3]
Unidirectional tape E752LT/AS4 (Skin)	117.9	9.7	4.8	4.8	4.8	0.34	1648	1034	64	228	71	1550
PW Fabric AS4/8552 (Ribs and Spars)	62.1	62.1	5	4.8	4.8	0.045	279	266	279	266	70	1550

The result of both wingbox optimizations are shown in Figure 6.12. Based on these results, we see that the 2.5 g buckling and failure constraints are actively sizing most of the upper skin of the wingbox for both designs, while the 2.5 g failure and -1 g buckling constraints largely sized the lower skins. By looking at the panel thickness distribution, we can see that the tow-steered structure is noticeably thinner near the root on both the skins and spars, which accounts for the difference in structural weight. This is due to the optimizer taking advantage of the fiber steering to locally shift the load paths of the wing and aligning tow paths closer to local principal stress directions. It is important to remember that the wingbox is structurally supported by the boundary conditions at the symmetry plane (clamped) and wing-fuselage intersection (no vertical displacement). For the portion of the skins inside the fuselage the optimizer rotates the tow paths to be perpendicular to its supports. This maximizes the compression strength of the skins in this region. As the skins exit the fuselage, the optimizer rotates the tow paths to be roughly parallel with the sweep of the wing. This improves the strength along the wing's bending axis. Toward the tip of the structure the only slight steering variations are utilized. This is because the stresses and sensitivity of the mass of the design in these regions is relatively small compared to the root of the wing. Near the tip we also find that the panel thickness contours become evenly spaced, a sign the thickness gradient constraint is active in this region.

	Variable/function	Description	variables #
Minimize	M_{wing}	Wingbox mass	
with respect to	x_{ribs}	Panel thickness (ribs)	49
	$x_{\text{stiff thick}}$	Stiffener thickness (skin/spars/ribs)	238
	$x_{\text{stiff height}}$	Stiffener height (skin/spars/ribs)	238
	$x_{\text{stiff pitch}}$	Stiffener pitch	4
	$x_{\text{panel length}}$	Panel length (skin/spars/ribs)	238
	$x_{t^{\text{cp}}}$	Panel thickness control points (skin/spar)	280
	$x_{\theta_0^{\text{cp}}}$	Tow offset control points (skin)	240
		Total design variables	**1287**
Subject to	$L_{\text{panel}} - x_{\text{panel length}} = 0$	Target panel length	238
	$\text{KS}_{\text{stress}} < 1.0$	2.5 g Material failure	4
	$\text{KS}_{\text{buckling}} < 1.0$	2.5 g and -1.0 g Buckling	6
	$\left\| x_{\text{stiff thick}_i} - x_{\text{stiff thick}_{i+1}} \right\| \leq 0.0005$	Stiffener thickness adjacency	183
	$\left\| x_{\text{stiff height}_i} - x_{\text{stiff height}_{i+1}} \right\| \leq 0.0005$	Stiffener height adjacency	183
	$\left\| x_{\text{stiff thick}} - x_{\text{panel thick}} \right\| < 0.0025$	Maximum stiffener-skin difference	238
	$-\frac{1}{r_{\min}} < \text{KS}_{\kappa} < \frac{1}{r_{\min}}$	Tow-path turning radius	96
	$-\psi_0 < \text{KS}_{\psi} < \psi_0$	Tow-path divergence	96
	$\text{KS}_{\|\nabla t_p\|} < \|\nabla t_0\|$	Panel thickness gradient	189
		Total constraints	**1233**

Table 6.4: Structural optimization problem formulations

6.4.1 Local minimum study

Next, we will test the tow-steered wingbox optimization for the presence of local minima. While gradient-based optimization techniques guarantee rapid convergence to a minima of the optimization problem, there is no guarantee that the converged minima is in fact a global minimum. This problem of local optimality is a well-known weaknesses of gradient-based optimization methods and can lead to difficulties in improving design performance if the problem is severely multi-modal. Multi-modality in aerodynamic shape optimization for wing designs has already been explored in great detail by Lyu et al. [79] and Bons et al. [110]. Both of these studies concluded that when the necessary physics are modeled and appropriate design variables and constraints are applied, the design problem can be reduced to a single-modal optimization problem featuring only one global minimum. This gives us confidence that that the aerodynamic discipline will not add multi-modality to the aerostructural design optimization problems presented in the following sections. The goal of this study is to perform a local minimum study for a tow-steered wing design optimization on the structural discipline side as well. Of primary concern are the tow angle variables θ_0^{cp}, because of the inherent multi-modal nature of the trigonometric functions ($\sin$, $\cos$, etc.) used to rotate the stiffness matrices for each ply in the classical laminate theory (CLT) formulation. If through structural optimization we can verify that multi-modality is not a concern for the wing design considered throughout the remainder of this thesis, then we can extend this conclusion to remaining aerostructural optimizations as well.

To check for local minima and multi-modality we will begin the optimization from four different starting points: the initially unsteered layup $0°$ layup that was the starting point for the the steered optimization presented in the previous section and three randomized initial tow-steered patterns. For the random starting points the design variables corresponding to the tow-path control points, θ_0^{cp}, are set to random values at the beginning of the optimization. The thickness at all four starting point remains the same. A breakdown of all four starting tow orientation values is given in Table 6.5 Where $\boldsymbol{U}(-30, 30)$ is a vector with each component taking on a uniformly random value from $-30°$ to $30°$. An offset of $\pm 15°$ is added to random cases 2 and 3, to gauge the effect that varying the initial average direction of the of the tow paths has on the optimization result.

Table 6.5: Randomized starting points

Design variable	Nominal case	Random case 1	Random case 2	Random case 3
$\boldsymbol{\theta}_0^{cp}$	$0°$	$0° + \boldsymbol{U}(-30, 30)$	$15° + \boldsymbol{U}(-30, 30)$	$-15° + \boldsymbol{U}(-30, 30)$
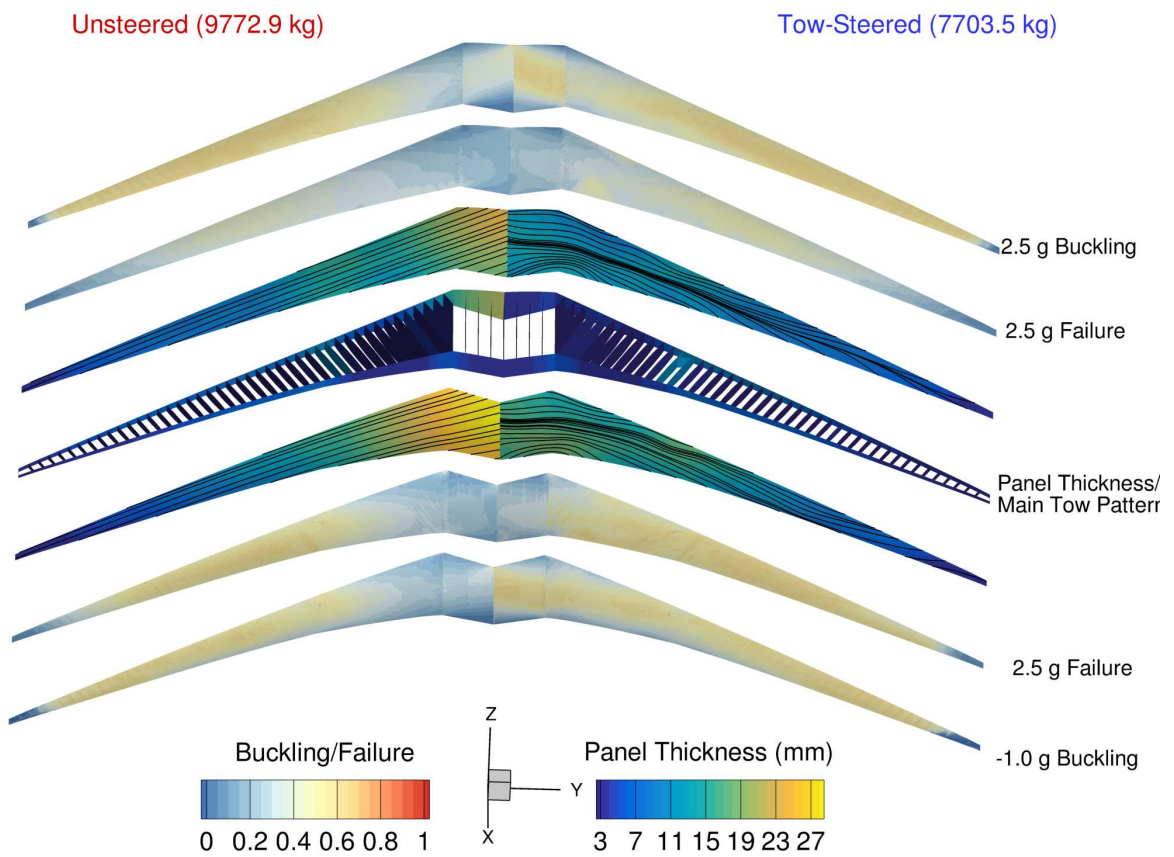
Figure 6.12: Result of structural optimization of uCRM-9: unsteered (left) vs. tow-steered (right)

The initial and optimized thickness and main tow path patterns for the upper and lower skins and corresponding final masses for all four cases are shown in Figure 6.13. From these results it can be seen that all four starting points converge to roughly the same final structural weight, with the largest difference between cases being only 0.17%. Not only do the overall masses match between the four designs, but distribution of mass, as shown by the panel thickness contours, are indistinguishable. Finally, by comparing the main tow patterns for the upper and lower skins of each design, we see that the tow paths are nearly identical as well. The only location where slight difference can be observed are at the locations of tips. For each case, in these regions the tow paths seem to remain at the at initial orientation defined in the region at the starting point. Again, this is likely due to the low design sensitivities in this region of the wing, leading to relatively flat design space as the optimizer attempts to converge these regions.

From these results, it seems safe to conclude that the presence of local minima is not a problem for the tow-steered wingbox parametrization considered in this work. To be rigorous, it should be noted that by the periodic nature of the angular variables used to define the tow-paths (i.e. $\theta = \theta + n2\pi$) there will be multiple solutions that represent exactly the same design. However, as long as these are the only minima that occur, we can restrict the optimization to a subset of the periodic domain (i.e. $0 \leq \theta \leq 2\pi$) and ensure that the minima located is likely globally optimal. Of course there still exists the possibility of local minima in locations of the design space that may have been missed by this random sampling of the design space. In general, it is difficult to guarantee global convexity of general optimization problems. Instead, we will use this case study to conclude that the design optimization appears to be convex in a large region of the design space. Finally, the conclusion of this study should not be used to disprove the concern of local minima introduced by the chosen parametrization for all structural design problems, but merely for the wingbox case studies considered in the remainder of this work.
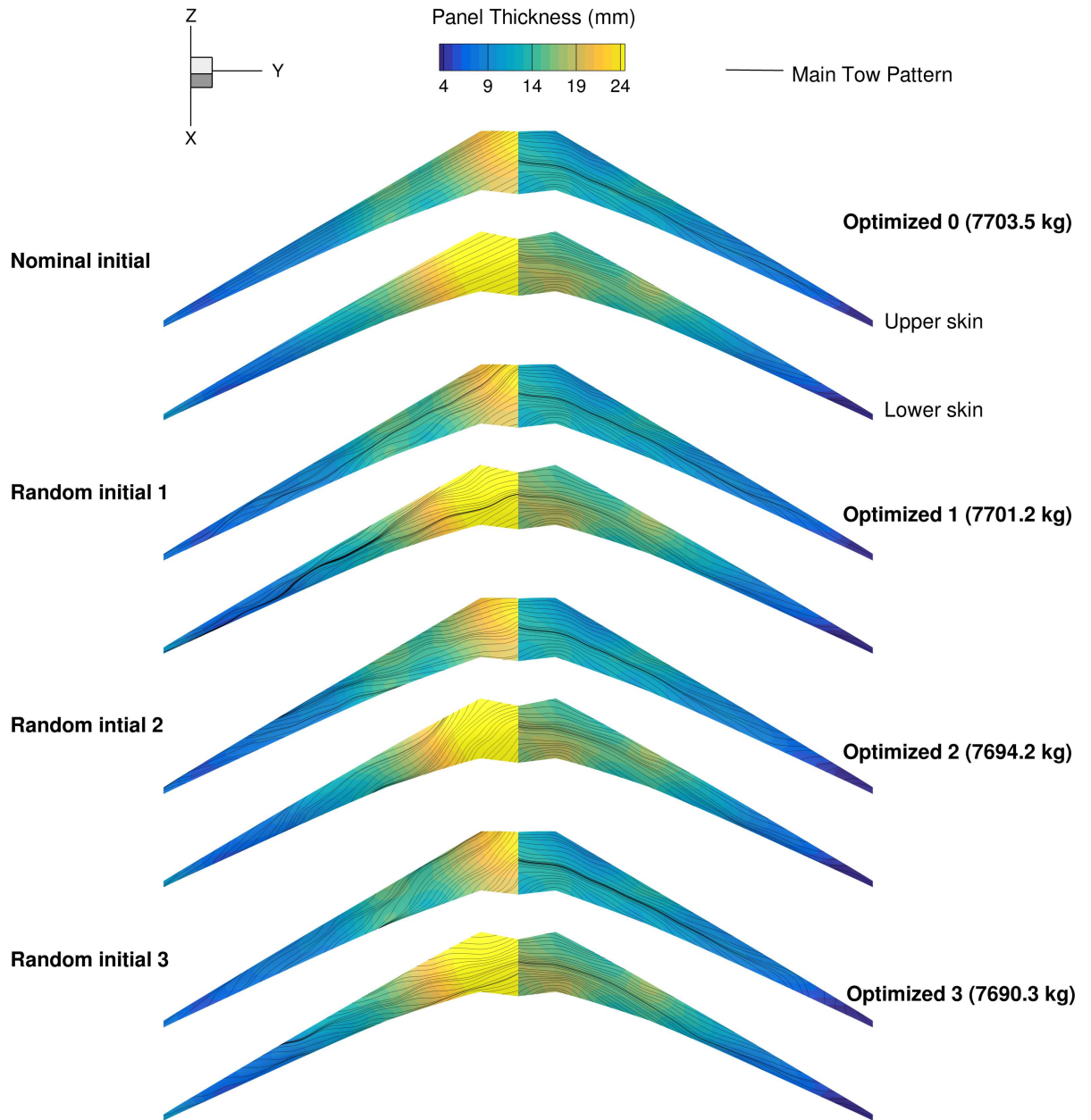
Figure 6.13: The resulting main pattern and panel thickness distribution from each starting point

CHAPTER 7

Fuel burn optimization

In the previous chapter, a series of structural optimization problems were solved to gain some insight into the structural benefits of tow-steered composite optimization. In this chapter, the insights will be extended to the aeroelastic benefits specific to wing design. To this end, a series of fuel burn minimization problems will be performed on the uCRM-9. To quantify the benefits, the optimizations are run with both a tow-steered and fixed ply orientation conventional composite wingbox design. The benefits of tow-steering will then be reassessed with a conventional design where the plies of the wing skins are free to be rotated by the optimizer. Next, the performance penalty associated with the manufacturing constraints introduced in Chapter 5 will be quantified by re-optimizing the tow-steered design without them. The tow-steered and fixed ply orientation conventional composite design optimizations will then be performed on the uCRM-13.5. Including this design provides insight into the benefits of tow steering with respect to high-aspect-ratio wing design. Finally, the effect of aspect ratio on the wing design performance will be refined. This will be accomplished by re-optimizing the tow-steered and fixed ply orientation conventional composite designs on the uCRM model for a wing aspect ratio of 7.5, 9, 10.5, 12, and 13.5 and analyzing the resulting trends in performance.

7.1   Problem formulation

In this section, the optimization problem is described by detailing the objective function, design variables, and constraints that are enforced. Each optimization requires three aerostructural analysis: a cruise condition for evaluating the fuel burn performance, and two conditions for which the structural constraints are enforced: a $-1.0\,\mathrm{g}$ dive and $2.5\,\mathrm{g}$ pull-up maneuver condition. The lift of the cruise condition is set to be that of the nominal CRM ($C_L = 0.5$), while the lift of the maneuver conditions are based on the maximum take off weight (MTOW) of the aircraft. The parameters for these three conditions are listed in

Table 7.1.

Table 7.1: Optimization flight condition parameters

Parameter	Cruise	2.5g	-1.0g
Mach number	0.85	0.64	0.64
Altitude (ft.)	37 000	0	0
C_L/Lift	0.5	$2.5 \cdot \text{MTOW}$	$-1.0 \cdot \text{MTOW}$

7.1.1 Objective

The objective of the optimization problem is to minimize the fuel burn of the aircraft at cruise, calculated using Equation (3.2). The fuel burn makes for a good multi-disciplinary objective function due to its dependence on both structural performance, through the empty weight, as well as aerodynamic efficiency, through L/D. In addition, its relationship to the aircrafts' direct operating cost (DOC) makes it an appropriate metric for the aircrafts performance.

7.1.2 Design variables

Similar to the optimization of the aluminum uCRM designs in Section 3.3.2, the design variables are broken down into structural, aerodynamic, and geometric variables. As was already mentioned, in this study a number of different design parametrization are considered. These design parametrizations include: tow-steered composite (TS), conventional (C) and conventional rotated (CR) composite, tow-steered composite without manufacturing constraints (TS-NM), and tow-steered and conventional composite with varying wing aspect ratio (TS-AR and C-AR, respectively). Each one of these parameterizations contain their own set of design variables and are summarized in Table 7.2. The definition of all possible design variables is shown in Figure 7.1.

Variable/function	Description	TS	C	CR	TS-NM	TS-AR	C-AR
$x_{\text{stiff thick}}$	Stiffener thickness (skin/spar/ribs)				238		
$x_{\text{stiff height}}$	Stiffener height (skin/spar/ribs)				238		
$x_{\text{stiff pitch}}$	Stiffener pitch (skin/spar/ribs)				4		
$x_{\text{panel length}}$	Panel length (skin/spar/ribs)				238		
$x_{t^{\text{cp}}}$	Panel thickness control points (skin/spar)				280		
x_{ribs}	Panel thickness (ribs)				49		
$x_{\theta_0^{\text{cp}}}$	Tow offset control points (skin)	240	0	2	240	240	0
x_{α_i}	Angle of attack for each case				3		
x_{tail}	Tail trim angle for each case				3		
x_{shape}	FFD control points				240		
x_{twist}	Wing twist				8		
x_{chord}	Chord scaling	0	0	0	0	1	1
x_{span}	Span	0	0	0	0	1	1
x_{sweep}	Sweep	0	0	0	0	1	1
	Total design variables	**1541**	**1301**	**1303**	**1541**	**1544**	**1304**

Table 7.2: Fuel burn optimization design variables
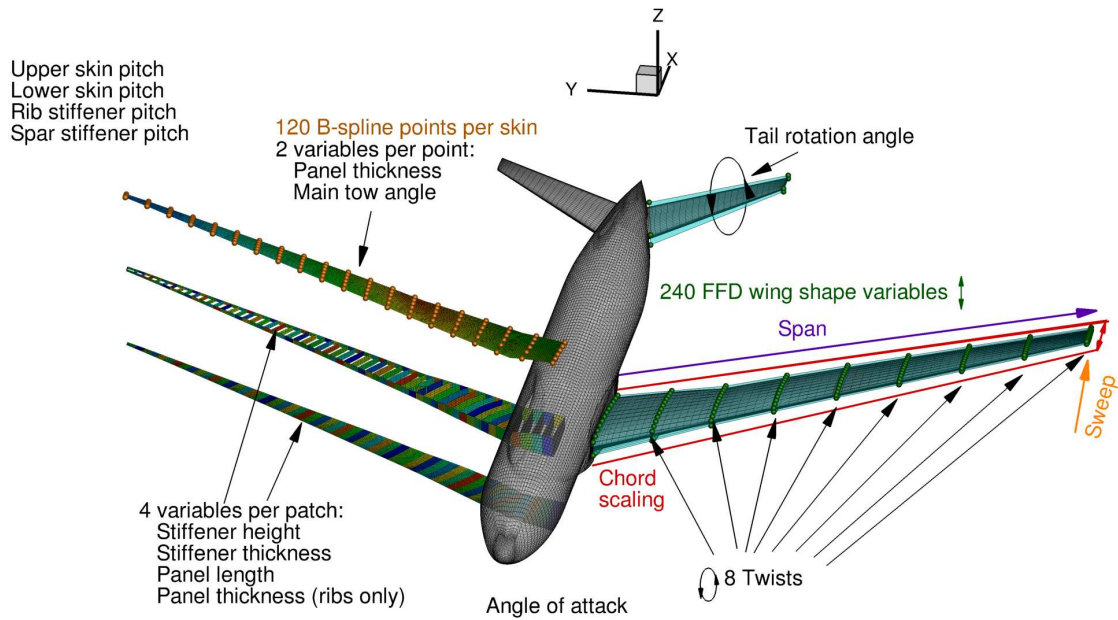
Figure 7.1: Design variables for fuel burn minimization study.

The structural variables differ slightly from the aluminum aerostructural optimizations performed in Chapter 3. The structural variables still include the panel thickness, stiffener height, and stiffener thickness, and panel length for each panel shown in Figure 7.1, for a total of 287 of each of these types of variables. In addition, the upper skin, lower skin, ribs, and spars each share a stiffener pitch variable, for a total of 4.

The difference for these composite designs is that the panel thickness is set parametrically using 120 B-spline control points distributed over each skin, and 20 control points distributed over each spar. This means 280 panel thickness control point variables and leaves 58 panel thickness variables for the ribs. In addition, the tow-steered design parametrization (TS, TS-NM, and TS-AR) also includes the tow-offset control point variable, θ_0^{cp}, on each skin, for a total of 240 additional variables. The main ply orientations in the skins for the conventional composite designs (C and C-AR) are forced to remain parallel to the the leading edge of the wing. This restriction is relaxed for the conventional rotated design (CR) by setting one tow-offset design variable for each skin. This gives the optimizer the freedom to rigidly rotate the plies of each skin with respect to the wing.

The aerodynamic and geometric design variables used in this study are largely the same as the aluminum case. The aerodynamic design variables include the angle of attack and tail rotation angle for each flight condition, for a total of 3 each. The geometric design

114

variables include 240 FFD shape variables and 8 span-wise twist variables.

The last set of geometric design variables control the planform of the wing. These design variables are only active for the variable aspect ratio designs, TS-AR and C-AR. These design variables include one chord variable, used to uniformly scale the chord of all of the wing's spanwise cross-sections. A single design variable is used to control the span of the wing. Finally, the sweep can be controlled by translating the tip of the wing in stream-wise direction.

7.1.3 Constraints

For the optimization problem to be well posed and to obtain practical design results, a number of constraints are required. As was the case for the design variables, only a select set of constraints are applied to each design parametrization. The constraints for each case are summarized in Table 7.3.

The majority of constraints considered in this study were also used in the optimization of the aluminum uCRM-13.5 baseline described in Section 3.3. For the aerodynamic constraints, these include lift and trim constraints for each flight condition. For the geometric constraints, these include: leading-edge radius, trailing-edge thickness, trailing-edge spar height, fixed leading/trailing-edge, fuel volume, and panel length constraints. Finally, for the structural constraints, this includes a material failure, buckling, and stiffener adjacency constraints.

The new constraints include the AFP-specific manufacturing constraints, defined in Chapter 5. These include a constraint on the panel thickness gradient of the skins and spars, which is the continuous analogue to the discrete adjacency constraint applied to the panel thickness for the aluminum design. The maximum thickness gradient value, $||\nabla t_0||$, is set to $1.3 \frac{\text{mm}}{\text{m}}$, a value chosen to be comparable to the discrete adjacency constraint of the aluminum design. The tow-steering-specific manufacturing constraints are applied to cases TS and TS-AR, while the constraints are removed for TS-NM. These include a constraint on the tow-path turning radius of each steering pattern, which is constrained to a minimum allowable turning radius, R_{min}, of 70 in. This value is determined by recommendation from designers at Aurora Flight Sciences for a 0.5 in wide prepreg tape. As mentioned in Chapter 5, while more aggressive values of tow-path curvature could be pursued through the use of narrower prepreg tape, this results in an increase in layup time and manufacturing cost. The final manufacturing constraint, the minimum tow cut and add lengths, is constrained to a value of $L_{\text{cut}} = L_{\text{add}} = 1$ m, assuming a 50% gap/ 50% overlap rule ($a_g = a_o = 0.5$).

Variable/function	Description	TS	C	CR	TS-NM	TS-AR	C-AR
$C_L = 0.5$	Cruise lift conditions				1		
$L_i = n_i\,\text{TOGW}$	Maneuver lift conditions				2		
$c_{m_y}^i = 0$	Trimmed flight				3		
$t_{LE}/t_{LE_{init}} \geq 1.0$	Leading-edge radius				20		
$t_{TE}/t_{TE_{init}} \geq 1.0$	Trailing-edge thickness				20		
$(t/c)_{\text{TE Spar}} \geq 0.80(t/c)_{\text{TE spar}_{init}}$	Minimum trailing-edge spar height				20		
$\Delta z_{\text{TE,upper}} = -\Delta z_{\text{TE,lower}}$	Fixed trailing edge				8		
$\Delta z_{\text{LE,upper}} = -\Delta z_{\text{LE,lower}}$	Fixed leading edge				8		
$V - V_{\text{fuel}} \geq 0.0$	Minimum fuel volume				1		
$L_{\text{panel}} - x_{\text{panel length}} = 0$	Target panel length				238		
$\text{KS}_{\text{stress}} < 1.0$	2.5 g Material Failure				4		
$\text{KS}_{\text{buckling}} < 1.0$	2.5 g and -1.0 g Buckling				6		
$\left|x_{\text{stiff height}_i} - x_{\text{stiff height}_{i+1}}\right| \leq 0.0005$	Stiffener height adjacency				183		
$\left|x_{\text{stiff thick}_i} - x_{\text{stiff thick}_{i+1}}\right| \leq 0.0005$	Stiffener thickness adjacency				183		
$\left|x_{\text{stiff thick}} - x_{\text{panel thick}}\right| < 0.0025$	Maximum stiffener-panel difference				238		
$\text{KS}_{||\nabla t_p||} < ||\nabla t_0||$	Panel thickness gradient				183		
$-\frac{1}{R_{\min}} < \text{KS}_\kappa < \frac{1}{R_{\min}}$	Minimum tow-path turning radius	96	0	0	0	96	0
$-\frac{\ln\left(\frac{1+a_g}{2(1-a_o)}\right)}{L_{\text{cut}}} < \text{KS}_\psi < \frac{\ln\left(\frac{1+a_g}{2(1-a_o)}\right)}{L_{\text{add}}}$	Minimum tow cut/add length	96	0	0	0	96	0
$\text{AR} = [7.5,\ 9,\ 10.5,\ 12,\ 13.5]$	Aspect ratio	0	0	0	0	1	1
$\Lambda_{c/4} = 34.8°$	Quarter-chord sweep	0	0	0	0	1	1
$S_{\text{ref}} = 191.8\,\text{m}^2$	Reference area	0	0	0	0	1	1
Total constraints		**1316**	**1124**	**1124**	**1124**	**1319**	**1127**

Table 7.3: Fuel burn optimization constraints

Additional geometric equality constraints are also placed on the variable planform cases, TS-AR and C-AR. This includes a constraint on the aspect ratio of the wing. An optimization will be run for each of these cases with an aspect ratio of 7.5, 9, 10.5, 12, and 13.5. A constraint is placed on both the wing quarter-chord sweep, $\Lambda_{c/4}$, and reference area, S_{ref}, to force the wing to retain the original values of uCRM-9. These three constraints are enough to uniquely prescribe the planform for each aspect ratio.

7.2 Bend-twist coupling quantification

When comparing the amount of passive load alleviation introduced into the design through material bend-twist coupling, it is useful to define a metric to measure the local degree of coupling in the wing. It is well known from CLT that the bend-twist coupling in a laminate structure is closely related to the laminate bending stiffness matrix, D. This stiffness matrix relates the mid-plane bending curvatures of a laminate panel, κ, to the moment resultants, M, as shown below:

$$
\begin{bmatrix} M_{xx} \\ M_{yy} \\ M_{xy} \end{bmatrix} = \begin{bmatrix} D_{11} & D_{12} & D_{16} \\ D_{12} & D_{22} & D_{26} \\ D_{16} & D_{26} & D_{66} \end{bmatrix} \begin{bmatrix} \kappa_{xx} \\ \kappa_{yy} \\ \kappa_{xy} \end{bmatrix}
$$

Where D_{11}, D_{66}, D_{16}, and D_{26} are components of the bending stiffness matrix, D. The degree of spanwise bend-twist coupling due to material is determined by the magnitude and sign of the off-diagonal term, D_{16}. The typical way of increasing this term is by using increasingly unbalanced ply orientations in the laminate layup.

Shirk et al. [15] introduced a non-dimensional coupling parameter to measure the magnitude of this term given by:

$$
\psi_1 = \frac{D_{16}}{\sqrt{D_{11} D_{66}}} \tag{7.1}
$$

This parameter was originally derived for the aeroelastic analysis for a cantilevered composite plate. In this work, we will extend this for use on a thin-walled wingbox by treating it as a "sandwich" structure. This allows the effective bending stiffness matrix, D^{eff}, to be computed for each pair of wing skin panels along the span of the wingbox, as shown in Figure 7.2.

In this calculation, we neglect the effect of the spars and ribs. This is acceptable, as we only wish to develop a metric to measure the bend-twist coupling added to the wing due to the directional stiffness tailoring of the skins, because the spars and ribs consist of balanced

plies they make no contribution to this. The effective bending stiffness matrix can then be computed from its definition in CLT:

$$\boldsymbol{D}^{\text{eff}} = \int_{-d/2-t_l/2}^{d/2+t_u/2} z^2 \boldsymbol{Q}\left(z\right) dz, \tag{7.2}$$

where $\boldsymbol{Q}$ is the in-plane material stiffness matrix. This assumes that the wingbox mid-plane coincides with the neutral plane, the plane about which there is zero in-plane stress for pure bending load. Because there is no material in between the skins this integral reduces to:

$$\boldsymbol{D}^{\text{eff}} = \int_{-d/2-t_l/2}^{-d/2+t_l/2} z^2 \boldsymbol{Q}_l\left(z\right) dz + \int_{d/2-t_u/2}^{d/2+t_u/2} z^2 \boldsymbol{Q}_u\left(z\right) dz \tag{7.3}$$

Now, translating the z variable of each integral to their respective skin coordinate, z_u and z_l, yields:

$$\boldsymbol{D}^{\text{eff}} = \int_{-t_l/2}^{t_l/2} \left(z_l - \frac{d}{2}\right)^2 \boldsymbol{Q}_l\left(z_l\right) dz_l + \int_{-t_u/2}^{t_u/2} \left(z_u + \frac{d}{2}\right)^2 \boldsymbol{Q}_u\left(z_u\right) dz_u \tag{7.4}$$

Since, for a wingbox, the local panel depth, d, is much larger than the skin thickness, t_u and t_l, this equation can be simplified further to:

$$\boldsymbol{D}^{\text{eff}} = \int_{-t_l/2}^{t_l/2} \left(\frac{d}{2}\right)^2 \boldsymbol{Q}_l\left(z_l\right) dz_l + \int_{-t_u/2}^{t_u/2} \left(\frac{d}{2}\right)^2 \boldsymbol{Q}_u\left(z_u\right) dz_u \tag{7.5}$$

Finally, recognizing the definition of the membrane stiffness matrices for each skin, $\boldsymbol{A}_u$ and $\boldsymbol{A}_l$, yields:

$$\boldsymbol{D}^{\text{eff}} = \left(\frac{d}{2}\right)^2 \left(\boldsymbol{A}_l + \boldsymbol{A}_u\right) \tag{7.6}$$

With this equation, $\boldsymbol{D}^{\text{eff}}$ can now be evaluated for each spanwise pair of skin panels. The components of $\boldsymbol{D}^{\text{eff}}$ can then be substituted into Equation (7.1). Upon closer examination, when these components are substituted, the effect of the wingbox depth, d, cancels out. This leads to the relationship below:

$$\psi_1 = \frac{A_{l_{16}} + A_{u_{16}}}{\sqrt{\left(A_{l_{11}} + A_{u_{11}}\right)\left(A_{l_{66}} + A_{u_{66}}\right)}} \tag{7.7}$$

This means that ψ_1 ultimately only depends on the components of the membrane stiffness of each skin panel, $\boldsymbol{A}_u$ and $\boldsymbol{A}_l$. Because in this study the panel thickness and ply orientation vary within the panel, and thus so do $\boldsymbol{A}_u$ and $\boldsymbol{A}_l$, the membrane stiffness for each panel is approximated by averaging the values in each panel. Computing the cou-
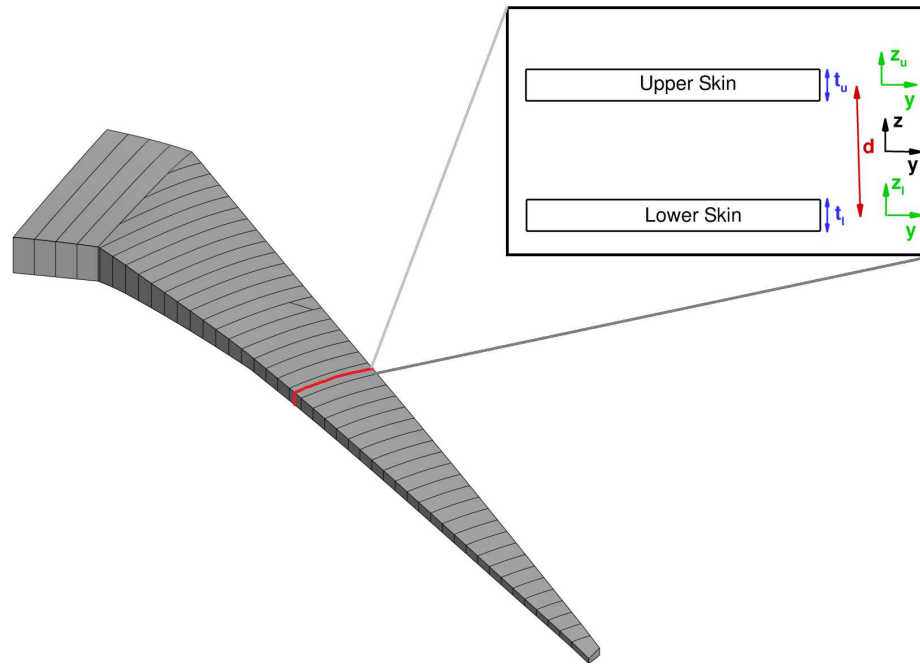
Figure 7.2: Cross-sectional view of typical wingbox skin panels

pling parameter at each spanwise wingbox section will allow us to identify regions of the wingbox design for which the optimizer is taking advantage of the additional aeroelastic tailoring offered by anisotropic wing designs.

7.3 Results

In this section, the results for all of the optimizations will be presented. First, the benefits of tow-steering for a typical wide-body transport aircraft will be presented by performing a series of tow-steered and conventional composite design optimizations on the uCRM-9. Next, the effect that tow-steering has on high-aspect-ratio wing design will be explored by performing conventional and tow-steered composite design optimization on the uCRM-13.5. Finally, the effect of aspect ratio on the design's performance will be extended by comparing a series of tow-steered and conventional composite design optimizations with varying wing aspect ratios.

7.3.1 uCRM-9 optimization

Here, we will analyze the results of the first four optimization cases based on the uCRM-9 model. The results will be presented in this order: First, we will compare the performance
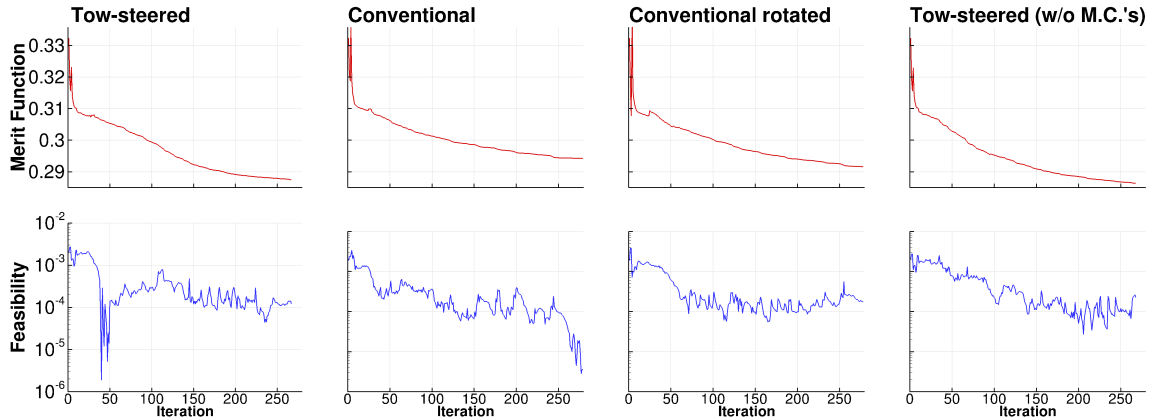
Figure 7.3: Optimization convergence histories for each uCRM-9 case

of the tow-steered and conventional composite designs. Next, we will quantify how much of these benefits can be recovered on the conventional design by giving the optimizer the freedom to rotate the orientation of the plies of each skin. Finally, we will assess the effect of the tow-steering manufacturing constraints by removing them, re-optimizing the design, and comparing the performance to original constrained design.

The convergence history for each uCRM-9 optimized case is shown in Figure 3.17. Each optimization is run for a total of 48 hours with a total of 300 processors (roughly 100 per flight condition). From these optimization histories, we can see that the designs converge gradually before hitting their respective exit conditions. This gradual convergence is likely due to the highly coupled nature of the aerodynamic and structural disciplines featured in these problems.

7.3.1.1 Conventional versus tow-steered composite

The resulting designs from the conventional and tow-steered composite optimizations are summarized in Figure 7.4. This compares the aerodynamic and structural performance of the tow-steered (left) and conventional (right) composite wing designs. In the upper left corner of this figure, is a top view of the aerodynamic pressure distribution on the wing at cruise as well as several key performance metrics for both designs. Just below this is a front view of the aircraft, showing the relative deflection of the wing at each flight condition. On the bottom left corner, the structural information about the wingbox designs are shown. This includes a plot showing the panel thickness distribution for each design and the tow paths for the main tow patterns for each skin. In addition, this structural information includes contours for the failure and buckling constraints on the wing skins for the 2.5 g and -1 g maneuver conditions. On the right side of the figure, are various

120

spanwise metrics measuring the passive load alleviation and bend-twist coupling of each design. Starting from the top, we have the normalized lift distribution for the cruise and 2.5 g flight conditions, which represents the distributed lift per unit span over either aircraft. Below this, is the aeroelastic spanwise twist distribution for both wing designs. Finally, in the bottom right is a plot of the spanwise non-dimensional bend-twist coupling parameter, ψ_1, introduced in Section 7.2.

From Figure 7.4, we can see that there is a 2.3% and 2.5% improvement in the fuel burn and takeoff gross weight, respectively, of the tow-steered relative to the conventional composite winged aircraft. The optimizer can accomplish this through a significant reduction in structural weight (24%) for almost no aerodynamic penalty, as seen in the L/D performance of both designs (approximately 0.1% difference). To see how this was achieved, we can examine the normalized lift distributions for each design. What we find from this is that both designs achieve a relatively elliptical lift distribution at cruise, which minimizes the induced drag of the aircraft and improves the L/D. Where the two designs differ, is in the passive load alleviation for the maneuver flight conditions. For these conditions, the tow-steered wing is able to shift more of the lift distribution inboard at the 2.5 g maneuver condition. This means that the tow-steered design can more effectively reduce the bending moment in the wing for this condition. This allows the optimizer to reduce some of the weight in the wingbox, most noticeably at the root and Yehudi break. The additional load alleviation contributes only in part to the lower structural weight seen on the tow-steered design. As will be seen in the following section, the second component is owed to the local tailoring of the load paths in the structure.

The cause of this additional load alleviation can be explained by examining the spanwise twist distribution of both wings. What we find is that the twist distribution for both designs are nearly identical for the cruise condition. Again, this is due to the fact that both designs desire an elliptical lift distribution for this case. Where the two designs differ is in the fact that there is more spread in the aeroelastic twist deformation about the cruise condition for the tow-steered design. This allows the tow-steered structure to aeroelastically twist the wing tips down even further on the maneuver condition and leads to the additional passive load alleviation benefit seen in the lift distribution. The tow-steered design features 2.1° more washout at the wing tip for the 2.5 g maneuver than the conventional composite design.
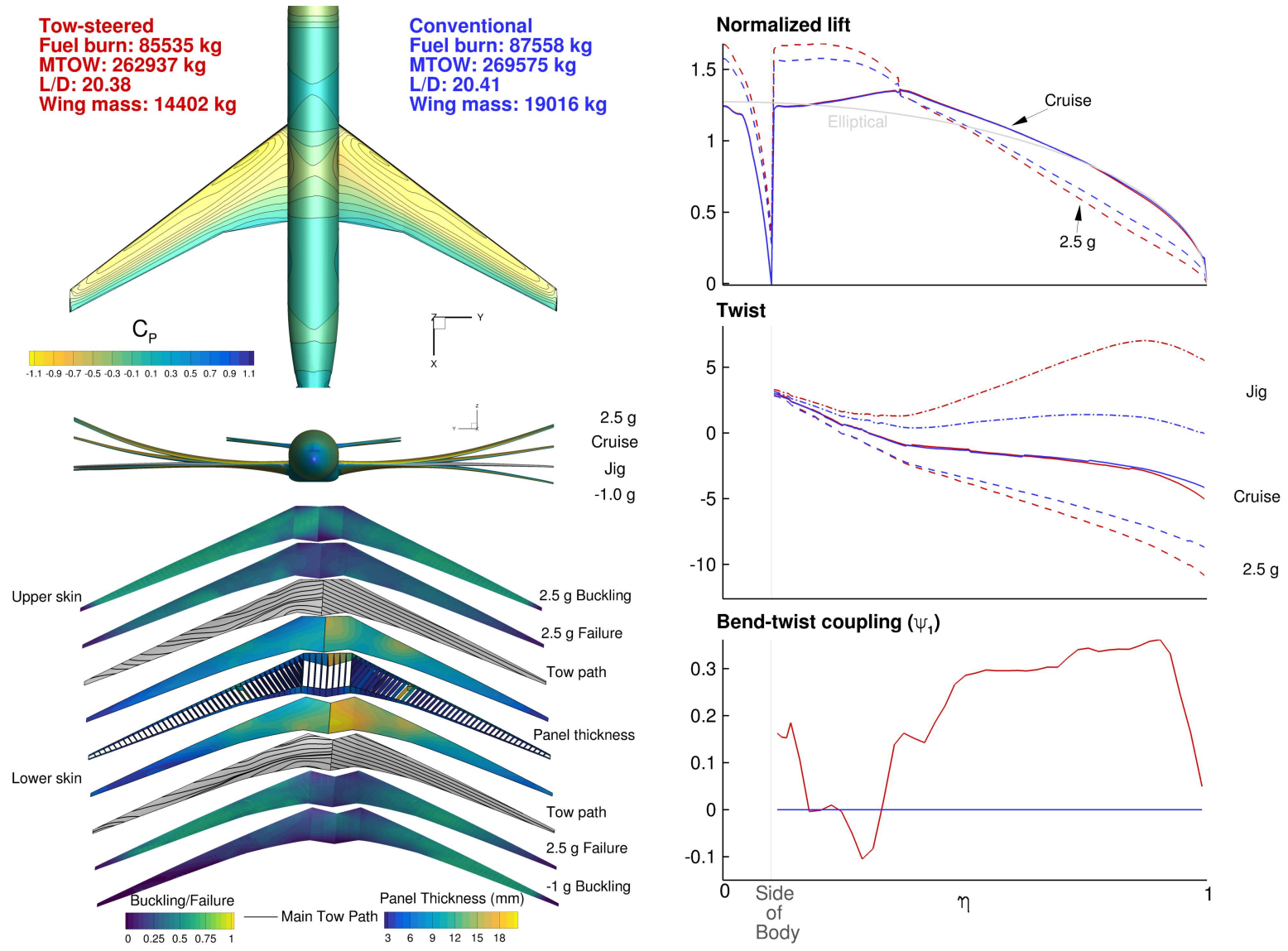
Figure 7.4: Comparison of optimal tow-steered (left) vs. conventional (right) composites aerostructural results for uCRM-9

Examining the spanwise bend-twist coupling due to material, we see that, in general, the coupling increases along the span before hitting a maximum value and dropping off rapidly toward the tip. The reason for this sudden decrease in use of coupling near the tips is that as we approach the wing tips of the design, while the aeroelastic deflections increase, there is also less remaining region of the wing span left to tailor. These two factors counteract each other and lead to a peak in the effectiveness of the coupling occurring slightly before the tip of the wing. Near the fuselage junction of the wing the coupling initially drops, even becoming negative. This is because the small degree of deformation leaves little ability to tailor the structure aeroelastically in this region. This suggest that the optimizer is focusing more on tailoring the strength of the structure in this region. From the twist distribution, we can also see that the optimizer twists the wing jig shape even further up on the tow-steered design. This is because as the bend-twist coupling of the tow-steered design is increased, the wing tips of the cruise and maneuver condition will aeroelastically twist further down. In general, the change in aeroelastic twist on the 2.5 g maneuver due to this increase in coupling will be larger than that seen on the cruise shape. The optimizer, therefore, needs to increase the jig twist on the wing to keep the normalized lift distribution for the cruise case elliptical.

The source of this additional bend-twist coupling can be found by analyzing the main tow paths for the tow-steered wing. If we compare the tow paths for the structurally-optimized tow-steered wing from Chapter 6 with those from the aerostructurally-optimized design from Figure 7.4, new insight can be gained. Figure 7.5 provides an appropriate means of comparing the two. By comparing these two tow-steered designs we find that the most noticeable difference is that the aerostructurally optimized design sweeps the tow paths forward toward the tip of the wing. The use of swept-forward plies in this region leads to the increase in bend-twist coupling at the tip of aerostructurally-optimized tow-steered design in Figure 7.4. The reason why the structurally optimized tow-steered structure does not take advantage of this benefit is because the aerodynamic loads were fixed throughout its optimization. This means that for the structurally-optimized design, the optimizer sees no coupling between the external aerodynamic loads and structural deformation, and hence there is no possibility for aeroelastic tailoring. This leads to the conclusion that the tow paths in this region of the aerostructurally-optimized tow-steered structure are purely for the purpose of global load manipulation through aeroelastic tailoring. In contrast, if we look at the root of the structure of both designs in Figure 7.5, the tow paths match very well. This implies that the benefit of the steering in this region is purely structural and due to local tailoring of the load paths and structural strength.

Looking at the structural performance of both wingboxes in Figure 7.4 gives additional
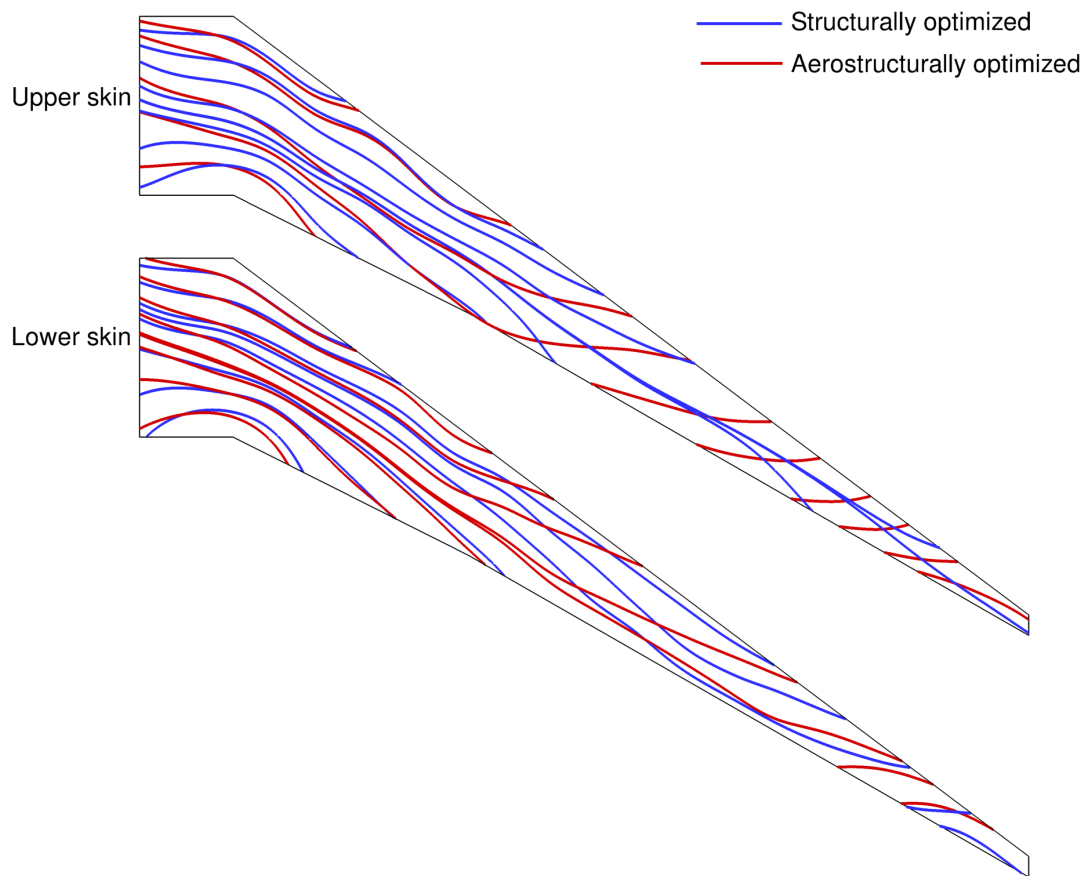
Figure 7.5: Comparison of structurally (blue) vs. aerostructurally (red) optimized tow paths for tow-steered wing skins

information about the structural sizing for the maneuver cases. For the 2.5 g maneuver, we can see that due to the upper skins being in compression, they are almost entirely sized by the buckling constraint for both designs. For this flight condition, the failure constraint is also actively sizing most of the lower skins for both designs. Despite the fact that the region for both design where these constraints are active is largely the same, the tow-steered structure is noticeably thinner near the root and Yehudi break on both the skins and spars. This difference accounts for the reduction in structural weight mentioned earlier. Again, this reduction is due to a combination of improvements in both global aeroelastic tailoring and local structural tailoring seen on the maneuver flight conditions.

7.3.1.2 Conventional rotated versus tow-steered composite

Next, we relax the restriction on the conventional composite design by allowing the optimizer to rotate the wing skin plies. This is accomplished by giving the optimizer a single rotation design variable for each skin. These design variables control the orientation of the tow path for each skin by rigidly rotating all the plies in the layup. This gives the optimizer the freedom to control the bend-twist coupling of the conventional wing and thus gives it the ability to aeroelastically tailor the design. Once these design variables were added, the conventional optimization was re-run and the results compared to the tow-steered design (see Figure 7.6).

From Figure 7.6, it can be seen that by rotating the skin plies of the conventional composite design, the optimizer has cut the improvement margin in fuel burn and maximum takeoff weight to 1.4% and 1.5% , respectively, relative to the previous case. In addition, the structural weight improvement is now only 15.7%. By looking at the lift and twist distributions, it is clear that the optimizer was able to reduce this margin by increasing the load alleviation of the conventional design. In fact, the load alleviation performance for the 2.5 g maneuver is nearly identical between the two designs now. This means that any remaining benefit coming from the tow-steered design must be accounted for entirely by the local structural tailoring capability of the design. Using this information and the results from the previous case, it is possible to conclude that the benefit in fuel burn performance due to aeroelastic tailoring of the tow-steered design, when compared to the conventional design from the previous case, makes up roughly 0.9% of the previous 2.3% total. This means that the remaining 1.4% is due to local structural tailoring. Looking back at the tow paths of the conventional rotated design in Figure 7.6, we see that the additional improvement in load alleviation is made possible by rotating the plies forward relative to the leading-edge spar of the wing, increasing the bend-twist coupling of the structure.

By examining the lift distribution on the 2.5 g maneuver of the conventional rotated

design in Figure 7.6, a small dip in the lift distribution can be seen at roughly the 40% span location (indicated on plot). To explore the cause of this phenomenon in more detail, we can plot aerodynamic streamlines of the flow on the upper surface of the wing in this region. Plotting this and the contour of the separation sensor introduced in Chapter 3, Figure 7.7, reveals that the dip in the lift distribution in this region is due to small region of separated flow on the upper wing surface. Comparing the airflow in this region for the conventional and tow-steered composite designs, shows that this separated flow region is small for the conventional design, but grows larger for the tow-steered and conventional rotated designs. This is because as load alleviation is added into the design, the lift on the inboard of the wing must increase to offset the loss of lift at the tips. This increase in lift causes the airflow over the inboard of the wing to separate. This puts a potential upper limit on the maximum amount of load alleviation achievable by an aeroelastically tailored design. Because lower-fidelity aerodynamic models, such as panel methods and Euler-based CFD, do not possess the physics required to properly model separation, this highlights a benefit of using high-fidelity analysis in design optimization.
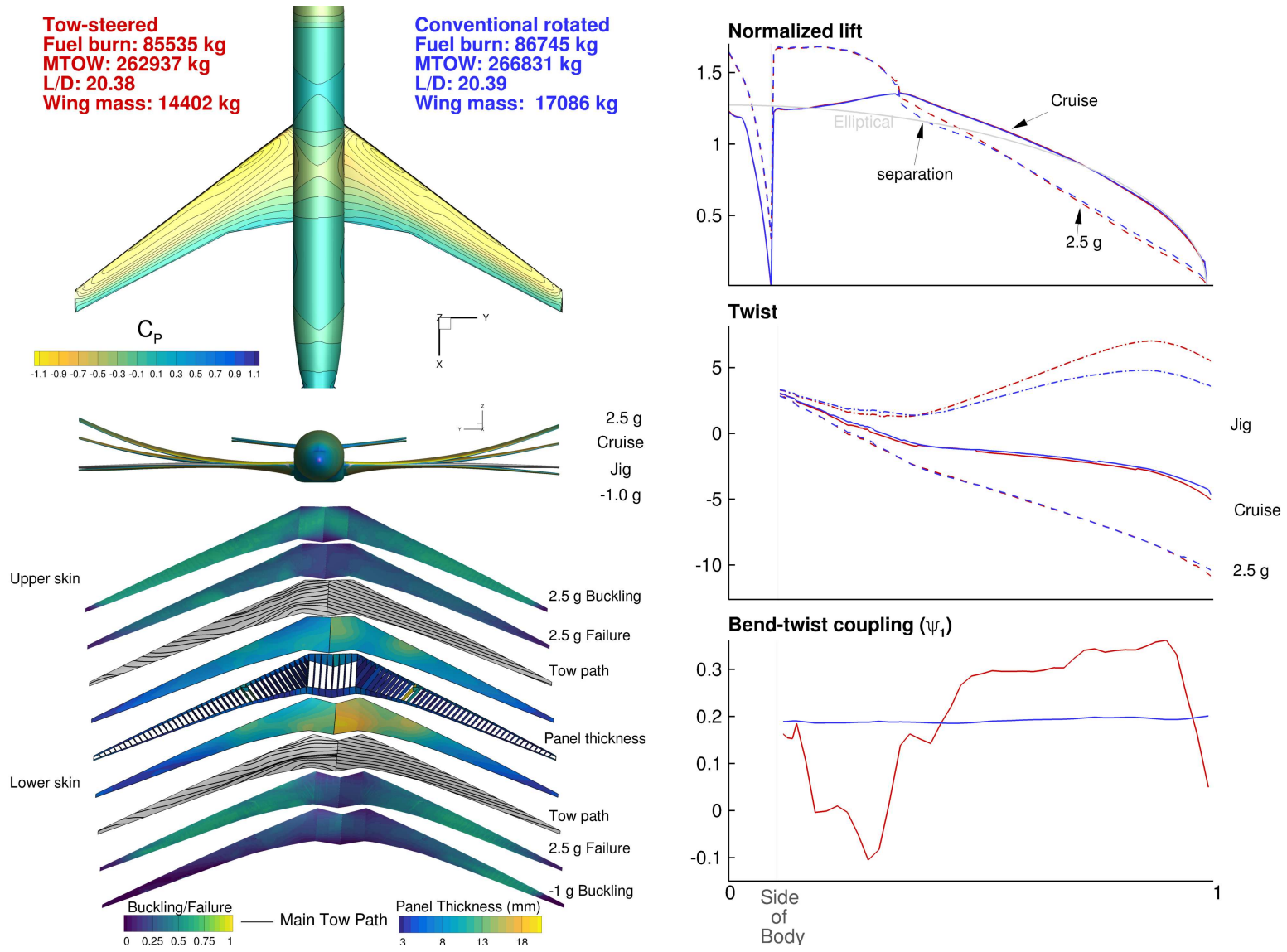
Figure 7.6: Comparison of optimal tow-steered (left) vs. conventional rotated (right) composite aerostructural results for uCRM-9
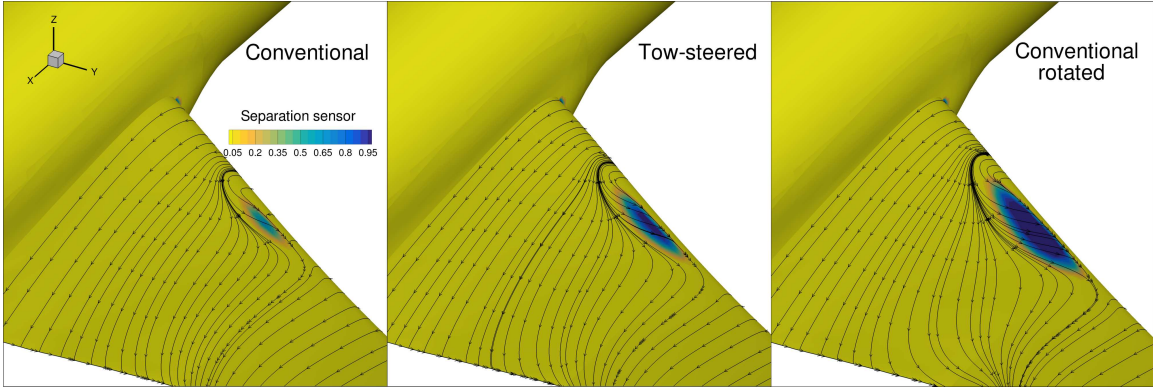
Figure 7.7: Separation sensor contour and airflow streamlines show region of separated flow on the 2.5 g for the tow-steered and conventional rotated composite designs.

7.3.1.3 The effect of manufacturing constraints

Next, the effect of the manufacturing constraints on the tow-steered designs' performance will be investigated. To do this, we drop the minimum curvature and tow cut/add length constraints from the tow-steered optimization problem. The optimization is then re-run and the results compared to the tow-steered optimized design with manufacturing constraints used in the previous two cases. Figure 7.9 compares the designs for these two cases.

From Figure 7.9, we see that removing the AFP manufacturing constraints from the design problem leads to an additional improvement of 0.4% in fuel burn and 0.4% in MTOW. Similarly, the structural weight is reduced by an additional 4.5%. By looking at the lift, twist, and bend-twist coupling distribution it can be seen that both designs feature the same load alleviation performance. From this, we can conclude that the manufacturing constraints do not hinder the ability of the tow-steered design to aeroelastically tailor the structure. This means that the benefits in performance from removing the manufacturing constraints from the design must be purely due to local structural tailoring.

To show the severity of the AFP manufacturing constraints for the tow-steered wingboxes, we plot the tow-path divergence contours for each pattern in Figure 7.8. For conciseness, we only plot the tow-path divergence. However, the tow-path curvature can be found by using the curvature-divergence relationship for offset patterns—see Equations (5.22) and (5.23). As expected, by removing the tow-path curvature and divergence constraints from the design optimization, the optimizer converged to tow paths with much higher values for these quantities. In particular, we can see that the most severe tow-path curvature and divergence occurs near the root of the wingbox, with a small amount near the tip. This agrees well with the conclusion that the manufacturing constraints largely effect only regions of local structural tailoring. From this figure, we also see that the locations and

Tow-steered   Upper skin   **Tow-steered (without man. constraints)**

Pattern 4 $(\theta_0 + 90^\circ)$

Pattern 3 $(\theta_0 - 45^\circ)$

Pattern 2 $(\theta_0 + 45^\circ)$

Pattern 1 (θ_0)

Lower skin

Pattern 1 (θ_0)

Pattern 2 $(\theta_0 + 45^\circ)$

Pattern 2 $(\theta_0 - 45^\circ)$

Tow-path divergence (m^{-1})

Pattern 4 $(\theta_0 + 90^\circ)$

0.2 0.6 1 1.4 1.8 2.2 2.6 3
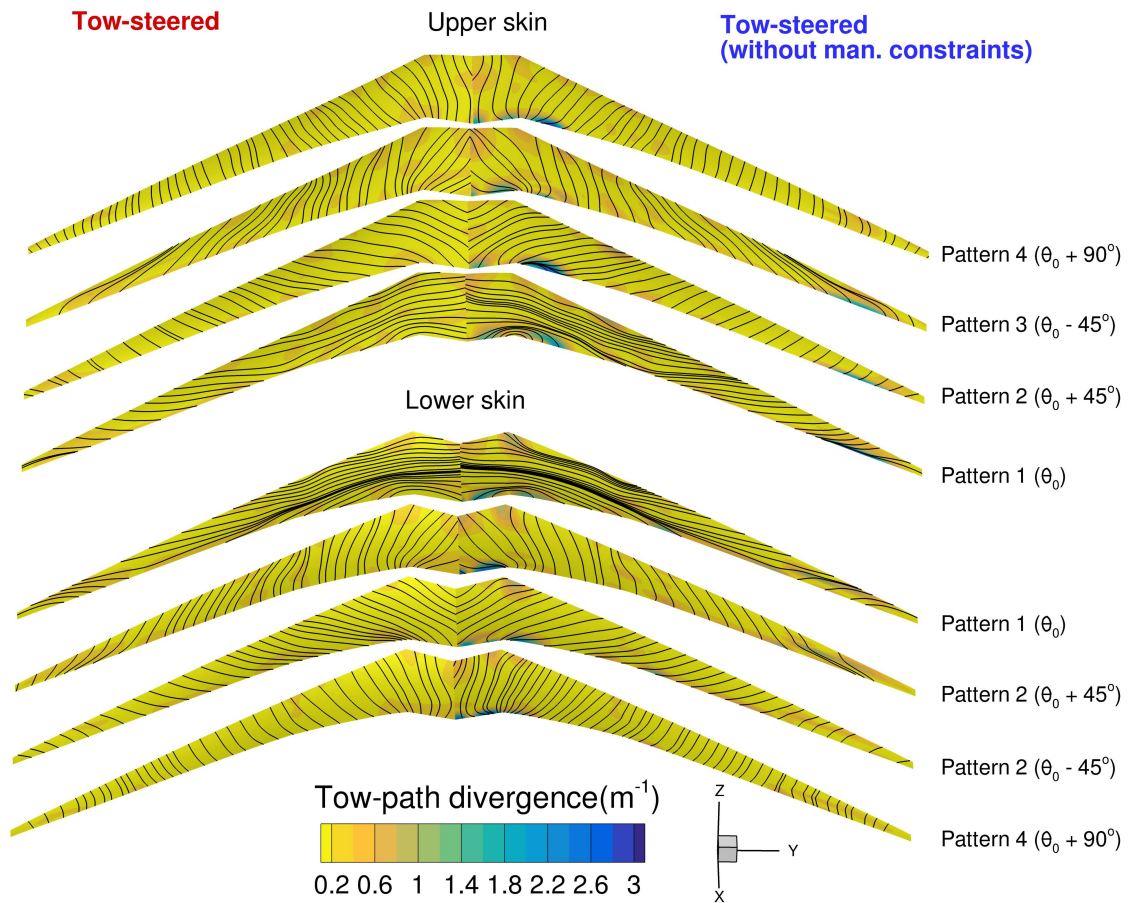
Figure 7.8: Comparison of tow-path divergence contours for aerostructurally optimized tow-steered design with (left) and without (right) manufacturing constraints.

magnitudes of these constraint values differ slightly from pattern to pattern. This highlights the importance of considering the manufacturing constraints for all patterns in the layup, not just the main tow pattern.
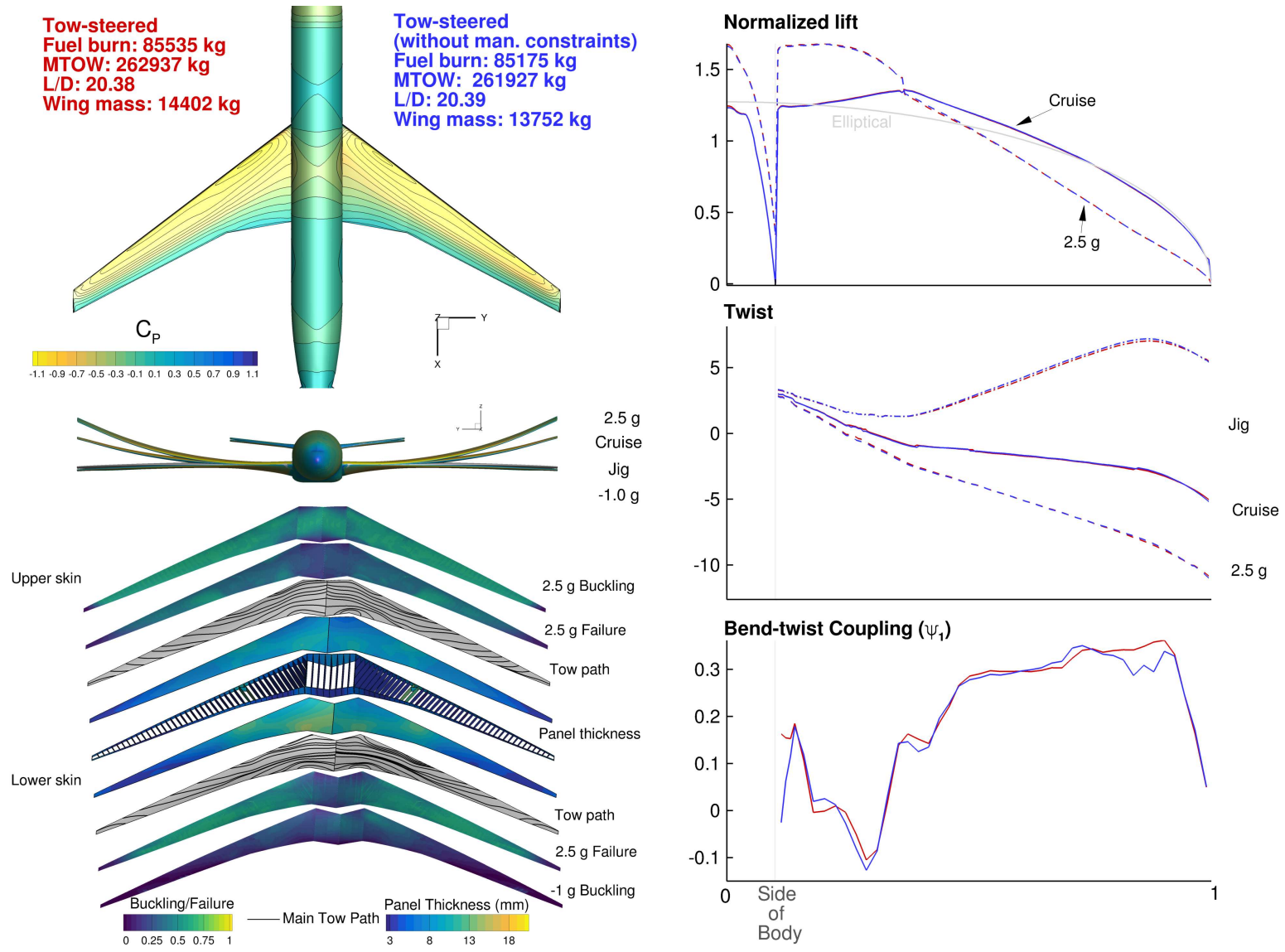
Figure 7.9: Comparison of optimal tow-steered designs with (left) and without (right) manufacturing constraints

7.3.2 uCRM-13.5 optimization

Now, optimization results for the higher aspect ratio uCRM-13.5 model will be presented. For this case, two additional aerostructural optimizations are run: one with a tow-steered wing design (with manufacturing constraints), and one with a conventional composite design (fixed skin ply orientation). The results are then plotted and compared in Figure 7.10.

First, comparing the performance of the uCRM-9 designs in Figure 7.6 with those of the uCRM-13.5 in Figure 7.10, reveals similar trends to that seen in the comparison of the aluminum designs in Chapter 3. Specifically, we see the fuel burn on both high aspect ratio designs have decreased relative to their uCRM-9 counterparts. Comparing the L/D of each design, we see that this is due to the reduction in induced drag owed to the designs' larger span. In addition, due to the longer moment arm on the wing structure, the structural weight increases for the uCRM-13.5 designs. From Figure 7.10, we see that adding tow-steering to the high aspect ratio design improves the fuel burn performance by 1.5% and MTOW by 1.5% relative to the conventional design. This benefit comes from the 14% reduction in weight seen on the tow-steered design.

By looking at the lift and twist distribution, we see that, unlike for the uCRM-9 case, the optimizer is not able to add any additional load alleviation to the tow-steered design. This means that the performance improvements seen on this design are almost entirely accounted for through local structural tailoring. Upon closer examination of the two high-aspect-ratio designs in Figure 7.10, we see that while the spanwise twist distributions are nearly identical for the cruise and maneuver conditions, the initial jig twist of the tow-steered design is noticeably higher. This would suggest that the bend-twist coupling of the tow-steered wing as measured from the jig (unloaded) to cruise wing shape is different than that measured from the cruise to 2.5 g maneuver shape. This same asymmetry in twist distribution can be seen in the comparison of the tow-steered and conventional uCRM-9 designs in Figure 7.6. This suggests that something is reducing the amount of bend-twist coupling seen on the 2.5 g maneuver condition compared to what otherwise should be expected. This is an inherently nonlinear behavior, and because the structural model used in this work is linear, the cause must be either from the aerodynamics or aeroelastic coupling.

By plotting the airflow on the upper surface of the wing for the 2.5 g maneuver, we find that, unlike for the uCRM-9 cases in Figure 7.7, the additional load alleviation is not being prevented by separated flow at the root of the wing. This suggests that the cause is not aerodynamic.
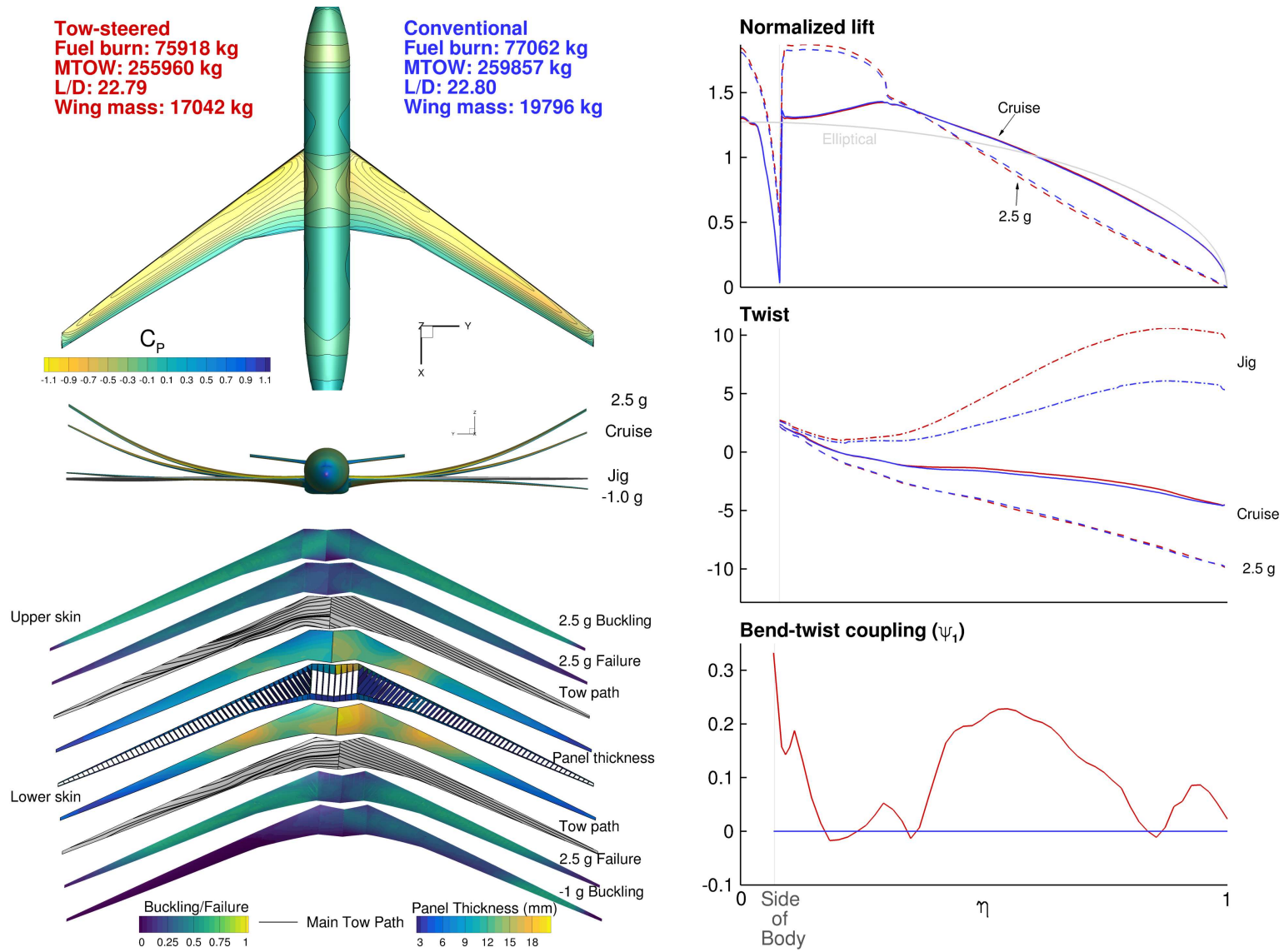
Figure 7.10: Comparison of optimal tow-steered (left) vs. conventional (right) composite aerostructural results for uCRM-13.5
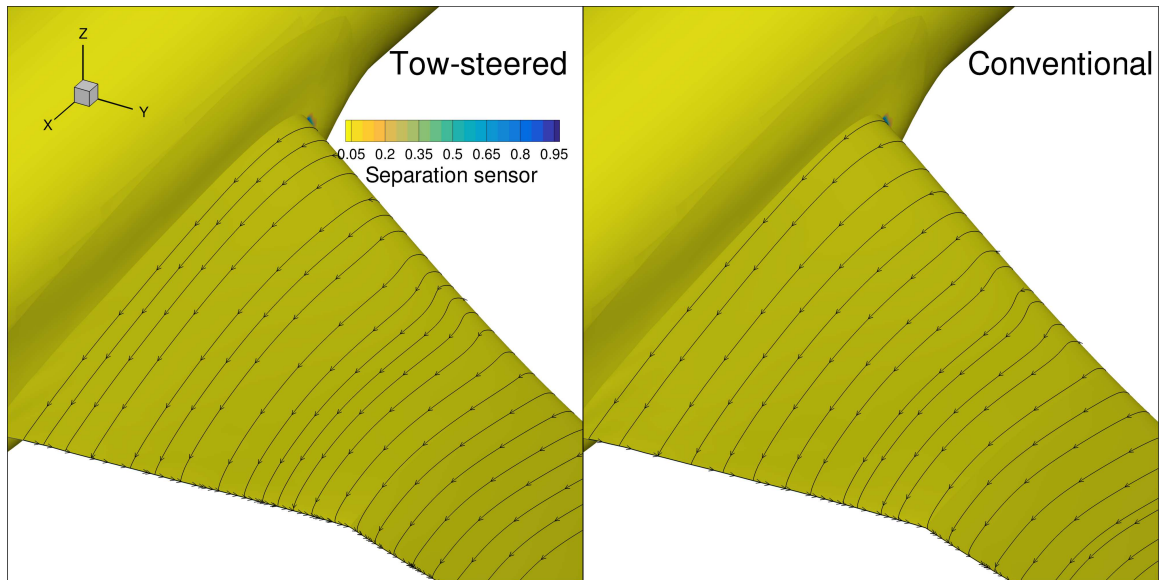
Figure 7.11: Separation sensor contour and airflow streamlines show now separated flow on uCRM-13.5 designs for 2.5 g maneuver.

7.3.2.1 Twist effectiveness

If the cause of the lack of additional load alleviation in the tow-steered uCRM-13.5 model is not aerodynamic, then the only remaining possible explanation is aeroelastic coupling. From aeroelastic theory, it is well known that as wings become more flexible, the effectiveness of the control surfaces—ailerons—used to maneuver the aircraft is reduced. This is because when the aileron is deflected downward, for example, while the local lift in this section of the wing increases, so too does the torsional load on the wingbox. This increase in torsional load leads to an aeroelastic twisting of the wing, in this case nose-down twist, which counteracts the desired effect of the aileron. For this reason aeroelasticians typically define the control effectiveness as the ratio of the response, increase in roll moment, of the elastic wing due to the deployment of the control surface, to the expected response for a rigid wing.

The FFD twist parametrization used throughout this work can be thought of as behaving in an analogous fashion to a control surface. For instance, as we twist the jig of the wing down at the wing tip using the FFD, the flying shape of the wing will similarly experience an decrease in twist at its tip. In response, the aeroelastic twist of the inboard of the wing will increase. This response counteracts some of the reduction in inboard bending moment expected from twisting the tip down with the FFD variable and leads to a loss in sensitivity of the bending moment with respect to wing twist. This effect is illustrated in Figure 7.12. In this figure, the wing jig shape of the design is twisted down near the tip by twisting one
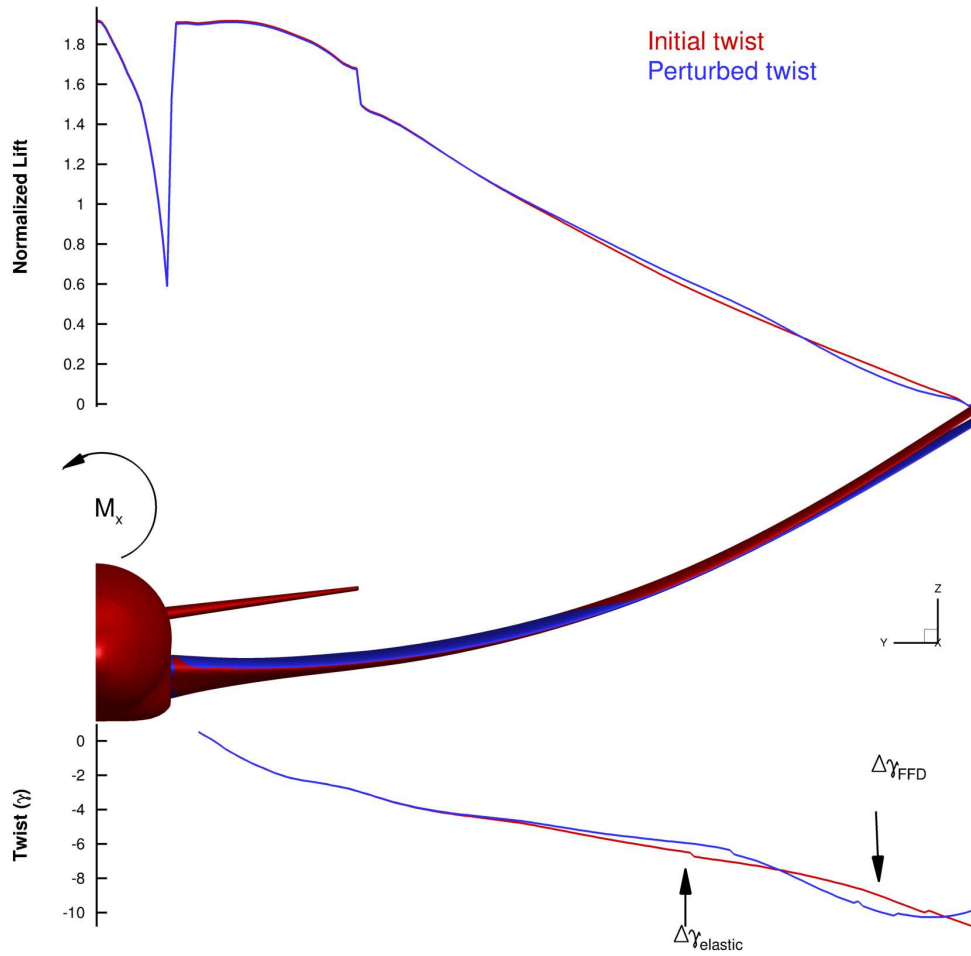
Figure 7.12: Example of loss in FFD twist sensitivity of bending moment due to aeroelastic deformation.

of the spanwise FFD segments (shown in Figure 7.13) down. While this results in a net twisting down in this location of the wing on the 2.5 g wing shape, it is counteracted by a corresponding aeroelastic upward twist deformation further inboard. This effect leads to a decrease in the sensitivity of twist in this location for the maneuver condition.

To this end, similarly to what is done for a control surface, we can define the effectiveness of each span-wise FFD twist variable, γ_i, as:

$$\eta_\gamma = \frac{\left(\frac{dC_{M_x}}{d\gamma_i}\right)_e}{\left(\frac{dC_{M_x}}{d\gamma_i}\right)_r}, \tag{7.8}$$

where $\frac{dC_{M_x}}{d\gamma_i}$ is the derivative of total root bending moment of the aircraft with respect to
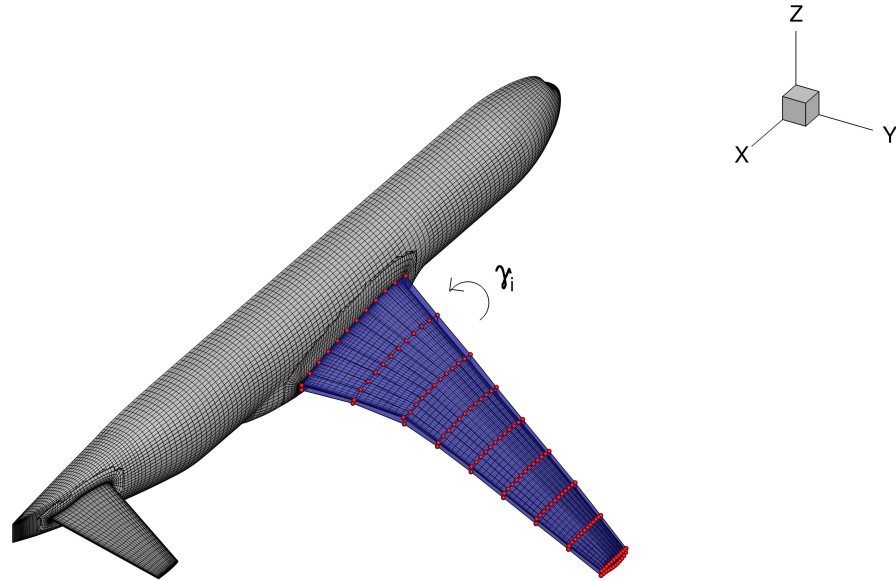
Figure 7.13: FFD twist variables used in the study.

each twist variable. The "e" subscript denotes the elastic or aerostructural derivative, while the the "r" subscript denotes the rigid or aerodynamic derivative. The elastic derivative can be computed by solving the coupled adjoint for the aerostructural problem. The rigid derivative can be computed by freezing the aeroelastic shape and solving only with the aerodynamic adjoint. This value gives a measurement of how much sensitivity is lost for each spanwise twist variable due to the effect of aeroelasticity or wing flexibility. If the aeroelastic effects are small this value should be close to unity.

The twist effectiveness for the 2.5 g maneuver condition of the conventional and tow-steered optimized designs on both the uCRM-9 and uCRM-13.5 are compared in Figure 7.14. As would be expected, near the root of the wing, where the aeroelastic effects are smallest, this value is closer to unity. As we move along the span of the wing toward the tip the effectiveness declines. It is interesting to note that for the most flexible cases this value actually becomes slightly negative, meaning that as these locations are geometrically twisted up the bending moment actually decreases due to the effect of the aeroelastic deflections inboard, a phenomena similar to control reversal.

Loss of control effectiveness is an aeroelastic phenomena typically seen in very flexible aircraft wings. This trend is typically exacerbated as the bend-twist coupling in the wing is increased, often by sweeping the wing further back. From Figure 7.14, we can see that for the uCRM-9 cases, as the optimizer increases the bend-twist coupling of the tow-steered

Figure 7.14: Comparison of twist effectiveness for root bending moment 2.5 g maneuver.

design, the bending moment becomes less sensitive to the wing twist, especially near the tips, where the optimizer increases the coupling the most. This loss of sensitivity at the tips may prevent the optimizer from utilizing even more coupling, ultimately limiting the amount of additional load alleviation available. It can also be seen that the uCRM-13.5 designs have a lower effectiveness than the uCRM-9 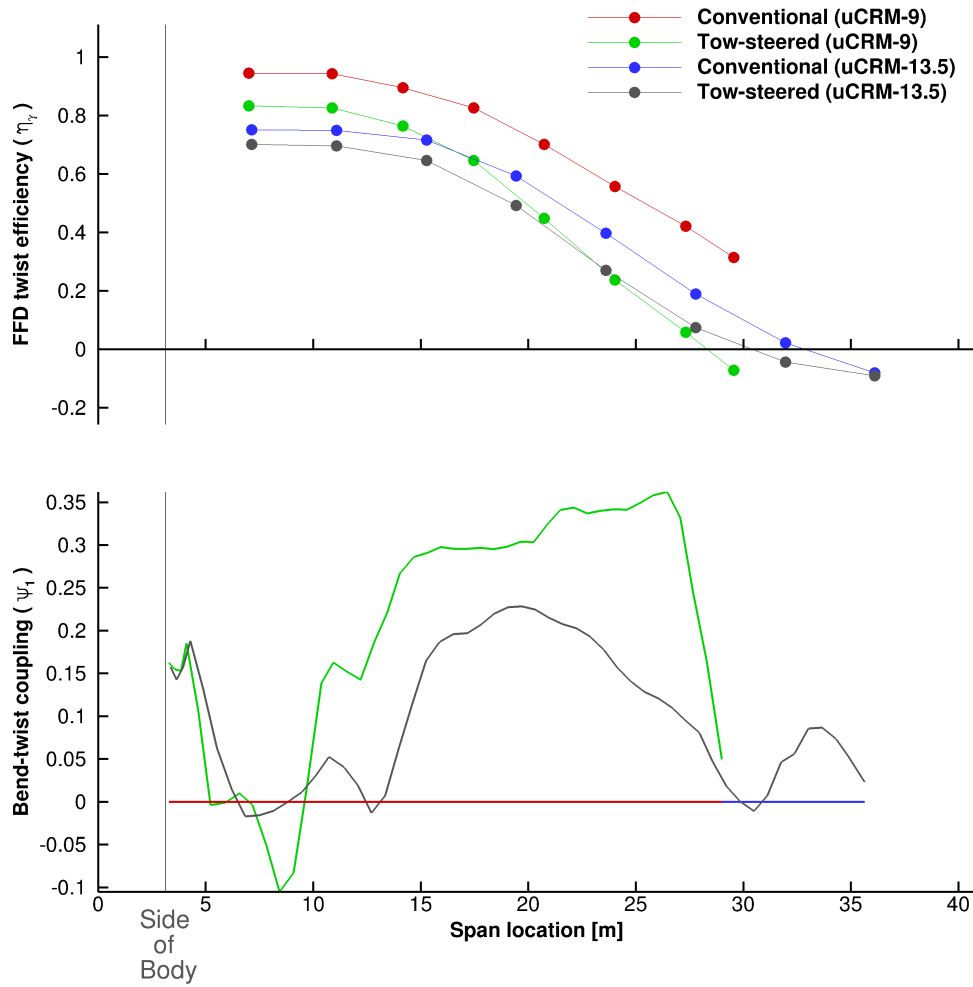designs, due to the increase in wing flexibility. Because the unsteered uCRM-13.5 design already starts with low sensitivity near the tip of the wing, the optimizer may not be able to add any further coupling in this region on the tow-steered design, preventing further load alleviation benefits.

7.3.3   The effect of varying aspect ratio

In the previous sections, we analyzed the aerostructural design benefits offered by adding tow-steering to a wing of aspect ratio 9 and 13.5. We now wish to extend this trend by performing a sweep of optimizations of tow-steered and conventional composite designs with varying wing aspect ratios. This is accomplished by taking the uCRM-9 design optimization problem and adding planform variables—span, sweep, and chord—to the FFD variables. The optimization for each design is then run with a series of different aspect ratio constraints (AR $= [7.5, 9, 10.5, 12, 13.5]$). The case for AR $= 9$ did not need to be run, as it was equivalent to the uCRM-9 tow-steered and conventional optimized cases presented earlier. The AR $= 13.5$ designs were not exactly equivalent to the uCRM-13.5 results presented earlier. The uCRM-9 and uCRM-13.5 designs feature different number of ribs, wing taper ratio, and fuselage positioning, none of which is varied during this aspect ratio study on the uCRM-9. Because of this, the resulting 13.5 aspect ratio version of the uCRM-9 ends up being slightly different. The wing planform for each aspect ratio design is shown in Figure 7.15.

The trend for fuel burn, MTOW, L/D, and wing structural mass for the optimal-fuel-burn designs as a function of aspect ratio is shown in Figure 7.16. From this, we can see that in general adding tow steering to the design provides benefit in fuel burn, MTOW, and wing mass for all aspect ratio designs. Similarly to the previous cases, L/D is largely unaffected by the use of tow-steering. This figure shows that as the aspect ratio is increased the fuel burn decreases. However, we find toward the higher aspect ratios the benefit in fuel burn begins to decrease. By analyzing the trend in L/D, we can conclude that this is because as the aspect ratio increases the amount of induced drag on the design left to be reduced becomes smaller, while the viscous and compressibility drag begin to dominate. Next, analyzing the trend in MTOW, we see that as the aspect ratio increases, the MTOW decreases, with exception of the last design (AR $= 13.5$). By comparing the trends in fuel
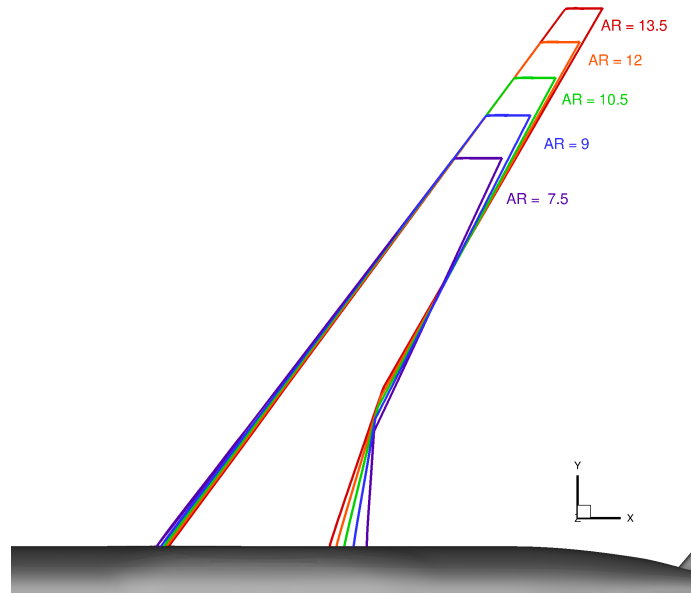
Figure 7.15: uCRM planforms for variable aspect ratio study

burn and wing mass, we find that this increase in MTOW is due to the fact that as the aspect ratio increases the improvements in fuel burn begin to taper off, while the rate of increase in wing mass continues to increase. This causes the increase in wing structural mass to eventually outpace the decrease in fuel burn, which leads to an increase in MTOW.

The trend for passive load alleviation of each design can be seen in Figure 7.17. All designs feature a roughly elliptical lift distribution with some load alleviation on the maneuver. Another prominent dip in the 2.5 g lift distribution of the tow-steered AR = 7.5 case can be seen, indicating flow separation. This indicates that lower aspect ratio designs are more likely to be susceptible to this type of flow separation. The reason for this is likely because, according to Figure 7.16, these designs have higher maximum takeoff weights, meaning that the designs will have to meet higher lift requirements for their maneuver conditions. We also see that as the aspect ratio increases, the amount of bend-twist coupling utilized on the tow-steered design by the optimizer, particularly near the tip, decreases. This confirms the trend seen earlier in Section 7.3.2, that is as the aspect ratio of the wing is increased the amount of additional load alleviation used by the tow-steered design decreases.
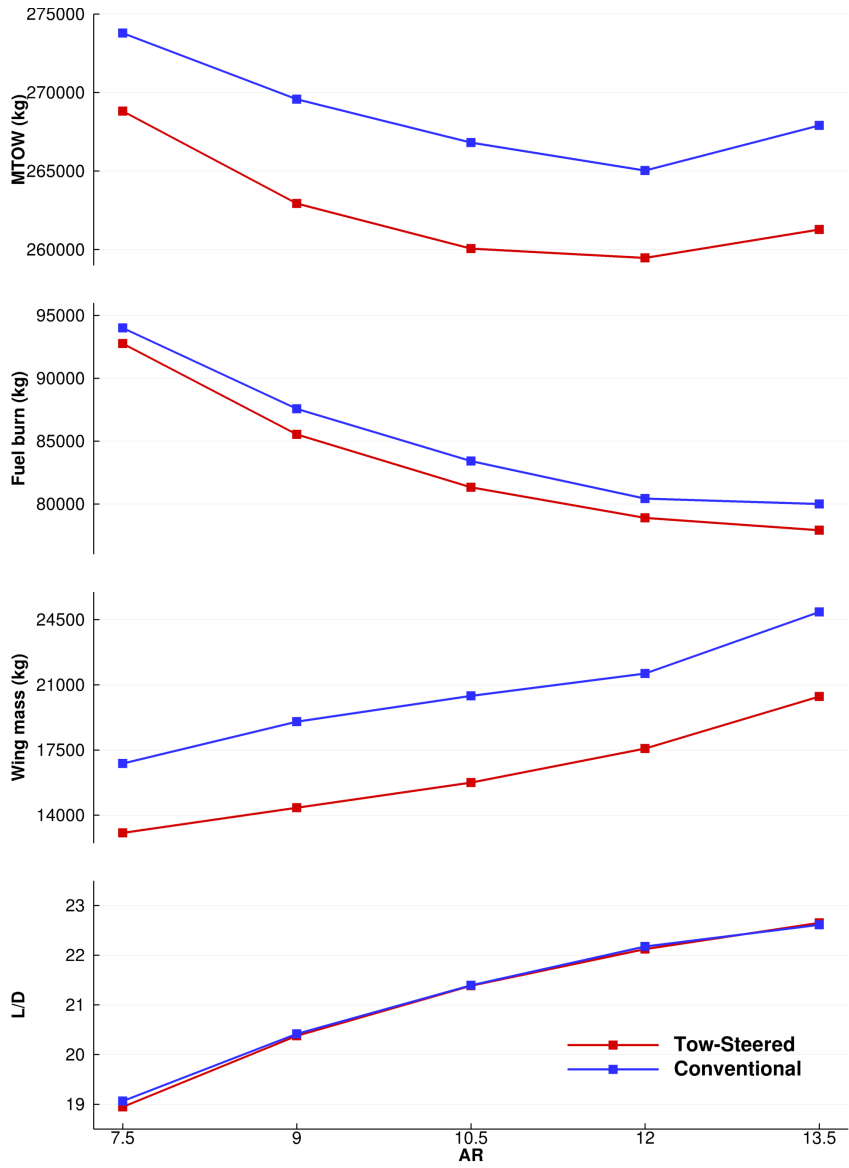
Figure 7.16: Fuel burn, MTOW, L/D, and wing mass trend for increasing aspect ratio
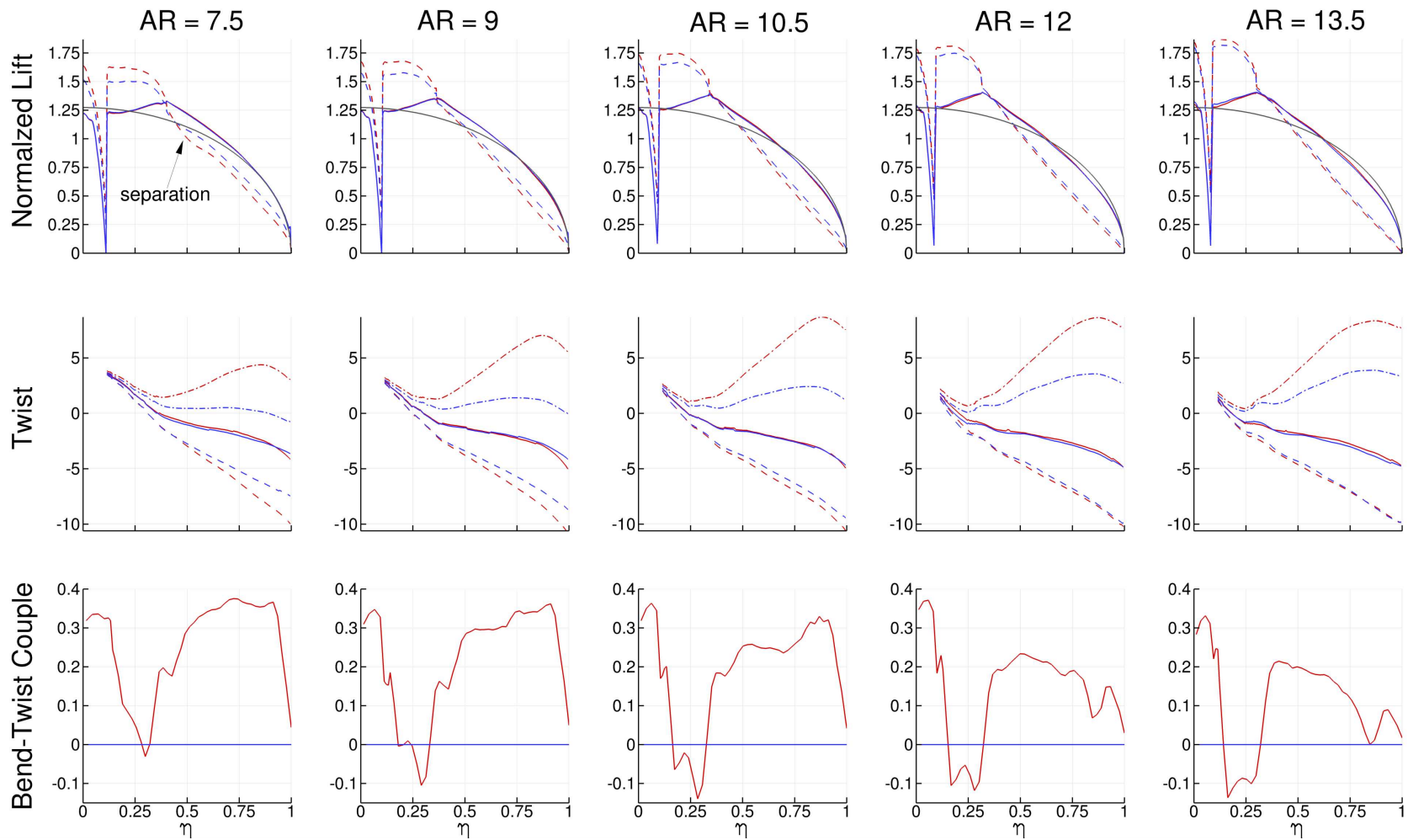
Figure 7.17: Passive load alleviation trend for increasing aspect ratio

7.4 Summary

In this chapter, the aeroelastic benefits of tow-steering as applied to flexible wing design have been investigated. To accomplish this, a series of high-fidelity gradient-based aerostructural fuel burn optimizations are performed on both tow-steered and conventional composite wing designs for both the uCRM-9 and uCRM-13.5 designs. The optimization problem included both geometric variables (shape and twist) as well as structural variables (panel thickness, tow path, etc.). Comparing the results of each design optimization provides insight into the benefits that tow-steering manufacturing has to offer for flexible-wing design.

The first set of insights come from the results run on the uCRM-9 model. These results are summarized in Table 7.4. From these results, we found that the aircraft fuel burn and MTOW could be reduced by 2.3% and 2.5%, respectively, relative to a conventional composite design. This improvement was due to a 24% reduction in structural weight of the tow-steered design, owed to improvements in the design's structural and aeroelastic tailoring. When the conventional composite design is allowed to rotate the plies in the skins, the improvements in fuel burn and MTOW offered by tow steering drop to 1.4% and 1.5%, respectively, while the structural weight benefit falls to 15.7%. This is because the optimizer is largely able to match the load alleviation performance of the tow-steered design with the conventional design. From this, it was possible to gleam that roughly 0.9% of the 2.3% decrease in fuel burn seen in the comparison between the tow-steered and conventional design's performance was owed to the additional load alleviation, while the remaining amount came from structural tailoring. Finally, the tow-steered design was re-optimized without a minimum tow-path curvature and cut/add length manufacturing constraint. Removing these constraints led to minor improvements in design performance. The constraints were found to only affect the structural tailoring performance of the design.

Table 7.4: Summary of results from uCRM-9 aerostructural optimization studies

Quantity	TS	C	CR	TS-NM
Fuel Burn [kg]	85 535	87 558	86 745	85 175
MTOW [kg]	262 937	269 575	266 831	261 927
Wing mass [kg]	14 402	19 016	17 086	13 752

On the uCRM-13.5 design, it was found that the tow-steered wing could reduce the structural weight of the wingbox by 14% and the fuel burn by 1.5%. This was made possible in large part by the increase in local structural tailoring of the wing design. When compared to the uCRM-9 design, the uCRM-13.5 tow-steered design featured nearly no

passive load alleviation improvement relative to the conventional composite design. This suggests that aspect ratio plays a role in the amount of optimal load alleviation available for the tow-steered design.

Finally, to generalize this trend, the uCRM-9 design was re-run with a sweep of different wing aspect ratios, varying from 7.5 to 13.5. From this, a diminishing return in fuel burn improvement was found for increasing wing aspect ratio. From this study, it was possible to conclude that the amount of additional load alleviation utilized by the tow-steered design relative to the conventional design decreased with increasing aspect ratio.

The results presented here show that tow-steered wing designs have the potential to decrease aircraft fuel burn and structural weight relative to conventional composite designs. Further insight into the design process might be revealed by allowing the optimizer the freedom to vary the planform—sweep, span, and chord—of the wings without restriction. This will allow the optimizer to find the optimal wing aspect ratio and planform to minimize fuel burn for both a tow-steered and conventional composite design. Another study of interest is evaluating the difference that changing the optimization objective would have on the design of both the tow-steered and conventional composite wing designs. This could be accomplished by producing a Pareto front between two objectives: one that focuses more on structural performance (e.g., structural weight) and another which focuses on aerodynamics (e.g., fuel burn). Finally, in this chapter, only three flight conditions—a cruise, a 2.5 g pull-up maneuver, and a -1 g push-over maneuver—were considered. This was done in order to simplify the problem and to allow us to more easily draw insights from the aerostructural performance of each design. Adding more flight conditions to the optimization problem will allow the optimizer to produce designs that are more robust. In particular, as was mentioned in Chapter 3, buffet-onset should be taken into consideration in order achieve feasible designs. These issues will be addressed in the following chapter.

CHAPTER 8

The trade-off between structural weight and fuel burn

In Chapter 7, the benefits of aerostructurally-optimized tow-steered winged designs for fuel burn performance was evaluated. However, fuel burn is not the only metric of aircraft performance. While fuel burn plays a big role in an aircraft's DOC, the aircraft's structural weight plays a role in the manufacturing cost, and thus acquisition cost. For this reason, aircraft manufacturers typically target an aircraft design with good fuel burn performance and low structural weight. The difficulty behind this is that these are conflicting objectives, which means that trade-offs between each objective inevitably have to be made in the design process.

The goal of this chapter is to better quantify the trade-offs between these two design objectives. To do this, an aerostructural Pareto front study will be performed. This study includes three different wing structural designs: aluminum, conventional, and tow-steered composite. Adding an aluminum wing design to the study in this chapter has the added benefit of giving context for the additional improvement in performance offered by adding tow-steering to composite wing design, compared to the improvement already offered by conventional composite relative to aluminum wing structures. The model used in this chapter is the uCRM-9, however the optimizer is given full freedom to vary the wing planform—aspect ratio, sweep, span, etc..

8.1 Problem formulation

In this section, the optimization problem is described by detailing the objective function, design variables, and constraints that are enforced. As mentioned previously, three designs are considered: a metallic aluminum, conventional composite, and tow-steered composite wing design. In order to isolate the benefits of each design specific to the performance of

the wing, only the structure for the wing is changed between the three designs, while the remaining aircraft structures and weights are assumed to remain the same (see Table 3.7 for corresponding weights). The skin main tow paths of the conventional composite design are again fixed to be parallel to the leading edge of the wing.

Each optimization requires six aerostructural analyses: a cruise condition for evaluating the fuel burn performance, two conditions for which buffet onset is constrained, and three conditions for which the structural sizing constraints are enforced. The fuel weight used to analyze the cruise condition was based on 20% of the total fuel capacity for the mission. This weight was chosen because it corresponds roughly to the lift generated by the CRM at its nominal flight condition [21]. As was the case in Chapter 3, the two buffet conditions are chosen to constrain buffet onset at two points: a high lift condition, and a high Mach condition. The first buffet point applies a 1.3 g margin to the cruise flight condition. The second buffet condition is at a higher Mach number (0.89) with the constraint that the lift match that of the cruise. The structural sizing conditions consists of a 1 g cruise with gust, -1.0 g dive, and 2.5 g pull-up maneuver conditions. The parameters for each flight condition are listed in Table 8.1.

Table 8.1: Flight conditions for Pareto front optimization

Number	Condition	Mach	Lift constraint	Altitude (ft)
1	Cruise	0.85	$\text{ZFW} + 0.2 \cdot \text{FB}$	37,000
2	High C_L Buffet	0.85	$1.3 \cdot (\text{ZFW} + 0.2 \cdot \text{FB})$	37,000
3	High M Buffet	0.89	$\text{ZFW} + 0.2 \cdot \text{FB}$	37,000
4	2.5 g maneuver	0.64	$2.5 \cdot \text{MTOW}$	0
5	-1 g maneuver	0.64	$-\text{MTOW}$	0
6	Cruise with gust	0.85	MTOW	27,300

8.1.1 Objective

As was already mentioned, we want to analyze the trade-offs between the objectives of fuel burn and wing structural weight. A useful way of visualizing this information is to plot each feasible design in the design space as a point in a multi-dimensional space, where the axes are defined by the competing objective values we wish to analyze. The Pareto front is defined as the boundary of all feasible designs in this design space. Each point on the front represents a design for which it is impossible to improve any one objective metric without making at least one of the remaining metrics worst. These design points can be found by defining a new objective function, which is a linear combination of all desired objective metrics. Varying the weighting on each objective metric and optimizing
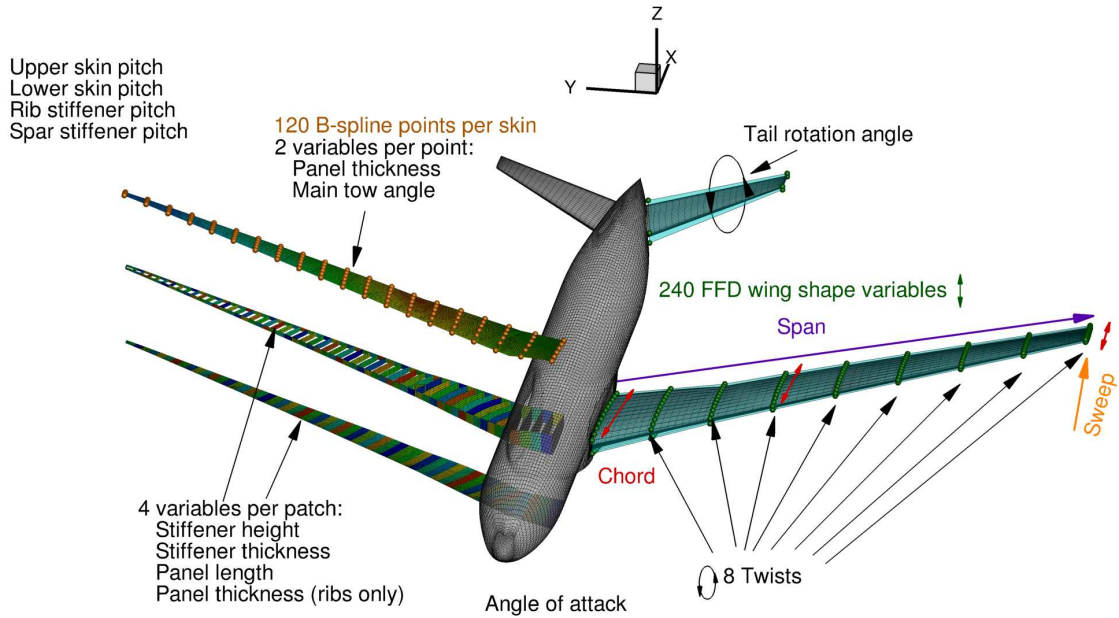
Figure 8.1: Pareto front optimization design variables.

the design with respect to this new function produces a series of design points lying on the Pareto front. For the two objective functions considered in this chapter, the Pareto front is a one-dimensional curve in the fuel burn-structural weight design space, and the combined objective function is:

$$I = \beta\text{FB} + (1 - \beta)\text{ZFW}, \tag{8.1}$$

where FB is the fuel burn, ZFW is the aircraft zero-fuel weight and β is the weighting parameter ($0 \leq \beta \leq 1$). The zero-fuel weight is the weight of the aircraft without fuel, which includes the aircraft structural weight, payload, etc., and is computed using Equation 3.4. The only component of this weight that is controlled by the optimizer is the weight of the wing structure, while the other components are fixed for all designs throughout the optimization.

In this study, six points on the Pareto front will be optimized for each design, corresponding to $\beta = [0,\ 0.35,\ 0.5,\ 0.65,\ 0.8,\ 1.0]$.

8.1.2 Design variables

The design variables used to parametrize each design are largely the same as those in Chapters 3 and 7. The design variables are summarized in Table 8.2 and shown in Figure 8.1.

Variable/function	Description	AL	CC	TS
x_{α_i}	Angle of attack for each case		——— 6 ———	
x_tail	Tail trim angle for each case		——— 6 ———	
x_shape	FFD control points		——— 240 ———	
x_twist	Wing twist		——— 8 ———	
x_chord	Chord		——— 3 ———	
x_span	Span		——— 1 ———	
x_sweep	Sweep		——— 1 ———	
$x_\text{stiff thick}$	Stiffener thickness (skin/spar/ribs)		——— 238 ———	
$x_\text{stiff height}$	Stiffener height (skin/spar/ribs)		——— 238 ———	
$x_\text{stiff pitch}$	Stiffener pitch (skin/spar/ribs)		——— 4 ———	
$x_\text{panel length}$	Panel length (skin/spar/ribs)		——— 238 ———	
x_ribs	Panel thickness (ribs)		——— 49 ———	
x_{t^cp}	Panel thickness control points (skin/spar)	0	280	280
$x_\text{panel thick}$	Panel thickness (skin/spar)	189	0	0
$x_{\theta_0^\text{cp}}$	Tow offset control points (skin)	0	0	240
	Total design variables	**1221**	**1312**	**1552**

Table 8.2: Pareto front optimization design variables for aluminum (AL), conventional composite (CC), and tow-steered (TS) designs

The geometric design variables are the same for all three designs. The first set of geometric variables consists of 240 FFD shape variables used to control the cross-sectional shape of the wing. Next, we have 8 FFD twist variables that control the spanwise twist of the wing. The remaining geometric design variables control the wing planform. The first of these are 3 chord variables: one to control the chord of the wing root, Yehudi break, and tip. The chord variables are defined in such a way as to keep the leading edge of the wing straight. The next planform variable controls the sweep of the wing by translating the wing tip in the stream-wise direction. The final planform variable controls the wing span.

The aerodynamic design variables are also the same for all three designs. The first of these is an angle-of-attack variable used to control the lift of each flight condition, for a total of 6. The second set of aerodynamic variables consists of the tail incidence variables, which control the pitching moment about the center of gravity of the aircraft for each flight condition, for another 6 variables.

The structural design variables differ slightly between the three designs. For this study, these variables consist of panel length, stiffener height, and stiffener thickness, each of which are set for each structural panel of the wingbox. A stiffener pitch variable is again shared by all panels of the upper skin, lower skin, ribs, and spars, for a total of 4 variables.

Variable/function	Description	AL	CC	TS
$L_i = n_i W_i$	Lift constraints		6	
$c_{m_y}^i = 0$	Trimmed flight		6	
$\mathrm{Sep}_i \leq 0.04$	Buffet separation constraints		2	
$t_{LE}/t_{LE_{init}} \geq 1.0$	Leading-edge radius		20	
$t_{TE}/t_{TE_{init}} \geq 1.0$	Trailing-edge thickness		20	
$(t/c)_{\mathrm{TE\ Spar}} \geq 0.80(t/c)_{\mathrm{TE\ spar}_{init}}$	Minimum trailing-edge spar height		20	
$\Delta z_{\mathrm{TE,upper}} = -\Delta z_{\mathrm{TE,lower}}$	Fixed trailing edge		8	
$\Delta z_{\mathrm{LE,upper}} = -\Delta z_{\mathrm{LE,lower}}$	Fixed leading edge		8	
$V - V_{\mathrm{fuel}} \geq 0.0$	Minimum fuel volume		1	
$L_{\mathrm{panel}} - x_{\mathrm{panel\ length}} = 0$	Target panel length		238	
$\mathrm{KS}_{\mathrm{stress}} < 1.0$	2.5 g and cruise w/ gust material failure		8	
$\mathrm{KS}_{\mathrm{buckling}} < 1.0$	2.5 g, -1.0 g, cruise w/ gust buckling		9	
$\left\|x_{\mathrm{stiff\ thick}} - x_{\mathrm{panel\ thick}}\right\| < 0.0025$	Maximum stiffener-skin difference		238	
$\left\|x_{\mathrm{stiff\ height}_i} - x_{\mathrm{stiff\ height}_{i+1}}\right\| \leq 0.0005$	Stiffener height adjacency		183	
$\left\|x_{\mathrm{stiff\ thick}_i} - x_{\mathrm{stiff\ thick}_{i+1}}\right\| \leq 0.0005$	Stiffener thickness adjacency		183	
$\left\|x_{\mathrm{panel\ thick}_i} - x_{\mathrm{panel\ thick}_{i+1}}\right\| \leq 0.0005$	Panel thickness adjacency	183	0	0
$\mathrm{KS}_{\|\nabla t_p\|} < \|\nabla t_0\|$	Panel thickness gradient	0	189	189
$-\frac{1}{R_{\min}} < \mathrm{KS}_\kappa < \frac{1}{R_{\min}}$	Minimum tow path turning radius	0	0	96
$-\psi_0 < \mathrm{KS}_\psi < \psi_0$	Tow path divergence	0	0	96
	Total constraints	**1133**	**1139**	**1331**

Table 8.3: Pareto front optimization constraints for aluminum (AL), conventional composite (CC), and tow-steered (TS) designs.

In addition to this, each rib is assigned a panel thickness variable for all three designs. A panel thickness variable is assigned to each structural panel of the spars and skins of the aluminum design. Conversely, to model the parametric nature of the AFP layup process for the composite designs, the panel thicknesses of the spars and skins are set through the B-spline control points distributed along each structural component. For the tow-steered design, 240 additional tow offset designs variables are assigned through the control points on each skin.

8.1.3 Constraints

Like the design variables, the constraints for this study should all be familiar from previous chapters. The constraints for each design are summarized in Table 8.3.

The aerodynamic constraints considered here include a lift and pitching moment constraint for each flight case. In addition to these constraints, we add the separation-based

buffet onset constraint for each buffet flight condition. Again, this constraint is added to ensure sufficient margin from the cruise flight condition to buffet onset.

The geometric constraints include again a leading-edge radius, trailing-edge thickness, and rear spar height constraint. The leading-edge and trailing-edge are constrained to be fixed with respect to the shape variables, this is to prevent redundancy relative to the twist variables. A volume constraint is placed on the fuel bay to ensure sufficient fuel capacity for the mission. The final geometric constraint ensures that the panel length design variables set by the optimizer remain consistent with the actual measured panel lengths.

The structural constraints include a set of aggregated buckling constraints for both the maneuvers and gust condition. An aggregated material failure constraint is applied only for the 2.5 g maneuver and gust condition. Adjacency constraints are applied to the stiffener height and thickness to ensure that they do not vary too abruptly between adjacent panels. Adjacency constraints are also applied to the panel thickness variables of the skins and spars of the aluminum design, since these variables are also assigned at the panel level. Due to the parametric nature of the composite panel thickness variables, an analogous thickness gradient constraint is applied to the skins and spars of these designs and aggregated in each panel with a KS function. The magnitude of this constraint, $1.3\,\mathrm{mm/m}$, is chosen to result in magnitudes of thickness changes between panels comparable to that allowed by the discrete adjacency constraint of the aluminum design. The last constraints are AFP manufacturing constraints, which are specific to the tow-steered design. A value of 70 in. is used for the minimum turning radius, R_{min}. The divergence constraint is again for simplicity set to the same value as the curvature constraint, this corresponds to a minimum cut/add length value of $0.72\,\mathrm{m}$ for a 50% gap/overlap rule.

8.2 Results

The Pareto fronts of aircraft fuel burn and zero-fuel weight are plotted for the aluminum, conventional, and tow-steered composite wings in Figure 8.2.

As should be expected, the conventional composite design consistently outperforms the aluminum design in both objective metrics at each corresponding location in the Pareto front, while the tow-steered design outperforms the conventional composite. For the fuel burn optimized designs ($\beta = 1$), we can see that switching material from aluminum to composite reduces the fuel burn by 6.3%, while adding tow-steering reduces fuel burn by an additional 1.5% relative to the conventional composite design. For the structural weight optimized designs ($\beta = 0$), the optimizer saves 3.7% by switching from aluminum to conventional composite, and saves an additional 1.6% by going from conventional to
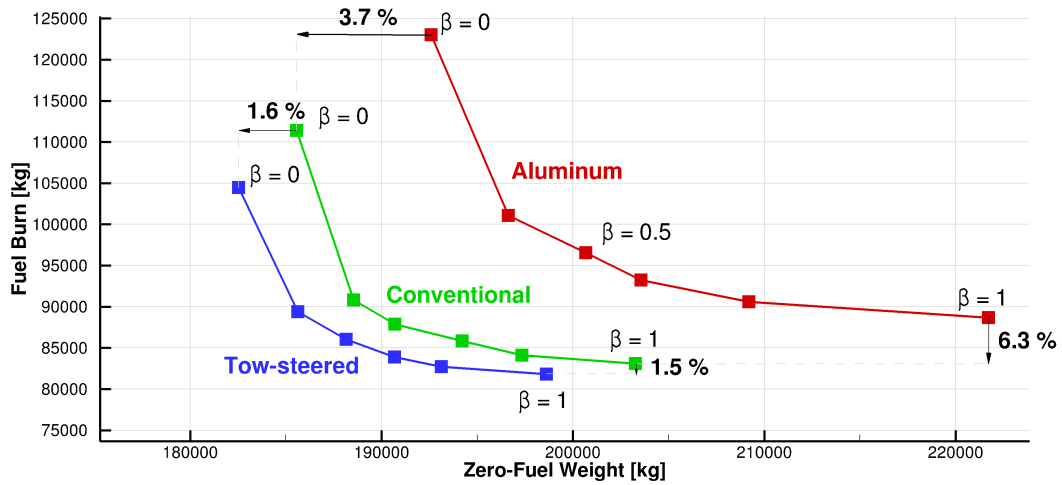
Figure 8.2: Pareto front trend-line for aluminum, conventional, and tow-steered composite wing designs.

tow-steered composite. From these two extremes, we conclude that tow-steering provides roughly the same benefit in reducing fuel burn and structural weight.

The Pareto front shown in Figure 8.2 shows that the objectives of fuel burn and structural weight become very nonlinear near either extreme. In these regions small improvements in one objective must come at a large cost in the other. For example, taking the aluminum design and comparing the points $\beta = 0.8$ and $\beta = 1$, shows that an improvement of only 2.1% in fuel burn in this region comes at the price of a 5.6% increase in structural wing weight. Recall that fuel burn and structural weight are approximate surrogates for aircraft DOC and acquisition cost, respectively. This means designs that focus solely on reducing the DOC (fuel burn) at the penalty of a significantly higher acquisition cost (structural weight), and vice-versa, is not desirable for airlines. These trends make it clear that the most economical design lies somewhere in between the extremes of these two objectives, perhaps $\beta \approx 0.65$.

Figure 8.3 shows the wing planform for each design. From this trend we see that as the weight on the fuel burn objective increases ($\beta \to 1$), so too does the wing span. This is because the optimizer begins focusing more on reducing induced drag on the wing, improving the aircraft L/D, which leads to further improvement in fuel burn performance. Conversely, as the emphasis on the structural weight objective increases ($\beta \to 0$), the wing span becomes shorter. This reduces the bending moment arm for the aerodynamic loads, allowing the designs to further reduce the structural weight of the wing.

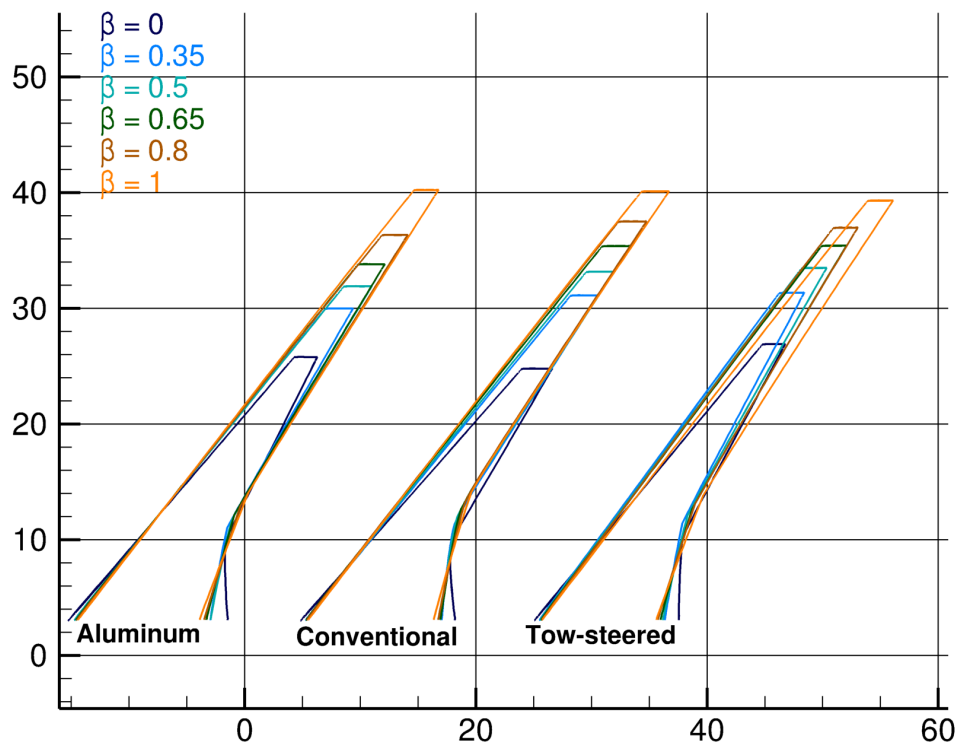Figure 8.4 shows additional trends for the fuel burn, structural weight, MTOW, and

Figure 8.3: Comparison of wing planforms for optimized aluminum, conventional, and tow-steered composite designs

cruise L/D. For all three designs, increasing β decreases the fuel burn monotonically. However, the improvement in fuel burn trend shows a diminishing return as $\beta \to 1$. In terms of structural weight, increasing β, and thus the optimal span, has the opposite effect. In this case, as β is increased, not only does the structural weight increase, but the rate of increase of structural weight also increases. Because MTOW is a combination of aircraft fuel burn and structural weight, this leads to the "bowl"-like shape seen in Figure 8.4. From this trend, we can see that the minimum aircraft MTOW occurs in between the extremes of the two objectives. When comparing the minimum MTOW value for all three designs, we find that the conventional composite design reduces the value by 6.7% relative to the aluminum design, while the tow-steered design provides an additional 1.6% benefit relative to the conventional composite design. Lastly, as β increases, and simultaneously the aspect ratio, so too does the cruise L/D. Again, this is a sign of the growing importance of aerodynamic performance for the fuel-burn-optimized designs. The trend in L/D and wing mass also explains why the fuel-burn-optimized designs do not exhibit even larger spans. This is because the increase in structural weight with respect to span begins to quickly outpace the improvement in aerodynamic performance through L/D increase.

Figure 8.5 shows the span-wise lift and twist distribution for each design. This plot shows that all designs take some advantage of load alleviation on their respective maneuver conditions. However, the designs with objectives more weighted toward structural weight exhibit the most washout at the the tips of each region. This is done to reduce load at the tips and thus decrease the bending moment on the structure at the cost of aerodynamic performance. As the design objective becomes more weighted toward fuel burn, this tip washout reduces and the lift distribution at cruise becomes more elliptical. This is again an effort to reduce the induced drag and thereby improve the fuel performance.

For all three designs, a noticeable dip in the lift distribution of the 2.5 g maneuver can be seen for the structural-weight-biased designs ($\beta = 0$, $\beta = 0.35$, and $\beta = 0.5$). By plotting the aerodynamic streamlines for these designs (in Figure 8.6) we can see that the flow is separated in the region of this dip. As the objective becomes more biased toward fuel burn, and aerodynamic performance becomes more critical, this region of separated flow disappears. This confirms the conclusion from the previous chapter that the lower aspect ratio designs are more susceptible to this phenomenon.

This region of separated flow on the maneuver condition of the structural-weight-biased designs is a similar result to what was found by Kennedy et al. [98]. In their work, they found that when aerostructurally optimizing an aircraft wing for MTOW using high-fidelity models, the optimizer tended to converge to a design featuring a large region of separated flow toward the tip of the upper surface of the wing for the maneuver condition. The
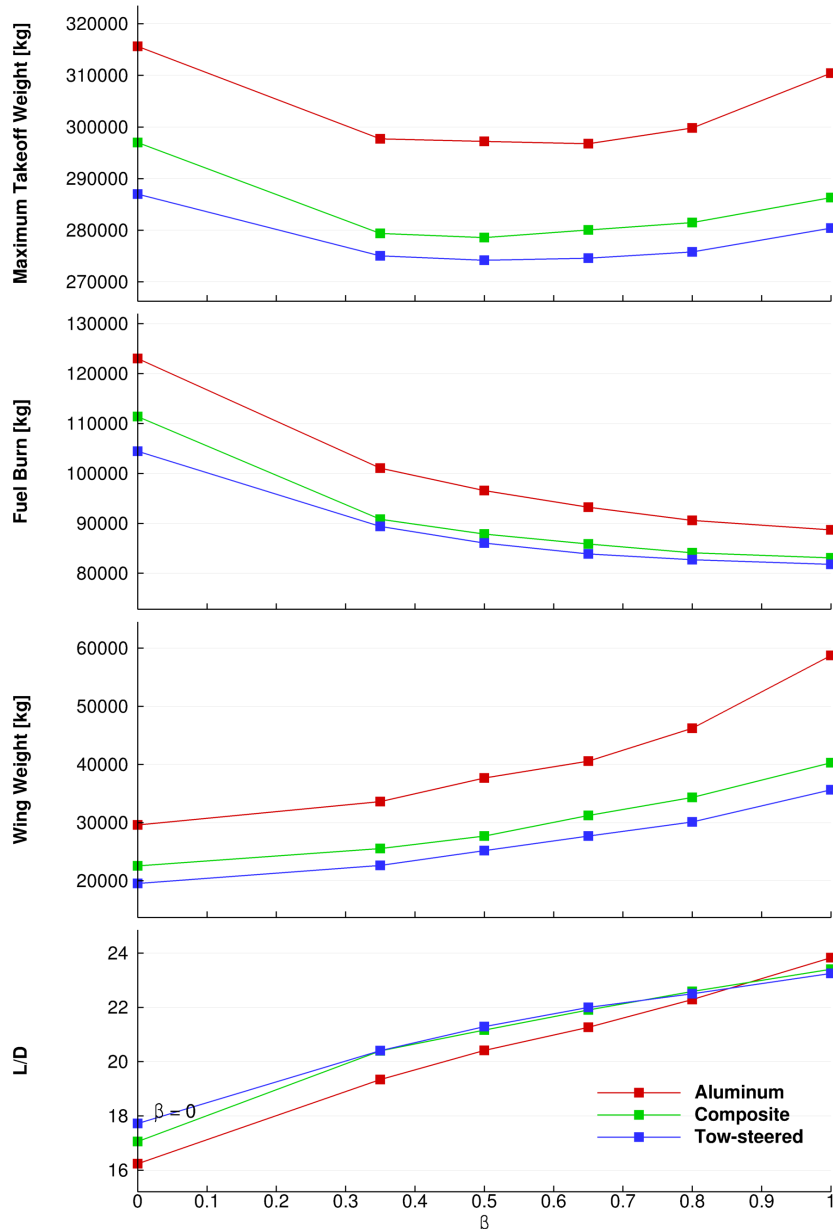
Figure 8.4: Pareto front trend-line for aluminum, conventional, and tow-steered composite wing designs for $\beta = [0, 0.35, 0.5, 0.65, 0.8, 1]$.

difference in this case is that the separated flow region is largely contained to the inboard of the wing. The more restricted region of separated flow on this condition is likely owed the inclusion of the separation-based buffet margins for the cruise condition in this study. While the buffet constraints do not directly constraint the separation on the maneuver condition, it still makes it difficult for the optimizer to separate larger portions of the wing on this condition, even for the structural-weight-biased designs. Though it is limited, separation in this region would still be undesirable, as it may lead to a loss in effectiveness in the ailerons of the aircraft. This shows that the separation-based buffet constraint applied to the buffet flight conditions is not sufficient to prevent separation on all flight condition, and emphasizes the need for an additional separation constraint to prevent aerodynamic stall in this region.

Figure 8.7 shows the optimized skin panel thickness for each design. From this figure, we can see that all designs feature local reinforcement at the wingbox root and Yehudi break. In addition, we see that as the span of the design increases, so too does thickness of the skins. Part of the reason for this is that these designs have larger moment arms for the aerodynamic loads, increasing the stress in the structure. The other contributing factor is that as the span increases, so too does the rib spacing, since the number of ribs remains constant. This means that to meet the same buckling requirements, the skins must become thicker.

Figure 8.8 shows the main tow paths for the conventional and tow-steered composite designs. In this figure, the tow paths on the conventional designs serve only as a reference for the tow-steered design, as their direction is not optimized. For the tow-steered designs, all designs take advantage of structural tailoring near the root. This is because all design objectives have some dependence of the structural weight of the wing, even the fuel-burn-minimized design, which is heavily skewed toward aerodynamic performance. Adding steering in this region reduces the structural weight with no aerodynamic penalty. Another interesting feature on the tow-steered designs is that as the aspect ratio increases, the amount of swept-forward tow paths utilized toward the tip decreases. This indicates that less load alleviation is utilized in the design as the objective is weighted more heavily toward fuel burn. This relationship between aspect ratio and optimal use of additional aeroelastic tailoring agrees well with the findings from the trend found in Chapter 7.

8.3   Summary

In this chapter, we investigated the design trade-offs between aircraft fuel burn performance and structural weight. This was accomplished by performing a series of aerostructural

(a) Aluminum

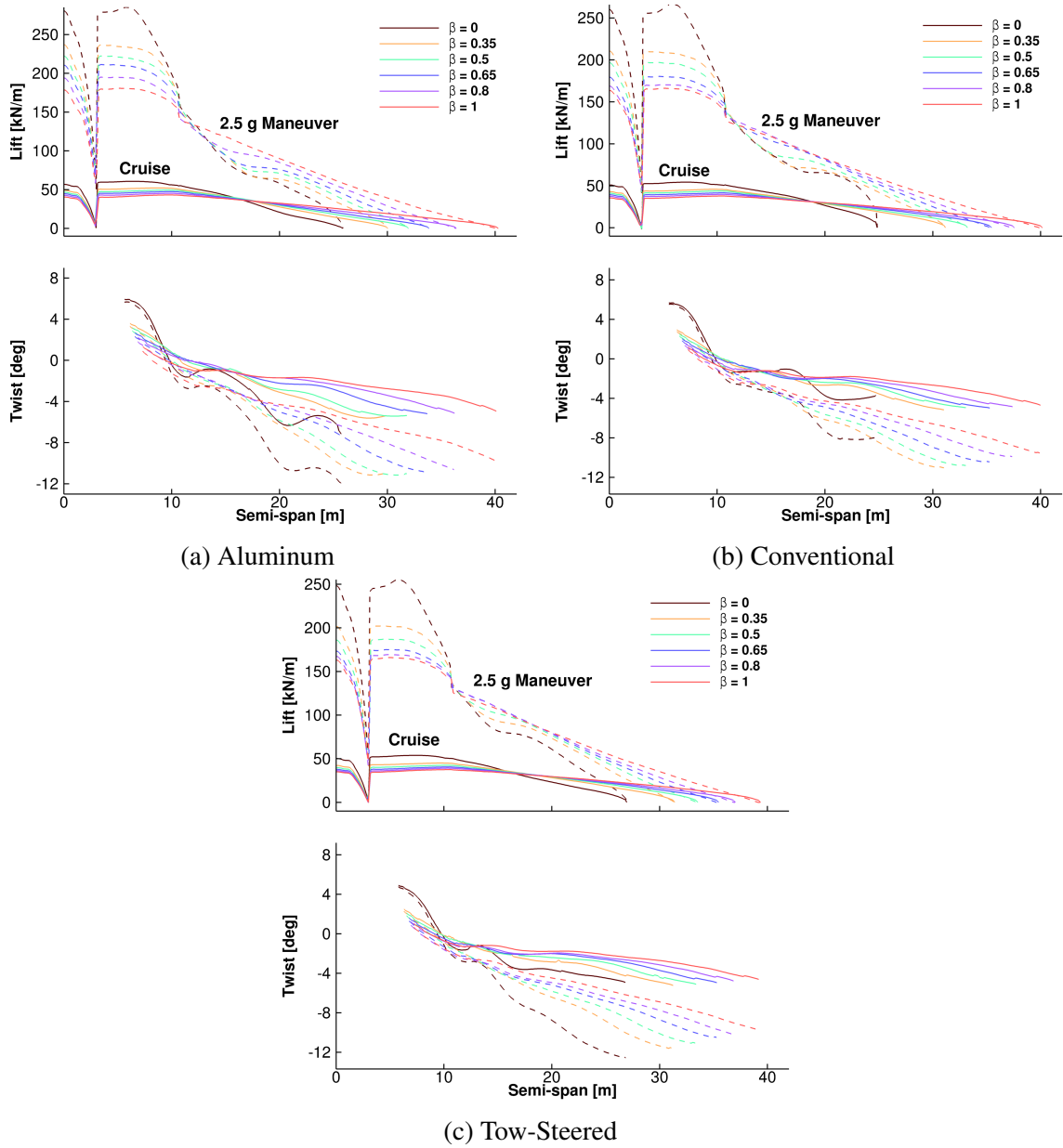(b) Conventional

(c) Tow-Steered

Figure 8.5: Comparison of lift and twist distribution for optimized aluminum, conventional, and tow-steered composite designs
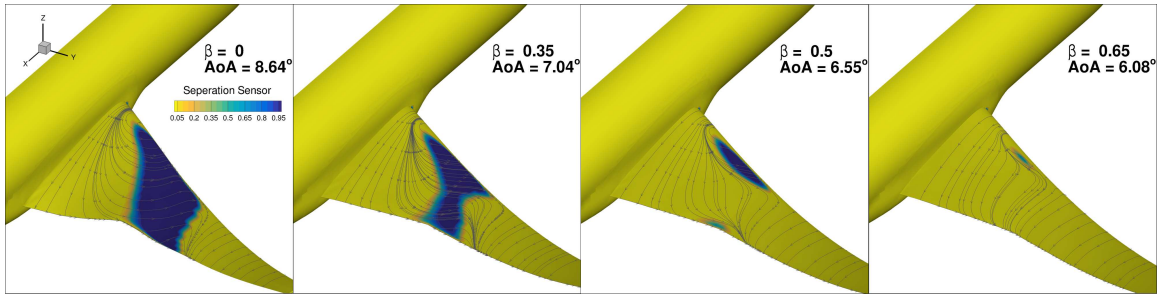
Figure 8.6: Separation sensor contour and airflow streamlines show region of separated flow on the 2.5 g for the tow-steered ($\beta = 0$, $\beta = 0.35$, $\beta = 0.5$) optimized designs.

optimizations, where the objective weighting between fuel burn and structural weight was varied to construct a Pareto front of optimal designs. This allowed us to glean further insight into the trade-offs between the competing objectives and the effect that the choice of aluminum, conventional, and tow-steered composite wing designs has on these trends.

From this study, we found that all designs shared the same general trends. When the objective favors structural weight, to reduce structural loads, the wing span decrease and wing tip washout increases. When the objective favors fuel burn, the wing span increases and the cruise span-wise lift distribution becomes more elliptical in an effort to reduce drag. All designs were found to take advantage of some amount of load alleviation on the high-lift maneuver condition. We also found that switching the wing structure from aluminum to conventional composite, and conventional to tow-steered composite, uniformly improves the performance of all Pareto-optimal designs. We saw that, for a fuel-burn-optimized design, going from an aluminum to conventional composite wing design saves roughly 6.3% in fuel burn, while switching from conventional to tow-steered composite saves an additional 1.5%. Likewise, for a structural weight optimized design, the conventional composite wing saves roughly 3.7% in structural weight relative to the aluminum design, while the tow-steered design saves an additional 1.6% relative to the conventional composite wing. From this study, we can conclude that tow-steering has the potential to offer further performance benefits in both fuel performance and structural weight relative to conventional structural designs. Though the benefits of transitioning from conventional to tow-steered composite wing designs was not found to be as dramatic as going from aluminum to conventional composite, the amount of improvement seen was still impressive, given that it required no change in materials used, only more efficient use of them.

Some of these results found in this study highlight the need for a separation-based stall constraint for the higher lift maneuver conditions. This particularly becomes necessary when the design objective is heavily skewed toward structural weight. Another area to improve on in this study would be to allow the number of ribs to vary. Since the amount of

(a) Aluminum

(b) Conventional
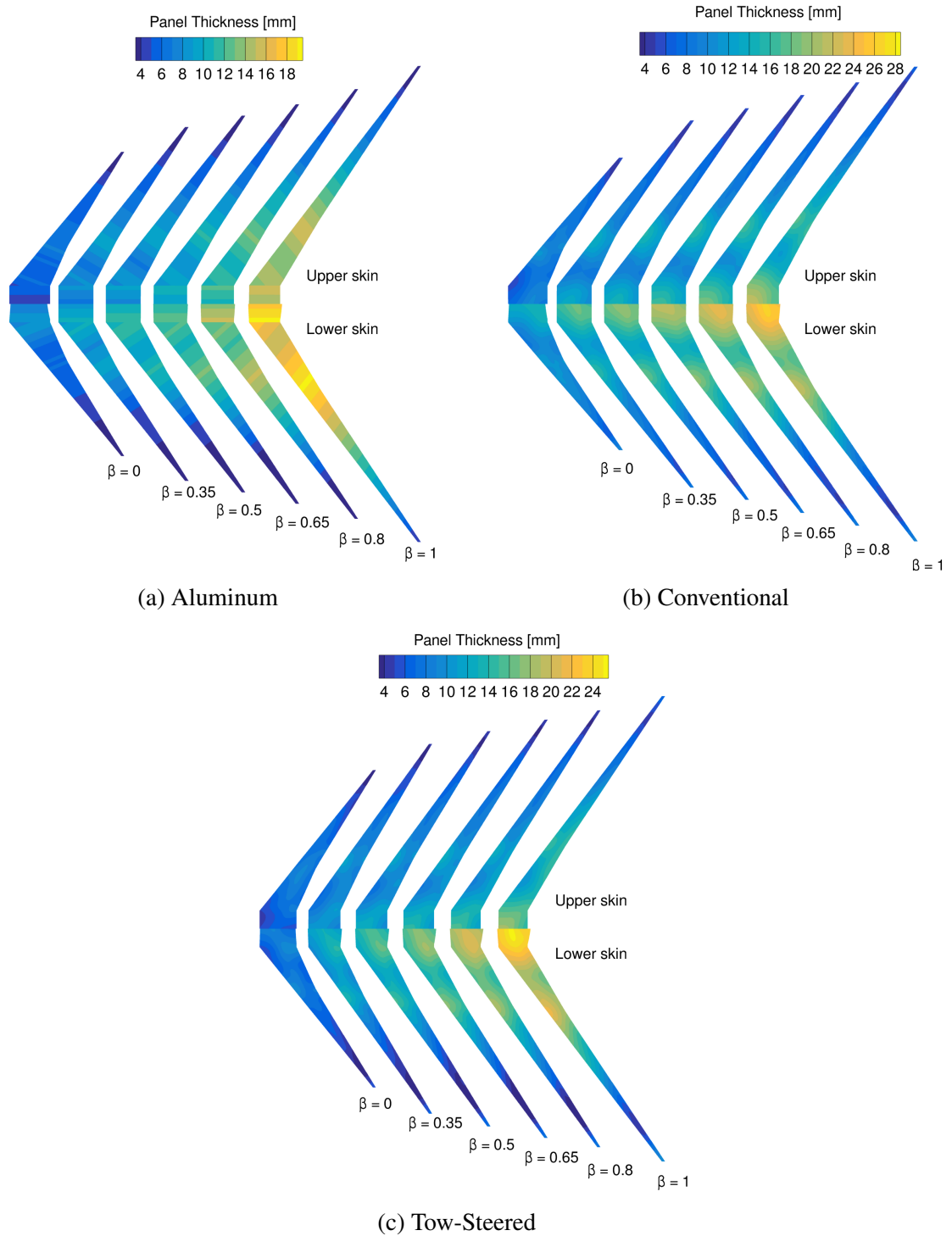
(c) Tow-Steered

Figure 8.7: Comparison of wingbox skin panel thicknesses for optimized metallic, conventional, and tow-steered composite designs

(a) Conventional   (b) Tow-Steered
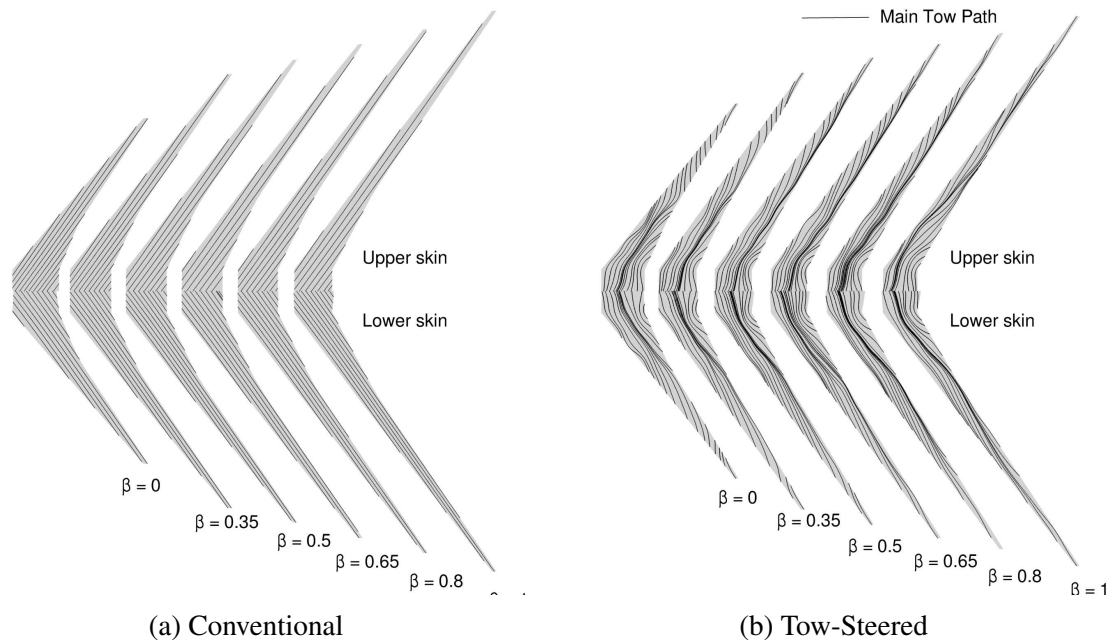
Figure 8.8: Comparison of tow paths for optimized composite wingbox skins designs

skin thickness required to meet the buckling constraints for each load case is highly dependent on rib spacing, keeping the number of ribs constant unfairly penalizes the structural weight of the high-span designs. Unfortunately, the number of ribs is inherently a discrete design variable, and as such not amenable to traditional gradient-based optimization. One way around this might be to homogenize the effect of the ribs into the skins and spars and allow the optimizer to treat the rib spacing as a design variable, similar to what is done here for the stiffeners. Another alternative might be adding topology optimization into the study to allow the optimizer to choose how many ribs to use and where to place them.

CHAPTER 9

Concluding remarks

9.1 Final remarks

In this chapter a review of the overall conclusions of this thesis will be given. Following this, the contributions that this work provides to the fields of tow-steered composite design and aeroelastic wing design will be summarized. Lastly, the contributions to the field of study will be provided, followed by suggestions for future work to improve even further upon these results.

9.2 Conclusions

Due to its environmental impact, the aviation industry will likely face great pressure to quickly improve aircraft efficiency and reduce emissions over the next few decades. This presents a great challenge for the commercial aircraft industry, one that will not likely be overcome through the continuation of conventional aircraft design techniques. While the growth in use of composites in aircraft designs has presented a great step toward improving this trend, further improvements are still available through the novel composite manufacturing technique known as tow steering. The potential benefits offered by tow-steering applied to wing design is still research question of great interest. In this work, I use the tools of high-fidelity MDO to quantify its potential relative to conventional wing designs. Specifically, the performance of tow-steering is compared to conventional composite and aluminum wing design for both moderate and high aspect ratio wings. These results provide valuable insights into the nature of the performance benefits made available by composite tow steering.

In Chapter 3, the need for a common benchmark model for the field of aeroelastic design and optimization is motivated. To address this issue, a conventional aluminum model based on NASA CRM through an inverse design procedure that includes the OML geometry of

the undeflected wing and the corresponding internal wingbox structure is developed. The original CRM wing has an aspect ratio of 9, so this model is referred to as "uCRM-9." Additionally, because modern transport aircraft are trending toward higher-aspect-ratio wing designs, a higher-aspect-ratio variant of this model is provided to assess next-generation wing designs with. This variant, called "uCRM-13.5," has an aspect ratio of 13.5 and is designed by using buffet-constrained multipoint aerostructural optimization. Through this study, the necessity for the consideration of multiple flight conditions and buffet onset in order receive robust design optimized results was demonstrated. The purpose of these models is to provide publicly available benchmarks, not just for the work presented here, but for the future study of aeroelastic wing analysis and design optimization.

In Chapter 5, it was demonstrated that tow paths of a general tow-steered pattern can be treated as the streamlines of a unit-vector field. Through this choice of definition, several manufacturing constraints can be intuitively related using vector calculus differential operators. In particular, it was demonstrated that the curl of such a vector field is equivalent to the tow path curvature of the layup. Through further derivation, it was also proven that the rate of growth of gaps and overlaps is directly related to the divergence of the vector field. In addition to relating each of the quantities to relevant AFP manufacturing constraints, analytical formulas are provided for their sensitivities.

In Chapter 6, we explore the performance of the parametrization scheme introduced in Chapter 4, by applying the technique to four parametric structural design optimization problems. In this chapter, the effect of varying number of control points on design performance is explored, and it was found that results from previous authors could be reproduced given a sufficient number of control points are used. In addition, the effect of the design constraints introduced in Chapter 5 was explored by varying the severity of each parameter for the various design problems considered. Next, the structural benefits of applying tow-steering to a wing design was shown by performing a structural design optimization problem with fixed aerodynamic loading. Finally, the presences of local minima in the design space was explored, by starting the wingbox design optimization from several random starting points. The design problem was found to be largely convex, with all random point designs converging to within 0.17% of the mass of the original optimized wingbox.

In Chapter 7, the benefits of tow-steering are extended to aerostructural wing design by considering a number of fuel burn optimization problems. In this chapter, it was found that when tow-steering is added to a composite wing design for a moderate aspect ratio wing, like the uCRM-9, fuel burn reductions of up to 2.3% could be achieved in addition to a reduction of 24% in wing weight relative to a balanced conventional composite wing. This was achieved through a combination of additional load alleviation and local structural

tailoring. It was found that the load alleviation benefits could be reproduced for the conventional composite design by allowing the optimizer to use unbalanced skin plies. However, the tow-steered design was still found to be superior in performance due to its local structural tailoring capabilities. The manufacturing constraints introduced in Chapter 5 were found to only reduce these local structural tailoring capabilities for the tow-steered wing, while the load alleviation performance was largely unaffected. When tow-steering was applied to a higher aspect ratio wing, the uCRM-13.5, the benefits in fuel burn and structural weight reduction were found to be 1.5% and 14%, respectively, when compared to the conventional balanced composite wing. These benefits were found entirely due to the local structural tailoring of the wing design. From this study, it was concluded that tow-steering has great promise for improving fuel burn performance of both moderate aspect ratio and high aspect ratio wing designs.

Finally, in Chapter 8, the trade-offs between the design objectives of fuel burn and structural weight were examined through the aid of a Pareto front. In this chapter, the performance of three wing designs were assessed: an aluminum, conventional and tow-steered composite wing. Wing planform variables—sweep, span, and chord— were added to allow the optimizer the freedom to find the optimal wing planform at each design point. From these results, it was found that tow-steering offered 1.5% improvement in fuel burn performance on a fuel-burn-optimized design relative to a conventional composite design, this is compared to a 6.3% improvement in fuel burn when comparing a conventional composite to aluminum wing design. Likewise, for the structural-weight-optimized design, a reduction of 1.6% was found in total aircraft structural weight on the tow-steered design relative to the conventional composite, compared to a 3.7% reduction when comparing the conventional composite relative to the aluminum design. This showed that tow-steering has the potential to offer similar benefit margins in both fuel burn performance and structural weight.

9.3   Contributions

The contributions of this thesis are as flows:

1. *Development of benchmark aeroelastic models for the future study of next-generation flexible-wing aircraft designs.*

   The uCRM designs produced in this work provide a much needed benchmark model for any groups wishing to study aeroelastic behavior of transonic transport aircraft. Both models were developed with the goal of having realistic design performance

over a large range of different flight conditions.

2. *I developed a general framework for the parametrization and optimization of tow-steered composite structures.*

In this work, I develop a general conceptual design tool for tow-steered structures, pySteer. This framework was shown to be able to scale up to $\mathcal{O}(10^3)$ design variables, allowing for very detailed design of such structures. This parametrization scheme was shown to be flexible enough handle designs that varied from simple plate structures to more sophisticated multi-component wingbox structures.

3. *I derived relevant AFP/tow-steering manufacturing constraints and corresponding sensitivities.*

In this work, a novel mathematical formulation was proposed to relate the manufacturing constraints typical of an AFP machine. This formulation allows for the curvature of the tow path and growth rate of gaps and overlaps to be locally measured and constrained in a tow-steered layup. The corresponding design sensitivities for each constraint were analytically derived, allowing them to be used in the context of gradient-based optimization. One of the optimized tow-steered wingbox structural models that resulted from this work was successfully constructed at a 27% scale by Aurora Flight Sciences, see Figure 9.1. This shows that the manufacturing constraints considered in this work were sufficient to ensure the manufacturability of a tow-steered wing design.

4. *I quantified the benefits of tow steering for static aeroelastic wing design*

In this work, I used high-fidelity gradient-based design optimization to quantify the benefits of tow-steering for static aeroelastic wing design. This was done by first performing a series of structural design optimizations to isolate and identify the purely structural benefits offered by tow-steering. Next, these benefits were extended to aeroelastic design by performing a variety of fuel burn minimization problems on both a tow-steered and conventional composite wing design. This study also examined the effect that varying the wing aspect ratio had on the performance of each design. Finally, these results were expanded upon by adding in an aluminum design, planform variables, and varying the objective between structural weight and fuel burn.

(a) Wingbox skins being laid up by AFP machine
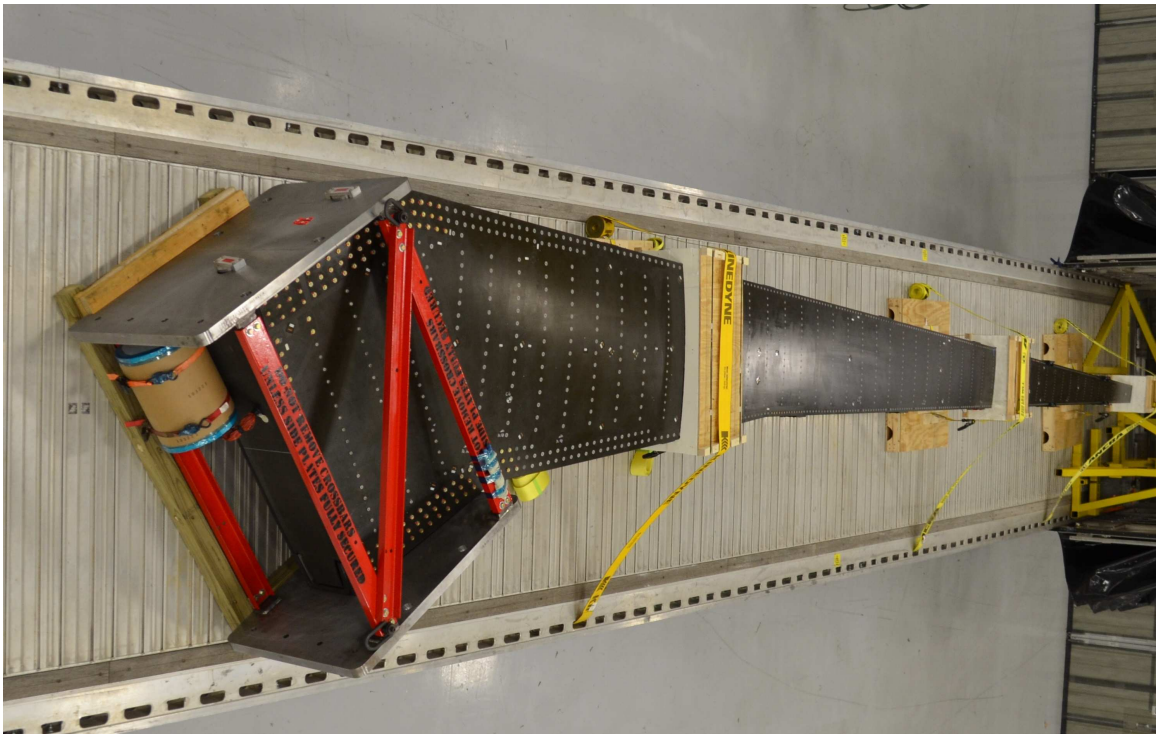
(b) Final assembled structural model in preparation for shipment to NASA Armstrong

Figure 9.1: 27% scaled tow-steered wingbox model manufactured by Aurora Flight Sciences

9.4   Recommended future work

During the pursuit of the contributions presented in this work, a number of additional avenues for future work to complement the results presented here were discovered. They are as follows:

- *Exploration of the effect of varying ply fraction*

  In this work, the fractions of plies of each tow pattern was assumed to remain spatially constant throughout either skin of the wingbox. In addition, the optimizer was not given the freedom to chose the percentage of each pattern in the layup which might be optimal. Further improvements to the tow-steered might be found by relaxing both of these restrictions and allowing the optimizer to tailor the ply fraction of each tow pattern spatially by adding it as a design variable. This could be done through the B-spline control points, in a similar fashion to how the thickness and tow angles are treated now.

- *Inclusion of tow-steering knockdown factors*

  In this work, tow-steering was idealistically assumed to be able to be applied to composite structural design without any reduction in performance due to the steering of the tows relative to an unsteered composite design. In reality, there is likely to be some penalty to be paid in the directional strength and stiffness of the tows related to how steered they are. This could be modeled by applying a knockdown factor, based on experimental data, to the nominal stiffness and strength values of the unsteered tow as a function of local tow-path divergence and curvature. Though such experimental data was not available at the time of writing this thesis, the recent construction of the scaled tow-steered wingbox structure by Aurora Flight Sciences, and later to be structurally tested by NASA, will provide valuable data on these deviations from idealized performance, from which such knockdown could be estimated. Once this is done, the optimizations in this work could be rerun and used to produce even more accurate performance estimates for tow-steered structures.

- *Inclusion of control effectiveness*

  As mentioned in Chapter 7 of this work, it is well-known that there is an aeroelastic trade-off between the bend-twist coupling of a flexible wing and the effectiveness of the control surface. This trade-off has been investigated in the domain of low-fidelity aerodynamic analysis by a few authors [60, 61]. With the relatively recent addition of the overset meshing capabilities to the aerodynamic solver, it is now, in

theory, possible to extend these studies to higher fidelity, increasing the accuracy of the model. This could be accomplished by including the control surface in the aerodynamic model as an overset component and simulating its deflection through the use of an FFD. Through this approach, an asymmetric rolling maneuver could be added to analyses considered in these studies. This could provide a means of ensuring the additional aeroelastic tailoring provided by the tow-steered wing does not come at the cost of control effectiveness.

- *Consideration for geometrically nonlinear structural deformations*

  The structural analysis presented in this work assumes purely geometrically linear structural deformations. As the aspect ratio of the wing increases, so too do the deformations expected on the wing. For this work, the tip deflection could become as high as 25% of the wing span during maneuver on the higher aspect ratio models. While linear analysis can still be used in this case to assess some basic trends of such structures, geometrically nonlinear deformational effects must be considered to produce more accurate results. For this reason, adding geometrically nonlinear FEA to the aerostructural analysis will provide more accurate performance predictions for the higher aspect ratio wing designs in this work.

- *Inclusion of dynamic aeroelastic effects in high-fidelity model*

  All of the aeroelastic considerations in this work were based on purely static analysis. In the general aircraft design procedure, there are a number of load cases and design constraints which require the consideration of dynamic aeroelastic phenomena. These include, just to name two, flutter onset for the wing and dynamic gust loads. Previous researchers have included some consideration for each of these effects through the use of a lower fidelity aerodynamic panel-method model [60, 61]. The accuracy of these results could be improved upon by utilizing more high-fidelity models in the analysis. The challenge is that to accurately capture these phenomena typically require either time-accurate or time-spectral analysis in high fidelity, a process that can prove to be computationally expensive. One way to get around this might be through a multi-fidelity approach, whereby a lower-fidelity aeroelastic model is used in conjunction with a series of higher-fidelity analyses during the optimization.

164

APPENDIX A

uCRM model files

As mentioned in Chapter 3, the files for the uCRM models—both uCRM-9 and uCRM-13.5—are publicly available[1]. The included files are detailed in Table A.1.
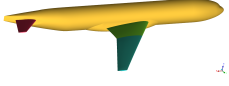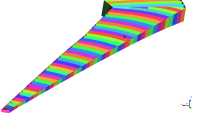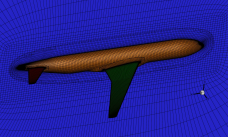
---

[1]http://mdolab.engin.umich.edu/content/ucrm
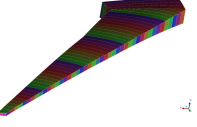
File	Description	Image
uCRM#_wbt.igs/.tin	uCRM OML geometry file; it includes the jig wing, fuselage, and horizontal stabilizer. The internal B-spline parametrization of the surfaces is identical to the original CRM geometry. To generate a different CFD mesh this file can be used as the underlying geometry. We include the files in a IGES format for general use, as well as a .tin format for use with meshing software ICEMCFD.	
uCRM#_box.igs/.tin	Geometry for the wingbox structure. Can be used to generate different structural meshes. This file was used with ICEMCFD to produce the Nastran BDF files listed below. The wingbox is geometrically "perfect"—all surface edges are coincident and do not require any manual cleanup before meshing.	
uCRM#_wbt_level.cgns	CFD volume meshes for each model. The files come in three different mesh levels: coarse, medium, and fine. The different mesh levels have roughly 1.23, 3.63, and 9.82 million volume cells, respectively. Both in a structured multiblock and overset meshes are provided.	
uCRM#_box_level.bdf	Nastran BDF file for the meshed wingbox geometry. The files come in three different mesh levels, corresponding to the three CFD mesh levels: coarse, medium, and fine. The different mesh levels feature roughly 25, 61, and 98 thousand second-order shell elements, respectively. Boundary conditions, material properties, and external masses are also specified.	
uCRM#_loads_coarse.bdf	Separate loads file for the coarse mesh. This set of loads applied to the uCRM#_box_coarse.bdf model yields the 1 g deflected geometry.	

Table A.1: uCRM File descriptions

Example of manufacturing constraints for analytic tow patterns

In Chapter 5, a mathematical derivation of the tow-path curvature and gap/overlap propagation for a general tow pattern was provided. To give an example of how these equations can be applied, we consider two simple tow patterns in this section. The patterns are chosen to be simple so that analytical expressions can be derived for their relevant quantities, and so that the results can provide an intuitive feel for their mathematical relationships.

B.1   Radially-diverging pattern

The first pattern we consider is a tow pattern whose paths emanate radially outward from its center, as shown in Figure B.1. It is convenient to write this vector field in polar coordinates:

$$\vec{v} = \hat{\mathbf{r}}$$

The curl and divergence of a vector field in polar coordinates, $\vec{v} = v_r \, \hat{\mathbf{r}} + v_\theta \, \hat{\boldsymbol{\theta}}$, is:

$$\kappa(\theta, r) = (\nabla \times \vec{v}) \cdot \hat{\mathbf{k}} = \frac{1}{r} \left(\frac{\partial r v_\theta}{\partial r} + \frac{\partial v_r}{\partial \theta} \right), \qquad \psi(\theta, r) = \nabla \cdot \vec{v} = \frac{1}{r} \left(\frac{\partial (r v_r)}{\partial r} + \frac{\partial v_\theta}{\partial \theta} \right)$$

Substituting in for the vectors components yields the curvature and divergence:

$$\kappa(\theta, r) = 0, \qquad \psi(\theta, r) = \frac{1}{r}$$

It should come as no surprise that the curvature is zero for this pattern, since all of the tow paths are straight lines. The divergence features a singularity at the center and decays with the inverse distance from the origin. The divergence decays to zero far away from the center of the pattern, since all tow paths become more locally parallel further away from
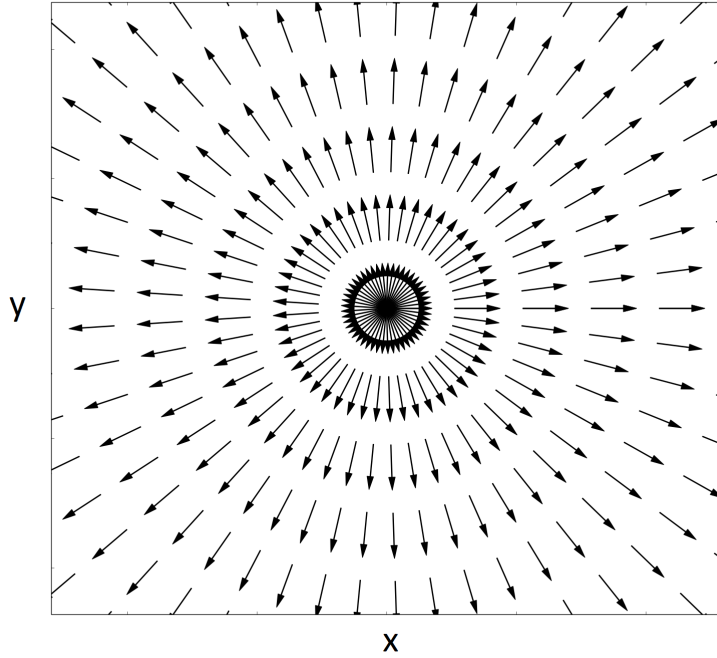
Figure B.1: Tow path vector field, $\vec{v}$, for radially diverging tow pattern.

the center.

To derive the gap propagation, $h_{g/o}/w(s)$, suppose we begin laying the prepreg tow down radially outward starting at a distance, R, from the center (see Figure B.2). The edges of the tows are assumed to be coincident at their initial seed location, $s = 0$, implying that $\delta = 1$. The divergence as a function of distance traveled along one of the tow paths, $\psi(s)$, is given by:

$$\psi(s) = \frac{1}{s + R}$$

Substituting the divergence, $\psi(s)$, into Equation (5.10) yields:

$$\frac{h_{g/o}}{w}(s) = \exp\left(\int_0^s \frac{1}{s' + R} \, \mathrm{d}s'\right) - 1$$

Evaluating the integral we get:

$$\frac{h_{g/o}}{w}(s) = \left|\frac{s}{R} + 1\right| - 1 \tag{B.1}$$
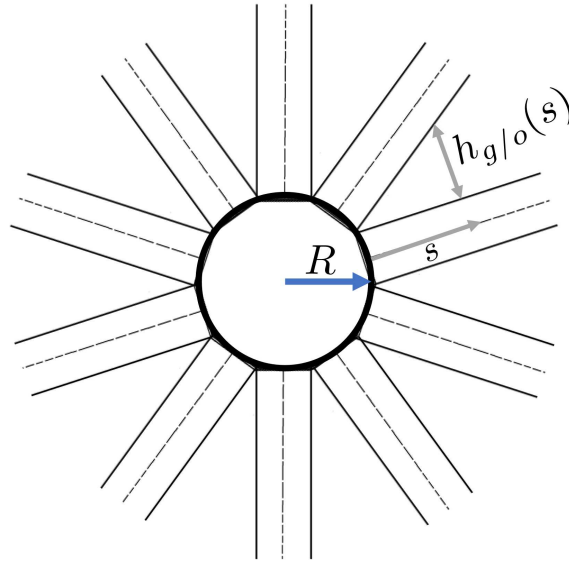
Figure B.2: Gap definition for radial diverging pattern.

As long as $s \geq -R$, this can be further simplified to:

$$\frac{h_{g/o}}{w}(s) = \frac{s}{R} \tag{B.2}$$

This states that the adjacent gaps between tow strips grow linearly as the tow is laid down. By evaluating Equation (B.2) at $s = -R$, we can show that if the tow path were to be continued backward, toward the center, there would exist a 100% overlap at the pattern's singularity. This conclusion can be quickly verified by analyzing Figure B.2.

B.2 Patterns with linear angle variation

A common tow pattern parametrization scheme developed for tow-steered composites is the linear angle variation scheme [41, 111, 47, 48, 52, 112]. This scheme was originally proposed by Olmedo and Gurdal [112]. In their work, they define the tow angle as varying piece-wise linearly along the x'-axis. The tow pattern is then parametrized by the fiber angle at the origin of the reference path, T_0, and the angle at the edges of the laminate, T_1, where $x' = [0, 2d]$. Thus the angle variation is:

$$\theta(x') = \begin{cases} \phi + \frac{T_0 - T_1}{d} x' + T_1, & \text{for} \quad 0 \leq x' < d \\ \phi + \frac{T_1 - T_0}{d}(x' - d) + T_0, & \text{for} \quad d \leq x' \leq 2d \end{cases} \tag{B.3}$$

169

Figure B.3: Linear-varying tow angle proposed by Gurdal et al. [111].

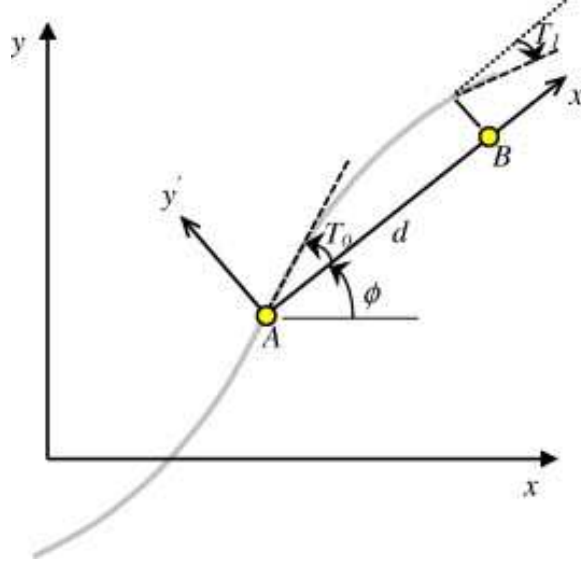They also introduced a compact notation for the pattern as $\phi\langle T_0, T_1\rangle$. Figure B.3 shows an example of the tow path resulting from the linear angle distribution described above. For simplicity, we assume that $\phi = 0$, and thus $x = x'$. However, the following derivation can be generalized for $\phi \neq 0$.

The curvature and divergence of the tow path can be found by applying Equations (5.2) and (5.4), respectively, to Equation (B.3).

$$\kappa(x) = \frac{\mathrm{d}\theta}{\mathrm{d}x}(x)\cos(\theta(x)) = \begin{cases} \frac{T_0-T_1}{d}\cos(\theta(x)), & \text{for} \quad 0 \leq x < d \\ -\frac{T_0-T_1}{d}\cos(\theta(x)), & \text{for} \quad d \leq x \leq 2d \end{cases}$$

$$\psi(x) = -\frac{\mathrm{d}\theta}{\mathrm{d}x}(x)\sin(\theta(x)) = \begin{cases} -\frac{T_0-T_1}{d}\sin(\theta(x)), & \text{for} \quad 0 \leq x < d \\ \frac{T_0-T_1}{d}\sin(\theta(x)), & \text{for} \quad d \leq x \leq 2d \end{cases}$$

Next, we derive the gap propagation, $h_{g/o}/w$, using Equation (5.10). We assume that the AFP tow paths begin on the left side, $x = 0$, of the pattern. Performing an integration variable transformation from s' to θ in Equation (5.10) gives:

$$\frac{h_{g/o}}{w}(x) = \delta \exp\left(\int_{\theta(0)}^{\theta(x)} \frac{\psi(\theta)}{\frac{\partial\theta}{\partial s}(\theta)}\,\mathrm{d}\theta\right) - 1$$

Recognizing the definition of curvature (i.e., $\partial\theta/\partial s = \kappa$) and substituting in the relevant

expressions yields:

$$\frac{h_{g/o}}{w}(x) = \delta \exp\left(-\int_{T_1}^{\theta(x)} \frac{\sin(\theta)}{\cos(\theta)} d\theta\right) - 1 = \delta \exp\left(-\int_{T_1}^{\theta(x)} \tan(\theta) \, d\theta\right) - 1$$

Finally, evaluating the integral and manipulating variables gives:

$$\frac{h_{g/o}}{w}(x) = \delta \exp\left(\ln(|\sec(T_1)|) - \ln(|\sec(\theta(x))|)\right) - 1$$

$$= \delta \exp\left(\ln\left(\left|\frac{\sec(T_1)}{\sec(\theta(x))}\right|\right)\right) - 1$$

$$= \delta \left|\frac{\sec(T_1)}{\sec(\theta(x))}\right| - 1$$

$$= \delta \left|\frac{\cos(\theta(x))}{\cos(T_1)}\right| - 1 \tag{B.4}$$

Equation (B.4) is significant in that it provides us an analytical expression for the gap/overlap size as function of location in the pattern. A typical method for deciding the shift distance for adjacent tow paths is to space the tow paths such that either no gaps occur between adjacent paths (only overlaps), overlap method, or no overlaps occur (only gaps), gap method [113]. Table B.1 gives the corresponding shift distance, δ, for the gap and overlap methods.

Table B.1: Shift parameter for gap/overlap method

Condition	Overlap method	Gap method
$\|\cos(T_1)\| \leq \|\cos(T_0)\|$	$\delta = \left\|\frac{\cos(T_1)}{\cos(T_0)}\right\|$	$\delta = 1$
$\|\cos(T_1)\| > \|\cos(T_0)\|$	$\delta = 1$	$\delta = \left\|\frac{\cos(T_1)}{\cos(T_0)}\right\|$

Next, the overlap propagation predicted in Equation (B.4) is compared with a laminate laid up by Tatting et al. [113]. In their work, the authors modeled and manufactured a 15 in. by 20 in. laminated plate, with a layup of $[\pm 45°/\pm\langle 45°, 60°\rangle_2/\pm\langle 30°, 15°\rangle_2, \pm\langle 45°, 60°\rangle_2]_s$ using the overlap method. The overlap pattern predicted by Equation (B.4) for the tow-steered layers of the laminate, $\pm\langle 45°, 60°\rangle$ (dark gray) and $\langle 30°, 15°\rangle$ (light gray) are shown in Figure B.4. From Figure B.4, it can be seen that the overlap size predicted by Equation (B.4) and the tow spacing predicted by Table B.1 are in good agreement with the overlap pattern found numerically by the authors.
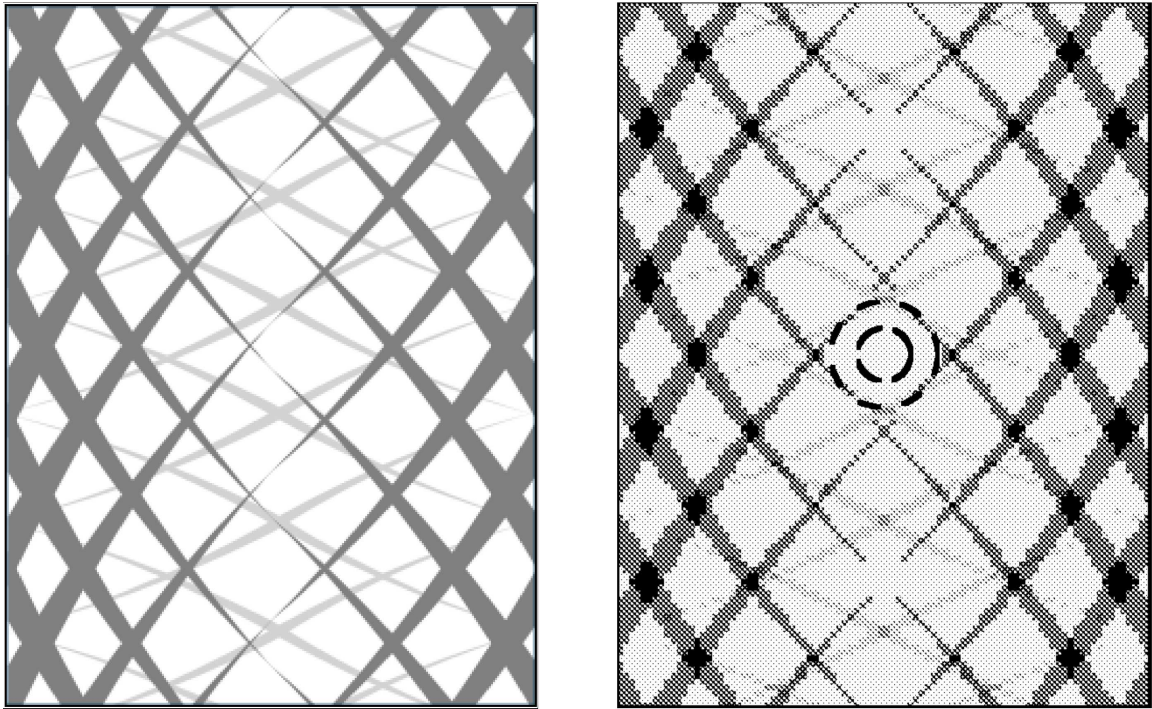
Figure B.4: The prediction of the overlap size and spacing given by Equation (B.4) (left) match well with the that found by Tatting and Gurdal [113] (right).

BIBLIOGRAPHY

[1] "2036 Forecast Reveals Air Passengers Will Nearly Double to 7.8 Billion," http://www.iata.org/pressroom/pr/Pages/2017-10-24-01.aspx, October 2017, Accessed: 2017-10-30.

[2] Kharina, A. and Rutherford, D., "Fuel efficiency trends for new commercial jet aircraft: 1960 to 2014," Tech. rep., The International Council on Clean Transportation, August 2015.

[3] Lee, D. S., Fahey, D. W., Forster, P. M., Newton, P. J., Wit, R. C., Lim, L. L., Owen, B., and Sausen, R., "Aviation and global climate change in the 21st century," *Atmospheric Environment*, Vol. 43, No. 22, 2009, pp. 3520 – 3537.

[4] Cumpsty, N. and Organization, I. C. A., *Report of the Independent Experts on the Medium and Long Term Goals for Aviation Fuel Burn Reduction from Technology: Report*, Doc (International Civil Aviation Organization), International Civil Aviation Organization, 2010.

[5] Dorey, G., "Carbon fibres and their applications," *Journal of Physics D: Applied Physics*, Vol. 20, No. 3, 1987, pp. 245.

[6] Evans, D. O., *Fiber Placement*, Vol. 21, ASM handbook, Materials Park, OH, miracle db and donaldson sl ed., 2001, pp. 1135–1140.

[7] Sloan, J., "ATL and AFP: Defining the megatrends in composite aerostructures," 06 2008.

[8] Grant, C., "Automated processes for composite aircraft structure," *Industrial Robot*, Vol. 33, No. 2, March 2006, pp. 117–121.

[9] Grant, C. G., "Fiber placement process utilization within the worldwideaerospace industry," *45th International SAMPE symposium*, Long Beach, California, USA, 2000.

[10] Oldani, T., "Increasing productivity in fiber placement processes. saeaerospace manufacuring and automated fastening conference & exhibition," North Charleston, South Carolina, USA, 2008.

[11] Lukaszewicz, D. H.-J. A., Ward, C., and Potter, K. D., "The engineering aspects of automated prepreg layup: History, present and future," *Composites Part B: Engineering*, Vol. 43, No. 3, April 2012, pp. 997–1009.

[12] Lozano, G. G., Tiwari, A., Turner, C., and Astwood, S., "A review on design for manufacture of variable stiffness composite laminates," *Proceedings of the Institution of Mechanical Engineers, Part B: Journal of Engineering Manufacture*, Vol. 230, No. 6, Sept. 2015, pp. 981–992.

[13] Hale, J. E., "Boeing 787 from the ground up," *Aero Magazine*, , No. 4, 2006.

[14] "A350 XWB," http://www.aircraft.airbus.com/aircraftfamilies/passengeraircraft/a350xwbfamily/, Accessed: 2017-10-24.

[15] Shirk, M. H., Hertz, T. J., and Weisshaar, T. A., "Aeroelastic tailoring — Theory, practice, and promise," *Journal of Aircraft*, Vol. 23, No. 1, 1986, pp. 6–18.

[16] Munk, M. M., "Propeller containing diagonally disposed fibrous material," Oct. 11 1949, US Patent 2,484,308.

[17] Burdette, D., Kenway, G. K. W., Lyu, Z., and Martins, J. R. R. A., "Aerostructural Design Optimization of an Adaptive Morphing Trailing Edge Wing," *Proceedings of the AIAA Science and Technology Forum and Exposition (SciTech)*, Kissimmee, FL, January 2015, AIAA 2015-1129.

[18] Burdette, D. A., Kenway, G. K., and Martins, J. R. R. A., "Performance Evaluation of a Morphing Trailing Edge Using Multipoint Aerostructural Design Optimization," *57th AIAA/ASCE/AHS/ASC Structures, Structural Dynamics, and Materials Conference*, American Institute of Aeronautics and Astronautics, January 2016.

[19] Burdette, D. A., Kenway, G. K. W., and Martins, J. R. R. A., "Aerostructural design optimization of a continuous morphing trailing edge aircraft for improved mission performance," *17th AIAA/ISSMO Multidisciplinary Analysis and Optimization Conference*, 06/2016 2016.

[20] Lyu, Z. and Martins, J. R. R. A., "Aerodynamic Shape Optimization of an Adaptive Morphing Trailing Edge Wing," *Proceedings of the 15th AIAA/ISSMO Multidisciplinary Analysis and Optimization Conference*, Atlanta, GA, June 2014, AIAA 2014-3275.

[21] Kenway, G. K. W. and Martins, J. R. R. A., "Multipoint High-Fidelity Aerostructural Optimization of a Transport Aircraft Configuration," *Journal of Aircraft*, Vol. 51, No. 1, January 2014, pp. 144–160.

[22] Kenway, G. K. W., Kennedy, G. J., and Martins, J. R. R. A., "Scalable Parallel Approach for High-Fidelity Steady-State Aeroelastic Analysis and Derivative Computations," *AIAA Journal*, Vol. 52, No. 5, May 2014, pp. 935–951.

[23] Kennedy, G. J., Kenway, G. K., and Martins, J. R. R. A., "A Comparison of Metallic, Composite and Nanocomposite Optimal Transonic Transport Wings," Tech. rep., NASA, March 2014, CR-2014-218185.

[24] Schmit, L. A., "Structural Design by Systematic Synthesis," *2nd Conference on Electronic Computation*, ASCE, New York, NY, 1960, pp. 105–132.

[25] Schmit Jr., L., A., "Structural Synthesis—Its Genesis and Development," *AIAA Journal*, Vol. 19, No. 10, October 1981, pp. 1249–1263.

[26] Haftka, R. T., "Optimization of Flexible Wing Structures Subject to Strength and Induced Drag Constraints," *AIAA Journal*, Vol. 14, No. 8, 1977, pp. 1106–1977.

[27] Haftka, R. T. and Shore, C. P., "Approximate Methods for Combined Thermal/Structural Design," Tech. Rep. TP-1428, NASA, June 1979.

[28] Gill, P. E., Murray, W., and Saunders, M. A., "An SQP algorithm for large-scale constrained optimization," *Society for Industrial and Applied Mathematics*, Vol. 47, No. 1, 2005.

[29] Dennis, J. E., Heinkenschloss, M., and Vicente, L. N., "Trust-region interior-point SQP algorithms for a class of nonlinear programming problems," *SIAM Journal on Control and Optimization*, Vol. 36, 1998, pp. 1750–1794.

[30] Kennedy, J. and Eberhart, R., "Particle Swarm Optimization," *IEEE International Conference on Neural Networks*, Vol. IV, Piscataway, NJ, 1995, pp. 1942–1948.

[31] Goldberg, D. E., *Genetic Algorithms in Search, Optimization and Machine Learning*, chap. 1, Addison-Wesley Longman Publishing, Boston, MA, 1989.

[32] Deb, K., Pratap, A., Agarwal, S., and Meyarivan, T., "A Fast and Elitist Multi-Objective Genetic Algorithm: NSGA-II," Tech. Rep. 200001, Kanpur Genetic Algorithms Laboratory, Indian Institute of Technology Kanpur, 2000.

[33] Dorigo, M., Maniezzo, V., and Colorni, A., "Ant system: optimization by a colony of cooperating agents," *Systems, Man, and Cybernetics, Part B: Cybernetics, IEEE Transactions on*, Vol. 26, No. 1, feb 1996, pp. 29 –41.

[34] Lyu, Z., Xu, Z., and Martins, J. R. R. A., "Benchmarking Optimization Algorithms for Wing Aerodynamic Design Optimization," *Proceedings of the 8th International Conference on Computational Fluid Dynamics*, Chengdu, Sichuan, China, July 2014, ICCFD8-2014-0203.

[35] Kennedy, G. J. and Martins, J. R. R. A., "A Laminate Parametrization Technique for Discrete Ply Angle Problems with Manufacturing Constraints," *Structural and Multidisciplinary Optimization*, Vol. 48, No. 2, August 2013, pp. 379–393.

[36] Hvejsel, C. F., Lund, E., and Stolpe, M., "Optimization strategies for discrete multi-material stiffness optimization," *Structural and Multidisciplinary Optimization*, Vol. 44, No. 2, Aug 2011, pp. 149–163.

[37] Lund, E. and Stegmann, J., "On structural optimization of composite shell structures using a discrete constitutive parametrization," *Wind Energy*, Vol. 8, No. 1, 2005, pp. 109–124.

[38] Niu, B., Olhoff, N., Lund, E., and Cheng, G., "Discrete material optimization of vibrating laminated composite plates for minimum sound radiation," *International Journal of Solids and Structures*, Vol. 47, No. 16, Aug. 2010, pp. 2097–2114.

[39] Zhang, J., Zhang, W.-H., and Zhu, J.-H., "An extended stress-based method for orientation angle optimization of laminated composite structures," *Acta Mechanica Sinica*, Vol. 27, No. 6, Dec. 2011, pp. 977–985.

[40] Khani, A., IJsselmuiden, S., Abdalla, M., and Gurdal, Z., "Design of variable stiffness panels for maximum strength using lamination parameters," *Composites Part B: Engineering*, Vol. 42, No. 3, 2011, pp. 546–552.

[41] Lopes, C., Gurdal, Z., and Camanho, P., "Tailoring for strength of composite steered-fibre panels with cutouts," *Composites Part A: Applied Science and Manufacturing*, Vol. 41, No. 12, 2010, pp. 1760–1767.

[42] Hyer, M. W. and Charette, R. F., "Use of curvilinear fiber format in composite structure design," *AIAA Journal*, Vol. 29, No. 6, June 1991, pp. 1011–1015.

[43] Ijsselmuiden, S. T., Abdalla, M. M., and Gurdal, Z., "Optimization of Variable-Stiffness Panels for Maximum Buckling Load Using Lamination Parameters," *AIAA Journal*, Vol. 48, No. 1, Jan. 2010, pp. 134–143.

[44] Setoodeh, S., Abdalla, M. M., IJsselmuiden, S. T., and Gurdal, Z., "Design of variable-stiffness composite panels for maximum buckling load," *Composite Structures*, Vol. 87, No. 1, 2009, pp. 109–117.

[45] Hyer, M. and Lee, H., "The use of curvilinear fiber format to improve buckling resistance of composite plates with central circular holes," *Composite Structures*, Vol. 18, No. 3, 1991, pp. 239–261.

[46] van Campen, J. M., Kassapoglou, C., and Gurdal, Z., "Generating realistic laminate fiber angle distributions for optimal variable stiffness laminates," *Composites Part B: Engineering*, Vol. 43, No. 2, 2012, pp. 354–360.

[47] Wu, Z., Weaver, P. M., Raju, G., and Kim, B. C., "Buckling analysis and optimisation of variable angle tow composite plates," *Thin-Walled Structures*, Vol. 60, No. 0, 2012, pp. 163 – 172.

[48] Dodwell, T. J., Butler, R., and Rhead, A. T., "Optimum Fiber Steering of Composite Plates for Buckling and Manufacturability," *AIAA Journal*, Vol. 54, No. 3, Jan. 2016, pp. 1146–1149.

[49] Peeters, D. M., Hesse, S., and Abdalla, M. M., "Stacking sequence optimisation of variable stiffness laminates with manufacturing constraints," *Composite Structures*, Vol. 125, No. Supplement C, 2015, pp. 596 – 604.

[50] Wu, Z., Raju, G., and Weaver, P. M., "Optimization of Postbuckling Behaviour of Variable Thickness Composite Panels with Variable Angle Tows: Towards Buckle-Free Design Concept," *International Journal of Solids and Structures*, 2017.

[51] Crothers, P., Drechsler, K., Feltin, D., Herszberg, I., and Kruckenberg, T., "Tailored fibre placement to minimise stress concentrations," *Composites Part A: Applied Science and Manufacturing*, Vol. 28, No. 7, 1997, pp. 619–625.

[52] Jegley, D., Tatting, B., and Gurdal, Z., *Optimization of Elastically Tailored Tow-Placed Plates with Holes*, American Institute of Aeronautics and Astronautics, 2014/05/31 2003.

[53] Parnas, L., Oral, S., and Ceyhan, ., "Optimum design of composite structures with curved fiber courses," *Composites Science and Technology*, Vol. 63, No. 7, 2003, pp. 1071–1082.

[54] Blom, A. W., Abdalla, M. M., and Gurdal, Z., "Optimization of course locations in fiber-placed panels for general fiber angle distributions," *Composites Science and Technology*, Vol. 70, No. 4, 2010, pp. 564–570.

[55] Haddadpour, H. and Zamani, Z., "Curvilinear fiber optimization tools for aeroelastic design of composite wings," *Journal of Fluids and Structures*, Vol. 33, No. Supplement C, Aug. 2012, pp. 180–190.

[56] Stodieck, O., Cooper, J. E., Weaver, P. M., and Kealy, P., "Optimization of Tow-Steered Composite Wing Laminates for Aeroelastic Tailoring," *AIAA Journal*, Vol. 53, No. 8, June 2015, pp. 2203–2215.

[57] Jutte, C. V., Stanford, B. K., Wieseman, C. D., and Moore, J. B., "Aeroelastic Tailoring of the NASA Common Research Model via Novel Material and Structural Configurations," *Proceedings of the AIAA 52nd Aerospace Sciences Meeting*, January 2014.

[58] Stanford, B. K. and Jutte, C. V., "Aeroelastic tailoring via tow steered composites," 2014, TM-2014-218517, NASA Langley Research Center, Hampton, VA.

[59] Stodieck, O., Cooper, J. E., Weaver, P., and Kealy, P., *Optimisation of Tow-Steered Composite Wing Laminates for Aeroelastic Tailoring*, American Institute of Aeronautics and Astronautics, 2014/05/31 2014.

[60] Stodieck, O., Cooper, J. E., Weaver, P. M., and Kealy, P., "Aeroelastic Tailoring of a Representative Wing Box Using Tow-Steered Composites," *AIAA Journal*, Vol. 55, No. 4, April 2017, pp. 1425–1439.

[61] Stanford, B. K. and Jutte, C. V., "Comparison of curvilinear stiffeners and tow steered composites for aeroelastic tailoring of aircraft wings," *Computers & Structures*, Vol. 183, No. Supplement C, 2017, pp. 48 – 60.

[62] Lyu, Z., Kenway, G. K., Paige, C., and Martins, J. R. R. A., "Automatic Differentiation Adjoint of the Reynolds-Averaged Navier–Stokes Equations with a Turbulence Model," *21st AIAA Computational Fluid Dynamics Conference*, San Diego, CA, Jul. 2013.

[63] Liem, R. P., Mader, C. A., and Martins, J. R. R. A., "Surrogate Models and Mixtures of Experts in Aerodynamic Performance Prediction for Aircraft Mission Analysis," *Aerospace Science and Technology*, Vol. 43, June 2015, pp. 126–151, 10.1016/j.ast.2015.02.019.

[64] Kennedy, G. J. and Martins, J. R. R. A., "Parallel Solution Methods for Aerostructural Analysis and Design Optimization," *Proceedings of the 13th AIAA/ISSMO Multidisciplinary Analysis Optimization Conference*, Fort Worth, TX, Sept. 2010, AIAA 2010–9308.

[65] Martins, J. R. R. A., Sturdza, P., and Alonso, J. J., "The Complex-Step Derivative Approximation," *ACM Transactions on Mathematical Software*, Vol. 29, No. 3, 2003, pp. 245–262.

[66] Martins, J. R. R. A., Alonso, J. J., and Reuther, J. J., "A Coupled-Adjoint Sensitivity Analysis Method for High-Fidelity Aero-Structural Design," *Optimization and Engineering*, Vol. 6, No. 1, March 2005, pp. 33–62.

[67] Liem, R., Kenway, G. K. W., and Martins, J. R. R. A., "Multimission Aircraft Fuel Burn Minimization via Multipoint Aerostructural Optimization," *AIAA Journal*, Vol. 53, No. 1, January 2015, pp. 104–122.

[68] Brooks, T. R., Kennedy, G. J., and Martins, J. R. R. A., "High-fidelity Multipoint Aerostructural Optimization of a High Aspect Ratio Tow-steered Composite Wing," *58th AIAA/ASCE/AHS/ASC Structures, Structural Dynamics, and Materials Conference*, American Institute of Aeronautics and Astronautics, Grapevine, TX, January 2017.

[69] Garg, N., Kenway, G. K. W., Lyu, Z., Martins, J. R. R. A., and Young, Y. L., "High-fidelity Hydrodynamic Shape Optimization of a 3-D Hydrofoil," *Journal of Ship Research*, Vol. 59, No. 4, December 2015, pp. 209–226.

[70] Mader, C. A., Kenway, G., and Martins, J. R. R. A., "Towards High-Fidelity Aerostructural Optimization Using a Coupled ADjoint Approach," *Proceedings of the 12th AIAA/ISSMO Multidisciplinary Analysis and Optimization Conference*, Victoria, BC, Sept. 2008, AIAA 2008-5968.

[71] Kennedy, G. J. and Martins, J. R. R. A., "A Parallel Finite-Element Framework for Large-Scale Gradient-Based Design Optimization of High-Performance Structures," *Finite Elements in Analysis and Design*, Vol. 87, September 2014, pp. 56–73.

[72] Uyttersprot, L., *Inverse Distance Weighting Mesh Deformation*, Ph.D. thesis, Delft University of Technology, 2014.

[73] Brown, S. A., "Displacement Extrapolation for CFD+CSM Aeroelastic Analysis," *Proceedings of the 35th AIAA Aerospace Sciences Meeting*, Reno, NV, 1997, AIAA 1997-1090.

[74] Perez, R. E., Jansen, P. W., and Martins, J. R. R. A., "pyOpt: A Python-Based Object-Oriented Framework for Nonlinear Constrained Optimization," *Structural and Multidisciplinary Optimization*, Vol. 45, No. 1, January 2012, pp. 101–118.

[75] Schmitt, V. and Charpin, F., "Pressure distributions on the ONERA-M6-wing at transonic mach numbers," Tech. rep., Office National d'Etudes et Recherches Aerospatiales, 92320, Chatillon, France, 1979.

[76] Brodersen, O. and Stuermer, A., "Drag prediction of engine-airframe interference effects using unstructured Navier-Stokes calculations," *19th AIAA Applied Aerodynamics Conference*, Fluid Dynamics and Co-located Conferences, American Institute of Aeronautics and Astronautics, June 2001.

[77] Vassberg, J. C., DeHaan, M. A., Rivers, S. M., and Wahls, R. A., "Development of a Common Research Model for Applied CFD Validation Studies," 2008, AIAA 2008-6919.

[78] Keye, S., Brodersen, O., and Rivers, M. B., "Investigation of Aeroelastic Effects on the NASA Common Research Model," *Journal of Aircraft*, Vol. 51, No. 4, April 2014, pp. 1323–1330.

[79] Lyu, Z., Kenway, G. K., and Martins, J. R. R. A., "Aerodynamic Shape Optimization Investigations of the Common Research Model Wing Benchmark," *AIAA Journal*, Vol. 53, No. 4, April 2015, pp. 968–985.

[80] Chen, S., Lyu, Z., Kenway, G. K. W., and Martins, J. R. R. A., "Aerodynamic Shape Optimization of the Common Research Model Wing-Body-Tail Configuration," *Journal of Aircraft*, Vol. 53, No. 1, January 2016, pp. 276–293.

[81] Kenway, G. K. W. and Martins, J. R. R. A., "Multipoint Aerodynamic Shape Optimization Investigations of the Common Research Model Wing," *AIAA Journal*, Vol. 54, No. 1, January 2016, pp. 113–128.

[82] LeDoux, S. T., Vassberg, J. C., Young, D. P., Fugal, S., Kamenetskiy, D., Huffman, W. P., Melvin, R. G., and Smith, M. F., "Study Based on the AIAA Aerodynamic Design Optimization Discussion Group Test Cases," *AIAA Journal*, February 2015.

[83] Vassberg, J. and Jameson, A., "Influence of Shape Parameterization on Aerodynamic Shape Optimization," Tech. rep., Von Karman Institute, Brussels, Belgium, April 2014.

[84] Telidetzki, K., Osusky, L., and Zingg, D. W., "Application of Jetstream to a Suite of Aerodynamic Shape Optimization Problems," *52nd Aerospace Sciences Meeting*, Feb. 2014.

[85] Carrier, G., Destarac, D., Dumont, A., Meheut, M., Din, I. S. E., Peter, J., Khelil, S. B., Brezillon, J., and Pestana, M., "Gradient-Based Aerodynamic Optimization with the elsA Software," *52nd Aerospace Sciences Meeting*, Feb. 2014.

[86] LeDoux, S. T., Young, D. P., Fugal, S., Elliott, J. K., Kamenetskiy, D. S., Melvin, R. G., and Huffman, W. P., "A Study Based on the AIAA Aerodynamic Design Optimization Discussion Group Test Cases," *53rd AIAA Aerospace Sciences Meeting*, American Institute of Aeronautics and Astronautics (AIAA), January 2015.

[87] Stanford, B. K., Jutte, C. V., and Wieseman, C. D., "Trim and Structural Optimization of Subsonic Transport Wings Using Nonconventional Aeroelastic Tailoring," *AIAA Journal*, Vol. 54, No. 1, Oct. 2015, pp. 293–309.

[88] Klimmek, T., "Parametric Set-Up of a Structural Model for FERMAT Configuration Aeroelastic and Loads Analysis," *Journal of Aeroelasticity and Structural Dynamics*, Vol. 3, No. 2, 2014, pp. 31–49.

[89] Keye, S., Klimmek, T., Abu-Zurayk, M., Schulze, M., and Ilic, C., "Aero-Structural Optimization of the NASA Common Research Model," *AIAA Aviation and Aeronautics Forum and Exposition (AVIATION)*, June 2017.

[90] Kenway, G. K. W., Kennedy, G. J., and Martins, J. R. R. A., "Aerostructural Optimization of the Common Research Model Configuration," *15th AIAA/ISSMO Multidisciplinary Analysis and Optimization Conference*, Atlanta, GA, June 2014, AIAA 2014-3274.

[91] Burdette, D., Kenway, G. K. W., Lyu, Z., and Martins, J. R. R. A., "Aerostructural Design Optimization of an Adaptive Morphing Trailing Edge Wing," *Proceedings of the AIAA Science and Technology Forum and Exposition (SciTech)*, Kissimmee, FL, January 2015, AIAA 2015-1129.

[92] Brooks, T. R., Kennedy, G. J., and Martins, J. R. R. A., "High-fidelity Aerostructural Optimization of a High Aspect Ratio Tow-steered Wing," *57th AIAA/ASCE/AHS/ASC Structures, Structural Dynamics, and Materials Conference*, American Institute of Aeronautics and Astronautics, January 2016.

[93] Chin, T. W. and Kennedy, G. J., "Large-Scale Compliance-Minimization and Buckling Topology Optimization of the Undeformed Common Research Model Wing," *57th AIAA/ASCE/AHS/ASC Structures, Structural Dynamics, and Materials Conference, AIAA SciTech*, 2016.

[94] Kenway, G. K. and Martins, J. R. R. A., "Buffet Onset Constraint Formulation for Aerodynamic Shape Optimization," *AIAA Journal*, 2016, (Submitted).

[95] Vassberg, J., "A Unified Baseline Grid about the Common Research Model Wing/Body for the Fifth AIAA CFD Drag Prediction Workshop (Invited)," *29th AIAA Applied Aerodynamics Conference*, Jul 2011.

[96] Anonymous, "777-200/300 Airplane Characteristics for Airport Planning," Tech. Rep. D6-58329, Boeing Commercial Airplanes, July 1998.

[97] Bucalem, M. L. and Bathe, K.-J., "Higher-order MITC general shell elements," *International Journal for Numerical Methods in Engineering*, Vol. 36, 1993, pp. 3729–3754.

[98] Kennedy, G. J., Kenway, G. K. W., and Martins, J. R. R. A., "High Aspect Ratio Wing Design: Optimal Aerostructural Tradeoffs for the Next Generation of Materials," *Proceedings of the AIAA Science and Technology Forum and Exposition (SciTech)*, National Harbor, MD, January 2014, AIAA-2014-0596.

[99] Akgün, M. A., Haftka, R. T., Wu, K. C., Walsh, J. L., and Garcelon, J. H., "Efficient Structural Optimization for Multiple Load Cases Using Adjoint Sensitivities," *AIAA Journal*, Vol. 39, No. 3, 2001, pp. 511–516.

[100] Poon, N. M. K. and Martins, J. R. R. A., "An Adaptive Approach to Constraint Aggregation Using Adjoint Sensitivity Analysis," *Structural and Multidisciplinary Optimization*, Vol. 34, No. 1, July 2007, pp. 61–73.

[101] Kenway, G. K. W. and Martins, J. R. R. A., "Buffet Onset Constraint Formulation for Aerodynamic Shape Optimization," *AIAA Journal*, 2017, (In press).

[102] Hwang, J. T. and Martins, J. R. R. A., "GeoMACH: Geometry-centric MDAO of Aircraft Configurations with High Fidelity," *Proceedings of the 14th AIAA/ISSMO Multidisciplinary Analysis Optimization Conference*, Indianapolis, IN, Sept. 2012, AIAA 2012-5605.

[103] Tatting, B. F. and Gurdal, Z., *Design and manufacture of elastically tailored tow placed plates*, Jan. 2002.

[104] Blom, A. W., *Structural Performance of Fiber-Placed, Variable-Stiffness Composite Conical and Cylindrical Shells*, Ph.D. thesis, Delft University of Technology, 2011.

[105] Sethian, J. A., "A fast marching level set method for monotonically advancing fronts," *Proceedings of the National Academy of Sciences*, Vol. 93, No. 4, 1996, pp. 1591–1595.

[106] Bruyneel, M. and Zein, S., "A modified Fast Marching Method for defining fiber placement trajectories over meshes," *Computers & Structures*, Vol. 125, No. Supplement C, 2013, pp. 45–52.

[107] Brampton, C. J., Wu, K. C., and Kim, H. A., "New Optimization Method for Steered Fiber Composites Using the Level Set Method," *Struct. Multidiscip. Optim.*, Vol. 52, No. 3, Sept. 2015, pp. 493–505.

[108] Lemaire, E., Zein, S., and Bruyneel, M., "Optimization of composite structures with curved fiber trajectories," *Composite Structures*, Vol. 131, No. Supplement C, 2015, pp. 895 – 904.

[109] Arreckx, S., Lambe, A., Martins, J. R. R. A., and Orban, D., "A Matrix-Free Augmented Lagrangian Algorithm with Application to Large-Scale Structural Design Optimization," *Optimization and Engineering*, Vol. 17, No. 2, 2016, pp. 359–384.

[110] Bons, N. P., He, X., Mader, C. A., and Martins, J. R. R. A., "Multimodality in Aerodynamic Wing Design Optimization," *18th AIAA/ISSMO Multidisciplinary Analysis and Optimization Conference*, 06/2017 2017.

[111] Gurdal, Z., Tatting, B., and Wu, K., "Variable Stiffness Composite Panels: Effects of Stiffness Variation on the In-Plane and Buckling Response," *Composites Part A: Applied Science and Manufacturing*, Vol. 39, No. 5, 2008, pp. 911–922.

[112] Olmedo, R. and Gurdal, Z., "Buckling Response of Laminates with Spatially Varying Fiber Orientations," Structures, Structural Dynamics, and Materials and Co-located Conferences, American Institute of Aeronautics and Astronautics, April 1993.

[113] Tatting, B. and Gurdal, Z., "Design and manufacture of elastically tailored tow placed plates," Tech. Rep. NASA/CR-2002-211919, NASA, Langley Research Center, Hampton, VA, 2002.